TECHNISCHE UNIVERSITÄT MÜNCHEN
INSTITUT FÜR LUFT- UND RAUMFAHRT

Hypersonic Orbiter Separation from a Carrier

Lei Jiang

Vollständiger Abdruck der von der Fakultät für Maschinenwesen der Technischen Universität München zur Erlangung des akademischen Grades eines

Doktor der Naturwissenschaften

genehmigten Dissertation.

Vorsitzender:		Univ. - Prof. Dr.-Ing. H. Baier
Prüfer der Dissertation:	1.	Univ. - Prof. Dr.-Ing. B. Laschka
	2.	Univ. - Prof. Dr.-Ing. F. Holzapfel
	3.	apl. Prof. Dr.-Ing., Dr. rer. nat. habil. R. Callies

Die Dissertation wurde am 22.11.2011 bei der Technischen Universität München eingereicht und durch die Fakultät für Maschinenwesen am 28.06.2012 angenommen.

ACKNOWLEDGEMENTS

Most of all, I would like to thank my supervisor, Prof. Dr. -Ing. Boris Laschka. He led me to this interesting research area and instructs my thesis even after I left the TUM. The relevant education and training benefit my professional career very much. Also many thanks to Prof. Dr. -Ing. Christian Breitsamter, he has also taught me a lot and spent much time correcting my presentations and theses.

I would like to thank Prof. Dr. -Ing. Florian Holzapfel and Prof. Dr. rer. nat. habil. Dr. -Ing. Rainer Callies for their valuable comments and recommendations. Further I express my gratitude to Prof. Dr. -Ing. Horst Baier for his management works related with my examination and with this thesis.

I will always be grateful to my family, especially to my father, Mr. Huazhong Jiang, my mother, Mrs. Guiying Zhang. Their encouragements and supports always accompany me, particularly in the period when I was working on this thesis. My son, Hanqiu Jiang, was not only the first audience of my presentation, but also a very good helper for me in these years.

Villingen-Schwenningen, October 28, 2012

Lei Jiang

ABSTRACT

To analyze the hypersonic separation process of a two-stage space transport vehicle, its aerodynamic characteristics are numerically simulated by the in-house software FLMNAV with different velocities of freestream, different angles of attack, different distances between two stages, and different separation velocities.

Corresponding to the arranged experiments, three-dimensional models are set up with a detailed orbital stage and a carrier stage idealized by a flat plate. The initial body-fitted meshes are generated by software ICEMCFD, and their orthogonality and smoothness are improved further by the in-house software GRIDFLM. All of the Navier-Stokes equations are transformed into dimensionless curvilinear system. Characteristic boundary conditions are used.

The numerical discretization is based on a finite-volume approximation. The modified AUSM and MUSCL schemes are applied to describe the inviscid flux terms and to catch the strong shock and boundary layer. The viscous flux vectors are discretized by the Chakravarthy method. Except in the region with strong shock and in the boundary layer with great velocity gradient, 2^{nd} order accuracy in space discretization and 1^{st} order accuracy in time discretization are achieved.

Related with the inviscid flow, laminar flow and turbulent flow around the two-stage vehicle, most of the numerical results about the aerodynamic properties are compared with available experimental results. These results present good consistencies. Therefore, the FLMNAV is suitable for simulating the flow physics associated with the two-stage separation process.

In the design environment, the numerical results point out that the separation process is dominated by the shock waves. At a suitable angle of attack, which should be greater than 2° in the beginning of the separation process, positive lift could be achieved. The influence of negative pitching moment in the whole separation process should be well controlled.

ZUSAMMENFASSUNG

Zur Analyse des Separationsmanövers eines zweistufigen Raumtransporters im Hyperschall sind die aerodynamischen Eigenschaften durch die hauseigene Software FLMNAV mit unterschiedlichen Parametern, wie Anstellwinkeln, Abständen zwischen zwei Stufen, Geschwindigkeiten von Anströmung, und Trennungsgeschwindigkeiten, numerisch simuliert worden.

Entsprechend den Experimenten sind dreidimensionale Modelle mit einem detaillierten Orbiter und einer Trägerstufe, idealisiert zu einer flachen Platte, gestaltet worden. Das erste strukturierte Rechennetz wurde von der Software ICEMCFD erzeugt. Ihre Orthogonalität und Glätte sind ferner durch die hauseigene Software GRIDFLM verbessert worden. Alle Navier-Stokes-Gleichungen wurden in dimensionslose krummlinige Systeme transformiert, unter Verwendung von charakteristischen Randbedingungen.

Die numerische Diskretisierung basiert auf einem Finite-Volumen-Verfahren. Die modifizierte AUSM-Diskretisierung und MUSCL-Extrapolation wurden angewendet, um die reibungslosen Flüsse zu beschreiben und um die starken Verdichtungsstöße und die Grenzschichtbereiche zu erfassen. Die reibungsbehafteten Flüsse wurden durch die Chakravarthy Methode diskretisiert. Außer den Regionen mit starken Verdichtungsstößen und drastischen Veränderungen in der Grenzschicht, ist die Genauigkeit der Diskretisierung des Raums zweiter Ordnung und der Diskretisierung der Zeit erster Ordnung erreicht worden.

Bezüglich der reibungslosen, der laminaren und der turbulenten Anströmung wurden die meisten numerischen Ergebnisse mit experimentellen Ergebnissen für zweistufige Raumtransporter verglichen. Beide Ergebnisse haben eine hohe Übereinstimmung. Daher ist die FLMNAV geeignet für die Simulation der Strömungsphysik mit dem zweistufigen Trennverfahren.

Mit der numerischen Simulation der aerodynamischen Eigenschaften kann gezeigt werden, dass das Trennverfahren in der geplanten Umgebung von Stoßwellen dominiert wird. Durch einen geeigneten Anstellwinkel, der größer als 2° am Anfang der Trennung ist, kann ein positiver Auftrieb erreicht werden. Der Einfluss vom negativen Nickmoment sollte im ganzen Separationsmanöver richtig kontrolliert werden.

LIST OF CONTENTS

Nomenclatures

Bold Latin Symbols:

$\mathbf{F, G, H}$	mass flux in curvilinear and dimensionless coordinate system
$\mathbf{J}$	Jacobi matrix for the coordinates transformation
$\mathbf{L}$	reference length of the orbital stage
$\mathbf{L}_{\mathbf{local}}$	reference length of local span of the EOS
$\mathbf{P}$	source terms in grid smoothing
$\mathbf{Q}$	vector of state variables in curvilinear and dimensionless coordinate system; source terms in grid smoothing
$\mathbf{R}$	right hand side of equation; source terms in grid smoothing
$\mathbf{S}$	surround surface of a control volume; the area value
$\mathbf{V}$	control volume; the volume value
$\mathbf{X}_{\mathbf{EOS}}, \mathbf{Y}_{\mathbf{EOS}}, \mathbf{Z}_{\mathbf{EOS}}$	axes of Cartesian coordinate system for EOS
$\mathbf{X}_{\mathbf{T313}}, \mathbf{Y}_{\mathbf{T313}}, \mathbf{Z}_{\mathbf{T313}}$	axes of Cartesian coordinate system in wind tunnel T-313
$\mathbf{f}^{\mathbf{I}}, \mathbf{g}^{\mathbf{I}}, \mathbf{h}^{\mathbf{I}}$	inviscid mass flux in (dimensionless) Cartesian coordinate system
$\mathbf{f}^{\mathbf{V}}, \mathbf{g}^{\mathbf{V}}, \mathbf{h}^{\mathbf{V}}$	viscous mass flux in (dimensionless) Cartesian coordinate system
$\mathbf{h}$	distance between the EOS and flat plate
$\mathbf{h}_{\mathbf{move}}$	distance of upward movement in unsteady case
$\mathbf{q}$	vector of state variables in Cartesian coordinate system
$\mathbf{r}$	coordinate vector

Normal Latin Symbols:

AUSM	Advection Upstream Splitting Method
B-L model	Baldwin-Lomax model
CAE	Computer-Aided Engineering
C_D	drag coefficient
CFD	Computational Fluid Dynamics
CFL	Courant - Friedrichs - Lewy number
C_L	lift coefficient
C_M	pitching moment coefficient

C_p	pressure coefficient
D	drag
DDN	geometry generator, sub-module of ICEMCFD
DNS	Direct Numerical Simulation
EOS	orbital stage of elliptical aerodynamic configuration
E_S	total energy density
Euler	the numerical solution in inviscid flow
Euler simulation	the numerical solution in inviscid flow
Experiment	the measured results in corresponding experiment
F	reference area
$\vec{F}$	force vector
FLMNAV	Navier-Stokes system solver developed by TUM and author
FVM	Finite Volume Method
GRIDFLM	mesh optimization software developed by TUM and author
HEXA	mesh generator, sub-module of ICEMCFD
$\overline{\overline{I}}$	unit tensor
ICEMCFD	commercial geometry creating & meshing software
ITAM	Institute of Theoretical and Applied Mechanics, Novosibirsk
J	Jacobian determinant of transformation
Kn	Knudsen number
L	lift; length
M	moment
M_∞	Mach number of freestream
MUSCL	Monotonic Upstream Scheme for Conservation Laws
N_A	Avogadro's number
Navier-Stokes	the numerical solution in viscous flow
NS	Navier-Stokes, the numerical solution in viscous flow
NS simulation	the numerical solution in viscous flow
Pr	Prandtl number
Pr_t	turbulent Prandtl number
R	specific gas constant
RANS	Reynolds-Averaged Navier-Stokes
Re	Reynolds number
Re_∞	Reynolds number of freestream
Re_m	unit Reynolds number
RWTH Aachen	Rheinisch-Westfälische Technische Hochschule Aachen
S_{aux}	surface area of the auxiliary cell
S_i	projection of surface area on a plane perpendicular to i axis

T	temperature
T_∞	temperature of free-stream
$T_{j,i}$	stress component
T_S	Sutherland's constant
TSTO	Two-Stage to Orbit
U, V, W	contravariant velocity components on ξ, η, ς axes
UFVSM	Upwind Flux-Vector Splitting Method
V_∞	velocity of free-stream
V_{ref}	reference velocity
W	help vector in AUSM; eigenvector
a	speed of sound in air
$\vec{a}$	acceleration
c_p	specific heat at constant pressure
c_v	specific heat at constant volume
$d\mathbf{S}$	infinitesimal surface of the control volume
$d\mathbf{V}$	infinitesimal control volume
e	specific internal energy
$\vec{e}_x, \vec{e}_y, \vec{e}_z$	unit vectors of x, y, z axes
f	force density
g^{ij}	covariant metric coefficients with superscripts i,j=1,2,3
k	coefficient of thermal conductivity
k_{red}	reduced frequency
$\vec{n} = (n_x, n_y, n_z)^T$	unit normal vector on a surface in Cartesian coordinates
p	air pressure
p_∞	freestream pressure
$\dot{q}$	rate of volumetric heat source
q_∞	dynamic pressure
q_i	heat transfer fluxes
t^*	dimensionless time
t_{real}	physical time
u, v, w	velocity components on x, y, z axes
x,y,z	Cartesian coordinates

Greek Symbols:

Δ	increment of some physical properties
$\Delta\alpha$	increment of the angle of attack
$\Lambda_{\xi,}\Lambda_{\eta,}\Lambda_{\zeta}$	eigenvalues of Jacobi matrix
Φ	numerical dissipation coefficient
α	angle of attack; parameter in AUSM for dissipation
α_0	initial angle of attack for a separation process
$\alpha_{\max}$	maximal angle of attack
β	scaling function in AUSM for dissipation
γ	ratio of specific heats
δ	parameter in AUSM for dissipation; thickness of the boundary layer
ε	parameter in AUSM to suppress limiting of solution
ξ,η,ζ	curvilinear coordinates
μ	coefficient of viscosity
μ_t	eddy viscosity
μ_{V}	second coefficient of viscosity
ρ	density
ρ_∞	freestream density
τ	stress vector; phase or time development in numerical simulation
$\bar{\bar{\tau}}$	shear stress tensor
$\tau_{i,j}$	components of stress
ϕ	any one of state variables
ω	verticity; parameter in AUSM for dissipation
$\bar{\bar{\sigma}}$	stress tensor
$\vec{\sigma}_n$	stress vector acting on the closed surface **S**

Upper Indices:

$\bar{\bar{}}$	tensor
$\rightarrow$	vector
*	dimensionless variable

I	index for inviscid flow
Mod AUSM	index for modified AUSM
T	matrix transformation
V	index for viscous flow
VL	index for van Leer formula
n	n-th iteration of the time

Lower Indices:

∞	index for freestream
0	variable on the boundary using a value in the last time step; initial value for an unsteady process
L	index for the left side
Numer	Corresponding variable for numerical model
R	index for the right side
b	variable on the boundary
i	variable on the inner point of the computing domain
i,*j*,*k*	index for the grid point; different coordinates $i, j, k = x, y, z$ or ξ, η, ς
inflow	variable takes the value of freestream in inflow
$k+\frac{1}{2}$	index for the point on the surface of a control cell
m	variable on the mirror point
n	normal direction of the surface
outflow	variable takes the value of freestream in outflow
ref	reference value

Other Symbols:

$\bullet$	inner product
$\times$	vector product
$\otimes$	tensor product
∇	gradient vector
$\mathbf{0}$	zero vector

1 Introduction

1.1 Background of Space Transportation and Separation Process

Flying as a bird in the sky was always the dream of mankind in ancient time. This dream was realized on December 17 in 1903 [68]. On that day, with a powered and heavier-than-air aircraft, Wright Brothers flied 12 seconds and 120 feet in their first flight. Since that historical moment aeronautics and its relative industries expand very rapidly. Already in the time of the Second World War, air forces have become the most powerful force and airplanes have been used as the most important traveling and transport vehicles in the world [3, 5, 68]. To provide more powerful engine than usual airplanes to enter the earth orbit and the outer space, on February 24, 1949, the first hypersonic flight was achieved by a multistage rocket in USA based on the German designed V-2 missile. On April 12, 1961, the world's first spaceship with pilot Gagarin was successfully launched into earth orbit by the Soviet Union [6]. With gradually maturated technique shown in these events, mankind flies more quickly, highly, and safely in the space. Nowadays, the space technique is already widely applied and becomes indispensable in many commercial and military activities as well as in our daily life. The most obvious examples could be easily found in the area of satellite navigation, satellite television, weather forecast, communication, geological exploration, and military reconnaissance.

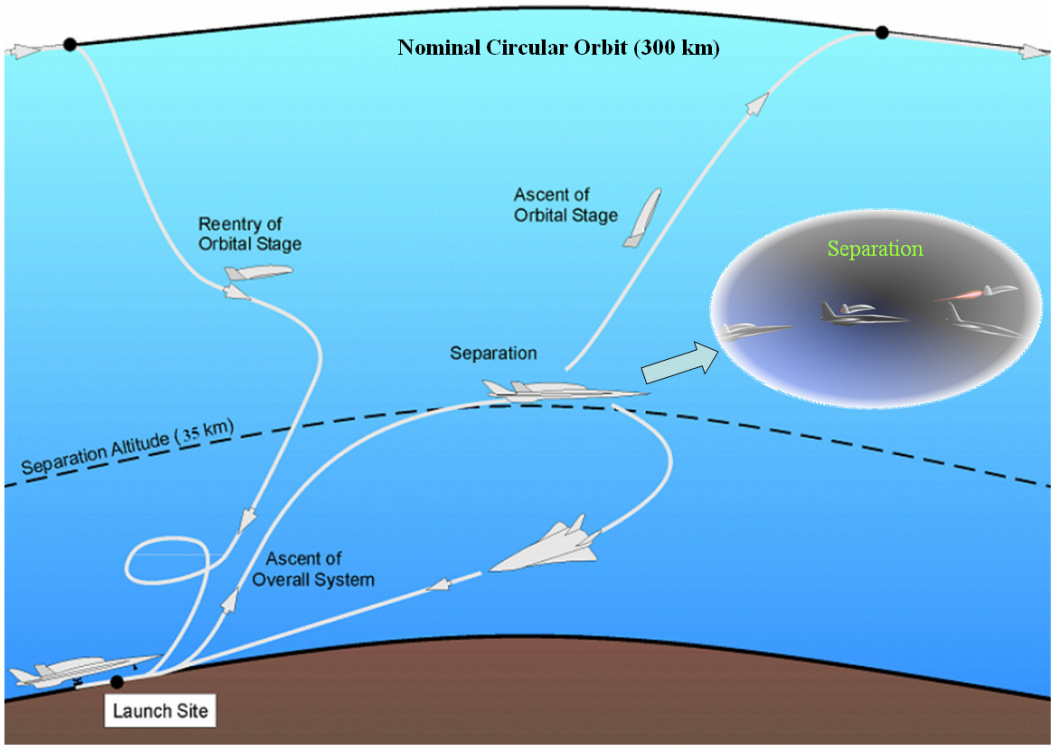

Figure 1.1: Typical flight mission of the two-stage space transportation system[1].

[1] Picture refers to M. Mayrhofer und G. Sachs, „Aspekte der Flugbahn-Optimierung für zweistufige Raumtransportsysteme", Seminar des Sonderforschungsbereichs 255, TUM, 12. Dez. 2002, pp89-102.

Even though the aeronautic and astronautic technologies become more sophistic, and mankind has already launched many space vehicles, it is still very expensive to send payloads into space. For example, it costs about 11000 US dollar per kilogram using the space shuttle or ARIANA rocket to carry payloads to the low earth orbit. To send satellites, machines, even people to orbit as cheaply as possible, many reusable space vehicle systems are developed [81].

A type of two-stage to orbit (TSTO) system is researched by many countries. It consists of a carrier stage and an orbital stage and both stages are intended to be reused. Its whole flying mission is illustrated in Figure 1.1. The carrier stage is used to replace the launching rocket. It is designed to take off and to land horizontally as an ordinary airplane to fully make use of ordinary airport. The orbital stage is designed as a space shuttle. It is attached on the back of carrier stage before the separation process. At the separation altitude of about 35 kilometers, a strut mechanism from carrier stage raises the orbital stage up with a designed angle of attack. Flying at Mach number of about 6.8, the orbital stage separates from the carrier stage as shown in a series of simulative pictures embedded in Figure 1.1. Next it climbs to an orbit around the earth by itself. After fulfilling its tasks, the orbital stage comes back to earth like the space shuttle. This type of TSTO could save much expenditure by reusing both carrier and orbiter many times. No new launching and landing bases should be built specially for these space vehicles.

Some carriers directly make use of huge conventional transport aircrafts to carry the orbital stage. This type of carrier could save much developing cost and has been researched in AN 225 / Interim HOTOL (Horizontal Take-Off and Landing) by Great Britain, which is exhibited in Figure 1.2. It is also been investigated in MAKS system by Russia. However, the rarity of the air at very high altitude confines the flight of usual airplane. The drawback using a conventional aircraft as a carrier is that the orbital stage has to carry more fuel to arrive to the earth orbit.

Figure 1.2: Conventional aircraft carrying an orbiter in the HOTOL model[2].

To carry the orbiter to a highest flight level with a maximal speed, some of the carriers are designed to equip with airbreathing hypersonic engines. They are studied in NASA Hyper-X program [35], in “Future European Space Transportation Investigations Program” (FESTIP) [57], in German development program “Technologies for Future Space Transport System” (Technologien für zukünftige Raumtransport-Systeme, TETRA) [16], and in France PREPHA program [63].

In Germany the TSTO models are developed originally according to the Sänger’s concept [31, 44,

[2] Photo from http://www.spacefuture.com/vehicles/designs.shtml.

56, 90] as shown in Figure 1.3. It is a two-stage vehicle with delta wings. The carrier stage is propelled by the airbreathing scramjet (supersonic combustion ramjet engines [5, 33]). Since this engine could combust the oxygen in the air, it could bring less fuel than rockets. Further it could propel the space vehicles to the height of about 35 km at Mach 6.8. In contrast, normal jet engines could not work properly in that attenuate air with scare oxygen. Usually the conventional airplanes could only reach the altitude of about 24 kilometers.

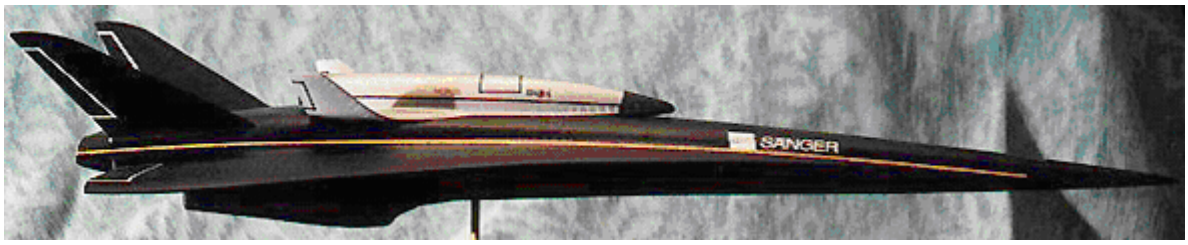

Figure 1.3: Configuration of the orbital and carrier stages in Sänger's concept.

On March 27, 2004, the NASA's second X-43A hypersonic research aircraft, equipped with an airbreathing scramjet, successfully flied at Mach 6.8. As shown in Figure 1.4, this flight was photographed at the altitude about 29 Kilometers. In a further flight on Nov. 16, 2004, its speed reached nearly Mach 10.

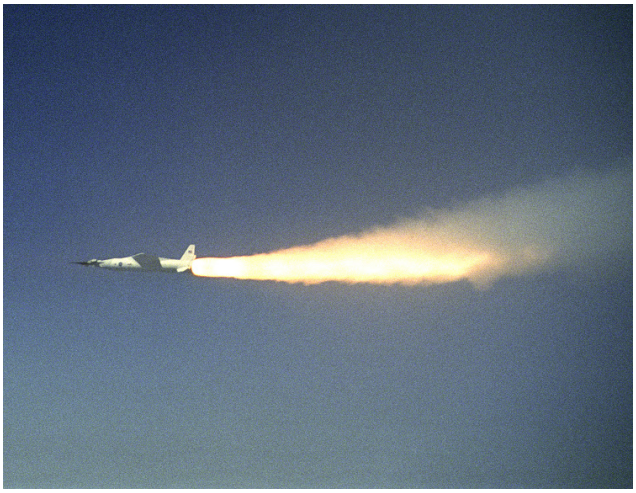

Figure 1.4: NASA's X-43A hypersonic research aircraft propelled by an air-breathing scramjet[3].

The whole flight mission shown in Figure 1.1 is a very complex procedure. One of the most critical phases is its separation process. There is a collision possibility when two stages separate at the altitude of about 35 kilometers with a hypersonic speed of Mach 6.8. Before this separation process begins, the two stages are closely aligned. In Figure 1.5, the separation process is further animated through a series of position changes of the orbiter. That is, the orbiter rises up, changes its angle of attack, and separates from the carrier. Because the separation time is very short, there is usually no much time to manually adjust the separation maneuver. The aerodynamic properties, such as lift, drag,

[3] NASA photo from http://www.dfrc.nasa.gov/Gallery/Photo/X-43A/Large/EC04-0092-32.jpg.

and pitching moment, decide the separation maneuver. These properties are mainly affected by shock waves, by expansion waves, and by boundary layers [8, 50, 54, 62]. For a safe maneuver, we should clearly know how the aerodynamic properties of two stages behave in the whole separation process.

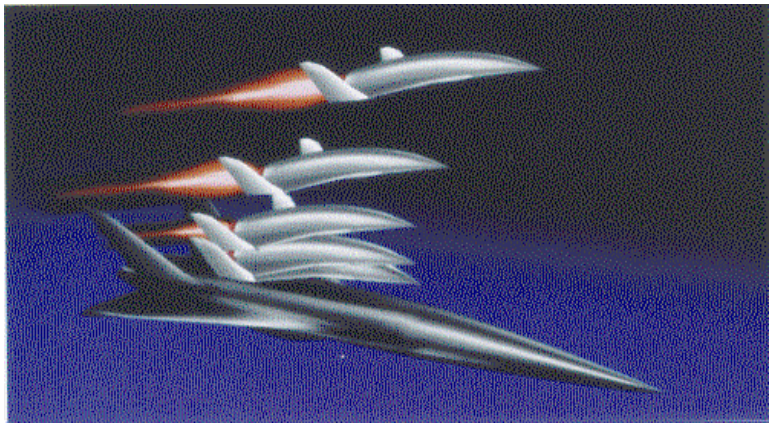

Figure 1.5: A series of position changes of an orbiter in a separation process.

1.2 Features of the Hypersonic Flight and Its Research Methods

Flying at hypersonic speed leads to many different critical characteristics compared to the lower speed regime. The hypersonic speed means that a velocity possesses a very high Mach number which is conventionally higher than 5. It is usually related with the phenomena at high altitude. Furthermore, the hypersonic flow characterizes with lower density flow, thin shock layers, stronger entropy gradient layer, stronger viscous interaction, and very high temperature [46, 76]. More detailed characters of hypersonic flow are listed in Appendix J.

By comparing to the environment at sea level [87], we illustrate the environment at the separation altitude. At sea level it is 1.2 kg/m^3. At the height of about 35 kilometers, the density of the air is about 8.2×10^{-3} kg/m^3. The air density at high altitude is only 0.68% of that at the sea level. The air density decreases with the increase of the altitude. Similarly, the air pressure is only 0.55% corresponding to the pressure at the sea level. The air temperature at the height of about 35 kilometers is about -36.10 °C. In Appendix K, detailed atmosphere properties related with different altitude in a steady state are presented and could be calculated by a short FORTRAN program.

To describe hypersonic flights, different theoretical models have been set up and many experiments have been conducted. Theory and experiment are two basic research tools in fluid dynamics. Generally speaking, it is not easy to get an analytical solution from theoretical models. On the other side, the corresponding experiments are very expensive and very difficult to generate the exact environment of the hypersonic flight in space. In the mid-1960s, a successful numerical simulation of the hypersonic flow field about the blunt body returning to earth atmosphere [70, 94] set up a new era about computational fluid dynamics (CFD). CFD has become the “third dimension” [4] of fluid dynamics in comparison to the theoretical and experimental methods. Now it already becomes indispensable for the research, design, and optimization, because it reduces the cost of

development; it enables us to simulate the situation that could not be exactly achieved by experiments; it could investigate many different configurations in a short time; it could provide the detailed flow field information in the whole computational domain. Actually, the aerodynamics of space vehicle in hypersonic flow is researched with the synergistic combination of pure theoretical analysis with high abstraction, carefully designed experiments, and CFD supported by high performance computer.

1.3 Relevant Research Works

Already in 1968 Decker and Gera have studied two parallel re-entry bodies and determined the aerodynamic characteristics relating with the alignment and position of the two stages [25]. Bernot researched the separation between liquid-fuel tank and the shuttle in 1970's [8]. Thereafter, Esch in 1990 measured the force induced from separation process in hypersonic wind tunnels [31]. Also in 1990, Mukovozov proposed an empirical method to determining the interference of the aerodynamic characteristics between fuel tank and the Buran vehicle during separation [71]. Schröder et al. divide the separation process into three flight phases and pointed out the pitching moment is the most susceptible coefficient in 1993 [82]. Brenner used an Euler program and gave a 3D numerical simulation of the vertical launched TSTO separation also in this year [14]. In 1995 Bonnefond et al. presented the aerodynamic interferences occurring in the separation of two winged stages [9, 10]. Weiland in 1996 indicated the complicated flow field in the gap between the both stages leading to aerodynamic and thermal loads [92]. The numerical simulations and experiments listed above show the early works related to some separation processes between two different objects.

To thoroughly investigate the aerodynamic properties of the two stages and assure the safe separation of TSTO system, systematic investigations have been done in the project "Trans-atmospheric Flight Systems" in Collaborative Research Center 255 of Technische Universität München supported by the German Research Association (Deutsche Forschungsgemeinschaft). These researches begin from some simple geometry shapes, such as a delta-wing [40] or a blunt cone [39]. Some uses 2D geometries [24]. Accompanying the development of the numerical tools, the simulated geometries have been extended to simplified 3D models [11, 48, 51] and even complete two-stages [12, 13, 50, 69]. Besides the mathematical models are evolved from Euler equation system [26, 79] to Navier-Stokes 2D- [24] and 3D- [20, 48] equation systems, and even to turbulence equation system regarded here. Further, the description of the separation process is developed from a set of steady points [67, 99] to continuous unsteady processes [20-23, 28, 49, 80].

Although the most important part of separation maneuver is actually an unsteady process [59, 60], it was only studied in inviscid flow or 2D case in viscous flow due to its complexity. Based on the results of Euler simulations, Rochholz et al. showed that the effects of unsteady flows during separation due to the shock interactions between the upper stage and lower stage are non-negligible [79, 80]. This indication is also supported by Cvrlje et al., who performed numerical simulations involving both roll- and yaw- motions of an orbital vehicle for different reduced frequencies [20-23]. Cvrlje also presented the effect of unsteady flows including laminar boundary layers on the

longitudinal motions of a 2D idealized two-stage hypersonic vehicle during separation [24]. For inviscid flow related with both the separation process and the vehicle returning to the atmosphere, some of the unsteady cases with complex geometry are given by Decker [26, 28]. Also with inviscid flow, the simulation works corresponding to the two complete geometries of TSTO system are mainly done by Moelyadi [50, 69]. Cvrlje has simulated three-dimensional EOS free flying in laminar flow at some small Mach numbers [20].

1.4 Thesis Outline

As presented by the relevant research works, the separation process has not been thoroughly investigated, especially in context with a 3D TSTO geometry in laminar flow and in turbulent flow. To investigate these topics, simplified geometries are built in Chapter 2. As a theoretical preparation, a brief outline about the derivation of the differential equations, such as Euler equations, Navier-Stokes equations, and turbulence model, is presented to describe the separation process theoretically. Due to the complexity about the theoretical derivation, many details have been moved to Appendixes A-H. Based on a numerical method - Finite Volume Method, a solver FLMNAV mainly for hypersonic flow is developed. Special numerical techniques are used to capture the shock and distinguish the slip lines. Except the above region they possess 2^{nd} order spatial accuracy and are discussed in Chapter 3. The FLMNAV is written in Fortran 90 and could be executed on both super computer using UNIX system and on PC using window system. These differential equations are discretized on a structured body-fitted grid. Software ICEM CFD package is used as a pre-processor of FLMNAV, and graphic software Tecplot as the post-processor. Another in-house software – GRIDFLM, which is mentioned in Chapter 4, improves the orthogonality and smoothness of the mesh.

Experiments are carefully arranged to study the separation process as described in Chapter 5. The carrier stage is idealized as a flat plate with a complex orbital stage, namely EOS (an abbreviation of ELAC's Orbital Stage) [11]. The experimental results are obtained in the ITAM SB T-313 [54] wind tunnel tests and in TH2-D [37, 74] shock tunnel tests with Mach numbers of 4.05 and 7.9, respectively. These experiments are used to validate the numerical solver FLMNAV for the hypersonic flow in this thesis.

Many steady and unsteady cases are numerically simulated for the TSTO space transportation system. The aerodynamic effects are analyzed in inviscid, laminar, and turbulent flow models. The investigations include three phases of the separation process as illustrated in Figure 1.5: The first phase describes TSTO vehicles flying with some fixed positions. This can be interpreted as the beginning of the separation or as approximating a dynamic separation process by some fixed positions. It is a steady case. The second phase describes the dynamic separation process. It consists of an unsteady case. The third phase shows the end of separation with the free flight of the orbiter.

Using the same environment as in the arranged experiments, many cases are numerically simulated and compared with the experimental results. Related to Mach numbers, angles of attack,

and separation distances, these simulations have been sorted at Mach 4.05 in Chapter 6 and at Mach 7.9 in Chapter 7. In Chapter 8, numerical predictions about the separation process of the TSTO are shown for steady and unsteady cases at Mach 6.8.

Except the appendixes already mentioned above, some more topics about the basic aerodynamic definitions and a real gas model are listed in Appendixes I and L. The latter is referred as an improvement in the future work.

Results from Chapters 6 – 8 clearly illustrate that a shock generated at the bow of the orbiter hits the carrier at first. Then the bow shock could rebound back and impinge again on the orbiter. Some expansions also appear in some regions. These shock systems strongly affect the aerodynamic properties of the two stages, such as pressure, density, and forces.

2 Physical and Mathematical Models

To simulate the separation process, a simplified TSTO geometry model has been set up as shown in Figure 2.1 corresponding to a series of experiments [11, 38, 54]. The Navier-Stokes equation system is applied to describe the flow field around the two stages. To make closure of the equations, the calorically perfect gas model is added into the differential equation system. The influence of the laminar flow model has been investigated in this separation process. Due to the complex nature of boundary layers, the effect of inviscid flow is researched as a NS model simplification. A turbulence model is also applied because of the great Reynolds number in the separation process. To construct a well posed differential equation system, characteristic boundary conditions are used and simple initial conditions are assigned in time-developing procedures.

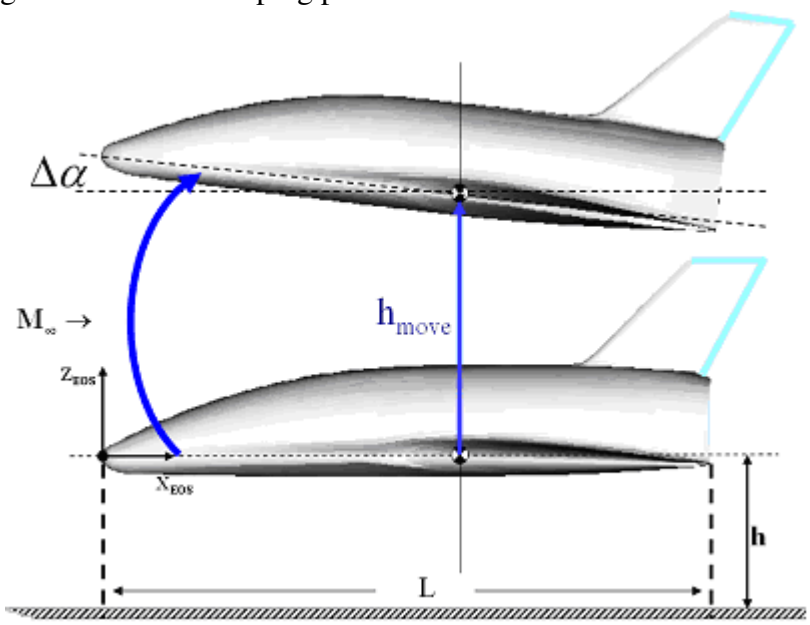

Figure 2.1: The EOS and the flat plate in simulating the separation process.

2.1 Geometry Models and Fluid Assumptions

As a simplified geometric model for the TSTO space transport system, a detailed orbital stage EOS (the lower EOS configuration in Figure 2.1) is used while the carrier stage is modeled by an infinite flat plate (the bottom plate in Figure 2.1). The parameter **h** refers to the distance from $\mathbf{X}_{\mathbf{EOS}}$-axis to the flat plate; **L** is the body length of the EOS. In the separation process the orbiter rises upwards and increases of the angle of attack. This procedure is also illustrated in Figure 2.1 by the simplified model. That is, the lower EOS configuration moves a distance $\mathbf{h}_{\mathbf{move}}$ upwards, changes its angle of attack $\Delta\alpha$, and finally arrives to the upper EOS configuration.

Developed from the Sänger's concept, the separation process will be arranged at an altitude of 35 kilometers above the sea level. As listed in Appendix K, some important environment parameters in that altitude are referred as: the density of air ρ=0.0082 kg/m^3, the pressure p=558.92 Pa, and temperature T=237.05 K. Related to the air characteristics, the mean free path could be calculated by

$$l_{mean\ free\ path} = \frac{R \cdot T}{\sqrt{2} \cdot \pi \cdot d^2 \cdot N_A \cdot p}, \tag{2.1}$$

where the universal gas constant R=8.314 J/(mol K), Avogadro's number N_A= $6.022 \cdot 10^{23}$ 1/mol, and the diameter of the air molecule $d \approx 3 \cdot 10^{-10}$ m. Consequently, the length of the mean free path $l_{mean\ free\ path} = 1.46 \cdot 10^{-5}$ m. Comparing with the designed length of the orbital stage **L** =28.8 m, the Knudsen number Kn is obtained by

$$Kn = \frac{l_{mean\ free\ path}}{\mathbf{L}} = 0.51 \times 10^{-6}. \tag{2.2}$$

Usually the air could be considered as a continuous fluid, if

$$Kn \le 0.01. \tag{2.3}$$

Therefore, at the altitude of 35 kilometers, the length of mean free path can be neglected comparing with the reference length of the orbiter. The molecules of the air are still dense enough to be considered as a continuous fluid, though the air density is already very small. The fluid continuum assumption is still acceptable in the investigation of the separation process.

In the following chapters, the separation process is simulated in different freestreams with Mach numbers of 4.05, 6.8 and 7.9, respectively. The Prandtl number of the air Pr = 0.72. The Reynolds number Re is in the range of 2.19×10^6 to 3.24×10^7 corresponding to different cases. Thereinafter, it is also assumed that the stress is linearly dependent on the rate of deformation. The entropy of the flow always increases.

Because of its relatively small mass, the orbital stage is more sensitive to the aerodynamic interaction than the carrier stage. Hence, we mainly study the aerodynamic properties of the EOS.

2.2 Navier-Stokes and Euler Equation Systems

The full Navier-Stokes equation system is used to predict the fluid dynamics around the two stages. Based on the continuum assumption of the fluid and the assumption of viscosity, this partial differential equation system is derived from the conservation laws of mass, momentum, and energy. Its derivation is attributed to Navier and Stokes in 19 century. Actually the theoretical research began as early as in 1726. Sir Isaac Newton recognized that both air and water move in similar ways. He also presented the dynamic forces dependent on the fluid density, on the fluid velocity, and on the shape and size of the object. In 1755 Euler gave a mathematical formulation of the principle of conservation of mass in terms of a partial differential equation. Modeled the dissipative effects in viscous flows by Navier and Stokes, the Navier-Stokes differential equations are now the most general system to describe the movements and energy changes for Newtonian fluid.

In Cartesian coordinates x, y, z, with time t, the Navier-Stokes differential vector equation [20, 45] is given as:

$$\frac{\partial \mathbf{q}}{\partial t}+\frac{\partial(\mathbf{f}^I-\mathbf{f}^V)}{\partial x}+\frac{\partial(\mathbf{g}^I-\mathbf{g}^V)}{\partial y}+\frac{\partial(\mathbf{h}^I-\mathbf{h}^V)}{\partial z}=\mathbf{0}, \tag{2.4}$$

with the state variable vector $\mathbf{q}=(\rho,\rho u,\rho v,\rho w,E_S)^T$, the density ρ, the velocity vector $\vec{V}=(u,v,w)^T$, the total energy density $E_S := \rho(\frac{|\vec{V}|^2}{2}+e)$, and the specific internal energy e. Further p denotes the pressure. The inviscid flux vectors are given as:

$$\mathbf{f}^I=\begin{bmatrix}\rho u\\ \rho u^2+p\\ \rho uv\\ \rho uw\\ (E_S+p)u\end{bmatrix},\ \mathbf{g}^I=\begin{bmatrix}\rho v\\ \rho vu\\ \rho v^2+p\\ \rho vw\\ (E_S+p)v\end{bmatrix},\ \mathbf{h}^I=\begin{bmatrix}\rho w\\ \rho wu\\ \rho wv\\ \rho w^2+p\\ (E_S+p)w\end{bmatrix}. \tag{2.5}$$

The viscous flux vectors are determined by:

$$\mathbf{f}^V=\begin{bmatrix}0\\ \tau_{xx}\\ \tau_{yx}\\ \tau_{zx}\\ \Pi_x\end{bmatrix},\ \mathbf{g}^V=\begin{bmatrix}0\\ \tau_{xy}\\ \tau_{yy}\\ \tau_{zy}\\ \Pi_y\end{bmatrix},\ \mathbf{h}^V=\begin{bmatrix}0\\ \tau_{xz}\\ \tau_{yz}\\ \tau_{zz}\\ \Pi_z\end{bmatrix}, \tag{2.6}$$

where

$$\Pi_x=u\cdot\tau_{xx}+v\cdot\tau_{yx}+w\cdot\tau_{zx}-q_x, \tag{2.7}$$

$$\Pi_y=u\cdot\tau_{xy}+v\cdot\tau_{yy}+w\cdot\tau_{zy}-q_y, \tag{2.8}$$

$$\Pi_z=u\cdot\tau_{xz}+v\cdot\tau_{yz}+w\cdot\tau_{zz}-q_z, \tag{2.9}$$

and τ_{ij} is a stress component and q_i is the flux of heat transfer with subscripts $i,j=x,y,z$.

The full Navier-Stokes equations still need the calorically perfect gas equation as a supplement. It describes the properties of specified gas as

$$p=(\gamma-1)\cdot[E_S-\frac{\rho}{2}(u^2+v^2+w^2)], \tag{2.10}$$

where $\gamma=c_p/c_v$ as the ratio of specific heats. c_v and c_p are the specific heats at constant volume as well as at constant pressure, respectively. For the air at standard condition $\gamma=1.4$.

The Navier-Stokes equations are additionally transferred into dimensionless form. Then the results from the numerical simulation could be applied to other phenomena with same similarity parameters, instead of possessing only one confined instance. Most of important similarity parameters could also be abstracted from the non-dimensionalized Navier-Stokes equations. The dimensionless variables are defined as

$$x = x^* \cdot L_{ref}, \quad y = y^* \cdot L_{ref}, \quad z = z^* \cdot L_{ref}, \quad t = t^* \cdot t_{ref}, \tag{2.11}$$

$$\rho = \rho^* \cdot \rho_{ref}, \quad u = u^* \cdot V_{ref}, \quad v = v^* \cdot V_{ref}, \quad w = w^* \cdot V_{ref}, \tag{2.12}$$

$$\mu = \mu^* \cdot \mu_{ref}, \quad T = T^* \cdot T_{ref}, \quad p = p^* \cdot p_{ref}, \quad E_S = E_S^* \cdot E_{ref}. \tag{2.13}$$

The superscript * presents the dimensionless variable, and with subscript *ref* as the reference value. A detailed derivation of non-dimensionalization for the Navier-Stokes equation system is given in Appendix D. For the reason of simplification, the superscript * is omitted in the following sections and chapters. Thereafter all equations are considered using the dimensionless form.

The geometrical shape of a body and its boundary layer play important roles in fluid dynamics. In order to describe the aerodynamic properties in the boundary layer and in its neighborhood more accurately, it is important that the mesh points are well distributed on the solid surface of the body. This body fitted mesh should not only describe the geometry exactly, but should also be easier to apply boundary conditions. Actually, it is much easier to make the mesh denser or sparser in the boundary layer or other domains by adjusting parameters in the meshing software, such as commercial software ICEM CFD, comparing to the meshing manipulation for the traditional rectangular meshes.

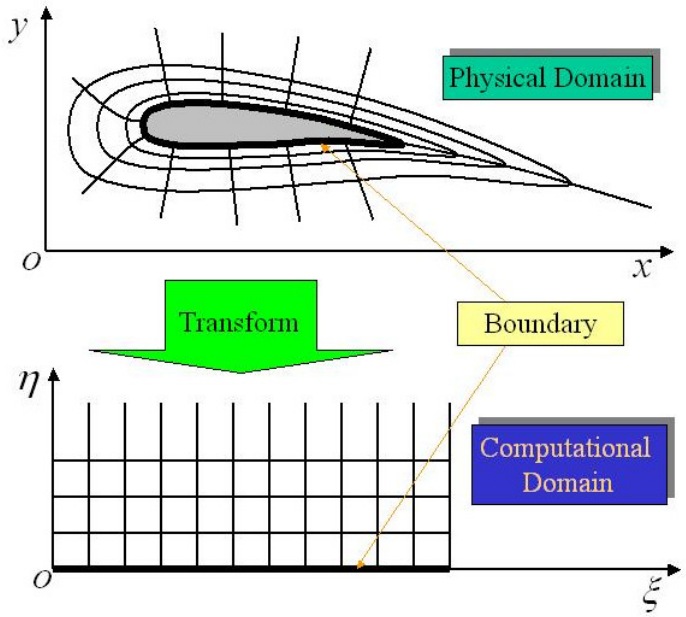

Figure 2.2: Transformation from physical domain to computational domain.

However, extra effort is needed to discretize the Navier-Stokes equations on the body fitted mesh. We transform the Navier-Stokes equations from the Cartesian coordinate system into the curvilinear form, and simultaneously transform the physical domain into computational domain. Figure 2.2 shows a 2D-transformation example from the physical domain in Cartesian coordinates (*x, y, t*) to the computational domain in curvilinear coordinates (ξ, η, τ). Hereby we see that a complex body fitted mesh is transformed into the traditional rectangular mesh system.

The 3-dimensional transformation from Cartesian coordinates (*x, y, z, t*) to curvilinear coordinates (ξ, η, ζ, τ) is defined as:

$$t = \tau, \tag{2.14}$$

$$x = x(\xi, \eta, \zeta, \tau), \tag{2.15}$$

$$y = y(\xi, \eta, \zeta, \tau), \tag{2.16}$$

$$z = z(\xi, \eta, \zeta, \tau). \tag{2.17}$$

The mathematical transformations defined by Eqs. (2.14) - (2.17) change the shape of geometry and the forms of Navier-Stokes equations. Their numerical accuracy plays a fundamental role in the numerical simulation.

The dimensionless Navier-Stokes vector equation is written in curvilinear form as:

$$\frac{\partial \mathbf{Q}}{\partial \tau} + \frac{\partial \left(\mathbf{F}^I - \mathbf{F}^V \right)}{\partial \xi} + \frac{\partial \left(\mathbf{G}^I - \mathbf{G}^V \right)}{\partial \eta} + \frac{\partial \left(\mathbf{H}^I - \mathbf{H}^V \right)}{\partial \zeta} = 0, \tag{2.18}$$

where the solution variables are

$$\mathbf{Q} = J\mathbf{q} = J\left(\rho, \rho u, \rho v, \rho w, E_S \right)^T. \tag{2.19}$$

The inviscid flux terms are obtained as

$$\mathbf{F}^I = J \begin{pmatrix} \rho U \\ \rho u U + \xi_x p \\ \rho v U + \xi_y p \\ \rho w U + \xi_z p \\ U(E_S + p) - \xi_t p \end{pmatrix}, \tag{2.20}$$

$$\mathbf{G}^I = J \begin{pmatrix} \rho V \\ \rho u V + \eta_x p \\ \rho v V + \eta_y p \\ \rho w V + \eta_z p \\ V(E_S + p) - \eta_t p \end{pmatrix}, \tag{2.21}$$

$$\mathbf{H}^I = J \begin{pmatrix} \rho W \\ \rho u W + \zeta_x p \\ \rho v W + \zeta_y p \\ \rho v W + \zeta_z p \\ W(E_S + p) - \zeta_t p \end{pmatrix}, \tag{2.22}$$

where the contravariant velocities are given by

$$U = \xi_x u + \xi_y v + \xi_z w + \xi_t, \tag{2.23}$$

$$V = \eta_x u + \eta_y v + \eta_z w + \eta_t, \tag{2.24}$$

$$W = \zeta_x u + \zeta_y v + \zeta_z w + \zeta_t, \tag{2.25}$$

and the viscous flux terms are expressed as

$$\mathbf{F}^V = J\left(\xi_x \mathbf{f}^V + \xi_y \mathbf{g}^V + \xi_z \mathbf{h}^V\right), \tag{2.26}$$

$$\mathbf{G}^V = J\left(\eta_x \mathbf{f}^V + \eta_y \mathbf{g}^V + \eta_z \mathbf{h}^V\right), \tag{2.27}$$

$$\mathbf{H}^V = J\left(\zeta_x \mathbf{f}^V + \zeta_y \mathbf{g}^V + \zeta_z \mathbf{h}^V\right). \tag{2.28}$$

More details about the above inviscid and viscous flux terms as well as the curvilinear transformation are described in Appendix E.

Mathematically the Navier-Stokes equation system (2.18) is a complex hybrid differential system. It represents elliptic, parabolic and hyperbolic characteristics corresponding to different cases. Some analytical solutions could be obtained only for extremely simplified cases. In Appendixes A - G, the complete Navier-Stokes equations are strictly derived in detail. Consequently, the definition of mathematical symbols, derivation of conservation equations, Navier-Stokes assumptions about stress and friction, dimensionless form, initial conditions and boundary conditions, which are used in this paper, could be found in these appendixes.

When the viscosity of fluid is very small, the heat conductivity terms could be also neglected due to no dissipative phenomena [42, 43]. With these assumptions, the Euler equation system [61] can be directly derived from the above Navier-Stokes equations. So Euler equation system describes an ideal case with no friction in flow. According to the Prandtl's boundary layer theory, the Euler equation system is suitable to depict the flows, which is located in the outside of the boundary layer and dominated by convective character. Actually, it is often used as an approximation and simplification of the Navier-Stokes equation system.

As Euler equation system physically is a wave transfer system and it describes some quantities propagating along characteristic lines. Based on this character, some numerical methods have been proposed and the characteristic boundary conditions are derived. The Navier-Stokes equation system also utilizes this type of boundary conditions.

Because Euler equation system needs not to describe the most difficult changes in very thin boundary layer, most of its solvers are sophisticatedly developed. These solvers use much less CPU time and memory space than the corresponding solvers for Navier-Stokes equation system. On the other hand, Navier-Stokes solvers directly use many techniques developed for Euler Solvers.

2.3 Turbulence Model

In the designed separation process, the corresponding Reynolds numbers range typically around the order of 10^7. Turbulent phenomena are of importance in the corresponding hypersonic flow field. It is generally characterized by a high irregular and full 3-dimensional flow including many vortices. Turbulent flow also causes rapid mixing and flow resistance. It increases heat transfer and enhances

the dissipation of energy. The smallest scale of turbulence is known as Kolmogorov microscale and generally much larger than the scale of the molecular mixing length.

The most exact simulation about turbulent phenomena is the direct numerical simulation (DNS). It directly solves the Navier-Stokes equations with resolving all of the important motions contained in the flow. To simulate not only the largest eddies in large scale, but also the kinetic energy dissipation in the size of very small Kolmogorov microscale, the number of the grid points should be of the order of $\mathrm{Re}^{9/4} \cdot 10^{-6}$ as mentioned by Ferziger and Peric [32]. This means to distinguish the all vorticities in the TSTO separation process, the number of the grid points should be in order of about $10^9 - 10^{10}$. More computing work is further needed to simulate the unsteady separation, because the time step size is related to the grid size. This demand of computational effort of DNS is still out of the capacity of our computers.

To overcome the unrealizability of DNS, many methods are developed using coarse meshes. Still describing most characteristics of the turbulent phenomena, some techniques, such as correlations, integral equations, averaged equations, two-point closures, and large eddy simulation, are used to reduce the computational effort. The simplest turbulence models are constructed by algebraic relations between the turbulence variables and the averaged flow quantities, i.e. zero equation models. In contrast, the complex models may involve one or more partial differential equations. They could account the effects of flow history, and etc. Turbulence models are usually developed from theoretical consideration supplemented with empirical relations. Developing an efficient and exact turbulence model is still one of the most difficult topics.

Nowadays, there is still no general turbulence model that is suitable for all flow problems. As an algebraic turbulence model developed originally for aeronautical complicated flow, the Baldwin-Lomax turbulence model (B-L model) provides a convenient closure to the Reynolds-Averaged Navier-Stokes (RANS) equations [7]. Usually it could describe high-speed flows with high Reynolds number and with thin attached boundary layers. It has the same form as the Navier-Stokes equations and could be solved using relatively less CPU time. Because it is easy to understand and implement, it is still used in many CFD codes.

Actually B-L model is a two-layer, algebraic, and eddy viscosity model. The viscosity in Navier-Stokes equations is replaced by the sum of viscosity $\mu + \mu_t$ in B-L model, where μ is the original viscosity in Navier-Stokes equations and μ_t is an extra viscosity to include the microscale effect of the turbulent flow. Simultaneously, the heat conductivity $k = c_p \cdot \mu / \mathrm{Pr}$ in Navier-Stokes equations is replaced by $k = c_p \cdot \left(\frac{\mu}{\mathrm{Pr}} + \frac{\mu_t}{\mathrm{Pr}_t} \right)$, where turbulent Prandtl number Pr_t is a ratio of eddy viscosity and eddy thermal diffusivity.

In the region near the wall the Prandtl model is used to calculus the eddy viscosity. When a point is far away from the wall, this viscosity is determined by empirical functions and constants. The point distinguishing above two layers could be automatically calculated. Baldwin and Lomax also gave a

different empirical force function in the wake region. Degani and Schiff [29] improved and modified the calculation of normal distance y_{max} in B-L model. More details of the B-L model could be referred in the Appendix H.

2.4 Boundary and Initial Conditions

To solve the Navier-Stokes equations, appropriate initial and boundary conditions should be assigned. These boundaries confine the size of computational domain. To include every possible influence in the computational domain, in a simplest way, the boundaries could be selected far away from the simulated TSTO space vehicle. However, to reach a satisfied mesh resolution, a big computational domain results to a great number of computational nodes. A tremendous hardware resource is prerequisite. Therefore, deliberately chosen and well-designed boundaries are very important to realize a numerical simulation in practice. At least it could save much computing time and much expenditure for computer hardware.

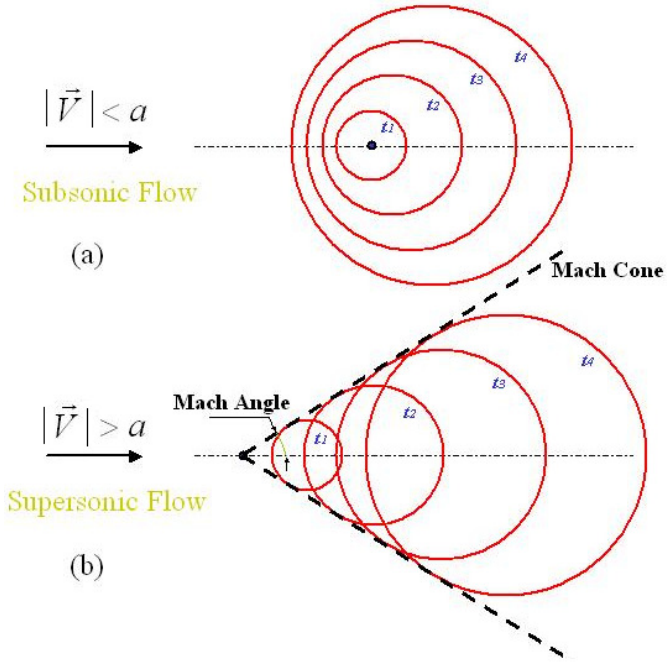

Figure 2.3: The wave transfer of disturbances in sub-/super- sonic flow.

Theoretically, there is still no general mathematical rule about the boundary conditions, even for the Euler equations. However, we could assign boundary conditions for the Euler equations by considering the wave transfer of a small disturbance as shown in Figure 2.3. As pointed by Yang [96], the Euler equations describe propagating waves, which are undamped due to without diffusive terms. A disturbance travels in speed of sound a like concentric spheres in a fluid at rest. In a moving flow, the disturbance propagates with speed a as in still fluid superimposing the fluid movement in freestream. Consequently, the wave transfers in a sphere shape corresponding to a fixed time. In Figure 2.3(a) these spheres are tagged at different times in a subsonic flow, and obviously these spheres could reach any position in the space. One disturbance from any point in the flow field

influences the whole space. In a supersonic flow, because the flow velocity of the freestream is greater than the speed of sound, the disturbance could not travel upstream. The disturbance of one point transfers only in a Mach cone shown in Figure 2.3 (b).

From the above analysis, it is concluded that a very big computing domain should be considered for the subsonic cases, because any disturbance from one point affects the other points in the whole flow field. The domain should be chosen so big, that the boundary condition on the far field should not affect or only very weakly affect the aerodynamic properties of the investigated space vehicle. In other words, the aerodynamic properties on the far field boundary should scarcely disturb the space vehicle. Because of the restricted capacity of the computer, only a suitable finite computing domain could be used in practice. Usually the distance from far field boundary to solid surface of the space vehicle is chosen about 6-12 times as long as the reference length. In these cases, all physical properties on all boundaries can be considered as in undisturbed flow.

Also from Figure 2.3 (b), it is known that a disturbance in supersonic flow affects only the flow field downstream. This means the disturbance in the downstream does not influence backwards to a point in the upstream. Hence, a much smaller computing domain could be confined. The inflow could be simply assigned as freestream. The outflow boundary may be extrapolated from the inner points of the computing domain.

On the solid surface, the flow movements are classified into two categories for our separation process: slip and non-slip boundary conditions. Since no flux should penetrate the solid surface, the normal component of the flow velocity against wall is zero. For viscous flow, tangential velocity is also zero on the wall, i.e. the non-slip boundary condition. For inviscid flow, tangential components of flow velocities are not zero and the flow slips along the wall. On the wall the used boundary condition about temperature is the adiabatic condition for the separation process. It assumes no heat transfers through the wall of the space vehicle. For the pressure on the wall, no gradient is usually considered.

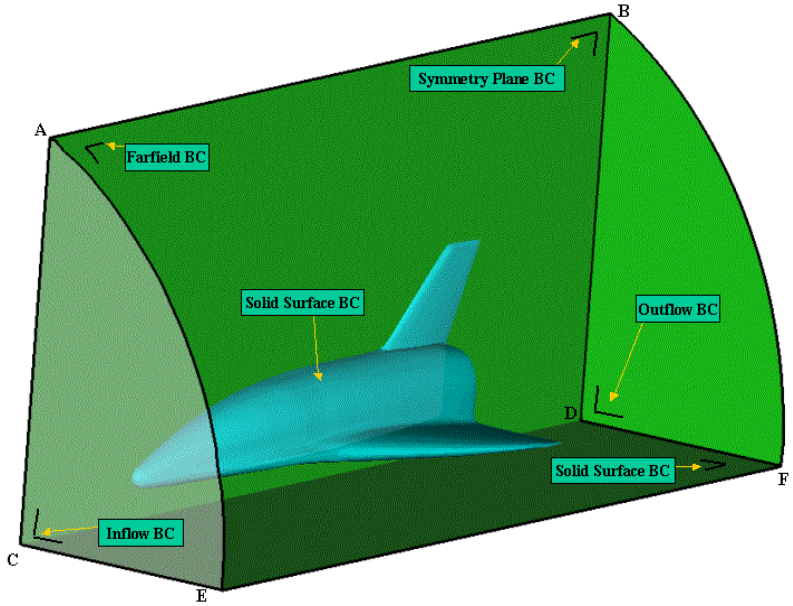

Figure 2.4: The boundary conditions for the flow in separation process.

To decrease grid nodes in the computing domain, the symmetry plane of a flying body is usually used as a boundary condition, which could reduce half of nodes. It is reasonable that the physical properties are also symmetric on two sides of this artificial cutting plane.

As a summary of above discussions, the boundary conditions used in this thesis could be categorized into five groups. As shown in Figure 2.4, they are far field (▱ABFE), inflow boundary (▱AEC), outflow boundary (▱BFD), solid surface (the EOS surface and the flat plate ▱CDFE), and symmetric surface (▱ABDC).

From mathematical point of view, a steady Euler equation system is a type of elliptic equation system in the area where Mach number is smaller than one. But in the area where Mach number is greater than one, it becomes hyperbolic equation system [76].

In the numerical simulation, steady Euler and Navier-Stokes equation systems are usually approximated by unsteady procedures [84]. When a term related to time has been added, the steady Euler equation system has changed into an unsteady system. Its mathematical type has completely been changed from a type of elliptic or hyperbolic system into a type of hyperbolic - parabolic system. With suitable initial and boundary conditions, this differential equation system could be well posed and could be sophisticatedly solved.

Its initial conditions are usually taken the same state as in freestream or no movement in the whole computing domain. In a time-developing process, the influence of the inlet boundary condition transfers downwards gradually and the effect of the geometry comes out little by little. Finally a stable state should been achieved. Numerically this procedure corresponds to an iterative process.

The above mentioned method of propagating waves for Euler equation system could be also applied for the Navier-Stokes equation system. However in the latter system, the propagating wave is already damped by the diffusive terms. The interaction between shock and boundary layer may affect the flows in whole domain even if in a hypersonic flow.

The boundary conditions have been further generalized into the techniques of characteristic boundary conditions. The far field could be derived from the characteristic inflow and outflow boundary conditions. In Appendixes F and G, systematical derivation of characteristic method is presented and initial and characteristic boundary conditions are given in detail.

3 Numerical Method

As one of the three methods in researching fluid dynamics, numerical simulation discretizes the differential equations into algebraic equations and solves them by using modern computers. A successful numerical method should be stable, convergent, and accurate in solving the Navier-Stokes equations. To simulate the separation process of a TSTO model numerically, extra robust and accurate numerical methods are required, because the numerical methods should distinguish all of hypersonic, supersonic, and subsonic flows around TSTO model as well as some special physical phenomena such as the strong shocks.

Based on a finite volume method (FVM), the Navier-Stokes equation system (2.18) is discretized and transformed into a nonlinear algebraic vector equation. The time-dependent flow vector is calculated by using the Strang-type of fractional step [23, 55, 79]. The inviscid flux vectors are treated by the modified AUSM method ("Advection Upstream Splitting Method") [77, 78]. The viscous flux vectors are discretized using the Gaussian integral theorem [19]. Second order accuracy in space for the smooth region and first order accuracy in time discretization is achieved.

Using the above-mentioned methods, the in-house software "FLMNAV" is developed. It is a stable, shock-capturing, and accurate code. As common phenomena in gas dynamics, weak solutions and non-uniqueness of shock could be encountered. In the code FLMNAV non-physical rarefaction shock is excluded by the second law of thermodynamics, that is, entropy increases in any process. The entropy increase is realized by the explicit use of filter, by adding artificial dumping terms, and by use inherently dissipative numerical schemes [20, 26, and 79].

The FLMNAV could be also applied to solve the Euler equation system, which could be treated as a simplified case of the Navier-Stokes equation system by neglecting viscous terms. Similarly, as described in Chapter 2.3 and Appendix H, the B-L turbulence model only changes two coefficients of Navier-Stokes equation system. The same numerical methods could be directly used to the B-L model. Therefore, the numerical realization is discussed only for the Navier-Stokes equation system in the following sections.

3.1 Basic Coordinate Transformation

The transformation from Cartesian coordinate system (*x, y, z, t*) to curvilinear coordinate system (ξ, η, ζ, τ) is defined in Eqs. (2.14) - (2.17). Their corresponding differential transformation reads

$$\begin{pmatrix} dt \\ dx \\ dy \\ dz \end{pmatrix} = \begin{pmatrix} 1 & 0 & 0 & 0 \\ x_\tau & x_\xi & x_\eta & x_\zeta \\ y_\tau & y_\xi & y_\eta & y_\zeta \\ z_\tau & z_\xi & z_\eta & z_\zeta \end{pmatrix} \begin{pmatrix} d\tau \\ d\xi \\ d\eta \\ d\zeta \end{pmatrix}. \tag{3.1}$$

This transformation matrix is called as the Jacobian matrix. It is composed of first order differentials about coordinates known as metrics. There is

$$\mathbf{J} \equiv \begin{pmatrix} 1 & 0 & 0 & 0 \\ x_\tau & x_\xi & x_\eta & x_\zeta \\ y_\tau & y_\xi & y_\eta & y_\zeta \\ z_\tau & z_\xi & z_\eta & z_\zeta \end{pmatrix} = \begin{pmatrix} 1 & 0 & 0 & 0 \\ \xi_t & \xi_x & \xi_y & \xi_z \\ \eta_t & \eta_x & \eta_y & \eta_z \\ \zeta_t & \zeta_x & \zeta_y & \zeta_z \end{pmatrix}^{-1} . \tag{3.2}$$

Because the metrics are of basic importance and are often used in computing the transformation of the Navier-Stokes equation system from Cartesian coordinate system to curvilinear coordinate, it is important to calculate these components very exactly. However, the computer could only provide a limited numerical precision. If the computing error for these metrics could not be well controlled, the numerical solution will deviate from the exact solutions somewhat.

In practice, these first order differentials about coordinates are not calculated directly from their original differential definitions, but derived from some general geometry shapes, that is, from the cell faces of control volumes. Corresponding to the hexagonal shape of the control volumes, the vectors of a cell face in the Cartesian coordinate system are defined by the coordinates of four vertices as below [19, 55].

$$\vec{S}_{1364} = \frac{1}{2}(\vec{r}_6 - \vec{r}_1) \times (\vec{r}_4 - \vec{r}_3) = \begin{pmatrix} (\overrightarrow{S_{1364}})_x \\ (\overrightarrow{S_{1364}})_y \\ (\overrightarrow{S_{1364}})_z \end{pmatrix} . \tag{3.3}$$

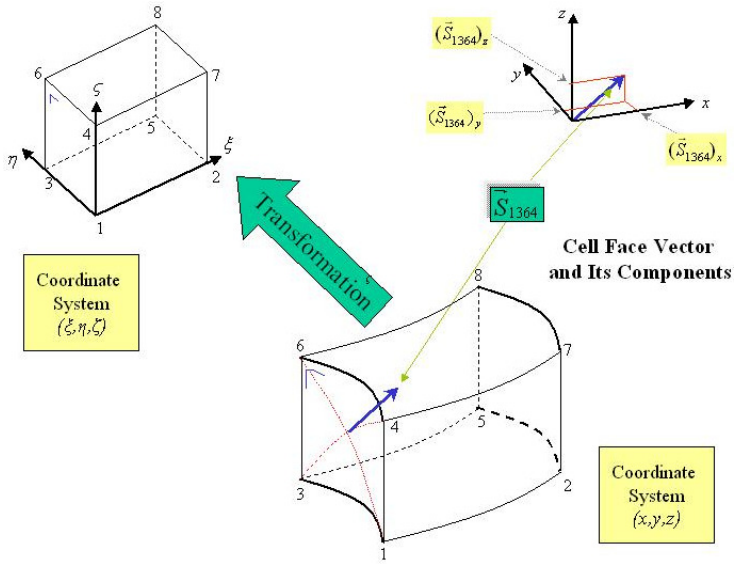

Figure 3.1: Coordinate transformation and the definition of the cell face vector.

The cell face vector $\vec{S}_{1364}$ is defined for the four-vertices-surface ▱ 1364 in the Cartesian coordinate. As illustrated in Figure 3.1, it has three projection components on the planes that are perpendicular to *x*, *y*, *z* axes respectively. $\vec{r}_1, \vec{r}_3, \vec{r}_4, \vec{r}_6$ present the vectors that begin from origin point of the Cartesian coordinate to the points 1, 3, 4, and 6 correspondingly. Though three points

could efficiently identify a plane, the above definition using four vertices in Eq. (3.3) could be applied in more general cases. It could define the face area of distorted meshes and allow faces collapse to an edge or even a point. From these cell face vectors, we get the components of the Jacobian matrix as

$$(J \cdot \nabla \xi)_{k-\frac{1}{2},l,m} = \vec{S}_{1364}, \tag{3.4}$$

$$(J \cdot \nabla \eta)_{k,l-\frac{1}{2},m} = \vec{S}_{1472}, \tag{3.5}$$

$$(J \cdot \nabla \varsigma)_{k,l,m-\frac{1}{2}} = \vec{S}_{1253}, \tag{3.6}$$

where $J=|\mathbf{J}|$ is the determinant of the Jacobian matrix, and $\nabla = (\frac{\partial}{\partial x}, \frac{\partial}{\partial y}, \frac{\partial}{\partial z})^T$. Still using these cell face vectors, the cell control volume could be obtained as

$$\mathbf{V}_{1-8} = \frac{1}{6}(\vec{S}_{1364} + \vec{S}_{1472} + \vec{S}_{1253} + \vec{S}_{2587} + \vec{S}_{3685} + \vec{S}_{4786}) \bullet (\vec{r}_8 - \vec{r}_1). \tag{3.7}$$

Usually in curvilinear system $\Delta\xi = 1, \Delta\eta = 1, \Delta\zeta = 1$ are selected. Derived from Eq. (E.18) in Appendix E, the determinant of the Jacobian matrix is equal to the volume of the control cell, that is

$$J = \mathbf{V}_{1-8}. \tag{3.8}$$

Referring Eqs. (E.12) and (E.13), the velocity of the cell face could be derived as

$$\xi_t = -x_\tau \xi_x - y_\tau \xi_y - z_\tau \xi_z. \tag{3.9}$$

Combining Eqs. (3.4) and (3.9), we could also express the cell face velocities from the cell face vector as in the following

$$(J \cdot \xi_t)_{k-\frac{1}{2},l,m} = -(\vec{S}_{1364})_x \cdot x_\tau - (\vec{S}_{1364})_y \cdot y_\tau - (\vec{S}_{1364})_z \cdot z_\tau. \tag{3.10}$$

In the same way, we have the formulas for the other cell faces,

$$(J \cdot \eta_t)_{k,l-\frac{1}{2},m} = -(\vec{S}_{1472})_x \cdot x_\tau - (\vec{S}_{1472})_y \cdot y_\tau - (\vec{S}_{1472})_z \cdot z_\tau, \tag{3.11}$$

$$(J \cdot \varsigma_t)_{k,l,m-\frac{1}{2}} = -(\vec{S}_{1253})_x \cdot x_\tau - (\vec{S}_{1253})_y \cdot y_\tau - (\vec{S}_{1253})_z \cdot z_\tau. \tag{3.12}$$

Combining Eqs. (3.4) - (3.6), (3.8), and (3.10) - (3.12), all elements of the Jacobian inverse matrix could be calculated by using the surface vectors and the volume of the control cell.

3.2 Discretization in Time and Space

The finite volume method is used to discretize the integral form of the Navier-Stokes equation system (2.18). Applying Gaussian integral theorem to that equation on every control volume **V** yields

$$\frac{\partial}{\partial t}\iiint_{\mathbf{V}} \mathbf{Q}\, d\mathbf{V} + \iint_{\mathbf{S}} \left[\left(\mathbf{F}^I - \mathbf{F}^V\right) \cdot n_\xi + \left(\mathbf{G}^I - \mathbf{G}^V\right) \cdot n_\eta + \left(\mathbf{H}^I - \mathbf{H}^V\right) \cdot n_\varsigma \right] d\mathbf{S} = 0, \tag{3.13}$$

where **S** is the surrounding surface of the control cell, and n_ξ, n_η, n_ς are the components of the outward unit normal vectors on **S**. The integration form, Eq. (3.13), does not exclude discontinuities as the differential form (2.18) does. Theoretically it is more suitable in capturing discontinuities and shocks. Because the flux terms of the FVM are defined exactly on the cell surfaces, the flux, which flows outward from one surface of the control cell, flows into the same surface of another control cell. This keeps the flow conservation in the whole discretization region. FVM could be easily applied to very complex 3D geometries. Due to these advantages, a lot of efficient numerical methods and software are originated from the fundamental idea of the FVM [73]. FVM could accommodate itself to both structured and unstructured meshes.

In this thesis, block-structured grid is used for the spatial discretization. The control volumes are very small cells and of hexahedral shapes. The state variables are discretized on the cell centers. If these variables locate on other positions, they will be calculated by suitable interpolations.

To catch the characteristics in the hypersonic flight, the inviscid part and viscous part in Eq. (3.13) are spatially discretized using complex numerical techniques. They are discussed separately in the following subsections. At first, the temporal discretization is discussed here.

Corresponding to a time-developing process, state variables are influenced by the inflow and outflow through a small cell iteratively. The time discretization with explicit method for the Navier-Stokes equation reads

$$\mathbf{Q}_{k,l,m}^{n+1} = \mathbf{Q}_{k,l,m}^{n} - \Delta\tau_{k,l,m} \cdot \mathbf{R}_{k,l,m}^{n} \cdot \mathbf{V}_{k,l,m}^{n}, \tag{3.14}$$

where lower indices *k, l, m* are used to depict corresponding space points in curvilinear coordinate and upper index *n* means that a variable is at the n-th step of the time iteration. Further

$$\begin{aligned}
\mathbf{R}_{k,l}^{n} = {} & (\mathbf{F}^I - \mathbf{F}^V)_{k+\frac{1}{2},l,m}^{n} \cdot (S_\xi)_{k+\frac{1}{2},l,m}^{n} - (\mathbf{F}^I - \mathbf{F}^V)_{k-\frac{1}{2},l,m}^{n} \cdot (S_\xi)_{k-\frac{1}{2},l,m}^{n} \\
& + (\mathbf{G}^I - \mathbf{G}^V)_{k,l+\frac{1}{2},m}^{n} \cdot (S_\eta)_{k,l+\frac{1}{2},m}^{n} - (\mathbf{G}^I - \mathbf{G}^V)_{k,l-\frac{1}{2},m}^{n} \cdot (S_\eta)_{k,l-\frac{1}{2},m}^{n} \\
& + (\mathbf{H}^I - \mathbf{H}^V)_{k,l,m+\frac{1}{2}}^{n} \cdot (S_\varsigma)_{k,l,m+\frac{1}{2}}^{n} - (\mathbf{H}^I - \mathbf{H}^V)_{k,l,m-\frac{1}{2}}^{n} \cdot (S_\varsigma)_{k,l,m-\frac{1}{2}}^{n}.
\end{aligned} \tag{3.15}$$

$\mathbf{V}_{k,l,m}^{n}$ is the volume value of the control cell and S_ξ, S_η, S_ς are the cell surface areas in the axis plane perpendicular to axis ξ, η, ς respectively. When $\Delta\xi = 1, \Delta\eta = 1,$ and $\Delta\zeta = 1$, the volume of control cell and the cell surface areas are all of one.

The time step size could be selected as

$$\Delta\tau_{k,l,m} = CFL \cdot \min(\Delta\tau_{k,l,m}^{I}, \Delta\tau_{k,l,m}^{V}), \tag{3.16}$$

where *CFL* is the Courant-Friedrichs-Lewy number in range of (0, 1) especially for the explicit iteration [42, 43]. $\Delta\tau_{k,l,m}^{I}$ and $\Delta\tau_{k,l,m}^{V}$ are the time step sizes for inviscid and viscous flux

respectively. A great time step size may lead to overlooking of certain physical phenomena. In the worst case, it could even result to a nonphysical flow or a breakdown of the iteration process. Principally, $\Delta\tau_{k,l,m}$ should be reciprocal to $|\vec{V}_{k,l,m}|$. That is, the time span should be smaller, when fluid moves very quickly. In practice, it could be determined by the idea of the eigenvalues from the decoupled Euler equations [39] as listed in Appendixes F and G. Because the components of the inverse Jacobian matrix relate with those eigenvalues, some symbols depending on the metrics of **J** are defined at first:

$$|\nabla k| = (k_x^2 + k_y^2 + k_z^2)^{1/2}, \text{ with } k = \xi, \eta, \varsigma, \tag{3.17}$$

and

$$\Psi(k) = |k_x \cdot k_y| + |k_x \cdot k_z| + |k_z \cdot k_y|, \text{ with } k = \xi, \eta, \varsigma. \tag{3.18}$$

The time step sizes for inviscid flux are assigned as

$$\Delta\tau^I_{k,l,m} = \frac{1}{(\Lambda^I_\xi + \Lambda^I_\eta + \Lambda^I_\varsigma)_{k,l,m}}. \tag{3.19}$$

Using the definition of (3.17), the velocity $\vec{V}$ and the speed of sound *a* on the point (*k*, *l*, *m*), the terms in the above equation could be calculated by

$$(\Lambda^I_\xi)_{k,l,m} = \vec{V}_{k,l,m} \bullet \nabla\xi_{k,l,m} + (a)_{k,l,m} \cdot |\nabla\xi_{k,l,m}|, \tag{3.20}$$

$$(\Lambda^I_\eta)_{k,l,m} = \vec{V}_{k,l,m} \bullet \nabla\eta_{k,l,m} + (a)_{k,l,m} \cdot |\nabla\eta_{k,l,m}|, \tag{3.21}$$

$$(\Lambda^I_\varsigma)_{k,l,m} = \vec{V}_{k,l,m} \bullet \nabla\varsigma_{k,l,m} + (a)_{k,l,m} \cdot |\nabla\varsigma_{k,l,m}|. \tag{3.22}$$

The time step sizes for viscous flux are given as

$$\Delta\tau^V_{k,l,m} = \frac{1}{(\Lambda^V_\xi + \Lambda^V_\eta + \Lambda^V_\varsigma)_{k,l,m}}, \tag{3.23}$$

where

$$\Lambda^V_\xi = 0.5 \cdot \frac{\mu_{k,l,m}}{\rho_{k,l,m}} [\frac{\gamma}{\mathrm{Pr}} (|\nabla\xi|^2_{k-\frac{1}{2},l,m} + |\nabla\xi|^2_{k+\frac{1}{2},l,m}) + \frac{1}{3}(\Psi(\xi)_{k-\frac{1}{2},l,m} + \Psi(\xi)_{k+\frac{1}{2},l,m})], \tag{3.24}$$

$$\Lambda^V_\eta = 0.5 \cdot \frac{\mu_{k,l,m}}{\rho_{k,l,m}} [\frac{\gamma}{\mathrm{Pr}} (|\nabla\eta|^2_{k,l-\frac{1}{2},m} + |\nabla\eta|^2_{k,l+\frac{1}{2},m}) + \frac{1}{3}(\Psi(\eta)_{k,l-\frac{1}{2},m} + \Psi(\eta)_{k,l+\frac{1}{2},m})], \tag{3.25}$$

$$\Lambda^V_\varsigma = 0.5 \cdot \frac{\mu_{k,l,m}}{\rho_{k,l,m}} [\frac{\gamma}{\mathrm{Pr}} (|\nabla\varsigma|^2_{k,l,m-\frac{1}{2}} + |\nabla\varsigma|^2_{k,l,m+\frac{1}{2}}) + \frac{1}{3}(\Psi(\varsigma)_{k,l,m-\frac{1}{2}} + \Psi(\varsigma)_{k,l,m+\frac{1}{2}})]. \tag{3.26}$$

After the time step size $\Delta\tau_{k,l,m}$ is calculated according to Eqs. (3.16) - (3.26), Eq. (3.14) could be

solved iteratively and explicitly. This explicit scheme defined as above is relatively simple to implement. It is also very robust when a reasonable *CFL* is selected. All of numerical simulations performed in this paper use this explicit scheme.

3.3 Modified AUSM and MUSCL Schemes for Inviscid Terms

In the discretization, every state variable ϕ is defined in the center of a control volume. As illustrated in the Figure 3.2, $\phi_{k,l,m}$ and $\phi_{k+1,l,m}$ are known on the cell centers. In the iteration process as presented in Eq. (3.15), the inviscid flux terms $\mathbf{F}^I$, $\mathbf{G}^I$, $\mathbf{H}^I$ on the cell surfaces are needed. Therefore, $\phi_{k+1/2,l,m}$ is needed to be determined by $\phi_{k,l,m}$ and $\phi_{k+1,l,m}$. To present more influence from upstream, weighted functions usually incline to the upstream points. That is, $\phi_{k+1/2,l,m}$ gets more information from $\phi_{k,l,m}$.

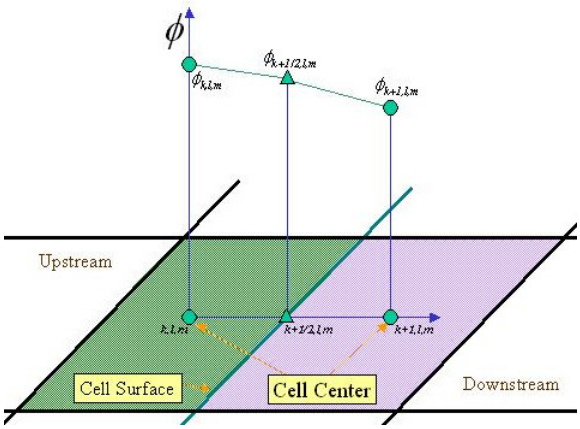

Figure 3.2: Upwind interpolation for inviscid term.

The modified AUSM is used to catch the shocks and to describe the slip lines. This method has only first order spatial accuracy. To get high order spatial accuracy, MUSCL (Monotonic Upstream Scheme for Conservation Laws) extrapolation is used.

3.3.1 Modified AUSM Scheme

In 1992, Liou and Steffen proposed an AUSM (Advection Upstream Splitting Method) scheme [66]. Its main idea is to split the inviscid flux functions into convective and pressure terms separately. The former terms are associated with the flow speed, while the latter terms with the acoustic speed. This method is further developed by Radespiel and Kroll [77, 78]. They presented the modified AUSM as an efficient method for shocks and shear layers. It is a hybrid method combing the advantages of AUSM and Upwind Flux-Vector Splitting Method (UFVSM). The UFVSM originates

from van Leer [88, 89] and is often mentioned as van Leer scheme. It splits the flux vector into two parts on the cell surface. According to the local Mach number and its sign, a forward or backward difference method is used for the each part of the flux to achieve an upwind effect. The modified AUSM could automatically switch to one of two methods mentioned above. That is, in the region with shear and boundary layers as well as contact discontinuity, AUSM is used and exhibits relatively small dissipation and high resolution. In the region with intensive shock waves, the UFVSM is used to capture the shock sharply and cleanly.

Because the three inviscid flux terms are composed of similar convective terms and pressure terms, to show the idea of the modified AUSM scheme, only one term of the inviscid flux term $\mathbf{F}^I$ through a cell surface, which is perpendicular to the ξ direction, is discussed subsequently. The terms $\mathbf{F}^I$ in η and ς directions as well as the other terms for $\mathbf{G}^I$, $\mathbf{H}^I$ could be discretized similarly.

The inviscid flux term $\mathbf{F}^I$ is discretized on a cell surface (*k+1/2*, *l*, *m*) as shown in the Figure 3.2 and its convective term and pressure term are separated as:

$$\mathbf{F}^{\mathrm{I}}_{k+1/2,l,m} = \mathbf{F}^{c}_{k+1/2,\,l,\,m} + \mathbf{p}_{k+1/2,\,l,\,m}, \tag{3.27}$$

and from Eq. (E.32) in Appendix E, we present

$$\mathbf{F}^{c}_{k+1/2,\,l,\,m} = J\begin{pmatrix} \rho\cdot U \\ \rho\cdot u\cdot U \\ \rho\cdot v\cdot U \\ \rho\cdot w\cdot U \\ \rho\cdot \mathrm{H}\cdot U \end{pmatrix}_{k+\frac{1}{2},\,l,\,m} \quad \text{and} \quad \mathbf{p}_{k+1/2,\,l,\,m} = J\begin{pmatrix} 0 \\ \xi_x p \\ \xi_y p \\ \xi_z p \\ -\xi_t p \end{pmatrix}_{k+\frac{1}{2},\,l,\,m}, \tag{3.28}$$

where the total enthalpy $\mathrm{H} = (E_S + p)/\rho$, and J is the determinant of Jacobian matrix.

The convective flux term $\mathbf{F}^{c}_{k+1/2}$ is equal to a sum of an average and a difference of the state variables on two sides of control volume in ξ direction, which are weighted by advection Mach number $M_{k+\frac{1}{2},l,m}$ and by a scalar dissipative term $\Phi_{k+1/2,\,l,\,m}$ respectively. That is

$$\mathbf{F}^{c}_{k+1/2,\,l,\,m} = \frac{1}{2}M_{k+1/2,\,l,\,m}(W^{+} + W^{-}) - \frac{1}{2}\Phi_{k+1/2,\,l,\,m}(W^{+} - W^{-}). \tag{3.29}$$

The state variables in curvilinear coordinates are

$$W^{+} = J\begin{pmatrix} \rho\cdot a \\ \rho\cdot u\cdot a \\ \rho\cdot v\cdot a \\ \rho\cdot w\cdot a \\ \rho\cdot \mathrm{H}\cdot a \end{pmatrix}_{k+1,\,l,\,m} \quad \text{and} \quad W^{-} = J\begin{pmatrix} \rho\cdot a \\ \rho\cdot u\cdot a \\ \rho\cdot v\cdot a \\ \rho\cdot w\cdot a \\ \rho\cdot \mathrm{H}\cdot a \end{pmatrix}_{k,\,l,\,m}, \tag{3.30}$$

where a is the speed of sound. The $M_{k+\frac{1}{2},l,m}$ in Eq. (3.29) could be determined with several different

ways. One of them is given by Liou and Steffen [66] as a combination of wave velocity M^+ and M^- on the cell (k, l, m) and ($k+1$, l, m) respectively. It is expressed as

$$M_{k+\frac{1}{2},l,m} = M^{+}_{k,l,m} + M^{-}_{k+1,l,m}. \tag{3.31}$$

The Mach number M^+ and M^- are given by Van Leer through a "Flux Vector Splitting" method in [88] as

$$M^{+} = \begin{cases} M & M \geq 1 \\ \frac{1}{4}(M+1)^2 & |M| < 1 \\ 0 & M \leq -1 \end{cases} \quad \text{and} \quad M^{-} = \begin{cases} 0 & M \geq 1 \\ -\frac{1}{4}(M-1)^2 & |M| < 1 \\ M & M \leq -1 \end{cases}. \tag{3.32}$$

The Mach number M is defined by

$$M = \begin{cases} U/a & \text{on Surface}\,(k \pm 1/2,\ l,\ m) \\ V/a & \text{on Surface}\,(k,\ l \pm 1/2,\ m) \\ W/a & \text{on Surface}\,(k,\ l,\ m \pm 1/2) \end{cases}. \tag{3.33}$$

The dissipative term $\Phi_{k+1/2,l,m}$ in Eq. (3.29) is introduced as a combination of numerical dissipation in van Leer scheme and in AUSM scheme:

$$\Phi_{k+\frac{1}{2},l,m} = (1-\omega)\Phi^{VL}_{k+\frac{1}{2},l,m} + \omega\Phi^{\mathrm{mod}\,AUSM}_{k+\frac{1}{2},l,m}, \tag{3.34}$$

where ω is a parameter in [0, 1], and it is defined as

$$\omega = \max(v_{k,l,m}, v_{k+1,l,m}), \tag{3.35}$$

and

$$v_{k,l,m} = \max\left(1-\alpha\left|\frac{p_{k-1,l,m} - 2p_{k,l,m} + p_{k+1,l,m}}{p_{k-1,l,m} + 2p_{k,l,m} + p_{k+1,l,m}}\right|, 0\right), \tag{3.36}$$

where $v_{k,l,m}$ and $v_{k+1,l,m}$ are two numerical dissipation parameters with a constant α=O(5). In the smooth region, where ω tends to 1, $\Phi_{k+\frac{1}{2},l,m}$ in equation (3.34) tends to AUSM scheme. In the vicinity of shocks where ω approximates to 0, van Leer scheme is emphasized.

The dissipation in van Leer scheme read

$$\Phi^{VL}_{k+\frac{1}{2},l,m} = \begin{cases} \left|M_{k+\frac{1}{2},l,m}\right| & if\ M_{k+\frac{1}{2},l,m} \geq 1 \\ \left|M_{k+\frac{1}{2},l,m}\right| + \frac{1}{2}(M_{k+1,l,m}-1)^2 & if\ 0 \leq \left|M_{k+\frac{1}{2},l,m}\right| < 1 \\ \left|M_{k+\frac{1}{2},l,m}\right| + \frac{1}{2}(M_{k,l,m}+1)^2 & if\ -1 < M_{k+\frac{1}{2},l,m} \leq 0 \end{cases}, \tag{3.37}$$

and the dissipation in AUSM scheme is expressed as

$$\Phi^{\mathrm{mod}\,AUSM}_{k+\frac{1}{2},l,m} = \begin{cases} \left| M_{k+\frac{1}{2},l,m} \right| & if \left| M_{k+\frac{1}{2},l,m} \right| > \tilde{\delta} \\ \dfrac{(M^{2}_{k+\frac{1}{2},l,m} + \tilde{\delta}^{2})}{2\tilde{\delta}} & if \left| M_{k+\frac{1}{2},l,m} \right| \le \tilde{\delta} \end{cases}. \tag{3.38}$$

The dissipation parameter $\tilde{\delta}$ is introduced to reduce or to eliminate the smearing of the boundary layer on the normal direction of the wall [77, 78]. Usually this small parameter ranges in an interval (0,0.5). It is not a constant, but is given as

$$\tilde{\delta}_{k+1,l,m} = \delta\beta_{k+1,l,m} \quad \text{with} \quad 0 < \delta \le 0.5, \tag{3.39}$$

where β is a scaling function. It is determined by the cell metrics. Considering the ξ-direction related with Eqs. (2.14) - (2.17), it is depicted as

$$\beta_{k+\frac{1}{2},l,m} = 1 - \min\left[\max\left(\frac{\xi_x}{\xi_y}, \frac{\xi_x}{\xi_z} \right), 1 \right]. \tag{3.40}$$

This scaling function improves the damping behavior of AUSM especially when grid quality is worse. In the same time, it does not spoil the accuracy of AUSM for the boundary layer calculation. With Eqs. (3.29) - (3.40), we give a complete calculation procedure for the convective term $\mathbf{F}^{c}_{k+1/2,\,l,\,m}$ in Eq. (3.27).

Similarly as Eq. (3.31), the pressure p on the cell surface (*k+1/2*, *l*, *m*) in Eq. (3.28) is defined as

$$p_{k+\frac{1}{2},l,m} = p^{+}_{k,l,m} + p^{-}_{k+1,l,m}, \tag{3.41}$$

where the terms for pressure on the cell center are given by a second-order weighted characteristic polynomial of velocity as

$$p^{+} = \begin{cases} p & if\ M \ge 1 \\ \dfrac{1}{4} p(M+1)^{2}(2-M) & if\ M < 1, \\ 0 & if\ M \le 1 \end{cases} \tag{3.42}$$

and

$$p^{-} = \begin{cases} 0 & if\ M \ge 1 \\ \dfrac{1}{4} p(M-1)^{2}(2+M) & if\ M < 1. \\ p & if\ M \le 1 \end{cases} \tag{3.43}$$

Then an exemplar calculation of inviscid flux term $\mathbf{F}^{I}$ on a cell surface is listed in formulas from Eqs. (3.27) - (3.43). It is noted that the flux terms discretized by the modified AUSM have only the first order spatial accuracy.

3.3.2 MUSCL Scheme

In the numerical simulation about the separation process, the MUSCL scheme is used to get a high order spatial accuracy except in discontinuous regions such as strong shocks and viscous shear layers. Herein, the MUSCL scheme is a series of methods using different limiters. It uses sloped lines or nonlinear curves to approximate the state variables in each cell. This approximation approaches state variables on the cell surface with different left and right values. On the cell surface point (*k+1/2*,*l*,*m*) as shown in Figure 3.3, there are two values $\phi^{-}_{k+1/2,l,m}$ and $\phi^{+}_{k+1/2,l,m}$. The cell with the cell center (*k*, *l*, *m*) takes $\phi^{-}_{k+1/2,l,m}$ as its state variable on the cell surface. Similarly, the cell with the cell center (*k+1*,*l*,*m*) applies $\phi^{+}_{k+1/2,l,m}$ as its state variable on the cell surface.

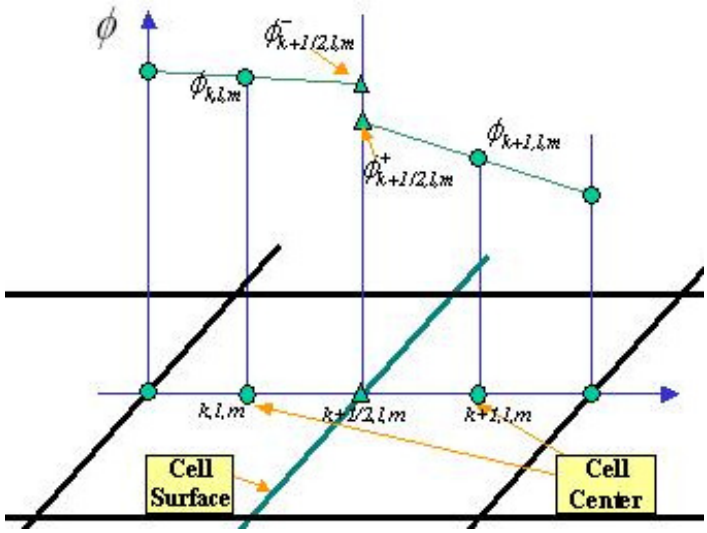

Figure 3.3: The left and right piecewise interpolation in a MUSCL scheme.

The van Albada limiter has a second order accuracy in a MUSCL approach. Using this limiter in this thesis, the state variables of W^{+} and W^{-} in Eq. (3.29) do not use the piecewise constant approximation in Eq. (3.30), but are calculated in the smooth region as

$$\phi^{-}_{k+1/2,l,m} = \phi_{k,l,m} + \frac{1}{2}\frac{(\Delta_{+}^{2}+\varepsilon)\Delta_{-} + (\Delta_{-}^{2}+\varepsilon)\Delta_{+}}{\Delta_{+}^{2}+\Delta_{-}^{2}+2\cdot\varepsilon}, \quad for \quad \phi = \rho, u, v, w, p. \tag{3.44}$$

$\phi^{-}_{k+1/2,l,m}$ is the value of the flow variables on the left side of cell surface (*k+1/2*, *l*, *m*) using the ϕ on (*k-1*, *l*, *m*), (*k*, *l*, *m*) and (*k+1*, *l*, *m*), where

$$\Delta_{+} = \phi_{k+1,l,m} - \phi_{k,l,m}, \tag{3.45}$$

and

$$\Delta_{-} = \phi_{k,l,m} - \phi_{k-1,l,m}. \tag{3.46}$$

The term ε suppresses the limiting of the solution in regions where the flow is nearly constant. It is defined by

$$\varepsilon = \max\{k_1 \cdot (\Delta\xi)^n, \quad k_2 \cdot (\Phi^{\mathrm{mod}\,AUSM}_{k+\frac{1}{2},l,m} - \overline{M})\}, \tag{3.47}$$

where $\Delta\xi = \xi_{k+1} - \xi_k$, k_1 and k_2 are empirical constants of O(10) and of O(100) respectively. Further $2 < n < 3$. $\overline{M}$ is the average of contravariant Mach numbers at (k, l, m) and (k+*1*, l, m). $\Phi^{\mathrm{mod}\,AUSM}_{k+\frac{1}{2},l,m}$ is given in Eq. (3.38).

As done as in Eqs. (3. 44) - (3.46), the state variables on the right side of element surface $\phi^{+}_{k+1/2,l,m}$ could be analogously obtained by the state variables ϕ on (k, l, m), (k+*1*, l, m) and (k+*2*, l, m) [39, 77, 78].

3.4 Chakravarthy Scheme for Viscous Terms

The viscous flux terms $\mathbf{F}^{\mathrm{v}}$, $\mathbf{G}^{\mathrm{v}}$, and $\mathbf{H}^{\mathrm{v}}$ in Eq. (3.15) are composed of the derivatives of the state variables. In the numerical spatial discretization, these derivatives are also needed on the cell surface. According to the method of Chakravarthy [19], the derivatives are derived by the state variables, which are defined on the center of the control volume.

These derivatives on the surface of the control volume are discretized by the Gaussian theorem again on an auxiliary cell like Figure 3.4. These derivatives could be presented by the state variables on the circumference points of the auxiliary cell. If some points, such as N and S, are not exactly on the center of the control volume as W and E, their state variables could be expressed by averages of the corresponding variables on the neighboring centers.

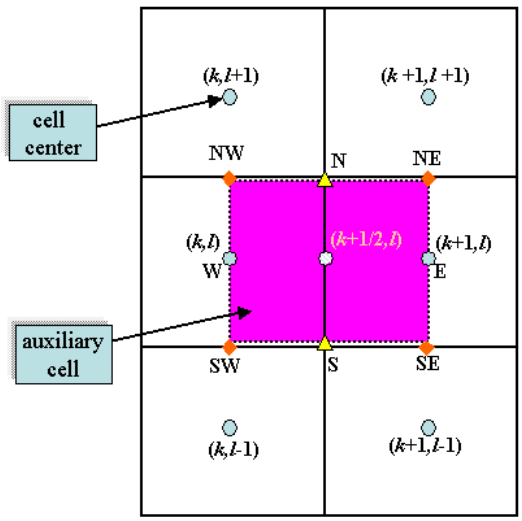

Figure 3.4: Auxiliary cell and its neighborhood for derivative calculations of viscous flux terms.

To clearly show the above principle, the discretization is performed in 2D case. Let's define the state variable ϕ is one of ρ, u, v, T. As derived in Appendixes E and D, the strains and heat fluxes in the viscous flux terms $\mathbf{F}^v$, $\mathbf{G}^v$, and $\mathbf{H}^v$ depend on x, y, ξ, η, ϕ, ϕ_ξ, ϕ_η, transformation matrix $\mathbf{J}$, and its determinant J. The coordinates x, y, ξ, η could be given by the software of grid generation. ϕ could be obtained in every iterative step. All components in $\mathbf{J}$ as well as determinant J have been determined in Chapter 3.1. Subsequently, ϕ_ξ and ϕ_η are the remaining terms to be determined for the viscous flux terms $\mathbf{F}^v$, $\mathbf{G}^v$, and $\mathbf{H}^v$ in this section.

In the discretization of Navier-Stokes equation system shown in Eq. (3.15), actually the numerical flux terms related with ϕ_ξ and ϕ_η are needed only on the position of cell surface (k+1/2, l). To calculate these derivatives of ϕ, 2D Gaussian integral theorem is used:

$$\oint_S \nabla \bullet \vec{g}\, d\mathbf{S} = \int_l \vec{g} \bullet \vec{n}\, d\boldsymbol{l}, \tag{3.48}$$

where $\vec{n} = \begin{pmatrix} n_\xi \\ n_\eta \end{pmatrix}$ is the outward normal vector of the line $\boldsymbol{l}$, which encloses the area $\mathbf{S}$. This formula is valid for any 2D vector $\vec{g}$. Substitute $\vec{g} = \begin{pmatrix} \phi \\ 0 \end{pmatrix}$ into Eq. (3.48) yields

$$\phi_\xi = \frac{1}{S_{aux}} \oint_l \phi \cdot n_\xi \cdot d\boldsymbol{l} = \frac{1}{S_{aux}} \oint_l \phi \cdot d\eta. \tag{3.49}$$

In the similar way another first order differential could be gotten as

$$\phi_\eta = \frac{1}{S_{aux}} \oint_l \phi \cdot n_\eta \cdot d\boldsymbol{l} = \frac{1}{S_{aux}} \oint_l \phi \cdot d\xi. \tag{3.50}$$

Let's note the corner points as NW, SW, SE, NE, and the middle points on the sideline as N, W, S, and E as shown in Figure 3.4. Assuming that the state variables ϕ on the points N, W, S, and E are constants, we get the discretization of the first order differential on the cell surface (k+1/2, l) as

$$(\phi_\xi)_{k+\frac{1}{2},l} \approx \frac{1}{S_{aux}} \left[\phi_E d\eta_E + \phi_N d\eta_N + \phi_W d\eta_W + \phi_S d\eta_S\right], \tag{3.51}$$

$$(\phi_\varsigma)_{k+\frac{1}{2},l} \approx -\frac{1}{S_{aux}} \left[\phi_E d\xi_E + \phi_N d\xi_N + \phi_W d\xi_W + \phi_S d\xi_S\right], \tag{3.52}$$

where $d\xi_i$ and $d\eta_i$ (i=N, W, S, and E) could be presented by the coordinates ξ and η

$$d\xi_E = \xi_{NE} - \xi_{SE}, \quad d\xi_W = \xi_{SW} - \xi_{NW}, \tag{3.53}$$

$$d\xi_N = \xi_{NW} - \xi_{NE}, \quad d\xi_S = \xi_{SE} - \xi_{SW}, \tag{3.54}$$

$$d\eta_E = \eta_{NE} - \eta_{SE}, \quad d\eta_W = \eta_{SW} - \eta_{NW}, \tag{3.55}$$

$$d\eta_N = \eta_{NW} - \eta_{NE}, \quad d\eta_S = \eta_{SE} - \eta_{SW}. \tag{3.56}$$

The state variables ϕ_W and ϕ_E are already known in the previous iteration process, because the points **W** and **E** are exactly the points (k, l) and (k+1, l) on the cell centers, correspondingly. The state variables ϕ_N and ϕ_S could be calculated as

$$\phi_N \approx \frac{1}{4}(\phi_{k,l} + \phi_{k+1,l} + \phi_{k+1,l+1} + \phi_{k+1,l}), \tag{3.57}$$

$$\phi_S \approx \frac{1}{4}(\phi_{k,l} + \phi_{k+1,l} + \phi_{k+1,l-1} + \phi_{k,l-1}). \tag{3.58}$$

For 3D case, the state variable ϕ could be one of the ρ, u, v, w, and T. The auxiliary cell includes 6 surfaces instead of 4 circumference lines as in 2D case. Further the areas used in 2D case are replaced by the volumes in 3D case respectively [20]. As Eq. (A.13) listed in Appendix A, a 3D Gaussian integral theorem is utilized as

$$\nabla\phi = \frac{1}{\mathbf{V}_{aux}} \oint_{\mathbf{S}} \phi \cdot d\mathbf{S}. \tag{3.59}$$

The discretization is as

$$\begin{aligned}(\nabla\phi)_{k+\frac{1}{2},l,m} = \frac{1}{\mathbf{V}_{k+\frac{1}{2},l,m}} \Big[&(\phi\cdot\vec{S}\bullet\vec{n}_k)\big|_{k+1,l,m} + (\phi\cdot\vec{S}\bullet\vec{n}_k)\big|_{k,l,m} + (\phi\cdot\vec{S}\bullet\vec{n}_l)\big|_{k+\frac{1}{2},l+\frac{1}{2},m} \\ &+ (\phi\cdot\vec{S}\bullet\vec{n}_l)\big|_{k+\frac{1}{2},l-\frac{1}{2},m} + (\phi\cdot\vec{S}\bullet\vec{n}_m)\big|_{k+\frac{1}{2},l,m+\frac{1}{2}} + (\phi\cdot\vec{S}\bullet\vec{n}_m)\big|_{k+\frac{1}{2},l,m-\frac{1}{2}} \Big],\end{aligned} \tag{3.60}$$

where $\vec{S}$ is the cell face vector, $\vec{n} = (\vec{n}_k, \vec{n}_l, \vec{n}_m)$ is an outward unit normal vector always pointing outside. Some temporary middle points on the surface could be computed as

$$\phi_{k+\frac{1}{2},l+\frac{1}{2},m} \approx \frac{1}{4}(\phi_{k,l+1,m} + \phi_{k+1,l+1,m} + \phi_{k,l,m} + \phi_{k+1,l,m}). \tag{3.61}$$

4 Computational Mesh

The discretization procedure includes dividing physical domains into meshes and rewriting Navier-Stokes equation system numerically on these grid points. Discretizing the differentials with one- to two- order accuracy, algebraic equations relating with the state variables on the cell centers are generated by the numerical methods described in Chapter 3. The discretized solution should approximate the continuous solution of the NS equation on all grid points [94].

If the state variables are of highly nonlinear distribution or they change dramatically, some small discretization errors may be much magnified in the numerical calculation. Finally it could result a false solution. Discretization error usually could be reduced by decreasing the mesh size. In the ideal case, the numerical solution converges to the analytical solution when the mesh size tends to zero. However, using enormous grid points may accumulate the round-off error and burden the computer hardware resource. Actually a suitable mesh should be selected for a satisfied accuracy. The quality and the size of mesh could greatly affect the rate of convergence as well as the solution accuracy.

In the separation process of the TSTO vehicle, because aerodynamic properties change significantly around the body surface, very dense mesh should be allocated around the body surface. The important aerodynamic properties should be clearly resolved there. Oppositely, the mesh points could be sparsely distributed in the less important region to reduce the grid points and the computing work.

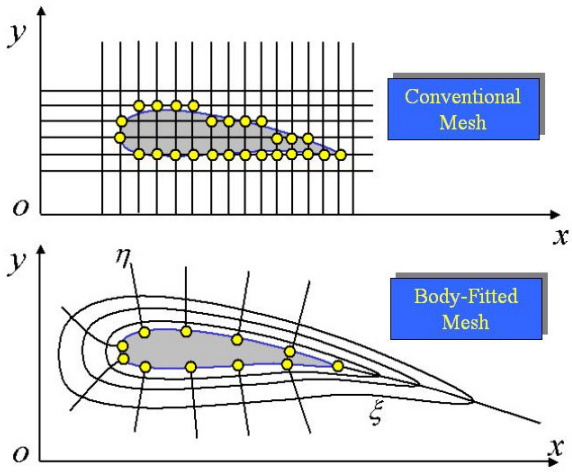

Figure 4.1: A comparison between rectangular Cartesian mesh and body-fitted mesh.

4.1 Meshing Methods

The shape of the space vehicle dominantly determines its aerodynamic properties. The simplest meshes with cuboids could not describe the solid surface of the space vehicle precisely, nor could they reasonably distribute grids according to the rate of the surface curving. A staircase-like approximation brings errors in the analysis of boundary layer as well as in the determination of the force. As an example in 2D case, Figure 4.1 shows a comparison between rectangular Cartesian mesh and the body-fitted mesh. Though the grids are distributed much denser using rectangular meshes,

their approximation to the shape of an airfoil looks still unreasonable.

To use the simplicity of the Cartesian system and reduce the geometry error in Cartesian meshes, an adaptive mesh refinement is used to refine meshes around boundaries automatically [2, 100]. Recently an immersed boundary method is developed and it amends the geometry error in Cartesian meshes by adding extra forces, which is related to the geometry, into the right hand of the control equation systems [36, 75].

In contrast, non-uniformly distributed and body-fitted mesh is widely used in CFD. As shown in Figure 4.1, the grid points locate exactly on the body surface and the grid points are distributed more reasonable.

The body-fitted mesh is not easier to generate. The meshing work is usually done with the help of some mesh generators. One of them is a software package ICEMCFD. Using one-to-one curvilinear mapping, the physical domain with body-fitted mesh in Cartesian coordinate system (x, y, z, t) is transformed into the computing domain in curvilinear coordinate system $(\xi, \eta, \varsigma, \tau)$. The latter uses conventional meshes composed of cuboids. Simultaneously the Navier-Stokes equations should also be transformed to the computing domain by using the same curvilinear mapping. This transformation could refer to Appendix E.

4.2 Basic Geometry and Initial Mesh

In the following numerical simulations, the configuration of the simplified EOS is exactly the same as used in experiments, which will be illustrated in Chapter 5. CAE tool gives the basic points and lines of the EOS configuration. One sub-module in ICEMCFD, i.e. DDN, imports these points and lines and generates a series of contour lines, surfaces, and domains. It further defines the geometries of EOS, flat plate, inflow area, outflow area and far field. Based on these geometries, the mesh is created by a HEXA interface, which is also a sub-module of the ICEMCFD. With O-grid technique, HEXA divides computing domain into 12 blocks by splitting edges, faces and blocks. A desired point distribution could be easily assigned for all edges. The hexahedral elements are the basic components. The whole space of computational domain is bounded by its bottom plane (in another name: the flat plate), by the symmetry plane, by inflow and out flow plane, and by far fields. Figure 4.2 shows boundary lines of the computing domain, meshes on the symmetry plane, meshes on the flat plate and meshes on the plane of outflow. In side view, this computational region is a rectangular square. When looking along the flow direction, the lower part is the flat plate and the upper part is the far field. The far field shapes as a part of a circle to reduce the size of computing domain. Because we mainly consider the supersonic or hypersonic flows, the boundary on the far field usually transmits no or very less information backwards to the EOS. So we could choose the far field and the outflow plane much closer to the vehicles. In Figure 4.2 it is shown that a great number of nodes are distributed around the EOS surface, above the flat plate, and in the possible regions of shocks. These denser grids are used to capture the shocks and describe the changes in boundary layers. Further these domains are used to trigger the turbulence calculation. In order to simulate an unsteady

flow during the separation maneuver, mesh points around the orbital stage EOS move with its solid surface dynamically. The surface of the inflow, outflow, and the far field are fixed. Then the movements of the grid points between these two surfaces are proportional to the distances among them.

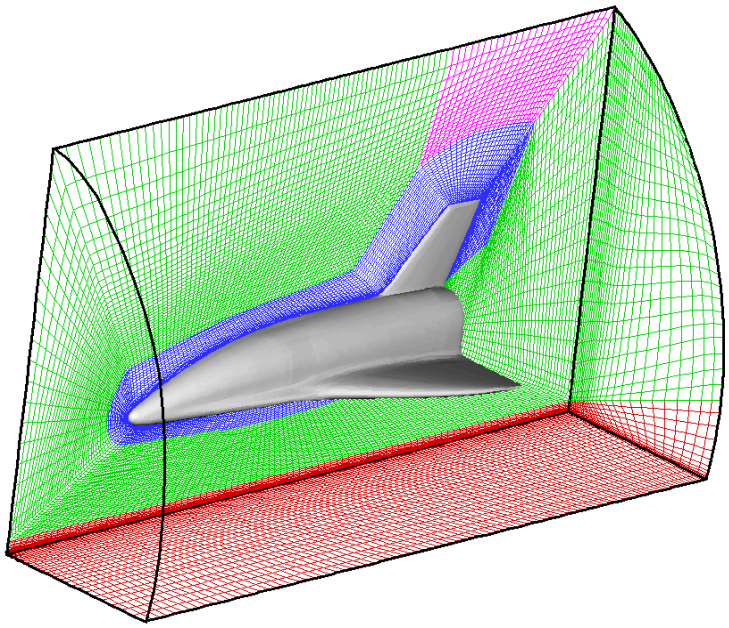

Figure 4.2: Initial mesh at the symmetric plane,
outflow plane, and flat plate generated by ICEMCFD.

In this paper, four kinds of grids with different resolutions are presented to show their influence to the numerical solution: one with 404990 nodes referred to as coarse grid, another with 645807 nodes referred to as standard grid, a third one with 1150142 nodes referred to as refined grid, and a fourth one with 1.8 million nodes referred to as much refined grid. The proportion of their node numbers is 1:1.6:2.8:4.5. The first off-body grid line is fixed at a distance of 5×10^{-4} L for the coarse and standard grids, and at a distance of 10^{-5} L for the refined and much refined grids. The coarse grid is used only once for a mesh comparison, and the much refined grid only for turbulence models. All other simulations use the standard and refined grids in the following chapters.

4.3 Orthogonalization and Smoothness

According to Eberle et al. [30] and Fletcher [34] and Su [84], good meshes should fit the physical boundary. Orthogonally and smoothly distributed meshes also decrease the numerical error of metrics in coordinate transformation formulas.

Because of some tapering configurations of the EOS, such as the geometry related with the stabilizer, the meshes generated from software HEXA are not smooth enough to fit our solver FLMNAV. Its quality affects the convergence greatly. To improve the distribution and orthogonality of the grid points, the meshes are further smoothed by our in-house software - GRIDFLM [27]. To get a new grid distribution in the original Cartesian coordinate system, this software redistributes grid

points by solving the system of Poisson vector equation [83, 86],

$$g^{11}(\mathbf{r}_{\xi\xi}+\mathbf{P}\,\mathbf{r}_{\xi})+g^{22}(\mathbf{r}_{\eta\eta}+\mathbf{Q}\,\mathbf{r}_{\eta})+g^{33}(\mathbf{r}_{\varsigma\varsigma}+\mathbf{R}\,\mathbf{r}_{\varsigma})=\mathbf{0}, \tag{4.1}$$

with $\mathbf{r}=[\,x,y,z\,]^T$. ξ,η,ς present curvilinear coordinates, and the contravariant coefficients g^{11},g^{22},g^{33} are given by

$$g^{11}=g_{22}g_{33}-g_{23}g_{32}, \tag{4.2}$$

$$g^{22}=g_{33}g_{11}-g_{31}g_{13}, \tag{4.3}$$

$$g^{33}=g_{11}g_{22}-g_{12}g_{21}. \tag{4.4}$$

The covariant metric coefficients g_{ij} $(i,j=1,2,3)$ read

$$g_{ij}=\sum_{n=1}^{3}\frac{\partial x^n}{\partial k^i}\cdot\frac{\partial x^n}{\partial k^j},\ \text{with } i,j=1,2,3. \tag{4.5}$$

Here two simplifications, $[x^1,x^2,x^3]^T:=[x,y,z]^T$ and $[k^1,k^2,k^3]^T:=[\xi,\eta,\varsigma]^T$, are used in Eq. (4.5).

Discretizing Eq. (4.1), it yields

$$\begin{aligned}x^n_{k,l,m}=\frac{1}{2(g^{11}+g^{22}+g^{33})}\Bigg\{&g^{11}\left[x^n_{k+1,l,m}\cdot(1+\frac{\mathbf{P}}{2})+x^n_{k-1,l,m}\cdot(1-\frac{\mathbf{P}}{2})\right]+\\&g^{22}\left[x^n_{k,l+1,m}\cdot(1+\frac{\mathbf{Q}}{2})+x^n_{k,l-1,m}\cdot(1-\frac{\mathbf{Q}}{2})\right]+\\&g^{33}\left[x^n_{k,l,m+1}\cdot(1+\frac{\mathbf{R}}{2})+x^n_{k,l,m-1}\cdot(1-\frac{\mathbf{R}}{2})\right]\Bigg\},\ \text{with } n=1,2,3.\end{aligned} \tag{4.6}$$

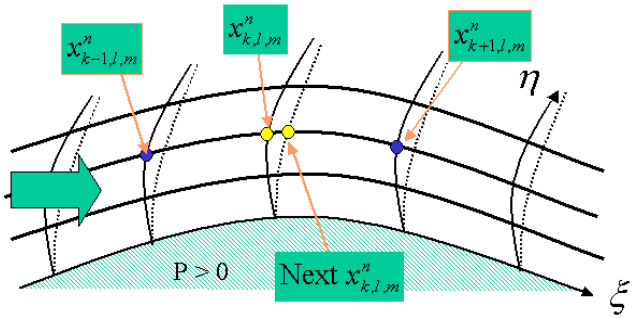

Figure 4.3: Point movement in the smoothing with source **P**.

We use above formula to generate the new mesh iteratively. The source terms **P**, **Q**, and **R** are responsible for the motion of the grid lines and provide the distribution control of grid points. Consider a case with only one source **P**>0. The next $x^n_{k,l,m}$ is generated by the iteration according to Eq. (4.6). It moves closer to the point $x^n_{k+1,l,m}$, because point $x^n_{k+1,l,m}$ is weighted more than the

points $x^n_{k-1,l,m}$. This point moving process is shown in Figure 4.3.

In GRIDFLM, the source terms are initially calculated on the surfaces of every block. The source terms on the surface are given by

$$\mathbf{P} = \frac{\xi_x \cdot X + \xi_y \cdot Y + \xi_z \cdot Z}{-J \cdot g^{11}}, \tag{4.7}$$

$$\mathbf{Q} = \frac{\eta_x \cdot X + \eta_y \cdot Y + \eta_z \cdot Z}{-J \cdot g^{22}}, \tag{4.8}$$

$$\mathbf{R} = \frac{\varsigma_x \cdot X + \varsigma_y \cdot Y + \varsigma_z \cdot Z}{-J \cdot g^{33}}, \tag{4.9}$$

where

$$X = g^{11} \cdot x_{\xi\xi} + g^{22} \cdot x_{\eta\eta} + g^{33} \cdot x_{\varsigma\varsigma}, \tag{4.10}$$

$$Y = g^{11} \cdot y_{\xi\xi} + g^{22} \cdot y_{\eta\eta} + g^{33} \cdot y_{\varsigma\varsigma}, \tag{4.11}$$

$$Z = g^{11} \cdot z_{\xi\xi} + g^{22} \cdot z_{\eta\eta} + g^{33} \cdot z_{\varsigma\varsigma}, \tag{4.12}$$

and the determinant of the Jacobi matrix is

$$J = x_\xi \left(y_\eta z_\zeta - z_\eta y_\zeta\right) - y_\xi \left(x_\eta z_\zeta - z_\eta x_\zeta\right) + z_\xi \left(x_\eta y_\zeta - y_\eta x_\zeta\right). \tag{4.13}$$

These surface source terms are smoothly distributed into inner points of every block by Laplace algorithms

$$\mathbf{P}_{\xi\xi} + \mathbf{P}_{\eta\eta} + \mathbf{P}_{\varsigma\varsigma} = \mathbf{0}, \tag{4.14}$$

$$\mathbf{Q}_{\xi\xi} + \mathbf{Q}_{\eta\eta} + \mathbf{Q}_{\varsigma\varsigma} = \mathbf{0}, \tag{4.15}$$

$$\mathbf{R}_{\xi\xi} + \mathbf{R}_{\eta\eta} + \mathbf{R}_{\varsigma\varsigma} = \mathbf{0}. \tag{4.16}$$

For very sharp geometry, special treatment for the source terms may be needed to avoid that grid points are moved into the solid body. In this thesis, mesh quality is greatly improved by the software GRIDFLM.

5 Experiments and Measurement Techniques

As one of three research methods in studying fluid dynamics, experiments play a very important role. Even before 1903, Wright Brothers had done numerous experiments with controlled kites and gliders. However, most of the Wright Brothers' success should be attributed to the experiments in their wind tunnel.

The Buckingham PI theorem [5, 65] tells us that the two flow fields are dynamically similar, if the shapes of two solid surfaces are geometrically similar and their similarity parameters are same. In the aerodynamic experiments, when Mach numbers and Reynolds numbers in two flows are the same, and a small airplane model is geometrically similar to a real size airplane, then the measurement of the lift-, drag-, and moment- coefficients of the small model in wind tunnel could be directly applied to the real size airplane. This theorem based on the theory of the dimensional analysis is a very popular procedure and has already saved much time and expenditure for us [9, 91]. Nevertheless, it is still very difficult to generate a hypersonic flow with the needed Mach numbers and Reynolds number for the separation process in wind tunnels.

With the agreements among the Collaborative Research Center SFB 255 in Technische Universität München, RWTH Aachen and ITAM SB RAS, many experiments are implemented to study the phenomena in the separation process. According to the types of tunnels, two different series of experiments are sorted here: one series was performed in a supersonic wind tunnel T-313 at ITAM SB RAS; the other series was performed in TH2-D, a hypersonic shock tunnel at RWTH Aachen. In these two tunnels steady flows corresponding with two Mach numbers, namely 4.05 and 7.9, are achieved for the simplified separation model with EOS and flat plate configuration. These results extend the knowledge on this class of complicated flows and provide good examples to verify the numerical software FLMNAV developed in TUM. The comparisons between numerical simulations and the corresponding experiments are given in Chapters 6 and 7.

5.1 Wind Tunnel T-313 and Its Set-Up

Located at ITAM (Institute of Theoretical and Applied Mechanics, Russian Academy of Sciences, Siberian Branch), Novosibirsk, Russia, the T-313 tunnel could generate the freestream of Mach 4.05. Many experimental results are obtained in T-313 tunnel for the simplified model EOS with flat plate [11, 54, 99]. They are achieved under conditions of temperature 297 K and unit Reynolds number of 50.0×10^6 1/m. These results are used as important references for the design of the TSTO vehicle and for the validation of the software FLMNAV.

Shown in Figure 5.1, the wind tunnel T-313 in ITAM is a supersonic blow-down wind tunnel. Its important components include a gas holder, an input pipeline, two pressure adapters, a plenum chamber, a technological insert with different sizes of throats, a nozzle block, a pressure chamber with a test section, a supersonic diffuser, two ejectors, an output pipeline, a noise-damping chamber, an extra input pipeline, an electric heater, and a plane contour nozzle. The gasholder is made of

stainless steel and has a volume of 4400 m^3. The dried air could be compressed up to 20 atmospheres in this gasholder. Making use of pressure difference, the compressed air generates a freestream with a high Mach number and blows down through the test section. When going through the ordinary input pipeline, the compressed air achieves in the test section up to Mach 4. When going through the extra input pipeline, the compressed air could reach Mach 5 or more. The electric heater makes the air warm to prevent air condensation. Adjusted by different inserts with different sizes of throats, the velocity of the freestream in the test section is controlled within the range of Mach 2 to Mach 7.

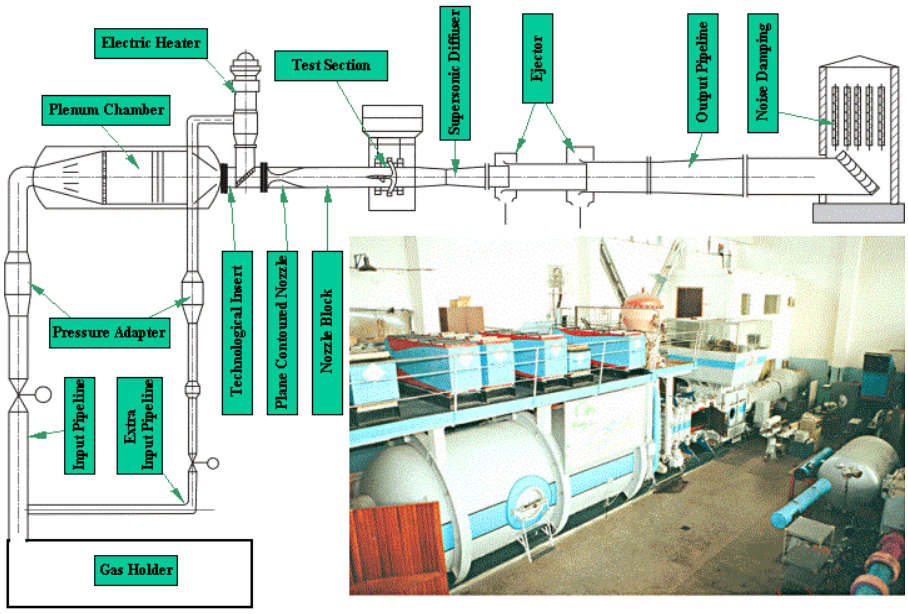

Figure 5.1: T-313 tunnel and its sketch.

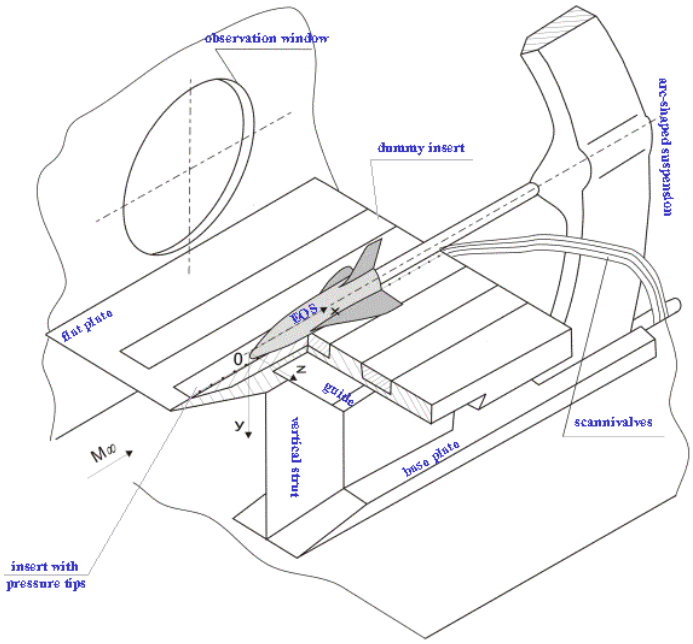

Figure 5.2: The arrangements of the EOS and flat plate in T-313.

As one of the most important components in the experiment, the test section is located in the pressure chamber. Its space is 2 meters long with a rectangular cross section of 0.6×0.6 square meters.

The EOS-plate model is arranged in this test section as shown in Figure 5.2. The flat plate is fixed on a guide. A vertical strut is connected to the base plate in the test section. This strut could adjust the distance between the EOS and the flat plate. The EOS is fixed by an arc-shaped suspension of a mechanical balance.

An insert on the plate contains 100 pressure taps, which are composed of MID-100 pressure meters, to measure the pressure influence from shock waves and reflected shock waves from the EOS. The distance between two pressure taps is 3.5 mm along the flow direction. The insert with pressure taps are located on the flat plate and just under the symmetric line of the EOS. The experiment could be watched and photographed through the observation window.

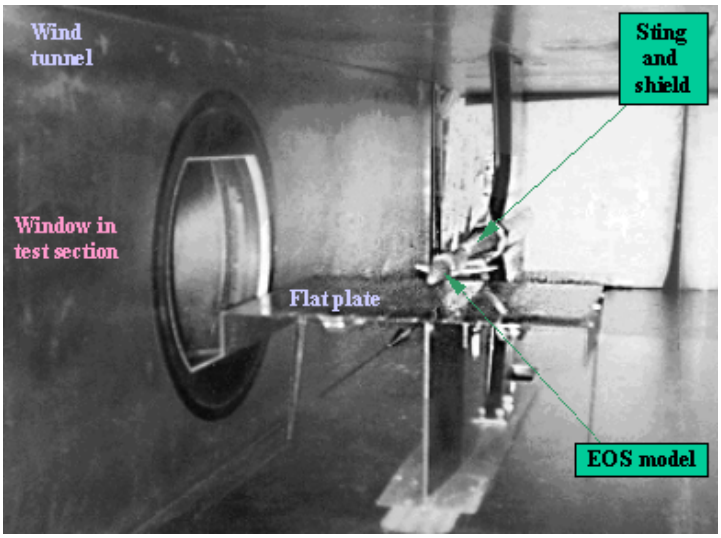

Figure 5.3: Front view of the EOS and flat plate in the test section of the wind tunnel.

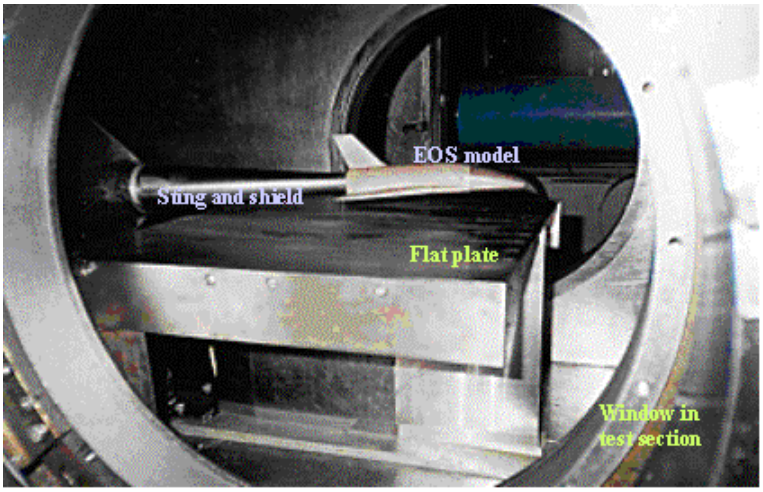

Figure 5.4: Side view of the EOS and flat plate looking from the observation window.

Figure 5.3 is photographed from the inner side of the wind tunnel and gives a front-view of model installation. To show a side-view of the EOS-plate model, Figure 5.4 is taken from the observation window in the test section.

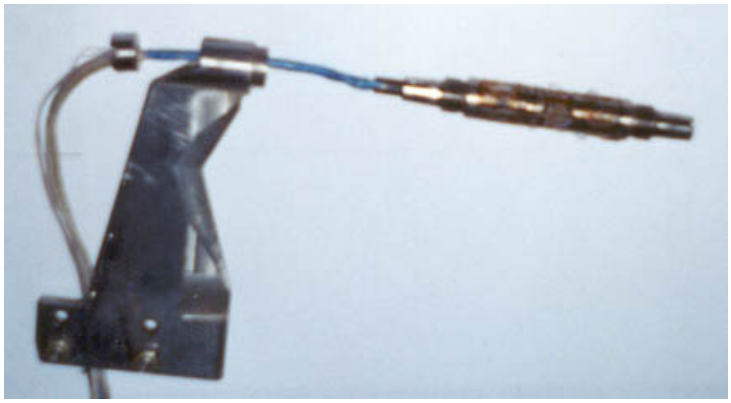

Figure 5.5: Internal six-component strain-gage balance I-210-348.

As shown in Figure 5.5, an internal six-component strain-gage balance I-210-348 is used to measure all six components acting on the EOS model. This balance is connected to the tail sting and mounted in the tail part of the EOS with a shield. Along the $\mathbf{X}_{\mathbf{T313}}$, $\mathbf{Y}_{\mathbf{T313}}$, $\mathbf{Z}_{\mathbf{T313}}$ axes shown in Figure 5.6, its measurements about the three corresponding aerodynamic forces limit to 150 N, 90 N, and 200 N, respectively. The maximum measurements about three aerodynamic moments, the rolling-, pitching-, and yawing- moments, are correspondingly 100 Nm, 250 Nm, and 100 Nm. The important aerodynamic coefficients could be calculated from those forces and moments.

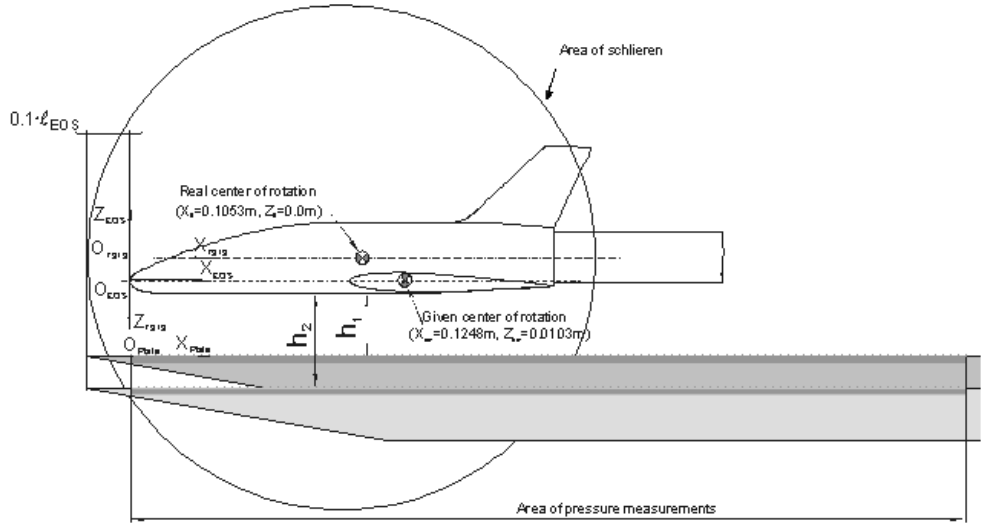

Figure 5.6: Coordinates and definitions for the configuration EOS and flat plate.

The maximum allowable stagnation pressure is 1.18 MPa in this pressure chamber. A rather wide range of unit Reynolds numbers Re_m from 9×10^6 to 60×10^6 1/m is allowed in the test section of the wind tunnel.

The duration of continuous operation could reach up to 10 minutes, if ejectors are switched off and the pressure in the plenum chamber is adjusted to its minimum for a given Mach number. When it requires a higher pressure in the plenum chamber or when it has to switch on the ejectors for low

Reynolds numbers, then the duration of the wind tunnel with desired air flow rate is usually no more than 3 minutes. In the test section, the relative root-mean-square deviations of the air velocity are less than 0.5 % from Mach 2 to Mach 4 and less than 1.0 % from Mach 5 to Mach 6.

Figure 5.7: CCD camera JAI-CVMIORS and its attachments.

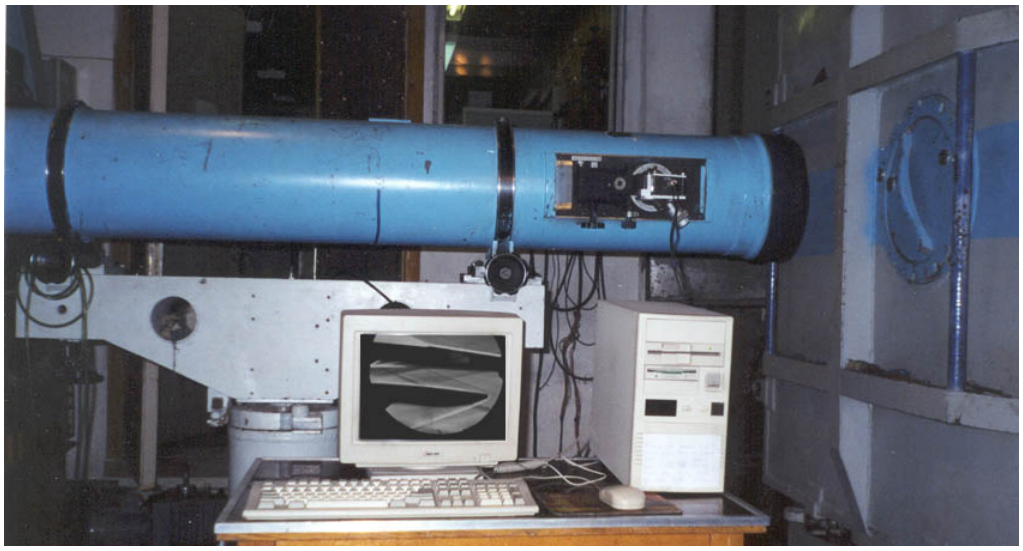

Figure 5.8: PC-EYE1 and the visualization equipment.

The airflow pattern was depicted by the gradients of the air density. It is visualized by a standard interference shadowgraph IAB-458. This IAB-458 instrument illustrates the air density by the optical difference of refraction, which is generated by the parallel beam of light travelling through the air. It is composed of a CCD camera JAI-CVMIORS, a special attachment device, and PC-EYE1 frame grabber. The CCD camera is a narrow-film camera and fixed on the attachment device as shown in Figure 5.7. The video signal from the CCD camera was transferred to a PC-EYE1 mounted in a computer. Together with a computer monitor, which is exhibiting a Schlieren picture, the visualization equipment is shown in Figure 5.8. In the experiment the upside of the EOS is arranged downwards, so its Schlieren picture looks top-down on the monitor.

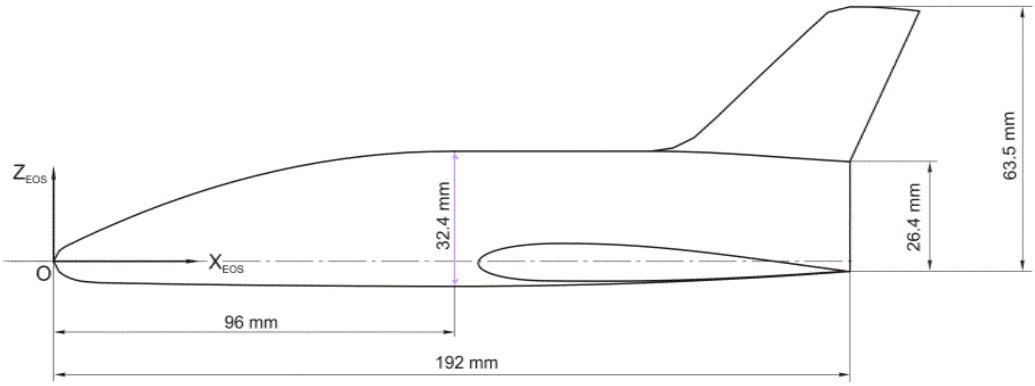

Figure 5.9: Size and side view of the EOS model in T-313 tunnel.

The EOS model was manufactured at ITAM with scale of 1:150 to the designed orbit stage. The size of the EOS model is constructed as shown in Figures 5.9 and 5.10.

A standard code transfers all of the results with respect to the experimental coordinate system $\mathbf{X_{T313}}$, $\mathbf{Y_{T313}}$, $\mathbf{Z_{T313}}$ to the results in the coordinate system $\mathbf{X_{EOS}}$, $\mathbf{Y_{EOS}}$, $\mathbf{Z_{EOS}}$. It also transfers the top-down manner to conventional manner, and the rotation center in experiment transfers in a similar way.

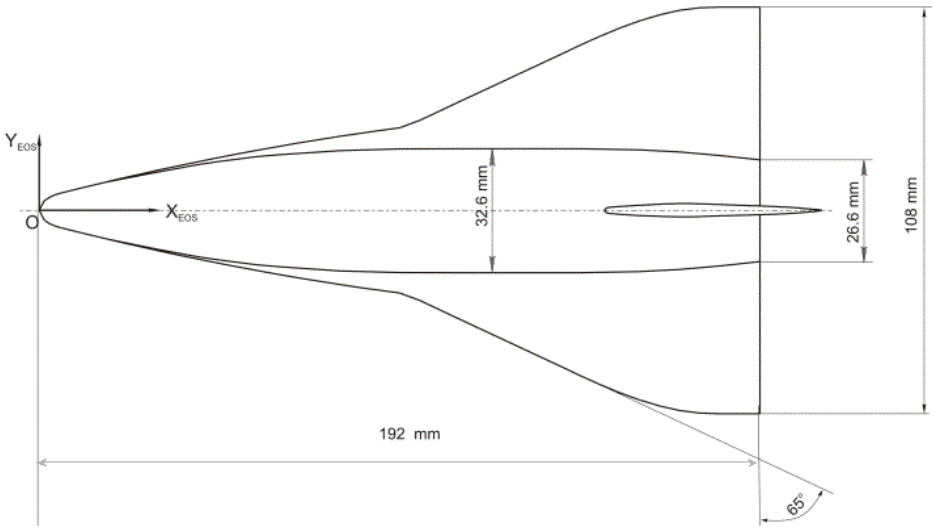

Figure 5.10: Size and top view of the EOS model in T-313 tunnel.

5.2 Shock Tunnel TH2-D and Its Set-Up

To acquire a hypersonic air flow, another series of experiments have been performed in the shock tunnel TH2-D of RWTH Aachen in Germany [38, 74]. The air stream in this tunnel is driven by a detonation of explosive gas. This kind of tunnels is especially suitable for the hypersonic space vehicles. The gas flow velocities could reach up to 4 km/s and stagnation temperatures could reach several thousand degrees in this tunnel.

The shock tunnel structure is illustrated in Figure 5.11. As listed in this sketch, the tunnel TH2-D mainly consists of damping section, detonation section, diaphragm chambers, initiation tube, steel-enforced concrete wall, recoil absorbing system, low pressure section, tube/endwall section, a slender conical nozzle, test section, dump tank, and vacuum pumps.

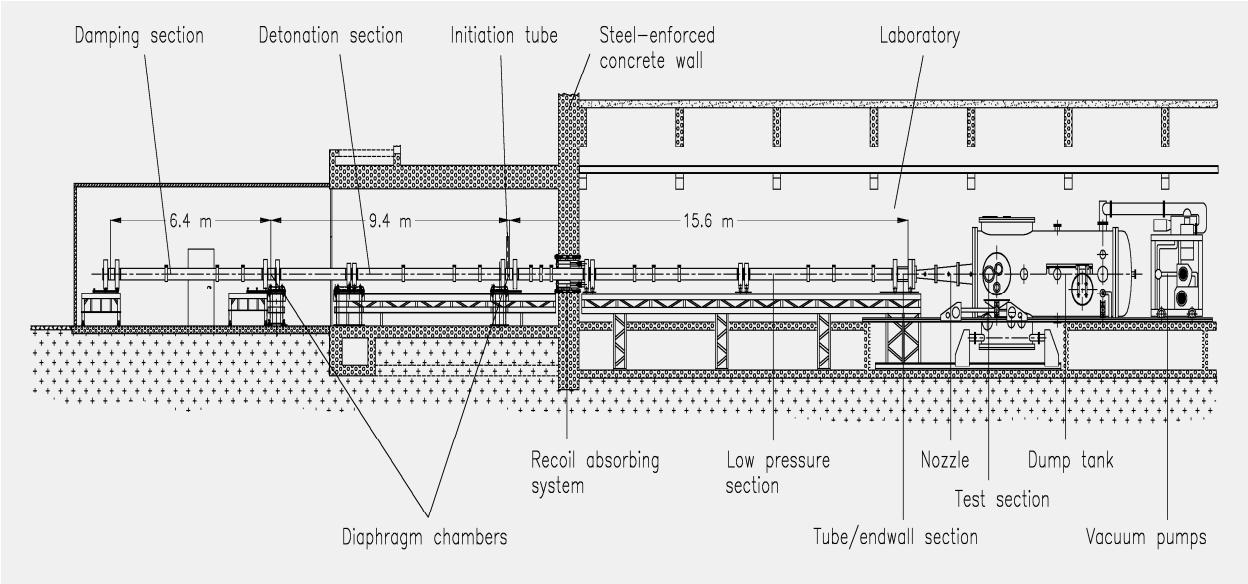

Figure 5.11: Sketch of shock tunnel TH2-D.

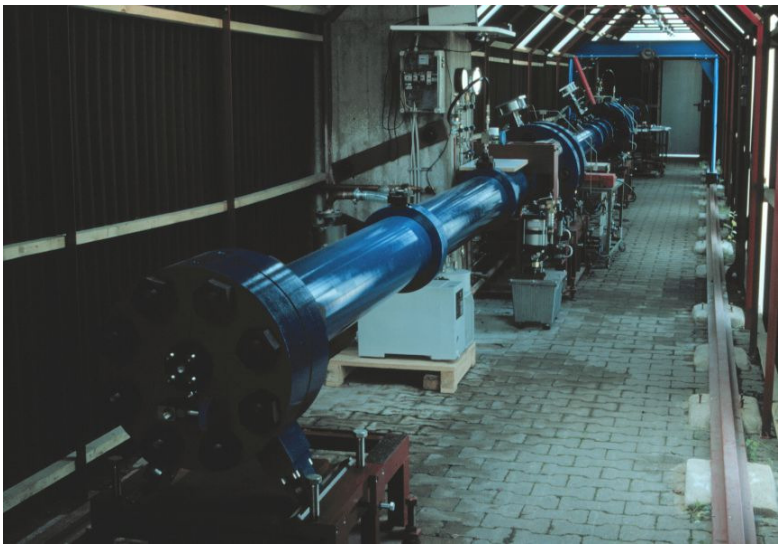

Figure 5.12: Damping and detonation sections of TH2.

The picture of damping and detonation sections of this tunnel is shown in Figure 5.12. In Figure 5.13 the low pressure and test sections are presented. The detonation sections and test sections are located in two different rooms. The tubes connecting most of the sections have an inner diameter of 140 mm. After explosion, the air travels from the detonation section to the test section through these tubes. Its maximum working pressure is 150 MPa.

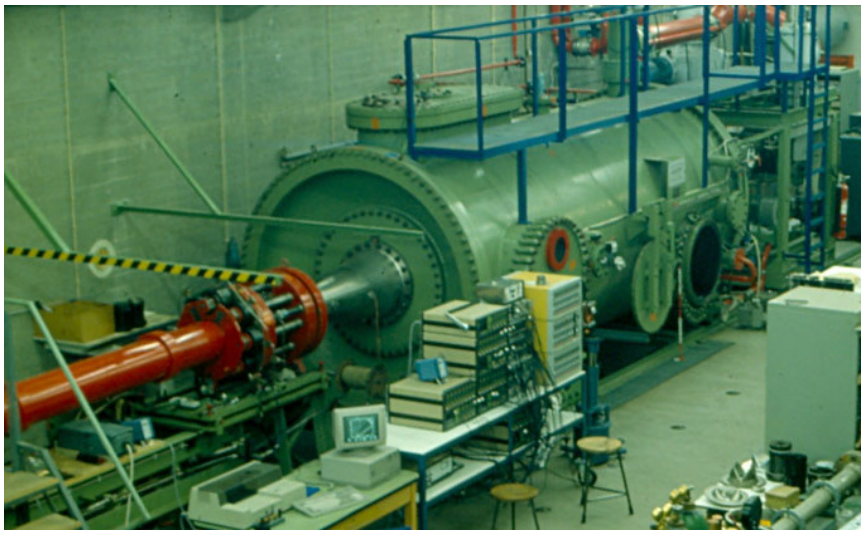

Figure 5.13: Low pressure and test sections of TH2.

In the preparation, the detonation section is filled with an oxyhydrogen mixture diluted with argon or helium. Conventional air is used in the downstream and its pressure could be adjusted between 0.1 and 10 bars. The dump tank is evacuated and closed by another thin diaphragm.

The detonative gas is ignited by an exploding wire located in the ignition tube. The subsequent detonation creates a high pressure between 100 and 1500 bar in the detonation section. The gas temperature is also very high. The high pressure bursts the diaphragm and drives the air to the test section. The relatively small central nozzle inlet reflects the shock wave and converts a high stagnation enthalpy into the energy, which accelerate the freestream additionally. In the test section, the Mach number of the freestream distributes in the range from 6.6 to 7.9, and unit Reynolds number from 0.8×10^6 to 7.9×10^6 1/m. Due to the character of the explosive process, the usable airflow through test section sustains only in a very short time. The time interval for measurement is about 2 to 8 milliseconds.

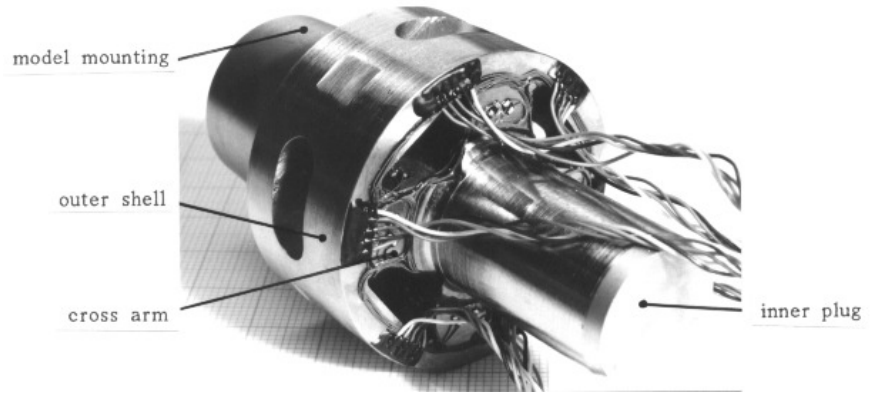

Figure 5.14: Stiff six-component balance to measure force and moment.

The high temperature and high pressure in the detonation section transfer to the other sections of the shock tunnel. The measurement equipment in the shock tunnel should work properly in a high temperature, high pressure and short-duration environment. Piezoelectric pressure transducers are

used as pressure sensors. One of them, Kistler 601 H, could record the pressure up to 1000 bar.

A stiff 6-component-DMS-balance as presented in Figure 5.14 could measure the forces and moments acted on the EOS. It is made by intensified carbon-fiber plastic and provides high eigen-frequency to fit the small figuration of the EOS. A sting uses an acceleration compensation to avoid its vibrations.

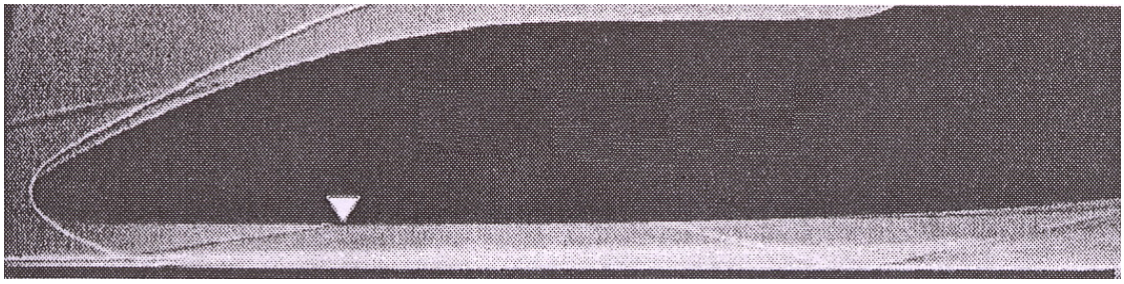

Figure 5.15: Experimental Schlieren picture of the EOS/flat plate configuration at $M_\infty = 7.90$, $\mathrm{Re}_m = 7.6\times10^6$, $\Delta\alpha = 0^\circ$, and **h/L** = 0.0662.

A Schlieren/shadow system consists of spherical mirrors 350 mm in diameter and 3.5 m in focal length. One of the black and white pictures is shown in Figure 5.15. Color Schlieren photographs as well as high-speed movie could be also taken. The typical time interval between two frames is 8.5 microseconds.

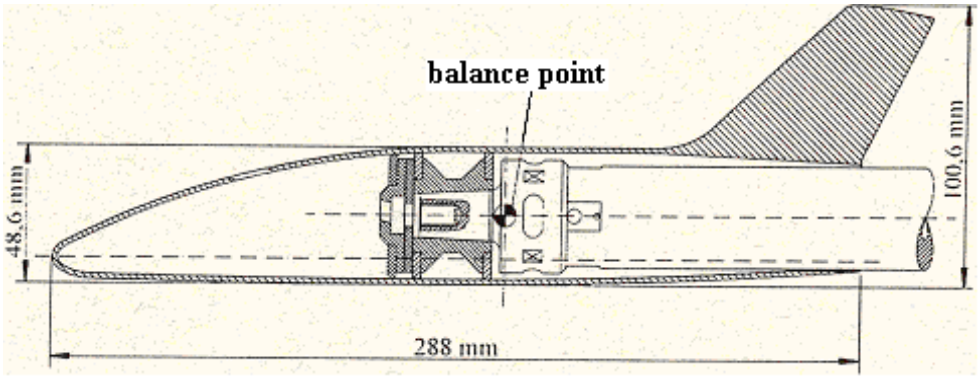

Figure 5.16: A construction chart of the EOS.

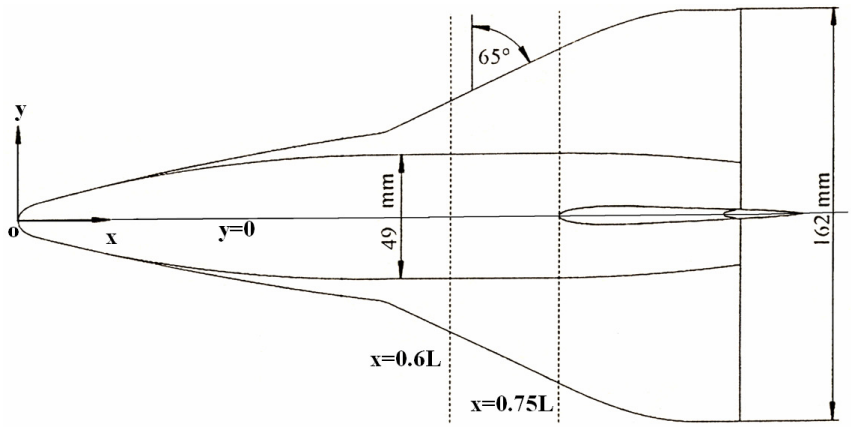

Figure 5.17: Three lines, x = 0.6**L**, x = 0.75**L**, and y = 0 on the lower surface of the EOS configuration.

The experimental EOS model is on the scale of 1:100 comparing to the designed model. It has the following sizes: reference length 288 mm, maximal body height 49 mm, middle height 48.6 mm, and half span 81 mm. The experimental equipment and its sizes are shown in Figures 5.16 and 5.17. The moment reference point locates on the middle point of the body length.

As shown in Figure 5.17, the line x = 0.6**L** is an interception line between the lower surface of the EOS and the plane at x = 0.6**L**. The lines with x = 0.75**L** and y = 0 are similarly defined and located on the lower surface of the EOS. Pressure sensors are equipped on these three lines. Pressure coefficients could be derived from these pressure measurements. In the following chapters, these three lines are quoted frequently to compare the experimental and numerical results.

A photo of the EOS configuration is shown in Figure 5.18. Many experimental results about the separation model of the EOS and flat plate are achieved in the hypersonic flow at Mach 7.9 [37]. Some more important parameters in a series of experiments are given in the following: unit Reynolds number $\mathrm{Re_m} = 7.6\times10^6$ 1/m, freestream temperature T_∞=180 K, freestream velocity V_∞=2120 m/s, freestream air pressure $p_\infty = 2.27$ kPa, and freestream density $\rho_\infty = 436$ kg/m^3.

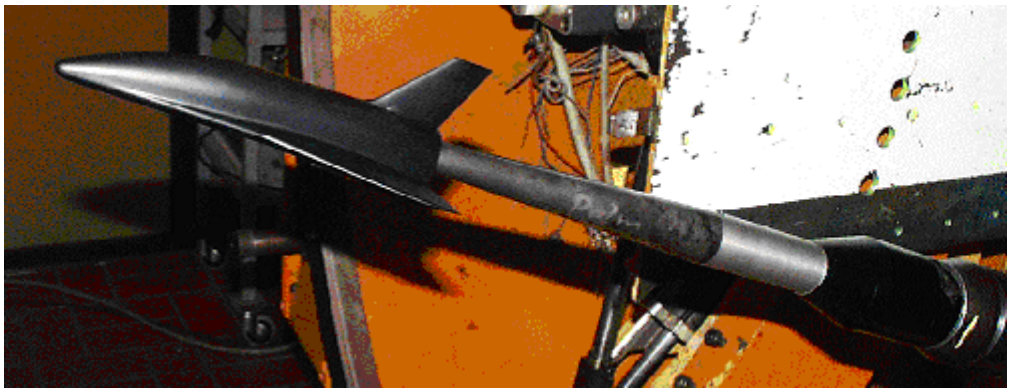

Figure 5.18: A photo of the EOS model for the TH2-D experiment.

6 Numerical Results Corresponding to the Experiments of ITAM

To simulate the aerodynamic properties of an orbital stage and a carrier stage in the separation process, a series of experimental and numerical simulations have been arranged and performed. As described in Chapter 5.1, the experimental results are obtained at Mach 4.05 in the supersonic wind tunnel T-313 in ITAM SB RAS [11, 54]. Corresponding to these experiments, many numerical computations are accomplished in this chapter. Not as restricted as in the experiments, numerical simulations could describe all of the aerodynamic properties on any point in the whole computational domain. Nevertheless, the experimental results are used to verify the reliability of the in-house numerical software.

The physical model in wind tunnel T-313 is built as in Chapter 5.1: the EOS and flat plate presenting a simplified model of orbital stage and carrier stage, Mach number of 4.05, Reynolds number per meter 50.0×10^6, temperature 279 kelvins, the length of the EOS 0.192 meters, and the ratio of specific heats 1.4. These environmental parameters are utilized exactly in the following numerical simulations in this chapter.

Using inviscid-, laminar-, and turbulent- flow models, the aerodynamic properties of the EOS and flat plate are analyzed in detail for both steady cases and unsteady cases. Four grids, which have been mentioned in Chapter 4.2 with different mesh points, are used in numerical simulations. Many numerical results are compared with the available experimental data.

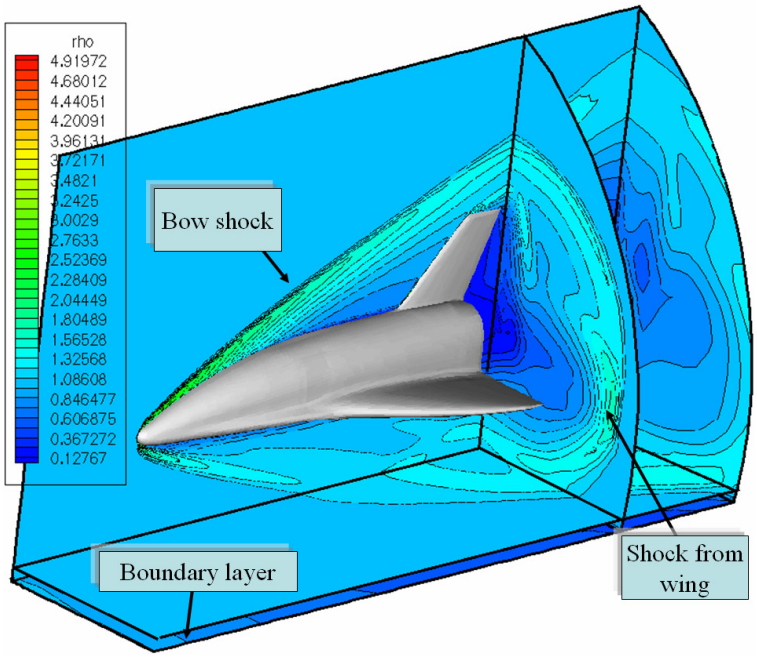

Figure 6.1: Numerical solution presented by the relative density contours ρ/ρ_∞ at $M_\infty = 4.05$, $\mathrm{Re_m} = 50.0\times10^6$, $\Delta\alpha = 0^\circ$, and **h/L** = 0.2562 (laminar flow and standard grid).

6.1 Steady Inviscid and Laminar Flows

As the carrier stage takes the orbital stage to the altitude for separation, the orbital stage is mechanically elevated from the carrier stage to a releasing position. The flow field in this releasing position is assumed as a steady state. To some extent, a series of steady states on different positions

could also be considered as an approximation of a continuous separation process on a series of discrete points.

Thereinafter, four different flying postures of the simplified TSTO model are discussed in steady inviscid and laminar flows. They are corresponding to different angles of attack $\Delta\alpha$ and different distances **h** between the center of the EOS and the flat plate. Numerical convergence criterions are defined as that the relative changes of the density are smaller than 10^{-5}.

For the steady laminar flow, Figure 6.1 shows a numerical solution of relative density contour ρ/ρ_∞ on the symmetry plane, on the flat plate, on a slice which is a little above the flat plate, and on two slices which are perpendicular to the freestream direction. In this picture it is clearly presented the bow shock, the shock from the wing, the wake expansion region, and the viscous effect on the flat plate. The maximal compression about ρ/ρ_∞ is 5.1.

The structures in inviscid flow are very similar as that in laminar flow, except the boundary layer. On an extra slice cutting the wing, Figure 6.2 shows the shock emanating from the wing and an evolution trace of the bow shock. The shock from the wing is weaker than the bow shock shown in Figure 6.1 and it is located behind the bow shock wave. These shocks hit the flat plate and are reflected by the flat plate to the rear part.

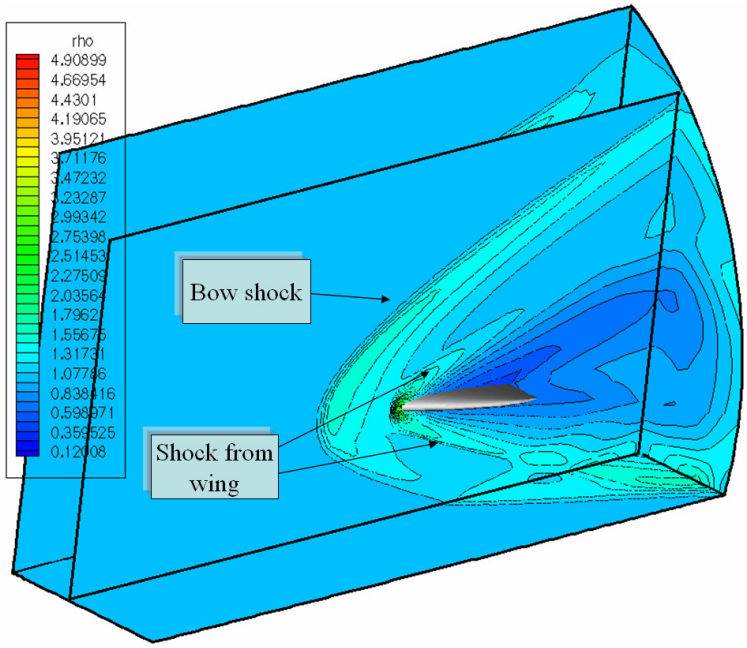

Figure 6.2: Shock emanating from the wing represented by the relative density contour ρ/ρ_∞ at $M_\infty = 4.05$, $\Delta\alpha = 0^\circ$, and **h/L** = 0.2562 (inviscid flow and standard grid).

As a synthesis of both the experimental data and the numerical results in laminar flow, in Figure 6.3, a Schlieren picture is compared with the relative density distribution from the numerical simulation in the symmetry plane. Both the experimental and numerical results present the phenomena of the EOS bow shock, the reflected bow shock, the shock emanating from the wing leading edges, and the very thin boundary layer on the flat plate. The overall consistency between the numerical calculation and the experiment on the shock evolution, impingement point and reflection angle is visually very good.

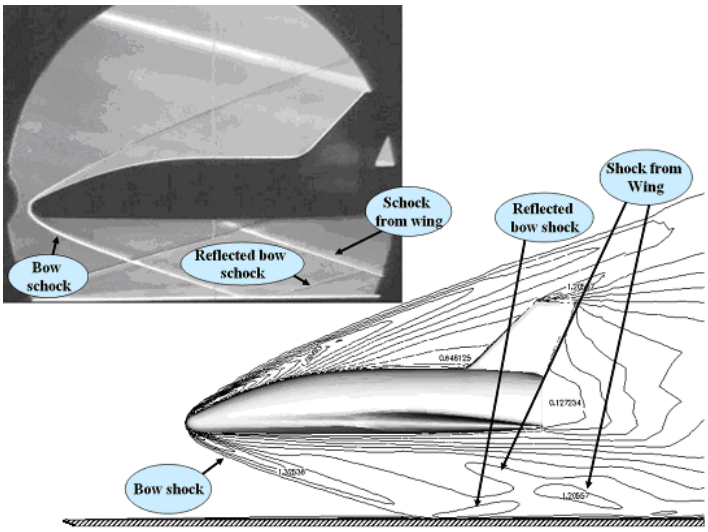

Figure 6.3: Comparison between Schlieren picture and numerical density distribution on symmetric plane using standard grid in laminar flow at $M_\infty = 4.05$, $\mathrm{Re}_m = 50.0\times10^6$, $\Delta\alpha = 0^\circ$, and **h/L** = 0.2562.

Because the pressure taps are only amounted on the dotted line as shown in Figure 6.4, the validations for the numerical software are restricted on this line. It is an intersect line between the EOS symmetry plane and the flat pate. In the computing domain, *x*-axis has a same direction with freestream and ranges from -0.3507L to 1.4583L. The numerical pressure is presented in the *x*-direction only from 0 to 1.4583L.

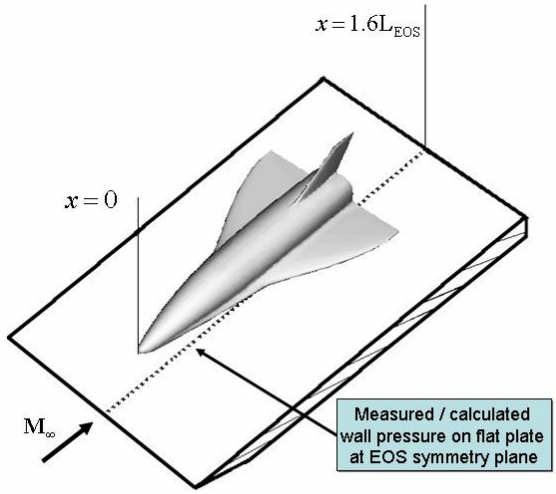

Figure 6.4: The positions of pressure taps in ITAM experiment.

At first, the standard grid is used to calculate the case with $\Delta\alpha = 0^\circ$ and h/L=0.1812. On the dotted line as shown in Figure 6.4, the corresponding pressure distribution shows a reasonable agreement between experimental and numerical data, referring to Figure 6.5.

The first peak is caused by the impact from bow shock, which emanates from the blunt nose of the orbital stage. The highest peak of Euler simulation is lower with respect to the experimental reference data, but higher than its counterpart of the NS simulation. Furthermore, the Cp-slope of the Euler simulation is also gentler than that of experiment, but steeper than the one of the NS simulation.

The second peak in Figure 6.5 is mainly impinged by the shock from the wing. Numerical simulations predict this peak a little more upstream than that in experiment. The peak position from NS simulation is located a little bit upstream comparing to its counterpart of Euler simulation. Between these two peaks, there is a high terrace of pressure. It is an extend impact effect from the bow shock. Besides these two peaks, good consistence about the pressure coefficients is presented among these three different simulations on the other points, especially the consistence between experiment and NS simulation. Figure 6.5 also shows that the shock waves bring significant force acting on the flat plate.

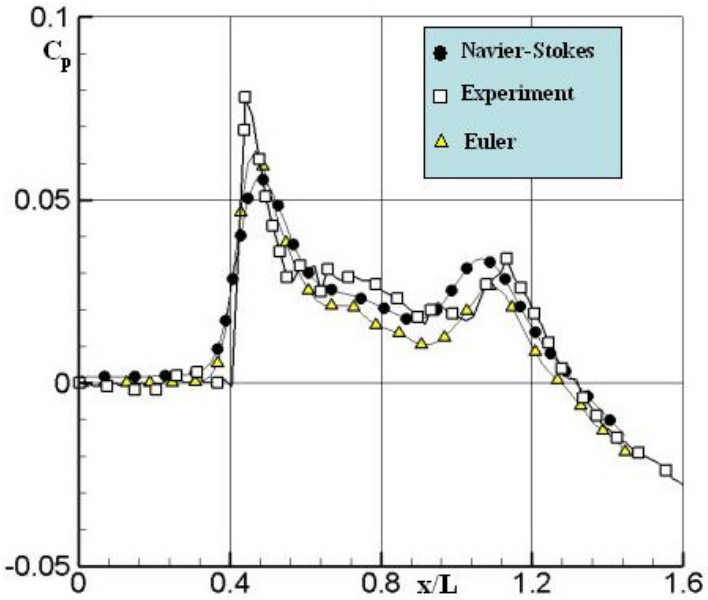

Figure 6.5: Comparison of measured and calculated pressure coefficients with the standard grid (645807 Nodes) for the dotted line shown in Figure 6.4, where $M_\infty = 4.05$, $\Delta\alpha = 0^\circ$, and **h/L** = 0.1812.

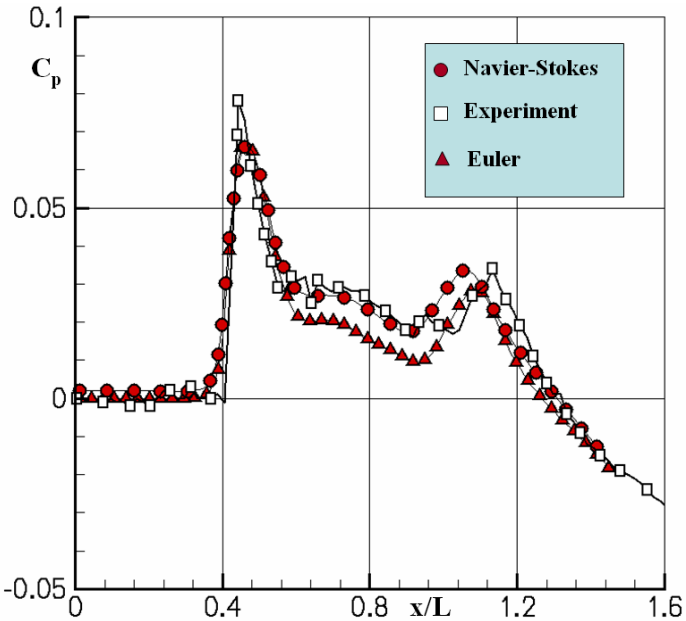

Figure 6.6: Comparison of measured and calculated pressure coefficients with the refined grid (1150142 Nodes) on the dotted line shown in Figure 6.4, where $M_\infty = 4.05$, $\Delta\alpha = 0^\circ$, and **h/L** = 0.1812.

To account for the influence of the numerical grid, the standard grid has been refined mainly in $\mathbf{X}_{\mathbf{EOS}}$-direction and within the boundary layer. This refined grid has 1.8 times nodes as many as the standard grid. Here it is used to simulate the same case just discussed above. Also on the dotted line as depicted in Figure 6.4, the distributions of the pressure coefficient are drawn in Figure 6.6 for the refined grid. Compared to Euler results, the first peak from NS simulation is higher than from Euler simulation. Its pressure coefficients show a better consistence with experimental results than the counterpart from Euler simulation.

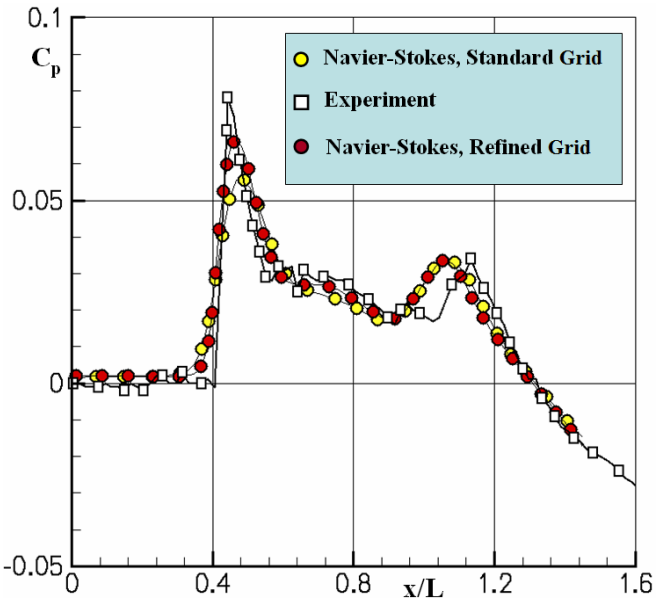

Figure 6.7: Pressure comparison of experimental data and NS simulations with standard and refined grids for the dotted line in Figure 6.4, where $M_\infty = 4.05$, $\mathrm{Re}_m = 50.0\times10^6$, $\Delta\alpha = 0^\circ$, and **h/L** = 0.1812.

The influence of the spatial resolution is more clearly presented in Figure 6.7 for the same laminar flow. Directly comparing the experimental result with two numerical solutions related with standard and refined grids respectively, we see that the mesh refinement improves the distinguishability about the first pressure peak with an acute Cp-slope. There is not much difference for the other points

Still using these two grids, comparison between Euler simulations and the experiment result is shown in Figure 6.8. Both Euler simulations are nearly the same. The solutions show almost no dependence with the mesh size any more. Consequently, the standard grid is already fine enough for the Euler simulation. A very fine mesh near the solid surface is not needed, when the separation process is simulated in inviscid flow.

The second validation case is designed with $\Delta\alpha = 0^\circ$, and h/L=0.2562. Based on the same refined grid, the simulation results are shown in Figure 6.9. Two numerical impingement points of the bow shock on the flat plate are nearly the same, and their positions are a little bit downstream comparing to the experimental counterpart. For the wing shock, the impingement points from numerical solutions are located a little bit upstream again. In contrast to the locations between the above-mentioned two impingement points, NS simulation approaches experimental result closer than Euler simulation.

Comparing Figure 6.9 with Figures 6.7 and 6.8, we see, the heights of the pressure peaks are reciprocal to the distance between the EOS and the flat plate. The pressure coefficient with h/L=0.2562 is only about 63% of that with h/L=0.1812.

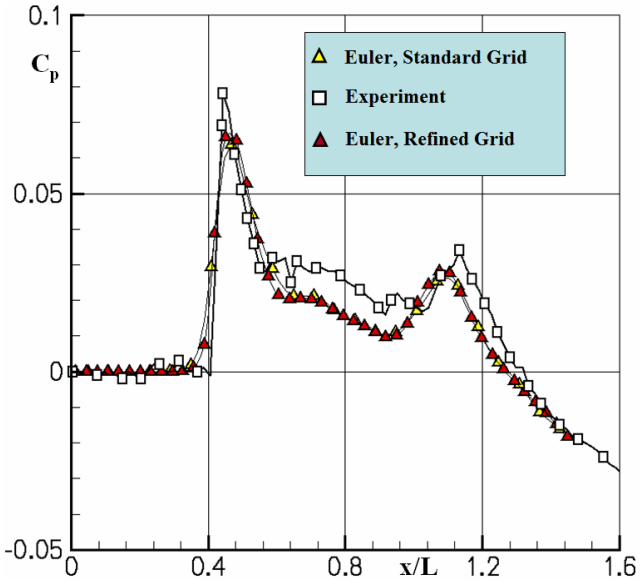

Figure 6.8: Pressure comparison of experimental data and Euler simulations with standard and refined grids for the dotted line shown in Figure 6.4, where $M_\infty = 4.05$, $\Delta\alpha = 0^\circ$, and **h/L** = 0.1812.

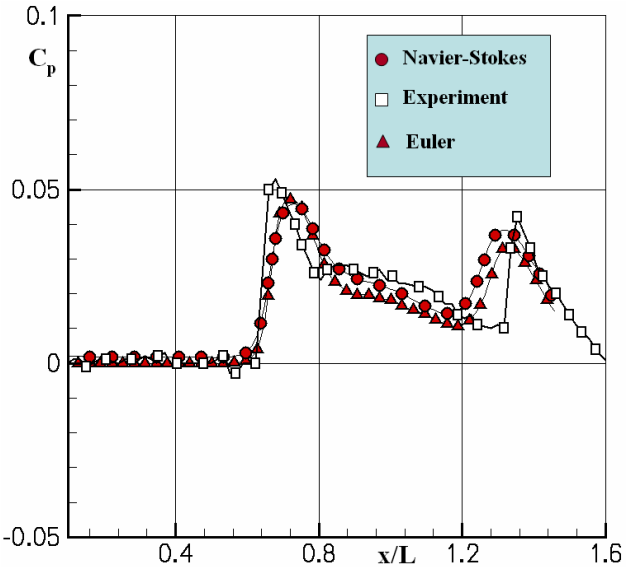

Figure 6.9: Comparison of measured and calculated pressure coefficients with the refined grid for the dotted line in Figure 6.4, where $M_\infty = 4.05$, $\Delta\alpha = 0^\circ$, and **h/L** = 0.2562.

Figure 6.10 also presents the difference of NS simulations resulting from different mesh resolutions. Compared the influence with the standard grid once more, the numerical pressure peaks using refined grid are closer to that of experiment. Slope of the pressure coefficient in experiment is much steeper than in numerical simulations. Except the two peak regions, all of the pressure coefficients have a good conformity.

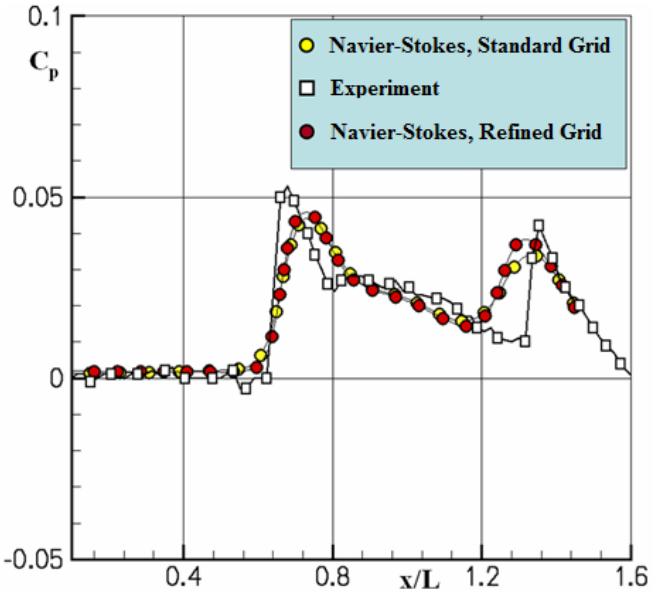

Figure 6.10: Pressure comparison between experimental data and NS simulations with standard and refined grids on the line shown in Figure 6.4, where $M_\infty = 4.05$, $\mathrm{Re}_m = 50.0\times10^6$, $\Delta\alpha = 0^\circ$, and **h/L** = 0.2562.

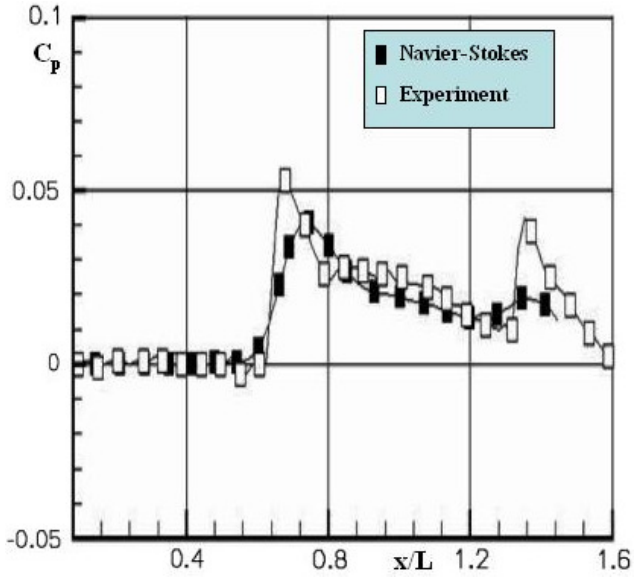

Figure 6.11: Pressure comparison of experimental data and NS simulations with coarse grid (404990 nodes) for the line shown in Figure 6.4, where $M_\infty = 4.05$, $\mathrm{Re}_m = 50.0\times10^6$, $\Delta\alpha = 0^\circ$, and **h/L** = 0.2562.

Additionally, the above case is also simulated using a coarse grid, which has nearly 2/3 times mesh points as many as the standard grid. As shown in Figure 6.11, the numerical solution fails to distinguish the second pressure peak induced from the shock of the wing. It presents a much smooth and smeared pressure peak there. This means, its mesh points are too less to precisely predict the shock peaks. Some important information could be lost when using this coarse grid. From the sense of the mesh convergence, its numerical solution is still far away in approaching to the theoretical solution. Therefore, the coarse grid will not be used any more in this thesis.

Using the standard grid as shown in Figure 6.10, the two peaks of shocks could be depicted much

better than using the coarse grid as shown in Figure 6.11. Additionally, using the refined grid could capture a little more information for the pressure peaks than using the standard grid. However, it consumes much more computer time and resource. Further in inviscid flow, the mesh refinement improves the solution nearly nothing. There is no need to make a fine resolution especially in the neighborhood of the solid surfaces in inviscid flow. As a result of compromise between accuracy and amount of computing work, the standard grid is mostly used in this thesis.

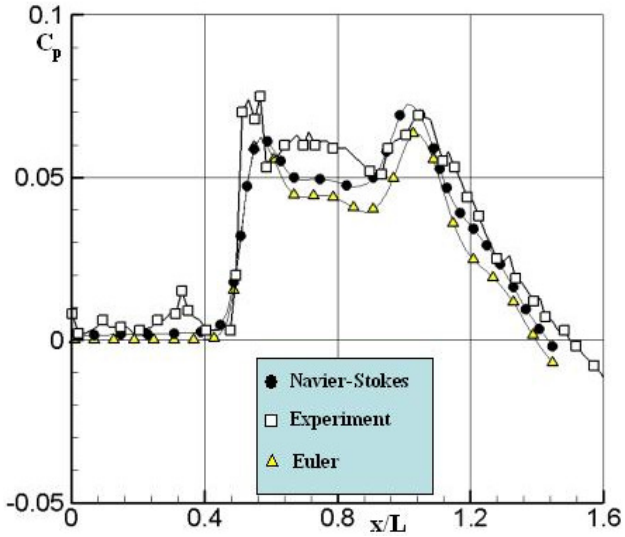

Figure 6.12: Comparison of measured and calculated pressure coefficients with the standard grid (645807 nodes) for the dotted line in Figure 6.4, where $M_\infty = 4.05$, $\Delta\alpha = 3^\circ$, and **h/L** = 0.1812.

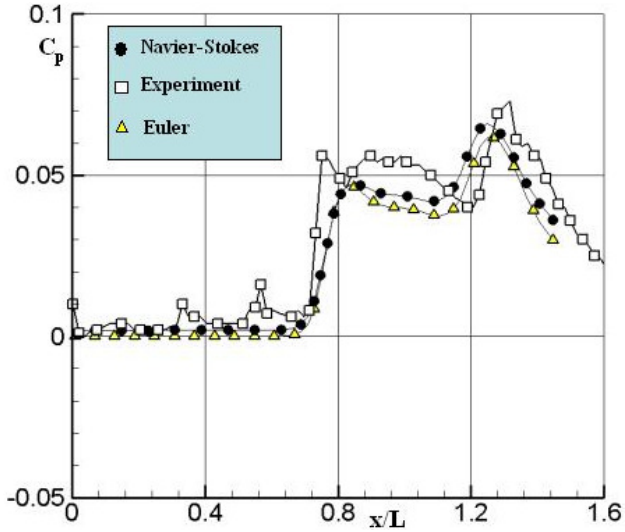

Figure 6.13: Comparison of measured and calculated pressure coefficients with the standard grid (645807 nodes) for the dotted line in Figure 6.4, where $M_\infty = 4.05$, $\Delta\alpha = 3^\circ$, and **h/L** = 0.2562.

In the third and fourth cases, the steady separation processes are simulated with the angle of attack of 3°. Their separation distances between $\mathbf{X_{EOS}}$-axis and the flat plate are **h/L**=0.1812 and **h/L**=0.2562 respectively. In these cases only the standard grid is used. Figure 6.12 and 6.13 present also the pressure coefficient distributions on the dotted line as marked in Figure 6.4.

Compared to the case of $\Delta\alpha = 0^\circ$ from Figure 6.5 to Figure 6.10, the impact points of the shocks on the flat plate are shifted downstream in the case of $\Delta\alpha = 3^\circ$ as shown in Figure 6.12 and Figure 6.13. Because the distance between the EOS nose and the flat plate increases, the strength of the pressure impinged by the bow shock tends to reduced. Contrarily, the wing moves closer to the flat plate and the impact strength from the shock of wing increases. Hence, the Cp values between the first peak and the second peak are of a same magnitude order in the case of $\Delta\alpha = 3^\circ$. In the fourth case with **h/L**=0.2562, the second pressure peak is even a little higher than the first peak.

Contrasting Figure 6.5 to Figure 6.9 with different distances **h/L**=0.1812 and **h/L**=0.2562, we find that the impingement point is affected by the distances and by the shock structures. The detached bow shock form and its shock angle are the same. When the orbital stage is near to the carrier stage, the impingement point locates on forepart of the flat plate. When orbital stage separates away from carrier stage, the impingement point will move backwards. Accompanying the increase of separation distance, all impingement points could leave away from the carrier stage. Similar results can also be concluded by comparing Figure 6.12 with Figure 6.13, where $\Delta\alpha = 3^\circ$.

The carrier stage in our model is much simplified as a flat plate. If it has a three-dimensional geometry, the shock structure will be more complicated. Not only the shock waves of orbital stage impinge to the carrier stage, but the shock waves of the carrier stage also impinge to the orbital stage in a similar way [50, 69].

As described in Chapter 5.1, a six-component strain-gage balance is used to measure the forces and moments. These forces and moments could be converted into some important aerodynamic coefficients in separation process, such as the drag coefficients C_D, lift coefficients C_L and pitching moment coefficients C_M. More details about their definitions and explanations could be referred to Appendix I. In the four cases discussed above, aerodynamic coefficients are also calculated in the FLMNAV solver for the simplified orbital stage - EOS around the rotation center (0.65, 0, 0). They are compared with the experimental results in Tables 6.1-6.4.

	C_D	C_L	C_M
Navier-Stokes, standard grid	0.02872	-0.01076	-0.01082
Navier-Stokes, refined grid	0.02942	-0.01051	-0.01071
Experiment	0.02940	-0.01150	-0.00410
Euler, standard grid	0.02788	-0.01358	-0.01093
Euler, refined grid	0.02805	-0.01341	-0.01098

Table 6.1: Comparisons of measured and calculated aerodynamic coefficients for the EOS with $M_\infty = 4.05$, $\Delta\alpha = 0^\circ$, **h/L** = 0.1812, and rotation center (0.65, 0, 0).

	C_D	C_L	C_M
Navier-Stokes, standard grid	0.02875	-0.01253	-0.01074
Navier-Stokes, refined grid	0.02940	-0.01131	-0.01088
Experiment	0.02990	-0.01200	-0.00590
Euler, refined grid	0.02811	-0.01404	-0.01074

Table 6.2: Comparisons of measured and calculated aerodynamic coefficients for the EOS with $M_\infty = 4.05$, $\Delta\alpha = 0^\circ$, **h/L** = 0.2562, and rotation center (0.65, 0, 0).

Referring to the standard grid, an overall good consistence between numerical and experimental results is shown for drag and lift coefficients. The pitching moment coefficients have some extent deviations. When using the refined grid, drag coefficients shows the best approximation to the experiments. For all four cases, the drag coefficients from Euler simulations are smallest. NS simulations present a better consistence with experiments. The same situation happens for the lift, too. For pitching moment coefficients, the situation is mixed. Usually the numerical pitching moments rotate the EOS anticlockwise more forceful than the experimental pitching moments do. In cases with $\Delta\alpha = 3^\circ$, these coefficients C_M from Euler simulations are closer to the measurements in experiments as shown in Tables 6.3-6.4.

	C_D	C_L	C_M
Navier-Stokes, standard grid	0.02937	0.02804	-0.00961
Experiment	0.02960	0.02640	-0.00750
Euler, standard grid	0.02839	0.02463	-0.00918

Table 6.3: Comparisons of measured and calculated aerodynamic coefficients for the EOS with $M_\infty = 4.05$, $\Delta\alpha = 3^\circ$, **h/L** = 0.1812, and rotation center (0.65, 0, 0).

	C_D	C_L	C_M
Navier-Stokes, standard grid	0.02935	0.02659	-0.00963
Experiment	0.03040	0.02930	-0.00620
Euler, standard grid	0.02843	0.02464	-0.00914

Table 6.4: Comparisons of measured and calculated aerodynamic coefficients for the EOS with $M_\infty = 4.05$, $\Delta\alpha = 3^\circ$, **h/L** = 0.2562, and rotation center (0.65, 0, 0).

When the angle of attack is $\Delta\alpha = 0^\circ$, the lift- and pitching moment coefficients obtained by numerical and experimental results are all negative. This means that the whole EOS is drawn to the flat plate and the nose of the EOS is anticlockwise rotated to the flat plate due to the aerodynamic properties. Therefore, it is very important to set the orbital stage at a certain angle of incidence to achieve a positive lift when it is released from the carrier stage. Otherwise there is a danger of collision between the orbital and carrier stage when the separation process takes place. Even if the angle of attack increases to $\Delta\alpha = 3^\circ$ and the lift coefficients become positive, the pitching moment coefficients are still negative. The decrease of $\Delta\alpha$ may result in the decrease of the lift. The negative pitching moment must be taken into account in the flight control system.

6.2 Unsteady Inviscid and Laminar Flows

After the orbital stage is released from the carrier stage, the orbital stage changes its angle of attack and leaves the carrier stage. Though the separation time lasts only from several milliseconds to several seconds, it is still a continuous maneuver [49, 50]. The aerodynamic forces separate the two stages. Comparing to experiment, numerical tools could simulate this unsteady separation process more freely and economically. This type of unsteady numerical simulation is much complex. It costs a lot of CPU time to achieve unsteady results.

In the following subsections, separation process is dissembled into two simple movements for the orbital stage, i.e. one pitching and one translation. The first only changes its angle of attack around its rotation center periodically. The second case raises the orbital stage merely upwards and downwards. Subsequently, complete unsteady separation maneuvers are also numerically simulated with different reduced frequencies. Moreover, everything is again arranged as the same as in ITAM experiments. The EOS/flat plate model replaces the designed two-stage model. The freestream is assumed as an inviscid or a laminar flow with $M_\infty = 4.05$. The ideal gas model is still used with the Pr = 0.72. It is assumed $\mathrm{Re_m} = 50.0\times10^6$ 1/m for the viscous flow, and $T_\infty = 297$ K. The adiabatic boundary condition is given for the solid surfaces of the EOS and the flat plate.

6.2.1 Pitching Movement in Inviscid Flow

As shown in the steady cases discussed in section 6.1, the EOS with a small angle of attack has a negative pitching moment. It endangers both two stages in the separation process. Consider the influence from the angle of attack, a dynamic pitching movement of the EOS is investigated. It is designed that the EOS rotates around the rotation center (0.65, 0, 0.0536) in continuous developing cases. The pitching movement is defined as

$$\Delta\alpha = \alpha_{\max} \sin(\tau \cdot k_{red}), \tag{6.1}$$

where $\Delta\alpha$ is the change of the angle of attack and τ is used to denoted as the phase development in numerical unsteady simulation. The freestream is modeled as an inviscid flow at $M_\infty = 4.05$. Some more physical characteristics are listed in Table 6.5.

Maximal angle of attack [°]	$\alpha_{\max} = 2$
Reduced frequency	k_{red}=0.1
Distance between the two stages	**h/L**=0.2562
Mean chord length [m]	$l_{\mu,Numerical} = 0.661458$
Ratio of the specific heat	$\gamma = 1.4$
EOS length [m]	$L_{ref} = 0.192$
Specific gas constant [J/(kgK)].	$R = 287$

Table 6.5: Physical parameters used in pitching movement.

In the code FLMNAV, the dimensionless time is defined as:

$$t^* = \tau * l_{\mu,Numerical} / (\sqrt{\gamma} \cdot M_\infty). \tag{6.2}$$

The real time could be derived in this environment as

$$t_{real} = t^* \frac{L_{ref}}{V_{ref}}. \tag{6.3}$$

Note that the reference velocity of the freestream V_{ref} in the above formula is

$$V_{ref} = \frac{V_\infty}{\sqrt{\gamma} \cdot M_\infty} . \tag{6.4}$$

Combining Eqs. (6.2), (6.3), and (6.4), the real time in the pitching movement could be written in another form as

$$t_{real} = \frac{\tau \cdot l_{\mu,Numerical} \cdot L_{ref}}{\sqrt{\gamma \cdot \mathrm{R} \cdot T_\infty} \cdot M_\infty} . \tag{6.5}$$

Substitute Eq. (6.5) into Eq. (6.1) yields the formula related to the real time as

$$\Delta\alpha = \alpha_{\max} \sin\left(\frac{t_{real} \cdot \sqrt{\gamma \cdot \mathrm{R} \cdot T_\infty} \cdot M_\infty}{l_{\mu,Numerical} \cdot L_{ref}} \cdot k_{red}\right) . \tag{6.6}$$

In the above pitching movement, the angle of attack changes as a sinusoidal function with respect to time.

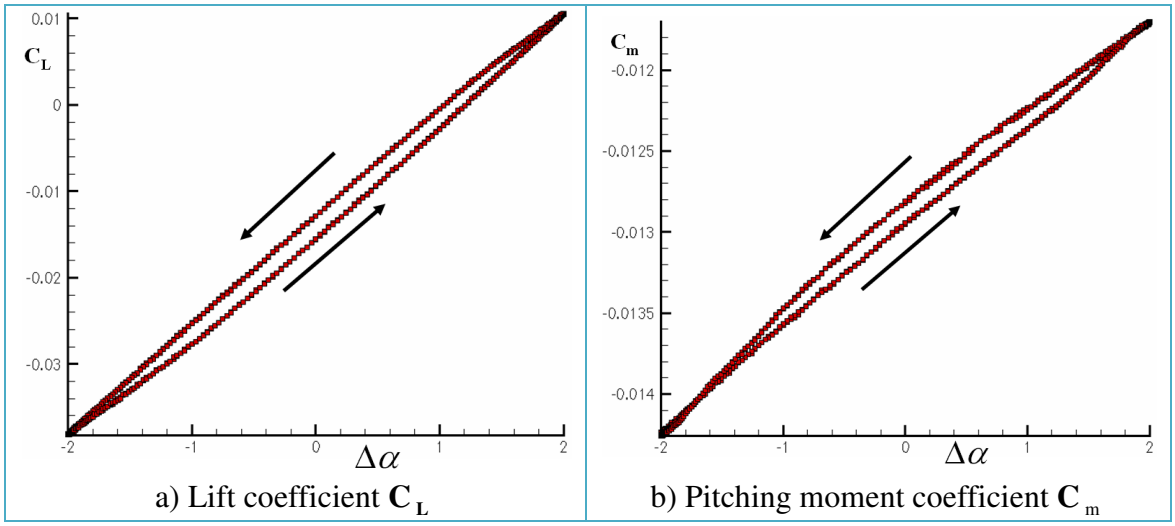

a) Lift coefficient $\mathbf{C_L}$ b) Pitching moment coefficient $\mathbf{C_m}$

Figure 6.14: Loop of lift- and pitching moment coefficients as function of $\Delta\alpha$.

As shown in Figure 6.14a, when $\Delta\alpha$ increases, the lift coefficient C_L also increases. If $\Delta\alpha$ increases to the maximum value, C_L achieves to the maximum value, too. When $\Delta\alpha$ decreases, the lift coefficient C_L just repeats the above process oppositely. Corresponding to a same value of $\Delta\alpha$, the lift coefficient C_L with an increase tendency is mostly smaller than with a decrease tendency. But near the position with positive and negative maximal values of α_{max}, the lift coefficient C_L with the increase tendency is slightly greater than that with the decrease of tendency. Only when $\Delta\alpha$ is greater than about 1.3 degrees, the lift coefficient C_L is greater than zero. A positive lift needed to separate the two stages.

The change of the pitching moment coefficient C_M is shown in Figure 6.14b. Its tendency is nearly the same as that for the lift coefficient, but all values are negative. The nose of the EOS turns down because of its negative pitching moments. This brings a trouble for the separation process. To avoid the EOS nose anticlockwise rotating down to the carrier stage, different rotation centers other

than (0.65, 0, 0.0536) should be chosen or auxiliary equipment is added to correct the pitching moment.

6.2.2 Translation in Inviscid Flow

As same as the pitching movement, translation is another simplified movement to describe the separation process. The EOS body moves upwards and downwards relative to the fixed flat plate periodically. Hereinafter, it is still assumed that $M_\infty = 4.05$ in the inviscid freestream. The other parameters are: the reduced frequency k_{red}=1.0; the fixed angle of attack $\alpha_0 = 3^\circ$ and the change of separation distance defined as:

$$\mathbf{h_{move}/L} = (\mathbf{h_{move}/L})_{\max} \cdot \sin(\tau \cdot k_{red}), \qquad (6.7)$$

where $(\mathbf{h_{move}/L})_{\max} = 0.075$. The nearest distance between the two stages is **h/L**=0.1812. The definitions of **h**, **L** and $\mathbf{h_{move}}$ could be referred to the Figure 2.1. As similar as the derivation to Eq. (6.6), the height of the translation also changes according to a sinusoidal curve corresponding to the physical time.

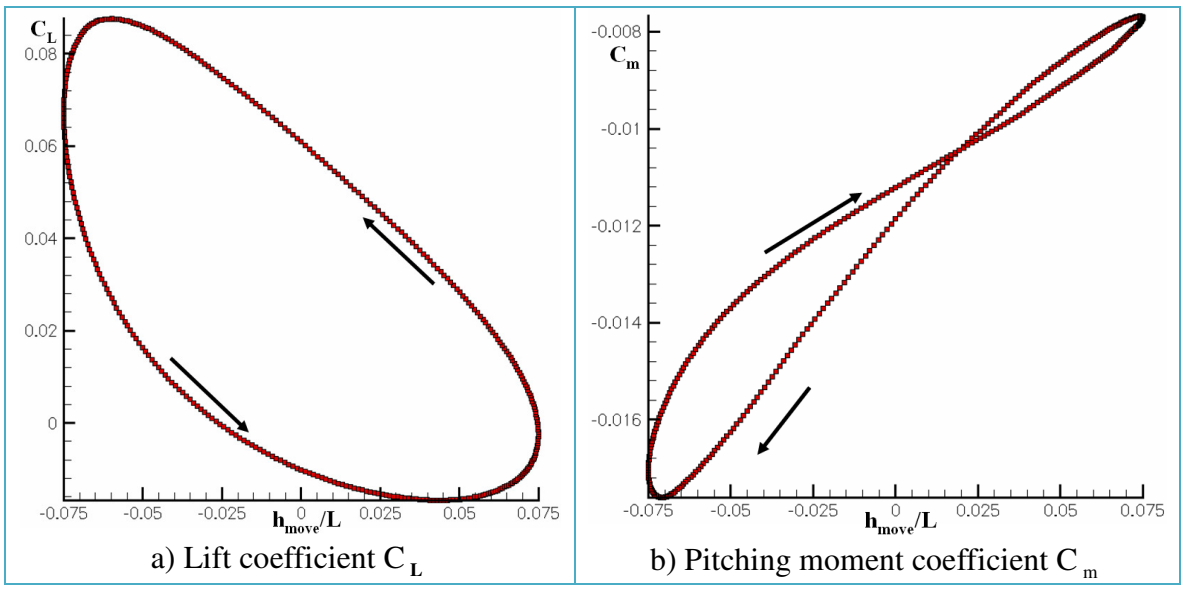

a) Lift coefficient C_L b) Pitching moment coefficient C_m

Figure 6.15: Loop of lift- and pitching moment coefficients as function of $\mathbf{h_{move}/L}$.

Look at Figure 6.15a, when $\mathbf{h_{move}/L}$ increases, the lift coefficient C_L decreases at $\mathbf{h_{move}/L}$=0, until $\mathbf{h_{move}/L}$ increase to the point 0.035. Afterwards, the lift coefficient C_L increases. This process continues even when the EOS converts its moving direction and approaches the flat plate. The increase tendency stops till $\mathbf{h_{move}/L}$ is at the position about -0.0065. Then C_L comes into a decrease region again. Most of the lift coefficient C_L is positive, except that $\mathbf{h_{move}/L}$ ranges in [-0.024, 0.075], where the EOS moves upwards apart from the flat plate.

As an example, we focus the case with **h/L**=0.1812 and $\alpha_0 = 3^\circ$, where $\mathbf{h_{move}/L}$=0. If the EOS is

moving upwards as shown in Figure 6.15a, the lift coefficient C_L=-0.011 is negative in a decrease tendency. At the same position, its lift coefficient C_L=0.061 is positive in an increase tendency, when the EOS is moving downwards. For the steady case as shown in Table 6.3, the lift coefficients C_L=0.028 are approximately the average value of above two tendencies. Due to k_{red}=1.0, the EOS translates very quickly. The lifts in unsteady case could deviate from the lift in steady case with a considerable magnitude.

With a fixed angle of attack of 3°, as we have seen in the steady case, the lift is positive and tends to separate the two stages. However, moving continuously upwards leads a negative lift. Therefore, the separation speed should keep a moderate manner. On the other side, if the EOS moves downward to the flat plate, the positive lift will automatically try to stop this tendency.

As shown in Figure 6.15b, a characteristic shape of "eight" in the pitch moment loop is clearly observed for motions at reduced frequency k_{red}=1.0. The pitching moment coefficients C_M for any height $\mathbf{h}_{move}$**/L** are negative. It becomes less negative with increasing height $\mathbf{h}_{move}$**/L**. But it becomes more negative with decreasing height $\mathbf{h}_{move}$**/L**. The pitching moment coefficients for both upwards and downwards moving are equal only at the position $\mathbf{h}_{move}$**/L**=0.02.

6.2.3 Separation Process in Inviscid Flow

Combining the pitching movement and the translation, we could describe a more complicated movement: a separation process with an arranged procedure. The fluid is considered as inviscid. The environment is as in the experiment of ITAM shown in Chapter 5.1. Further it is assumed that the initial distance between the two stages is **h/L**=0.1812; the initial angle of attack is $\alpha_0 = 0^\circ$, and the rotation center of the EOS is located at (0.65, 0, 0) at the beginning of the separation process. As drawn in Figure 2.1, the orbital stage continuously turns its nose clockwise and leaves the carrier stage in a short time. The separation distance is defined as

$$\mathbf{h_{move}/L} = (\mathbf{h_{move}/L})_{\max} \cdot (1 - \cos(\tau \cdot k_{red})) . \tag{6.8}$$

Similarly the angle of attack changes as:

$$\Delta\alpha = \alpha_{\max} (1 - \cos(\tau \cdot k_{red})) . \tag{6.9}$$

In the above equations (6.8) - (6.9), $(\mathbf{h_{move}/L})_{\max} = 0.1$, $\alpha_{\max} = 5^\circ$, and τ is the dimensionless time. In the similar way as Eq. (6.6) we could get

$$\mathbf{h_{move}/L} = (\mathbf{h_{move}/L})_{\max} \cdot (1 - \cos(\frac{t_{real} \cdot \sqrt{\gamma \cdot \mathrm{R} \cdot T_\infty} \cdot M_\infty}{l_{\mu,Numerical} \cdot L_{ref}} \cdot k_{red})) , \tag{6.10}$$

and the angle of attack changes as:

$$\Delta\alpha = \alpha_{\max} (1 - \cos(\frac{t_{real} \cdot \sqrt{\gamma \cdot \mathrm{R} \cdot T_\infty} \cdot M_\infty}{l_{\mu,Numerical} \cdot L_{ref}} \cdot k_{red})) . \tag{6.11}$$

Three different cases are numerically simulated corresponding to three different reduced

frequencies, k_{red} = 0.01, 0.1, and 1. They are used to scale different separation "velocities".

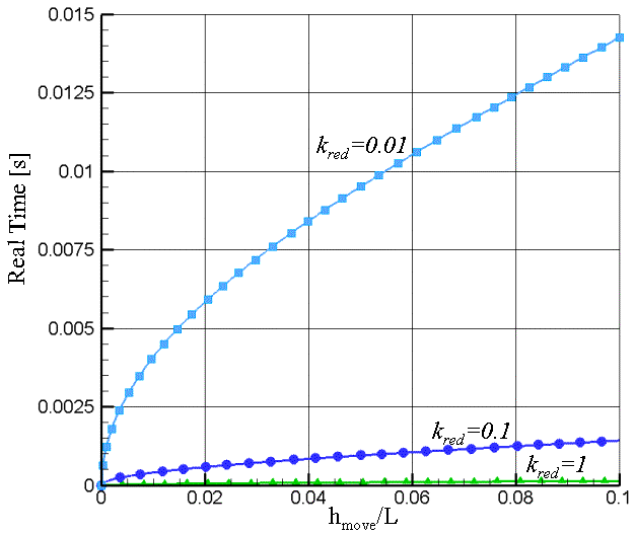

Figure 6.16: The dependency between distance $\mathbf{h_{move}/L}$ and the real time t_{real} in the unsteady separation processes with k_{red}=0.01, 0.1, and 1.

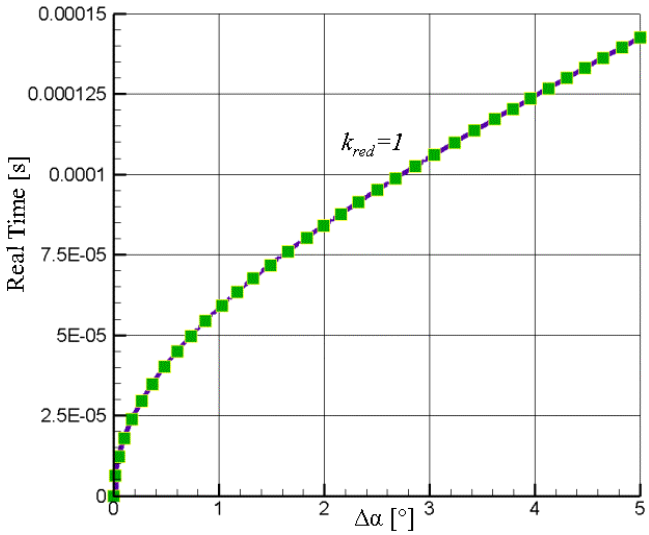

Figure 6.17: The dependency between the angle of attack $\Delta\alpha$ and the real time t_{real} in the unsteady separation process with k_{red} = 1.

In Eq. (6.10), the separation distance $\mathbf{h}_{move}\mathbf{/L}$ changes from 0 to 0.1 as a "one minus cosine" function of real time. When the separation distance reaches 0.1, as shown in Figure 6.16, the maximal time spans are 0.143E-1 seconds, 0.143E-2 seconds, and 0.143E-3 seconds corresponding to the reduced frequencies k_{red} = 0.01, 0.1, and 1.0, respectively. With the same distance, the separation processes are assigned with different time intervals corresponding to different reduce frequencies. The separation velocity with k_{red} = 0.1 is ten times faster than with k_{red} = 0.01. This is also true when comparing the separation process with k_{red} = 1 and with k_{red} = 0.1.

Like the separation distance, the angle of attack $\Delta\alpha$ has the similar relation related to the real

time. To look at the quickest separation process clearly, Figure 6.17 contains only one curve corresponding to Eq. (6.11) with k_{red} = 1. In this separation process, 0.143E-3 seconds are needed when the angle of attack turns 5 degrees.

The lift coefficients related with three different reduced frequencies in the separation processes are shown in Figure 6.18a. For the greatest reduced frequency k_{red} = 1.0, the corresponding lift coefficient decreases at the beginning because the orbiter moves upward very quickly. Later it increases a little due to the increase of the angle of attack. In the other two cases, the lift coefficients increase steadily. The smaller the reduced frequency is, the larger the lift coefficient is. With small reduced frequency, the angle of attack plays an important role for the lift. All of the lift coefficients corresponding to the greatest reduced frequency k_{red} =1.0 are negative, because the two stages separate too quickly and generate a suction effect between two stages. Corresponding to the other reduced frequencies $k_{red} = 0.1$ and $k_{red} = 0.01$, the lift coefficients become positive due to great angles of attack. The lifts are equal to zeros on $\mathbf{h}_{move}/\mathbf{L}$ =0.033 and $\mathbf{h}_{move}/\mathbf{L}$ =0.024 respectively.

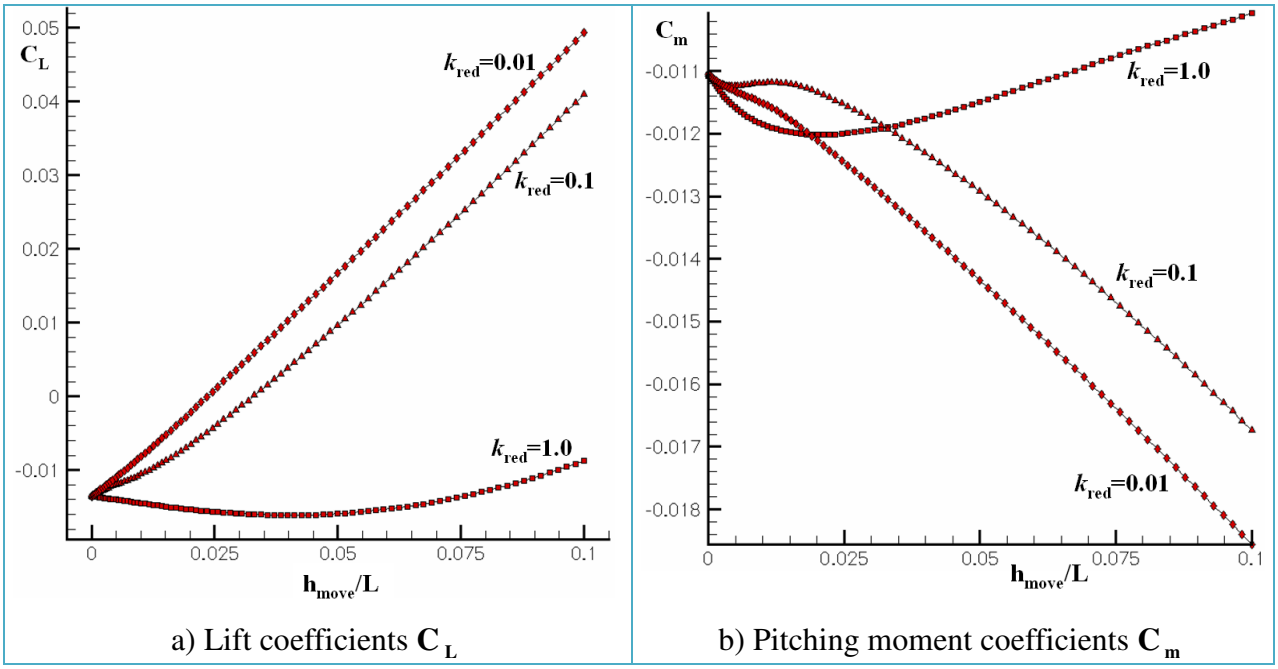

a) Lift coefficients $\mathbf{C}_L$ b) Pitching moment coefficients $\mathbf{C}_m$

Figure 6.18: Lift- and pitching moment coefficients as function of $\mathbf{h}_{move}/\mathbf{L}$ for the unsteady separation processes.

The pitching moment coefficients corresponding to the three different reduced frequencies are shown in Figure 6.18b. With the greatest reduced frequency k_{red} = 1.0, the pitching moment coefficient decreases at the beginning. Afterwards it increases accompanying with the increase of the separation distance. The pitching moment coefficients associated with the lower frequencies nearly decrease in the whole separation process. All of the pitching moment coefficients are negative. However, the magnitudes of the pitching moment coefficients change relatively small as shown in Figure 18b.

According to comparisons about lift in Figure 6.18a, it is recommended that the two stages should be separated moderately with a lower reduced frequency. The nose of the EOS will be rotated

anticlockwise if no other control technique is applied. Furthermore, if the angle of attack becomes smaller, the lift will decrease. As a consequence, it is possible that the lift will become negative, too. This case must be adequately addressed in the control of the separation process.

It is also suggested, that the EOS should be released with a given angle of attack, which is greater than the angle of attack corresponding to the zero point of the lift. Hence the lift could always be located in the positive zone in the separation process, even if the negative pitching moment turns the EOS nose downwards.

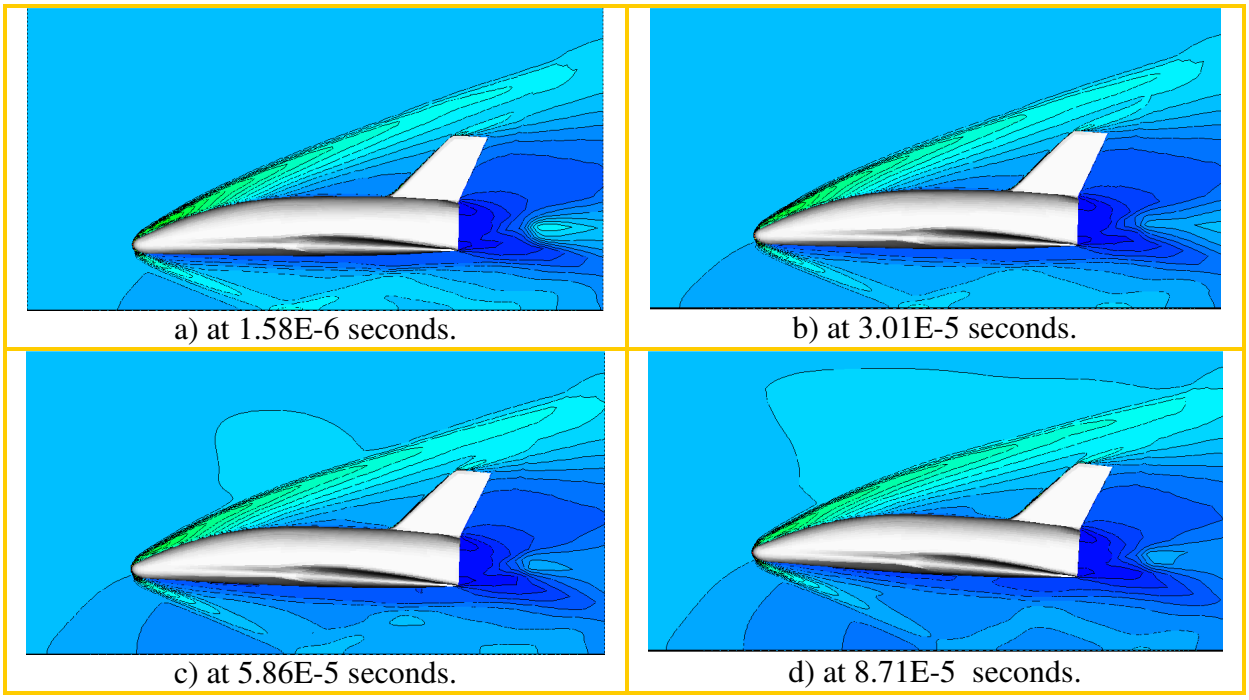

a) at 1.58E-6 seconds. b) at 3.01E-5 seconds.

c) at 5.86E-5 seconds. d) at 8.71E-5 seconds.

Figure 6.19: Contour of relative density ρ / ρ_{∞} at a reduced frequency of k_{red} = 1.0 for the unsteady separation process in inviscid flow.

The continuous separation process could be illustrated by a series of pictures in Figure 6.19 and Figure 6.20. The contours of relative density are shown on the symmetrical plane corresponding to two different reduced frequencies. The largest compression is concentrated on the bow region. The smallest densities are located in the wake region. In the region between the EOS and the flat plate, the gradient of density decreases accompanying the increase of the separation distance, especially in the neighborhood of the flat plate.

Because the EOS moves very quickly with reduced frequency of k_{red} = 1, the relative density between EOS and flat plate presents a suction zone ahead of the bow shock wave as shown in Figure 6.19. In the region above the EOS and before the bow shock wave, the relative density is squeezed. It appears at first at 5.86E-5 seconds. But with lower induced frequencies with k_{red} = 0.01, there are no such regions as shown in Figure 6.20. Except these two extra regions, the shock contours for all frequencies are very similar. At the beginning, the reflected shock wave hits the underside of the EOS, and later the impingement points move further downstream, until this point leaves the EOS. The impacts of the reflection shocks become weak accompanying the increase of the separation distance.

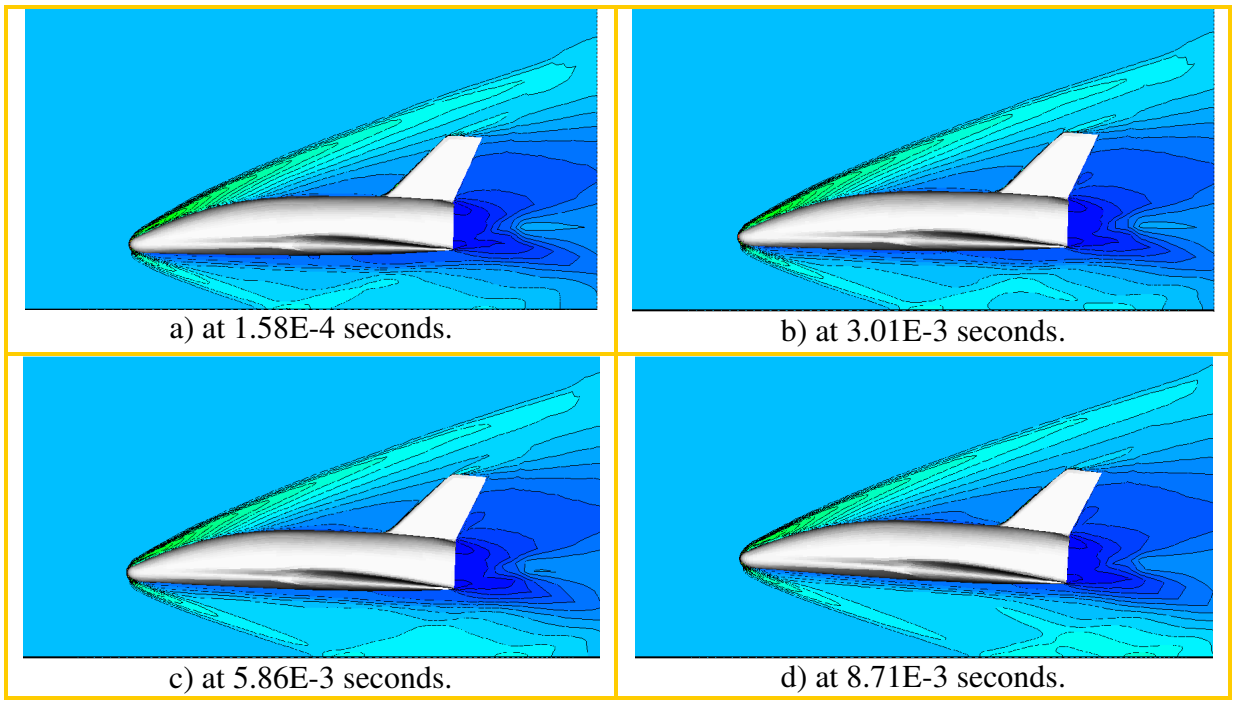

a) at 1.58E-4 seconds. b) at 3.01E-3 seconds.

c) at 5.86E-3 seconds. d) at 8.71E-3 seconds.

Figure 6.20: Contour of relative density ρ / ρ_{∞} at a reduced frequency of $k_{red} = 0.01$ for the unsteady separation process in inviscid flow.

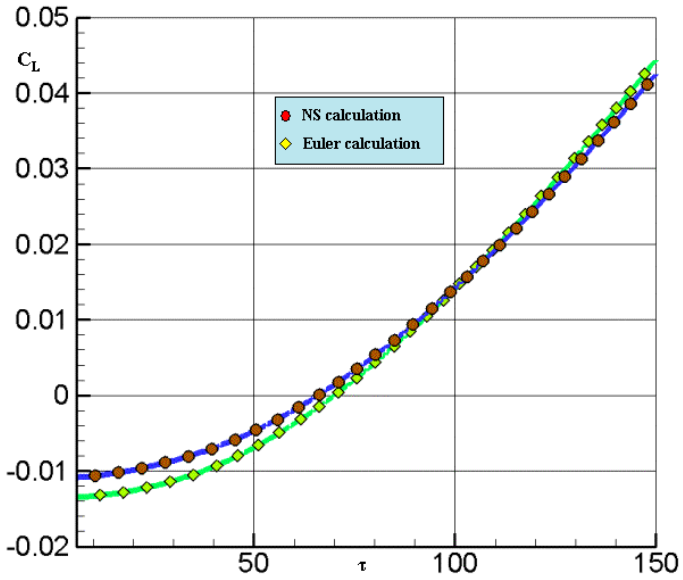

Figure 6.21: Comparison of lift coefficients using the standard grid in numerical simulations with $M_{\infty} = 4.05$, k_{red}=0.01 and $\mathrm{Re}_{\mathrm{m}} = 50.0 \times 10^6$.

6.2.4 Separation Process in Laminar Flow

Using the same parameters as in subsection 6.2.3 for inviscid flow, a continuous separation process is also simulated in laminar flow with $\mathrm{Re}_{\mathrm{m}} = 50.0 \times 10^6$ 1/m. Because of the computing expenditure and complexity in solving the full Navier-Stokes equations, a separation with the smallest reduced frequency k_{red}=0.01 is simulated corresponding to a slow velocity. Its results are also compared to the results in Chapter 6.2.3 with the same reduced frequency.

As shown as in Figure 6.21, the lift coefficients C_L for the EOS in both laminar and inviscid flows increase corresponding to the phase change τ. At the beginning part of the separation, all of them are negative, because the angle of attack is initially set to zero degree. From the point with τ=70.4 (t=6.4E-3 seconds or $\Delta\alpha$ about 2 degrees), the lift coefficients are greater than zero. The lift simulated in laminar flow is larger than that simulated in inviscid flow at the beginning part of the separation. However, the lift in laminar flow is surpassed by the lift in inviscid flow at about the 8.38E-3 seconds.

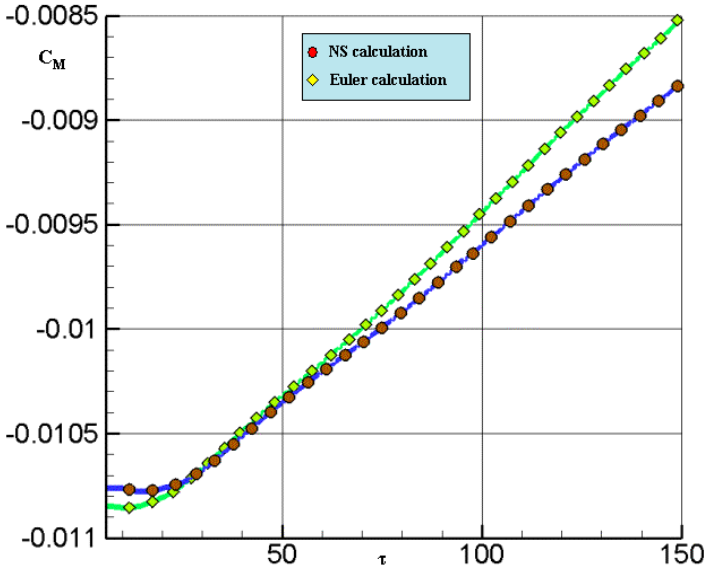

Figure 6.22: Comparison of pitching moment coefficients using the standard grid in numerical simulations with $M_\infty = 4.05$, k_{red}=0.01 and $\mathrm{Re}_m = 50.0\times10^6$.

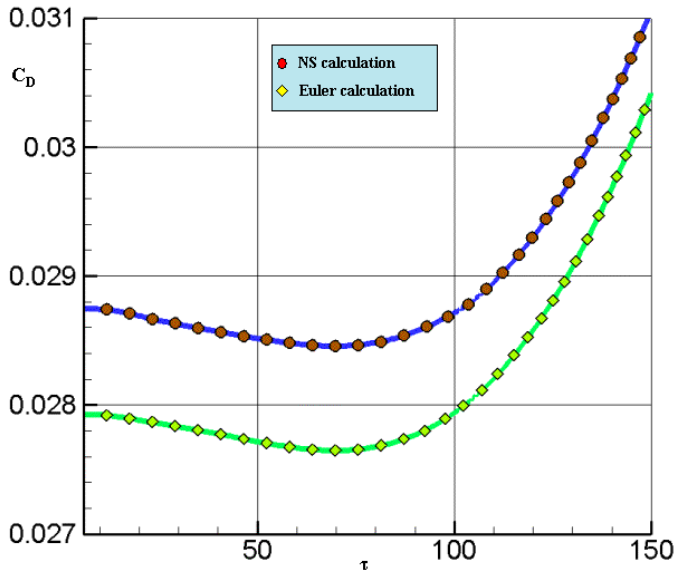

Figure 6.23: Comparison of drag coefficients using the standard grid in numerical simulations with $M_\infty = 4.05$, k_{red}=0.01 and $\mathrm{Re}_m = 50.0\times10^6$.

In Figure 6.22, the pitching moment coefficients C_m in two flows change with a similar tendency as the lift coefficients C_L in Figure 6.21. All C_m are negative. Accompanying the increase of the

distance, the reflected shock impinges weakly on the rear part of the EOS. Subsequently, the coefficients C_m become less negative in the separating process.

In Figure 6.23, the drag coefficients show a little different tendency. Both drags obtained from Euler simulation and from the NS simulation decrease until τ=69.2. The physical time is of about 6.3E-3 seconds. Thereafter, both drags increase nearly simultaneously. As in the steady cases, the drag coefficients in laminar flow are always greater than that in inviscid flow.

Analyzing the numerical unsteady simulation about the separation maneuver, we see that the tendencies of the dynamic properties in both laminar and inviscid flows show good consistency. They present, that the orbital stage has negative lifts as well as a negative pitching moments, when operating at a very small angle of attack. Accompanying with the increases of angle of attack and separation distance, lift also increases. In the same time, the pitching moment always tends to turn the nose of the EOS down. With the increase of the cross area in the freestream direction, drag changes its tendency from decrease to increase. These results agree with the prediction made in the steady simulations of section 6.1. Therefore, the separation maneuver should set a given incidence angle at the beginning to achieve a positive lift. The negative pitching moment must be carefully considered or controlled via the flap system.

6.3 Free Orbital Stage at $M_\infty = 4.05$

As the third phase in the end of separation process, a free flying orbital stage is simulated at $M_\infty = 4.05$, $\Delta\alpha = 0^\circ$, and rotation center (0.65, 0, 0) as the same as in the experiment. This phase is calculated using both laminar and inviscid flows and further validated by the experimental results.

	C_D	C_L	C_M
Navier-Stokes, standard grid	0.02895	-0.01423	-0.01040
Experiment	0.03000	-0.01450	-0.00500
Euler, standard grid	0.02810	-0.01396	-0.01062

Table 6.6: Comparisons of measured and calculated aerodynamic coefficients for the free EOS stage with $M_\infty = 4.05$ and rotation center (0.65, 0, 0).

The lift and drag forces as well as the pitching moment coefficients obtained from the experiment, from the Euler simulation and from the NS simulation are listed in Table 6.6. The lift coefficients and pitching moment coefficients are still negative at the angle of attack of $\Delta\alpha = 0^\circ$. The drag coefficient of the Euler simulation is smaller than that of the NS simulation, because inviscid flow lacks friction effect.

Simulating the dynamic properties at laminar flow, Figure 6.24 shows a contour plot of the relative density on the symmetric plane. The bow shock structures about orbital stage are clearly presented. Its maximal value of relative density is ρ / ρ_∞=4.99. Because there are no reflected shocks coming from carrier stage, the rear part and the wake region of the EOS are not interfered by aforementioned shocks any more.

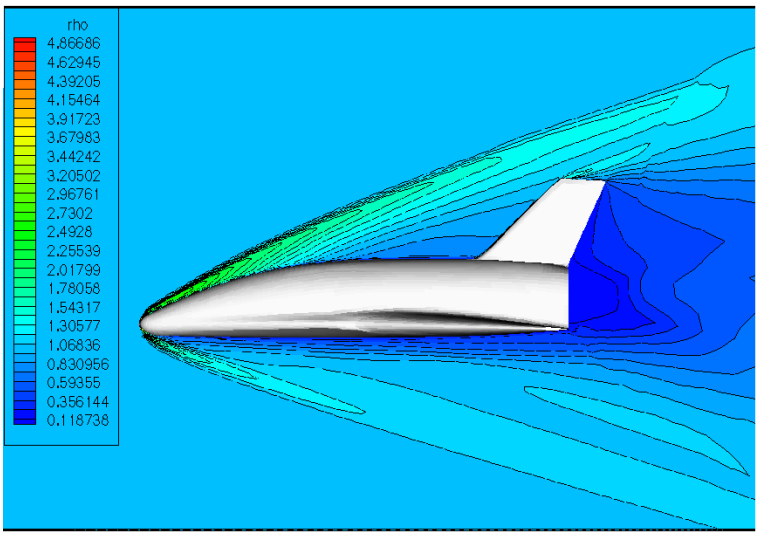

Figure 6.24: Numerical solution of relative density ρ / ρ_{∞} at $M_{\infty} = 4.05$, $\mathrm{Re}_{\mathrm{m}} = 50.0 \times 10^{6}$, $\Delta\alpha = 0^{\circ}$ in laminar flow.

	C_D	C_L	C_M
h/L = 0.1812	0.02872	-0.01076	-0.01082
h/L = 0.2562	0.02875	-0.01253	-0.01074
h/L = infinity	0.02895	-0.01423	-0.01040

Table 6.7: Comparisons of measured and calculated aerodynamic coefficients for different **h/L** with $M_{\infty} = 4.05$, $\mathrm{Re}_{\mathrm{m}} = 50.0 \times 10^{6}$, and rotation center (0.65, 0, 0) in laminar flow.

In Table 6.7, the dynamic properties in laminar flow are collected with different distances between the EOS and the flat plate. They are from **h/L**=0.1812 to **h/L**=0.2562, and to infinity. The numerical results are extracted from the Tables 6.1, 6.2, and 6.6 with the standard grid. The changes of the dynamic properties come from the interference effects between the two stages.

With the increase of the distance between two stages, the lift coefficients decrease, because the intensity of the reflected shocks hitting on the lower side of the EOS decreases. In contrast to the lift in the case with h/L=0.1812, the lift of free orbital stage decreases about 32%. With increasing distance h/L, the impingement points of the shocks reflected by the flat plate move downstream and finally do not hit on the undersurface of the EOS any more. The pitching moment coefficient of the free flying orbital stage becomes larger. The drag forces increase very slightly and are nearly the same. This results from the pressure decrease behind the tail region, because the impact of the reflected shock on this region becomes weaker and weaker.

6.4 Influence of Turbulent Flow

To describe the nature of irregularity, diffusivity, and vorticity in turbulent flow, different models have been proposed by Reynolds, Prandtl, Baldwin and Lomax, and etc. Many of milestone works and the detailed B-L model are referred in Appendix H.

As a simplest example, the development of the turbulent flow in boundary layer above a flat plate is shown in Figure 6.25. It is composed of the three development processes: laminar flow zone,

transition zone, and turbulent flow zone. Comparing the whole flow region, the boundary layer near the flat plate is very thin. It was pointed out by Prandtl that the boundary layer plays a very important role in the research about friction and heat transfer.

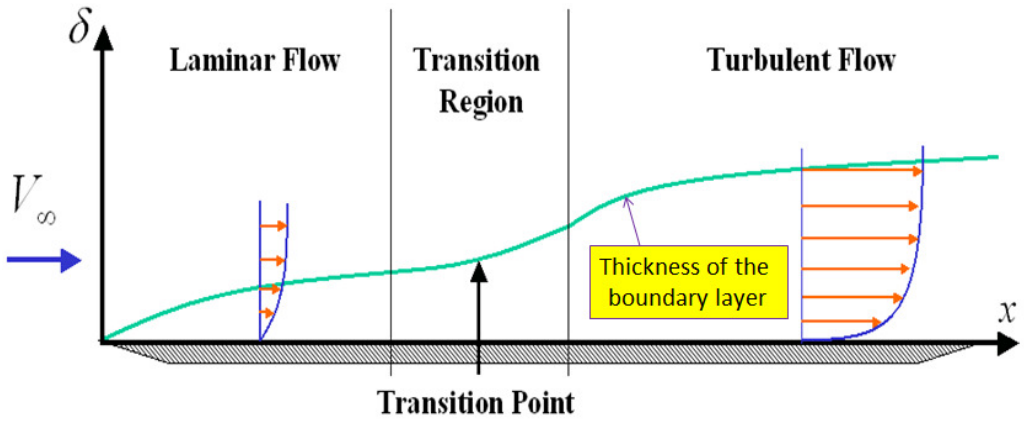

Figure 6.25: The laminar flow and turbulent flow over a flat plate.

In Figure 6.25, the thickness of the boundary layer δ is defined as the distance from the surface to the point where velocity $V = 0.99 \cdot V_\infty$. Due to theoretically complexity, the determination of δ is discussed only for some flows with simple geometries. The theoretical thickness formulas of the boundary layer over a flat plate [52, 72] are listed in Table 6.8.

Boundary layer thickness	Incompressible laminar flow	Compressible laminar flow	Incompressible turbulent flow	Hypersonic flow
$\delta =$	$\frac{5.0 \cdot x}{\mathrm{Re}_x^{0.5}}$	$\frac{5.0 \cdot x}{\mathrm{Re}_x^{0.5}} \cdot G\left(M_e, \mathrm{Pr}, \frac{T_w}{T_e}\right)$	$\frac{0.37 \cdot x}{\mathrm{Re}_x^{0.2}}$	$C \cdot \frac{\mathrm{M}_\infty^2 \cdot x}{\mathrm{Re}_x^{0.5}}$

Table 6.8: Formula describing the thickness of the boundary layer above a flat plate.

Following the Prandtl's boundary layer theory, Blasius derived the first boundary layer thickness about incompressible laminar flow in his dissertation. The formulas in Table 6.8 present the factors, which mainly affect the development of the boundary layer. Including the Reynolds number, the boundary layer of compressible flow is further related with the Mach number M_e on the outer edge of the velocity boundary layer, with Prandtl number Pr, and with the fraction of temperatures between the wall and the outer edge of thermal boundary $\frac{T_w}{T_e}$. Comparing with incompressible flow, the temperature of gas rises more slowly in a compressible flow. This phenomenon results in the decrease of density and increase of viscosity in the boundary layer. With the increase of friction effect and expansion of fluid in the neighbor region of wall, δ is thicker than that in a similar incompressible flow. Its thickness is proportional to the square of Mach number in hypersonic flow.

The separation process is simulated in turbulent flow by using the Baldwin and Lomax model, which is a two-layer, algebraic, and 0-equation model described in Chapter 2.3 and in Appendix H. It

is assumed that $M_\infty = 4.05$, $\mathrm{Re}_m = 50.0\times10^6$ 1/m, $\Delta\alpha = 0^\circ$, and **h/L** = 0.2562. A much refined grid with 1.8 million mesh points is used to show the effect of the boundary layer.

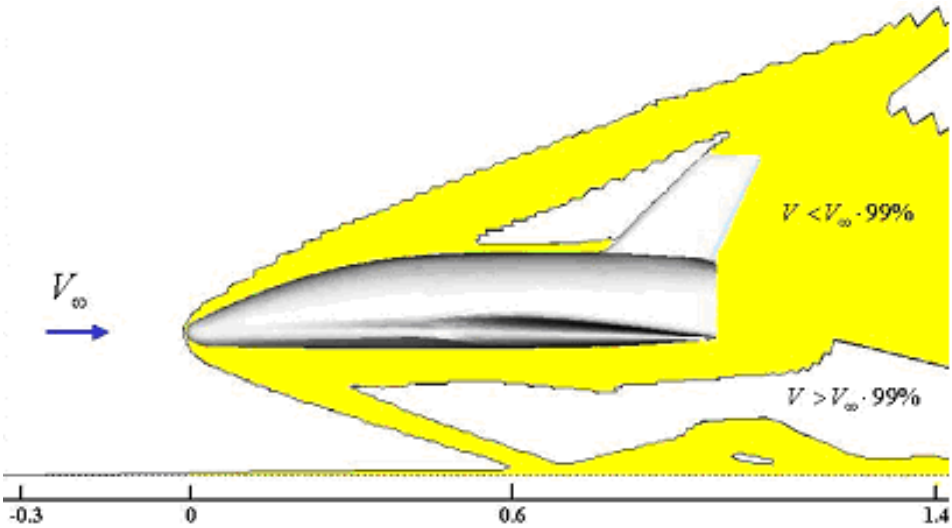

Figure 6.26: Velocity distribution on the symmetry plane with a much refined grid at $M_\infty = 4.05$, $\mathrm{Re}_m = 50.0\times10^6$, $\Delta\alpha = 0^\circ$, and **h/L** = 0.2562.

In Figure 6.26, the region painted with yellow color has a velocity, which is smaller than 99% of the non-disturbed velocity V_∞. Comparing the whole flow region, the boundary layer in the neighborhood of the flat plate is very thin before the bow shock reaches the flat plate. In the further downstream region, the boundary layer in the neighborhood of the flat plate is affected very much by the shock waves. The yellow region around the EOS body does not mainly result from the boundary layer, but from the effect of the bow shock and from the effect of the wake. The velocity becomes smaller after it crosses the bow shock and also in the wake region. The numerical thickness of the boundary layer, which is located above the flat plate and just before the impingement point from the bow shock, could be roughly approximated by the simple thickness formula for the incompressible turbulent flow.

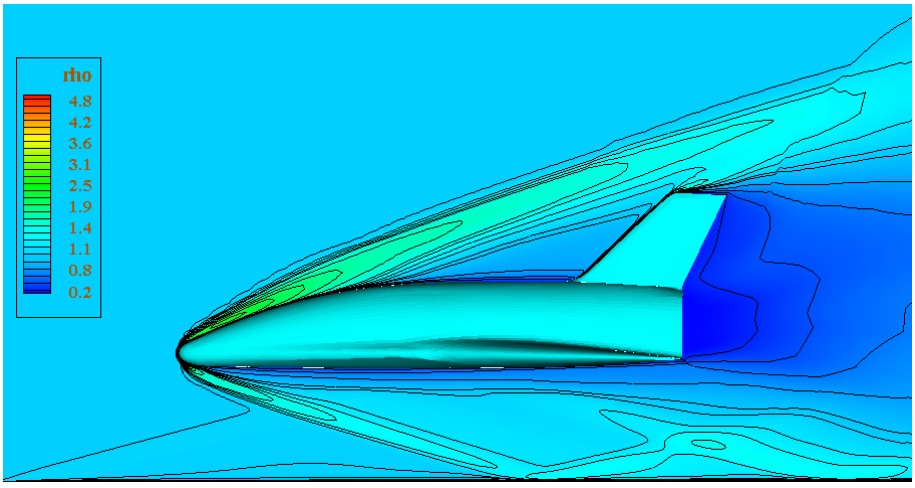

Figure 6.27: Contour of relative density ρ/ρ_∞ at $M_\infty = 4.05$, $\mathrm{Re}_m = 50.0\times10^6$, $\Delta\alpha = 0^\circ$, and **h/L** = 0.2562 in turbulent flow.

The contour of relative density ρ/ρ_∞ is presented for the turbulence flow field in Figure 6.27. Except demonstrating a thicker boundary layer above the flat plate than in laminar flow, it also presents some traces of a weak compression, which starts from the beginning of the flat plate. The weak compression is located in a relative wide upstream region before the bow shock and below the EOS. It belongs to a kind of very weak oblique shock, which is generated by the slope of the boundary layer above the flat plate. Because this slope of boundary layer is composed of gas instead of solid material, the generated oblique shock is quantitatively much weaker. The relative density ρ/ρ_∞ in this weak compression is around 1.03.

	C_D	C_L	C_M
Laminar flow with refined grid	0.0294	-0.0113	-0.0109
Experiment	0.0299	-0.0120	-0.0059
Turbulent Flow with much refined grid	0.0308	-0.0106	-0.0101

Table 6.9: Comparison of aerodynamic coefficients for the EOS with $M_\infty = 4.05$, $\mathrm{Re_m} = 50.0\times10^6$, **h/L** = 0.2562, $\Delta\alpha = 0^\circ$, and rotation center (0.65, 0, 0).

The aerodynamic coefficients are listed in Table 6.9. Comparing to NS simulation drags increases about 5%. The lift in the turbulent flow becomes greater than that in other flows. The pitching moment coefficient in turbulent flow is closer to the one in laminar flow.

7 Numerical Results Corresponding to the Experiments of RWTH

To further study the aerodynamic properties in the separation process and to validate the numerical software, some experimental and numerical simulations have been also performed in a hypersonic flow at $M_\infty = 7.9$. This Mach number is chosen due to the available flow conditions in the shock tunnel TH2-D for the separation process.

In the numerical investigations, the hypersonic flow is considered as a laminar flow. The inviscid flow is also researched as means of simplification and comparison. As the same environment as in the experiment of RWTH shown in Chapter 5.2, the following parameters are used: freestream temperature $T_\infty = 180$ K, rotation center at (0.5, 0, 0), angle of attack of $\Delta\alpha = 0^\circ$, and unit Reynolds number $\mathrm{Re_m} = 7.6\times10^6$ 1/m for the laminar flow. The idealized carrier stage and orbital stage are still defined as shown in Figure 2.1. It is again assumed that the calorically perfect gas model is valid with Prandtl number Pr = 0.72. Adiabatic boundary conditions are adopted around the solid surfaces of the EOS and the flat plate.

Corresponding to the experiments, three different cases are studied corresponding to different separation distances with **h/L** = 0.1812, 0.0812, and 0.0662. The standard grid with 645807 nodes is still used. The numerical and experimental results are compared on the three lines as defined in Figure 5.17. Often used for comparisons hereinafter, the lengths of local wingspan $\mathbf{L}_{\mathrm{Local}}$ are listed here corresponding to the *x*-coordinates. When $x = 0.6$ **L**, the measured local span $\mathbf{L}_{\mathrm{Local}}$ =0.15812 **L**. For $x = 0.75$ **L**, correspondingly $\mathbf{L}_{\mathrm{Local}}$ =0.228065 **L**.

7.1 Comparison between $M_\infty = 4.05$ and $M_\infty = 7.9$

In Chapter 6, the supersonic separation process with Mach number of 4.05 has been investigated in detail. In this section, the hypersonic flow fields at $M_\infty = 7.9$ are simulated and further compared with the results in the last chapter. To obtain the freestream flow at higher Mach number in the experiment, much complicated equipment is needed as described in Chapter 5.2.

Due to stronger viscous interaction as described in Appendix J, it is clear in Figure 7.1 that the boundary layer of the flat plate is quite thick. There is an extra weak compression layer above the boundary layer. It is a weak oblique shock wave generated by the boundary layer slope above the flat plate. It originates from the beginning of the flat plate, passes through the shrink part between the EOS and the flat plate, and intersects with the bow shock. After impinging on the bow shock, it further affects the aerodynamic properties on the low side of EOS. This weak shock is much thicker than the boundary layer.

This compression layer has not clearly appeared in the laminar flow field with the smaller Mach number 4.05, but already appears in the turbulence model as shown in Figure 6.27. There are two strong interaction zones between shocks and boundary layer of the flat plate. The interaction between boundary layers and bow shocks may affect whole flow field. These phenomena result in very

difficult convergences in numerical iteration.

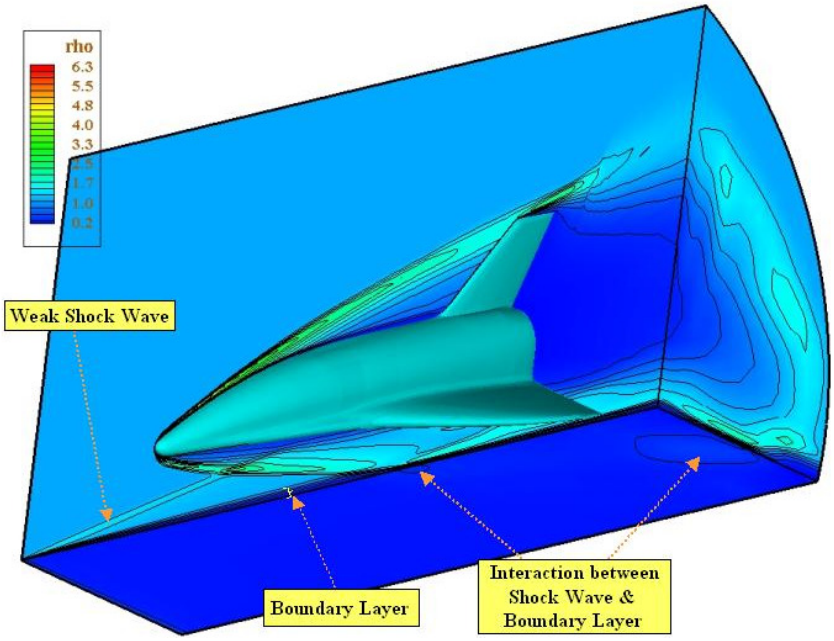

Figure 7.1: Contours of relative density for $M_\infty = 7.9$ and **h/L** = 0.1812 in laminar flow.

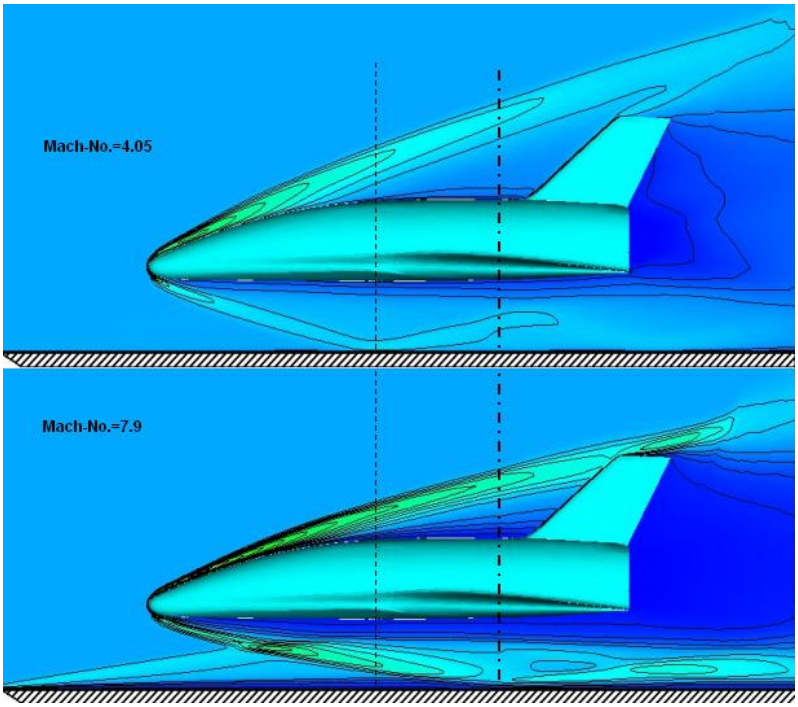

Figure 7.2: Comparison of shock waves between different Mach numbers at **h/L** = 0.1812 on the symmetry plane in laminar flow.

As a comparison of numerical simulations, Figure 7.2 shows that the bow shock with Mach 7.9 is stronger than that with Mach 4.05, the latter we have discussed in Chapter 6 in detail. Their maximal values about the compression of the density ρ / ρ_∞ are 6.5 and 5.1, respectively. Consequently, the contour lines of the relative density are denser for the case of high Mach number. The shock angle

between freestream direction and the shock wave with Mach 7.9 is smaller than the angle with Mach 4.05. The shock impingement point on the flat plate with Mach 7.9 moves further rearwards than that with Mach 4.05. The positions of the impingement points are labeled with two vertical lines in Figure 7.2. In the case with Mach 4.05, the shock reflected by the flat plate hits the rear part of the EOS. But in the case with Mach 7.9, the reflected shock impacts the wake region apart away from the tail of the EOS. Developing above the EOS body, the bow shock with Mach 7.9 hits the vertical stabilizer of the EOS. A strongly compressed zone appears in this region. In the case with Mach 4.05, the bow shock is still far away from this vertical stabilizer. It is also very obvious that the boundary layer in the flow with Mach 7.9 is much thicker than that with Mach 4.05, especially the boundary layer above the flat plate.

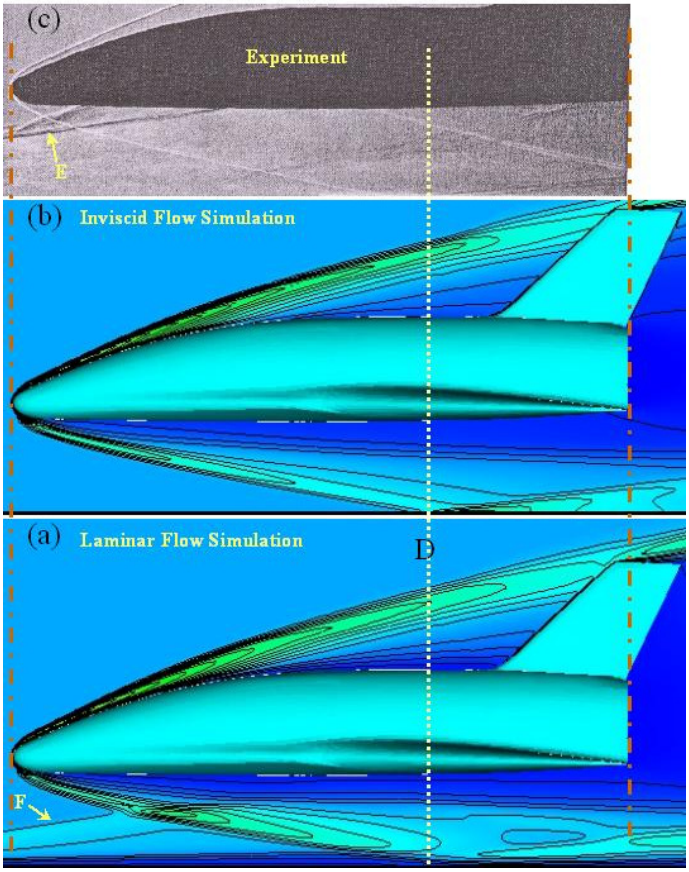

Figure 7.3: Comparison between Schlieren picture and calculated relative density ρ / ρ_∞ on the symmetry plane with $M_\infty = 7.9$, $\Delta\alpha = 0^\circ$, and **h/L** = 0.1812.

7.2 Pressure Distribution for h/L = 0.1812

Corresponding to the experiment with Mach 7.9 and h/L = 0.1812 as arranged in Chapter 5.2, a Schlieren picture for steady case is shown in Figure 7.3 (c). It describes the density gradient for the EOS flow field. In the same picture, Figure 7.3 (a) and (b) are the numerical results computing in laminar flow or inviscid flow respectively. They illustrate the contours of relative density ρ / ρ_∞ on the symmetry plane. Referring to the line "**D**", all of them show nearly same positions of

impingement points on the flat plate. Due to no boundary layer, the shock impingement point could be found easily on the flat plate in inviscid flow. For the Schlieren picture and numerical result in laminar flow, the impingement points could not been distinguished very clearly. Due to the interaction between bow shock and the boundary layer on the flat plate, the bow shock impingement points separate with the reflection points somewhat in pictures (a) and (c). The influence of the boundary layer and the compression between the EOS and flat plate perturb the bow shocks. The weak shock waves generated from the beginning of the flat plate are labeled as "**E**" in Figure 7.3 (c) and "**F**" in Schlieren picture 7.3 (a). Their intersections with the bow shock could be clearly seen in the region under the EOS. These weak shock waves could be clearly depicted with pressure magnitude subsequently. For the flow field with this great Mach number, the given length of the flat plate could affect the aerodynamic field of the EOS.

In Figure 7.3 (a), the shock from the wing in laminar flow shows only some weak traces in the rear part on the symmetry plane. In inviscid flow, there is nearly no trace in Figure 7.3 (b). The reason is that the shock from the wing is generated a little away from the symmetry plane. It could not show much relevant information in Figure 7.3 (a) and (b). On the other hand, since the Schlieren picture overlaps all traces from a 3D picture, the shock from the wing could also been clearly observed in Figure 7.3 (c), though it is not located on the symmetry plane.

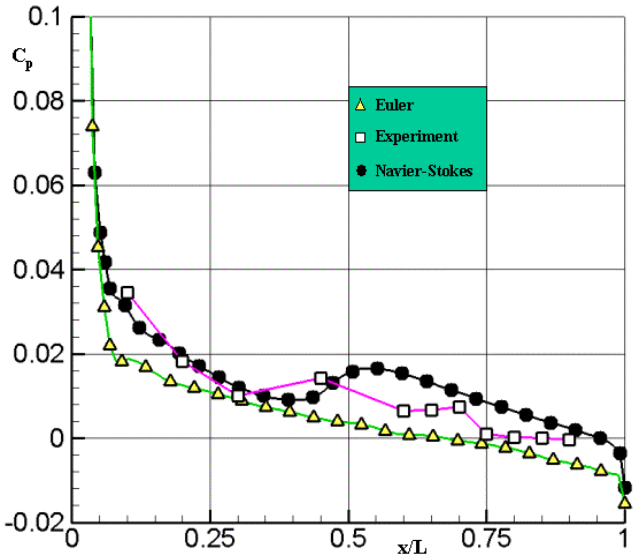

Figure 7.4: Comparison of measured and calculated pressure coefficients on the lower surface of the EOS with y = 0 at $M_\infty = 7.9$, $\Delta\alpha = 0^\circ$, and **h/L** = 0.1812.

A detailed comparison about the pressure coefficients is presented in Figure 7.4. These coefficients Cp are selected on the line with y = 0 as shown in Figure 5.17. It refers to a line on the lower surface of the EOS from the bow to the tail part. On the place close to the nose of EOS, which is corresponding to the region with x/**L** around zero, these coefficients Cp are much greater than that on the other points. This phenomenon is presented in all numerical and experimental simulations. These big pressures come from the compression of bow shock. With the increase of x/**L**, the influence of the bow shock becomes weak and the Cp becomes smaller. Comparing to the experimental results,

the NS simulation shows a better consistence with the experimental data. It even describes a small increase of pressure at x/**L**=0.55. Correspondingly, there is a similar area of increased Cp in experiment. This region of pressure increase mainly results from the weak shock wave stating from the beginning of the flat plate. There is no local pressure increase in inviscid flow, because of its lack of boundary layer. The Euler simulation is nearly the same as the NS simulation for the bow shock region. For the downstream, the inviscid solution underestimates the pressure comparing to both NS simulation and the experimental counterpart. Since there is an expansion region with low-pressure behind the EOS tail, both numerical solutions show negative pressure coefficients when a point is near the tail of the EOS.

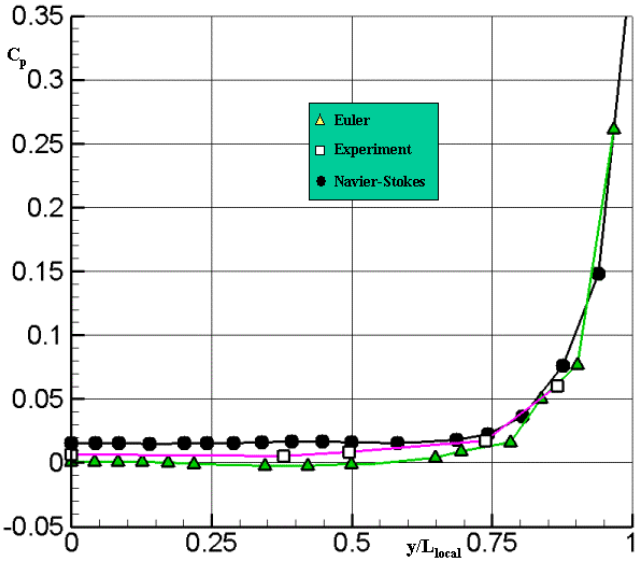

Figure 7.5: Comparison of measured and calculated pressure coefficients on the lower surface of EOS with x = 0.6**L** at $M_\infty = 7.9$, $\Delta\alpha = 0^\circ$, and **h/L** = 0.1812.

On the line with x = 0.6**L** as shown in Figure 5.17, all of the numerical and experimental results on the pressure distribution show good consistency in Figure 7.5. That line is positioned also on the lower surface of the EOS and cut the wing perpendicularly to the free steam direction. Considering the points on the wing, the pressure coefficient is affected by a shock generated from the wing leading edge. The closer the point to the leading edge of the wing is (i.e. y/$\mathbf{L}_{local} \rightarrow 1$), the bigger its pressure coefficient becomes. The magnitude of the measured pressure in most of the points is smaller than that of the numerical pressure in laminar flow, but bigger than that of the numerical pressure in inviscid flow.

In Figure 7.6 referring to the line as shown in Figure 5.17 with x = 0.75 **L**, which is also a line located on the lower surface of the EOS, three different simulations about pressure are presented. The pressure coefficient decreases a little bit, when the point is near the symmetry plane (i.e. y/$\mathbf{L}_{local} \rightarrow 0$. After the shock from the wing becomes more dominant, the pressure coefficients start to increase. Similarly as on the line with x = 0.6**L**, most of the pressure coefficients of the NS simulation are bigger than the experimental pressure coefficients on this line, except on some points which are very near the wing leading edge. Again the Euler simulations underestimate the pressure when comparing with the NS simulations as well as with experimental results.

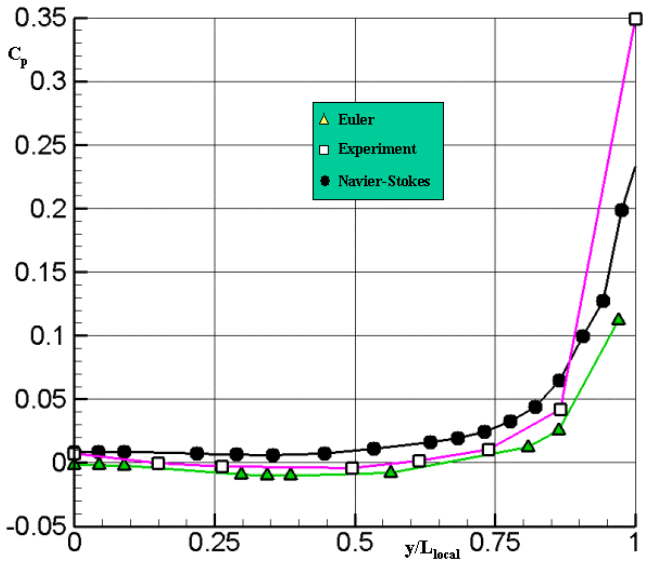

Figure 7.6: Comparison of measured and calculated pressure coefficients on the lower surface of the EOS with x=0.75**L** at $M_\infty = 7.9$, $\Delta\alpha = 0^\circ$, and **h/L** = 0.1812.

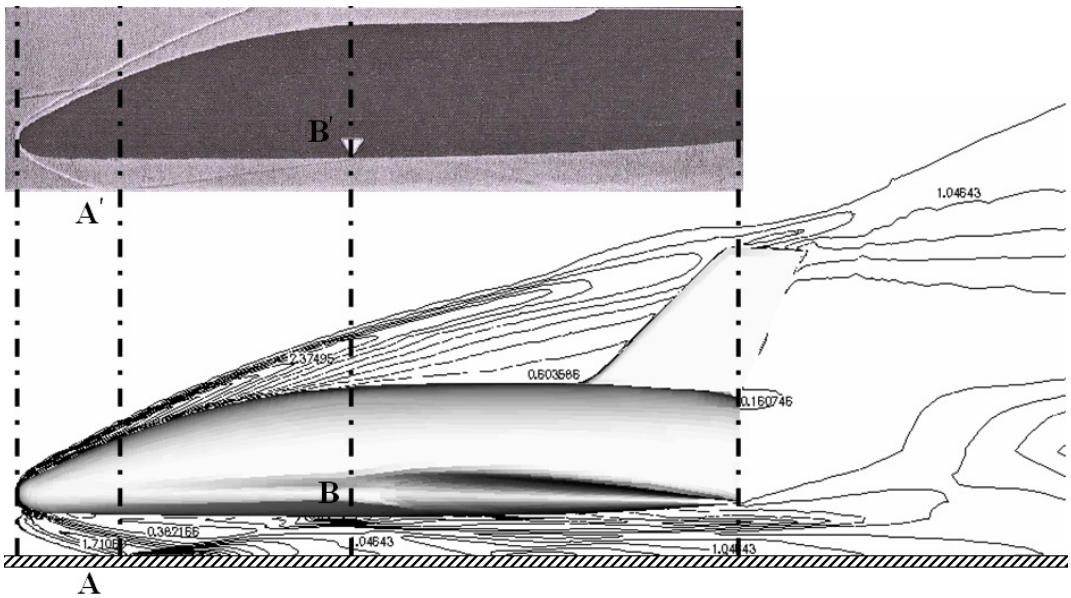

Figure 7.7: Comparison between Schlieren picture and calculated relative density ρ/ρ_∞ in inviscid flow on the symmetry plane with $M_\infty = 7.9$, $\Delta\alpha = 0^\circ$, and **h/L** = 0.0812.

7.3 Pressure Distribution for h/L = 0.0812

Considering the flow with the same flow environment as in last section, the orbital stage EOS is located closer to the flat plate with a smaller separation distance of **h/L** = 0.0812. The aerodynamic properties change more dramatically in this situation. The impingement points on the flat plate and on the lower surface of the EOS are shown in Figure 7.7. A good consistence can be detected by comparing the positions of the points **A**, **B** with **A**', **B**'. The EOS bow shock reflected at the flat plate hits the lower surface of the EOS at **B** or **B**' respectively, and another reflected shock from the flat plate hits the tail flow region only a little downstream.

The Euler and the NS simulations can be further compared with the experiment about their pressure coefficients. On the line with y = 0, which is the symmetry line along the under surface of the EOS shown in Figure 5.17, the pressure is again dominantly influenced by the bow shock. In Figure 7.8, the pressures coefficients show very great magnitude corresponding to very small x/**L**. After the bow shock wave propagates away from the EOS, the pressure coefficients become smaller. The bow shock hits the flat plate and is reflected back to the lower side of the EOS again. Correspondingly, the pressure coefficients in the impingement region become great. Further downstream, the reflected shock wave is detached from the EOS in another time, and the pressure coefficients become smaller again. Comparing to other two solutions, the Euler simulation presents a good consistency relative to the impingement points, but it underestimates the pressure again in most of the points, except in the region near the impingement point with x/**L** ≈ 0.43. Simulating the same case but in laminar flow, the pressure distribution demonstrates similar tendency. The pressure coefficients obtained in laminar flow are always greater than that in inviscid flow. The experimental results are nearly located on the middle position of the two numerical simulations.

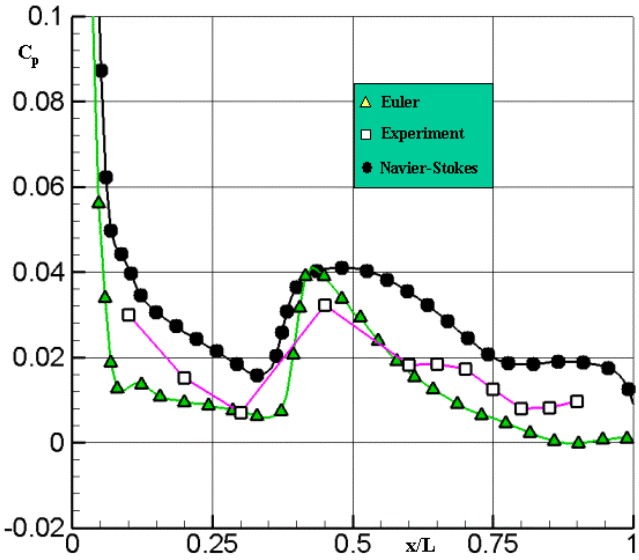

Figure 7.8: Comparison of measured and calculated pressure coefficients on the lower surface of the EOS with y = 0 at $M_\infty = 7.9$, $\Delta\alpha = 0^\circ$, and **h/L** = 0.0812.

Along the line of the EOS lower surface shown in Figure 5.17 with x = 0.6**L**, pressures coefficients are presented in Figure 7.9. The bow shock reflected by the flat plate impinges again on the lower surface of the EOS. This impingement point is afore the point with y = 0 and x = 0.6**L**. In the upstream of the line x = 0.6**L**, the shock is already reflected away by the lower surface of EOS. The pressure coefficients retains small. The pressure coefficients acquired numerically in inviscid flow are nearly equal the experimental ones. NS simulations are always a little bit bigger than others in this case. When $y/\mathbf{L}_{local}$ increases, the corresponding point approximates to the region, which is hit by the reflected bow shock. The pressure increases a little. In the region near the leading edge of the wing, the shock from the wing gives more influence and the pressure rises very much when $y/\mathbf{L}_{local} \rightarrow 1$.

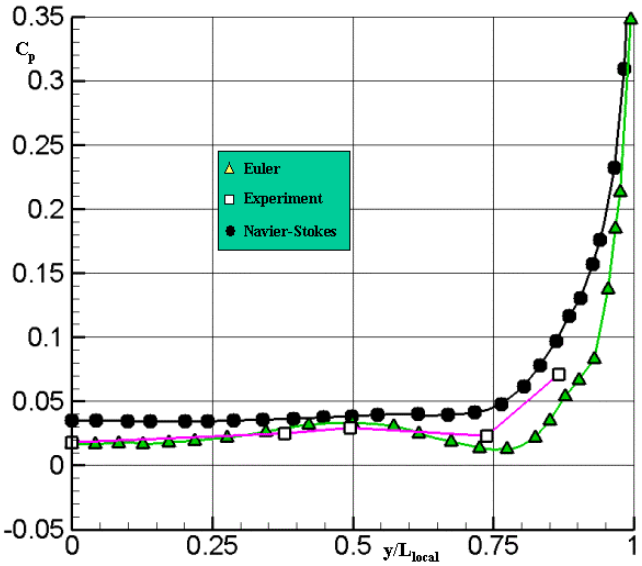

Figure 7.9: Comparison of measured and calculated pressure coefficients on the lower surface of the EOS with x = 0.6**L** at $M_\infty = 7.9$, $\Delta\alpha = 0^\circ$, and **h/L** = 0.0812.

Figure 7.10 presents a comparison of numerical and experimental pressure coefficients on the line shown in Figure 5.17 with x = 0.75**L**. The main characteristics about the pressure are like the case with x = 0.60**L** that has just been discussed above. The same tendency keeps well for the numerical and the experimental pressure coefficients. The biggest difference happens on the wing tip. The experimental pressure is the biggest. The NS simulation ranks the second. The Euler simulation is smaller than the others.

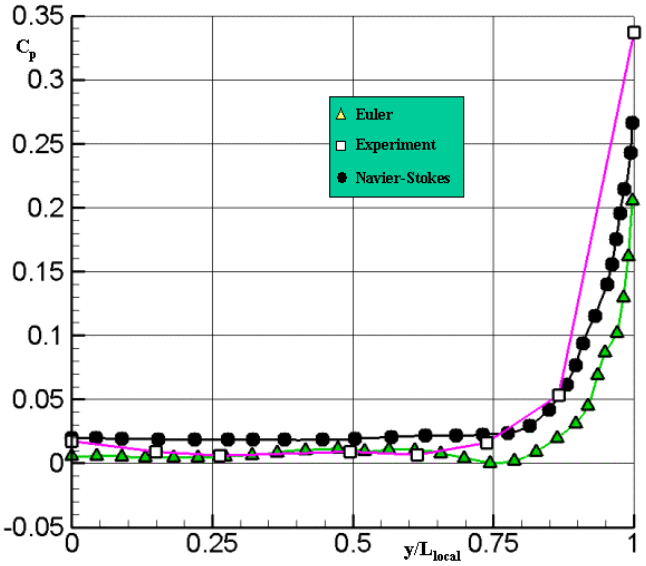

Figure 7.10: Comparison of measured and calculated pressure coefficients on the lower surface of the EOS with x = 0.75**L** at $M_\infty = 7.9$, $\Delta\alpha = 0^\circ$, and **h/L** = 0.0812.

7.4 Pressure Distribution for h/L = 0.0662

When the separation distance **h/L** tends to very small, the flow field between these two stages becomes more complicated. For the case with **h/L** = 0.0662, the shock and the boundary layer are

confined in a very small space, in which they interfere with each other. The bow shock is reflected many times between the two stages. The lines labeled from **A** to **E** in Figure 7.11 mark some important shock characteristics in the two pictures. The bow shock is generated from the position label with the **A** line and impinges on the flat plate at the **B** line. The interval **BC** near the flat plate is an interference region between shock and boundary layer. The **D** line labels the impingement point from the reflected bow shock. The **E** line shows the impacting point from the shock of the wing on the flat plate. After the shock is reflected by the EOS lower surface at the position labeled as **D**, its further development already becomes blurred in the experiment. The shock from the wing is still strong and exhibits a clear trace in impinging the flat plate in the Schlieren picture. However, there is not such a pronounced trace on the symmetry plane shown by the numerical results in laminar flow.

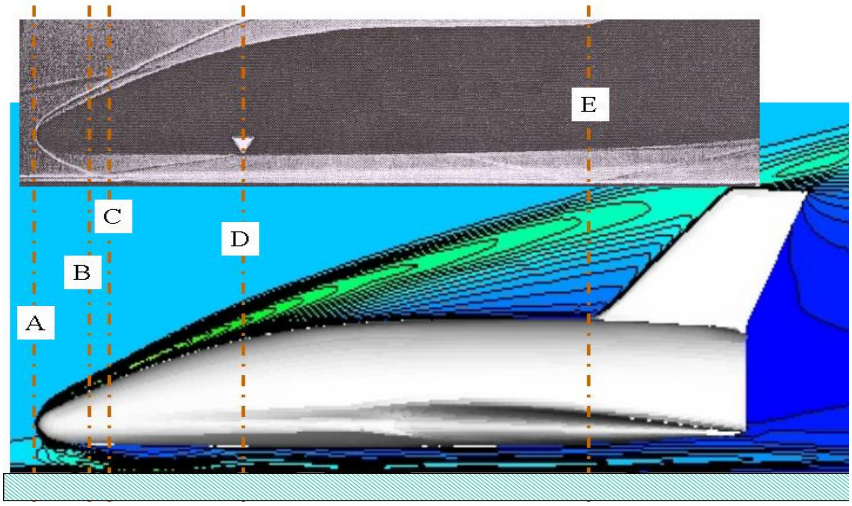

Figure 7.11: Comparison between Schlieren picture and calculated relative density ρ/ρ_∞ on the symmetry plane, where $M_\infty = 7.9$, $\mathrm{Re_m} = 7.6\times10^6$, $\Delta\alpha = 0^\circ$, and **h/L** = 0.0662.

The shock structure is quantitatively analyzed further by some measured and calculated pressure data. In Figure 7.12, the pressures vary dramatically because of the influence from the shocks. On the line shown in Figure 5.17 with y = 0, the pressure coefficient is around 1.0 due to the bow shock when x/**L** is close to the bow of the EOS. When x/**L** increases, the shock is spread away from the EOS and the pressure coefficient decreases to the interval from 0.012 to 0.025, up to the point x/**L** = 0.2. Thereafter, the first reflected shock develops and hits the EOS. Its impingement point is at x/**L** = 0.29. This is the position labeled as the line **D** in Figure 7.11. All numerical and experimental pressure coefficients exhibit a "jump" at this point, especially the Euler simulations. The numerical pressure coefficients reach the levels from 0.06 to 0.065. As a comparison, the experimental pressure coefficient is about 0.04. Downstream from this point, all pressure coefficients decrease very rapidly, due to the shock deflected from the EOS. The second shock reflected by the flat plate affects the pressure on the lower surface of the EOS differently. Both numerical simulations predict the second pressure peaks more upstream than that measured in the experimental results. The strength of the second reflected shock is weaker than the first one, because much of the shock energy has been lost.

The numerical pressure coefficients Cp range from 0.028 to 0.04. After two times hitting on the lower side of EOS, the shock is already very weak and all pressure coefficients decrease to levels less than 0.012. Along the symmetry line, experimental results are again roughly the average value of Euler and NS simulations on most points. However, this picture presents the biggest lift differences among the different simulations in this thesis.

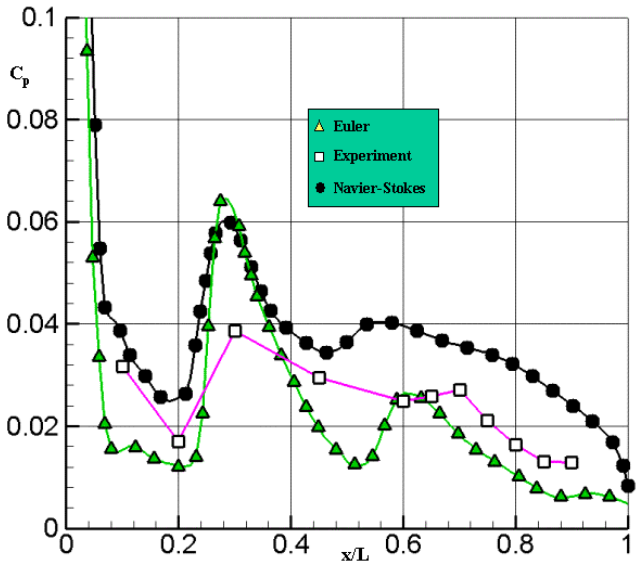

Figure 7.12: Comparison of measured and calculated pressure coefficients on the lower surface of the EOS with y = 0 at $M_\infty = 7.9$, $\Delta\alpha = 0^\circ$, and **h/L** = 0.0662.

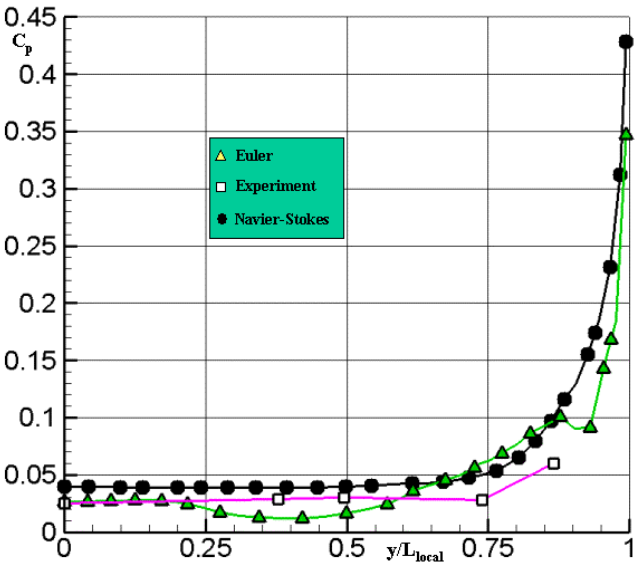

Figure 7.13: Comparison of measured and calculated pressure coefficients on the lower surface of the EOS with x = 0.6 **L** at $M_\infty = 7.9$, $\Delta\alpha = 0^\circ$, and **h/L** = 0.0662.

Consider the pressure distribution on the line as shown in Figure 5.17 with x = 0.6 **L**. In this case the line is located in the region between two reflected impinging waves. When $y/\mathbf{L}_{local}$ is small, as depicted in Figure 7.13, the pressure coefficients are smaller than 0.04. When $y/\mathbf{L}_{local}$ increases, the pressure changes only a little, until the points are near the region of the wing leading edge. After

$y/\mathbf{L}_{local}$ is greater than 0.75, the pressure coefficients are mainly affected by the shock from the wing. The greater the distance from the symmetry plane $y/\mathbf{L}_{local}$ is, the greater the pressure coefficient is. The maximum of Cp in the NS simulation reaches 0.43. The corresponding Cp in Euler simulation is 0.35. Near the leading edge of the wing, the Euler simulation fluctuates to a certain extent.

On another line with x = 0.75**L**, the situation is similar as on the line with x = 0.60**L**, except in the region near the wing leading edge. As shown in Figure 7.14, the greatest pressure coefficient Cp from the NS simulation is 0.28, which is closer to the experimental result 0.39 compared to Cp=0.19 from the Euler simulation. For the other points, a satisfying agreement is shown among these three simulations.

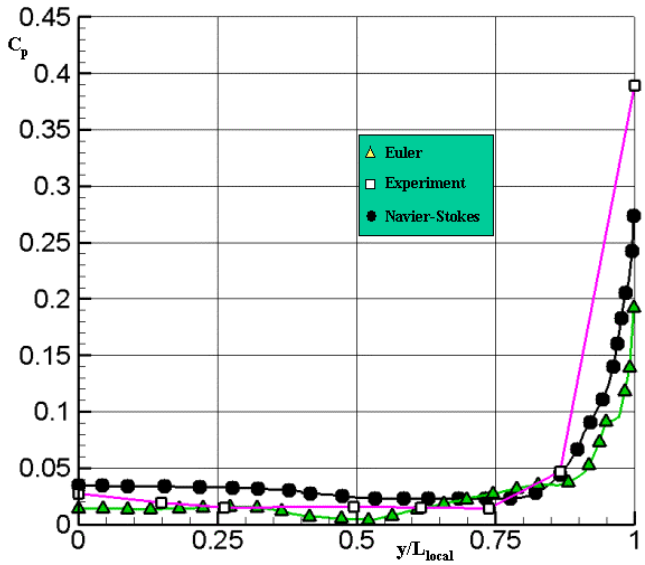

Figure 7.14: Comparison of measured and calculated pressure coefficients on the lower surface of the EOS with x = 0.75 **L** at $M_\infty = 7.9$, $\Delta\alpha = 0^\circ$, and **h/L** = 0.0662.

7.5 Aerodynamic Coefficient Comparisons

Compare three cases with **h/L** = 0.1812, 0.0812, and 0.0662. The numerical pressure coefficients obtained in NS simulation are greater than the corresponding experimental values. The corresponding coefficients in Euler simulation usually are the smallest. The pressure distribution of NS simulations is smoother than its counterpart of the Euler simulations. Their aerodynamic properties show good tendencies. However, the pressures are compared only on some points of the lower surface of the EOS in the last sections.

Except those pressure coefficients, the coefficients of lift, drag, and pitching moment at the same environment as discussed in sections 7.2, 7.3, and 7.4 are calculated and listed in Table 7.1. The rotation center is defined as (0.5, 0, 0). In this table the drag decreases with the increase of the distance **h/L** in laminar flow. Comparatively, this phenomenon does not appear in inviscid flow. With Mach number of 7.9, the lift is positive for a very small distance **h/L**. But with the increment of the distance, both NS and Euler simulations present a decrement of the lift. The lift in laminar flow is greater than that in inviscid flow. The pitching moment shows an increasing tendency accompanied

by the increase of the distance **h/L**. Nevertheless, all of them are negative.

	C_D	C_L	C_M
Navier-Stokes, **h/L** = 0.0662	0.0265	0.00934	-0.0111
Navier-Stokes, **h/L** = 0.0812	0.0260	0.00242	-0.00935
Navier-Stokes, **h/L** = 0.1812	0.0235	-0.00925	-0.00748
Euler, **h/L** = 0.0662	0.0220	0.00329	-0.01048
Euler, **h/L** = 0.0812	0.0216	-0.00701	-0.00791
Euler, **h/L** = 0.1812	0.0218	-0.01619	-0.00519

Table 7.1: Calculated aerodynamic coefficients for EOS with $M_\infty = 7.9$, $\Delta\alpha = 0^\circ$, and rotation center (0.5, 0, 0).

Applying the results of Table 7.1 to the separation maneuver with angle of attack of zero, we get that aerodynamic lift may support the stage separation at very small distances. But this effect is reduced with increasing distance. The negative pitching moment coefficients mean that the head of the EOS turns down to the flat plate. The same situation has been also presented in the cases with Mach 4.5. Compared to the case with the same distance **h/L** = 0.1812 and M_∞ = 4.05, the drag coefficients C_D are nearly the same. The lift coefficient C_L at Mach 7.9 becomes a little greater and the pitching moment coefficients C_M are a little bit greater, too.

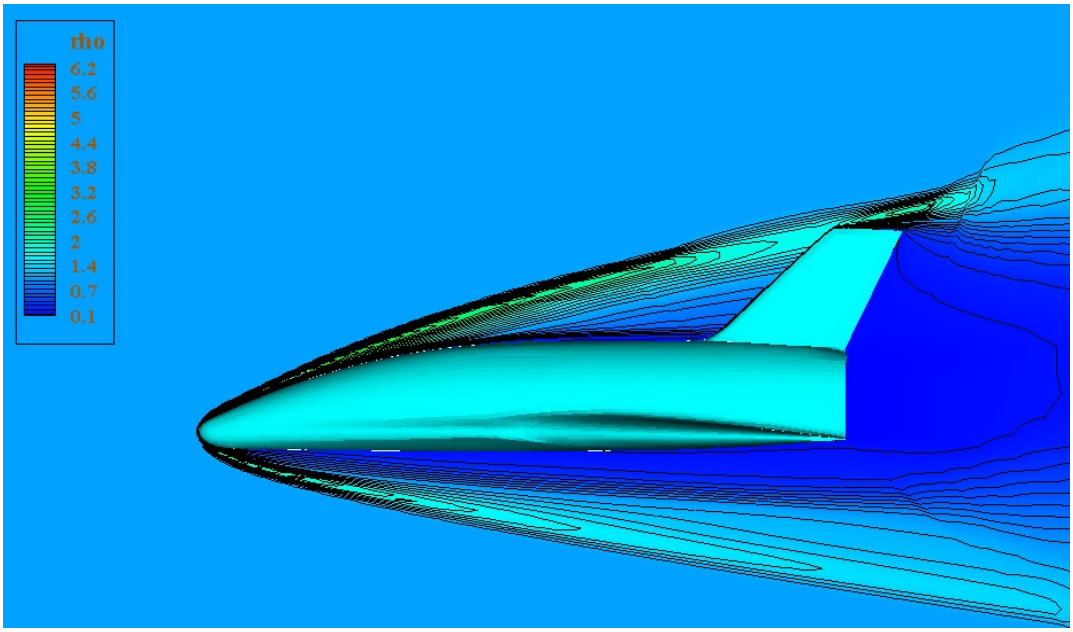

Figure 7.15: The contour of the relative density ρ / ρ_∞ at $M_\infty = 7.9$, $\Delta\alpha = 0^\circ$ in laminar flow.

7.6 Free Orbital Stage at $M_\infty = 7.9$

As the last phase in the end of the separation process, the free orbital stage EOS is studied herein. Figure 7.15 shows a steady flight of the free orbital stage at Mach 7.9 in laminar flow. There is no reflected bow shock any more. It is simulated also in inviscid flow. Both results of the aerodynamic properties in laminar and inviscid flows are gathered in Table 7.2. The biggest difference is 6.8%

about the pitching moment. Recalling the results in Chapter 6.3, the maximal value about relative density ρ / ρ_∞ in the case with $M_\infty = 4.05$ is 4.99. In the case with $M_\infty = 7.9$, the relative density is 6.32. Its lift and pitching movement coefficients are still negative with the angle of attack $\Delta\alpha = 0^\circ$. Further its lift is smaller than that with $M_\infty = 4.05$. The drag coefficient at $M_\infty = 7.9$ is smaller than in the case with $M_\infty = 4.05$, because the pressure in the rear part of the EOS becomes greater with a bigger Mach number. It should be pointed out, that the environments in these two cases are different. The definitions of the rotation center are also different. Though the Mach number plays a decisive role for separation process, the above comparison could be only considered as some reference.

	C_D	C_L	C_M
Navier-Stokes, standard grid	0.02316	-0.01598	-0.00484
Euler, standard grid	0.02177	-0.01600	-0.00517

Table 7.2: Comparisons of measured and calculated force- and moment- coefficients for the EOS with $M_\infty = 7.9$ and rotation center (0.5, 0, 0).

8 Prediction of the Aerodynamic Properties at Mach 6.8

Recalling to the original design, the TSTO should be separated at the altitude of 35 kilometers with Mach 6.8. Obviously, it is of the most importance that the aerodynamic properties in the separation process are analyzed in this designed environment.

Constricted by the experimental equipment, neither has a continuous separation process been measured, nor has an exact designed environment been generated in wind tunnel.

Contrarily, in numerical simulation supported even by a personal computer, the environment for the separation process at the altitude of 35 kilometers with Mach 6.8 could be reproduced. Actually, only environmental parameters in mathematical equations should be simply adjusted, though numerical techniques are greatly challenged in simulating this hypersonic flow.

In the designed environment, the separation process is intensively and numerically simulated in the following sections. Based on the data of US standard atmosphere at the altitude of 35 kilometers above the sea level, the air temperature is –36.1 °C, the air pressure 5600 Pa, and the air density 0.0082 kg/m^3. As same as in numerical simulations in Chapters 6 and 7, the ratio of specific heats is still assumed as constant, namely $\gamma = 1.4$. As designed in project SFB 255, the length of the EOS is taken as 28.8 meters. Two other standard values at sea level are: dynamic viscosity $\mu_0 = 1.7894 \times 10^{-5}$ kg/(m·s) and temperature T_0=288.15 K. At the altitude of 35 kilometers, it can be derived that the dynamic viscosity of the freestream is 1.531×10^{-5} kg/(m·s), the sonic speed in air is 309 m/s, and the unit Reynolds number is $\mathrm{Re_m} = 1.12 \times 10^6$ 1/m. Further the Reynolds number $\mathrm{Re} = 3.24 \times 10^7$. The formulas and calculations of these basic parameters are listed in Appendixes D and K.

Several different scenarios have been designed to analyze the separation process. They are simulated numerically related with different separation distances, as well as different angles of attack. The flow is dealt as an inviscid flow, or a laminar flow, or as well as turbulent flow to show the influences of the different physical models. Except steady cases, a continuous separation in inviscid flow is also simulated.

8.1 Shock Structure Analysis

In the separation process, we have already seen its shock structures at Mach 4.05 in Chapter 6 and at Mach 7.9 in Chapter 7. It has been shown that the shock structures greatly affect the forces acting on the EOS. Subsequently we analyze the shock structures and their developments at Mach 6.8 in the designed separation process.

8.1.1 Structure of EOS Bow Shock

As described in Chapters 6 and 7, the most important shock is generated at the nose of the EOS. To understand the aerodynamic characteristics of this bow shock more clearly, the aerodynamic field

in front of the EOS nose is investigated in detail. An example is shown in Figure 8.1 at $M_\infty = 6.8$ in laminar flow. To avoid much influence from the boundary layer and relevant shock waves generated by the flat plate, it is firstly assumed that the separation distance between EOS and flat plate is a little away from flat plate and namely **h/L** = 0.1812.

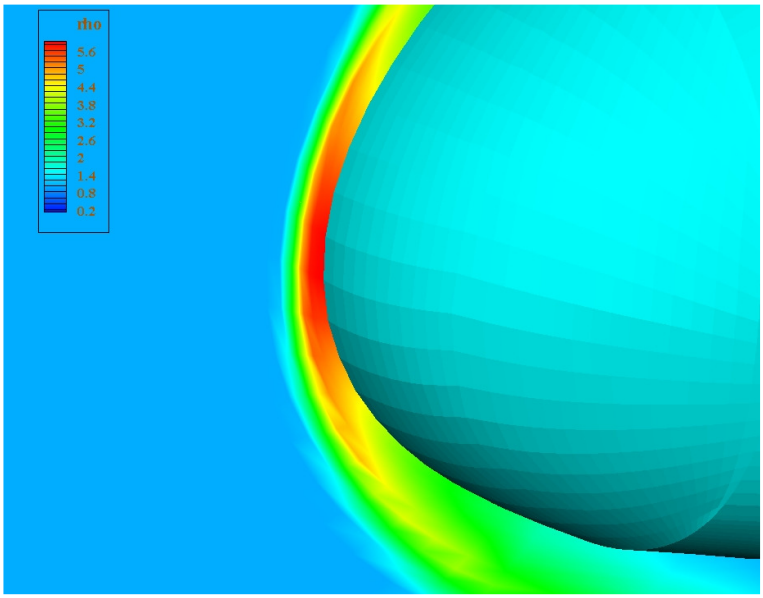

Figure 8.1: Relative density contour ρ/ρ_∞ in front of the nose of the EOS at $M_\infty = 6.8$, $\mathrm{Re_m} = 1.12\times10^6$, $\Delta\alpha = 0°$ in laminar flow.

Describing with relative density ρ/ρ_∞, a very strong gradient of density is presented across the shock layer in front of the EOS nose. The shock layer is compressed very closely to the surface of the EOS nose. The bow shock detaches from the blunt EOS nose and has a curved shape. The detachment distance is estimated about 0.0024L. In the following three pictures, the bow shock is depicted using different contours and different numerical techniques.

In Figure 8.2, the shock structure is illustrated with a contour of the relative pressure p/p_∞. It illustrates the same curved bow shock pattern as in shown Figure 8.1. Through the shock layer, the pressure increases dramatically before the nose of the EOS.

The air compression could be quantitatively expressed by the maximal value of the relative density and the relative pressure. In the above numerical simulation, we have the maximal value in front of the EOS nose as

$$\frac{\rho}{\rho_\infty} = 5.86, \tag{8.1}$$

and

$$\frac{p}{p_\infty} = 59.14. \tag{8.2}$$

These numerical results could be affirmed by the theory of fluid mechanics in some extent. Using the formulas describing the normal shock [5, 96] as well as the parameters listed in the beginning in this chapter, its maximal values could be calculated as:

$$\frac{\rho}{\rho_\infty} = \frac{(\gamma+1)M_\infty^2}{2+(\gamma-1)M_\infty^2} = 5.4, \tag{8.3}$$

and

$$\frac{p}{p_\infty} = 1 + \frac{2\gamma(M_\infty^2 - 1)}{\gamma+1} = 54, \tag{8.4}$$

where ρ and p present the values behind the normal shock and the ratio of specific heats $\gamma = 1.4$.

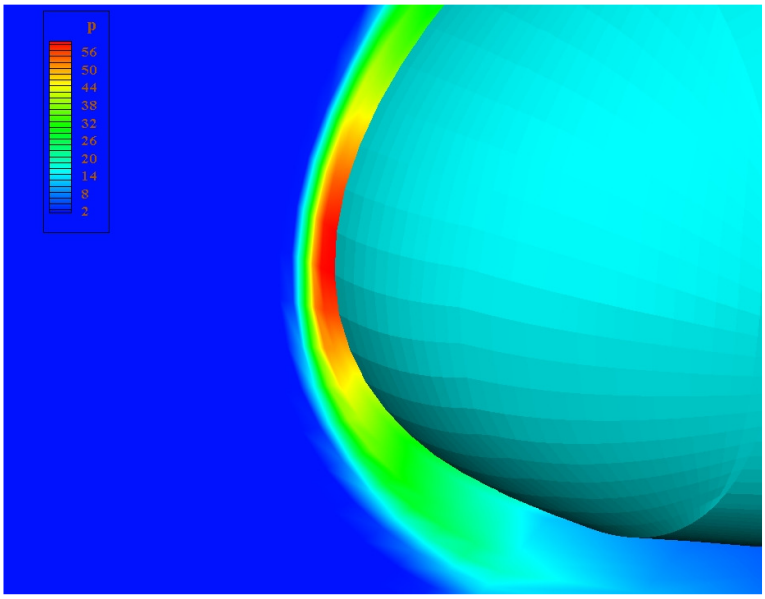

Figure 8.2: Relative pressure contour p/p_∞ in front of the nose of the EOS at $M_\infty = 6.8$, $\mathrm{Re_m} = 1.12\times10^6$, $\Delta\alpha = 0°$ in laminar flow.

The relative differences between numerical and theoretical results about ρ/ρ_∞ and p/p_∞ in Eqs. (8.1) - (8.4) are around 10%. Both ratios of (ρ/ρ_∞):(p/p_∞) are about 1:10 and nearly the same. It should be pointed out, that the normal shock theory estimates the bow shock in front of the EOS nose only approximately due to the blunt nose.

On the other hand, the maximal value about temperature in numerical simulation is overestimated comparing to real situation. In Eq. (2.10) the calorically perfect gas model is used. The ratio of specific heats is always assumed as a constant. This assumption leads to that the temperature increases very quickly in the cases with hypersonic flows. Actually this constant ratio of specific heats is greater than it should be in real case. Another overestimated factor is that the boundary condition around EOS nose is assumed adiabatic in the numerical computation. However, the aerodynamic properties are mainly emphasized in this thesis. The thermodynamic model mainly describes the heat convection and heat conduction effect. To get more accurate temperatures in the regions before the EOS nose as well as the shock standoff distance, a real gas model should replace the calorically perfect gas model [18, 64, 93]. As the temperature is much higher than 800 K, some non-ideal gas models could precisely describe the relationship among temperature, pressure, and density [15]. An example of the real gas model could be referred in Appendix L.

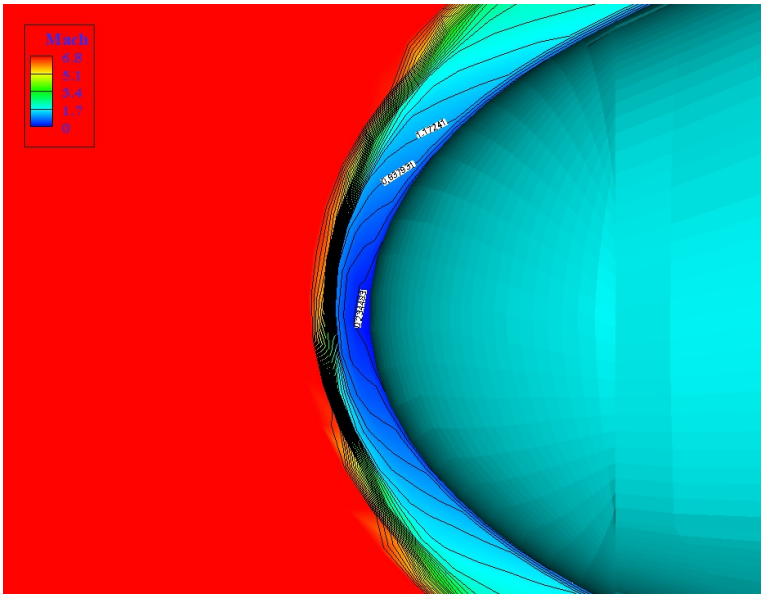

Figure 8.3: Contour of Mach number before the nose of the EOS at $M_\infty = 6.8$, $\mathrm{Re_m} = 1.12\times10^6$, $\Delta\alpha = 0°$ in laminar flow.

As another different presentation in describing the same flow field, contour lines related to Mach number are shown in Figure 8.3. Simulated still in laminar flow, the boundary layer around the EOS nose is shown clearly in this picture. The subsonic zone located on the nose head is also depicted. The Mach numbers decreases very quickly across the shock layer. Thereafter, the air velocities increase along the EOS surface downward, which is a little away from the boundary layer. Rapidly they become supersonic again.

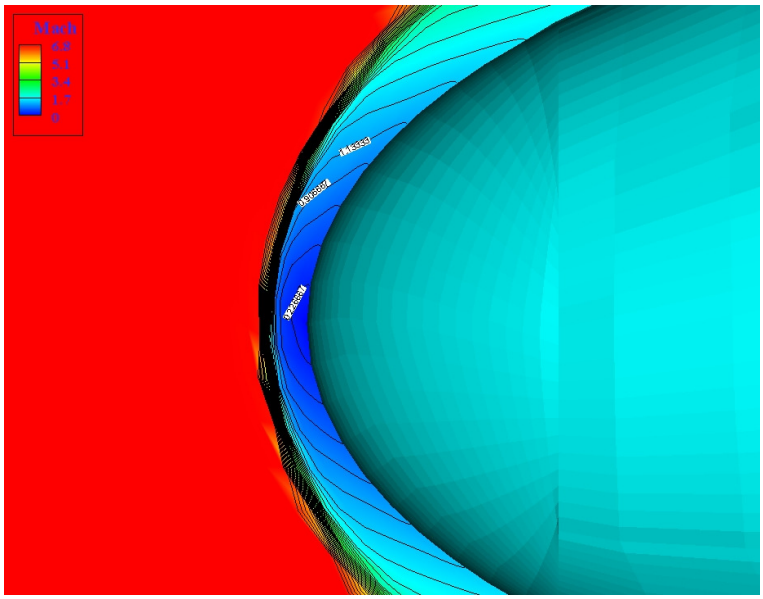

Figure 8.4: Contour of Mach number before the nose of the EOS at $M_\infty = 6.8$, $\Delta\alpha = 0°$ in inviscid flow.

Compare the result in laminar flow with the result in inviscid flow. The fields of Mach number are much different in front of the EOS nose, since different boundary conditions about velocity are

assumed on the EOS surface. In Figure 8.4, the Mach lines do not stretch to the downstream in inviscid flow, but directly connect with the surface of the EOS nose. In the outside of the boundary layer, the aerodynamic properties are nearly the same in both flows. Because of the viscous boundary layer and high Mach number, the field of Mach number in laminar flow changes much dramatically.

8.1.2 Shock Structures Dependent on Distances between the Two Stages

As discussed before, the contour plots of relative density ρ / ρ_∞ in inviscid stream could more clearly illustrate the shock impingement points, on which shock structures impact great force to the two stages. In the following example, the hypersonic flow field is simulated with the separation distance **h/L** = 0.1812 using the inviscid flow model at first.

After the bow shock emanates from the nose of the EOS, it travels downstream. In Figure 8.5, the bow shock expands rearwards somewhat like a curved cone around the body of the EOS with a thin shock layer. A part of the bow shock wave goes upwards and hits the stabilizer. Subsequently, a combination of bow shock and the shock originating at the stabilizer is generated. Similarly, a part of the bow shock strikes the wings. A superposition of the bow shock and the shock at the leading edge of the wing travels continuously to downstream.

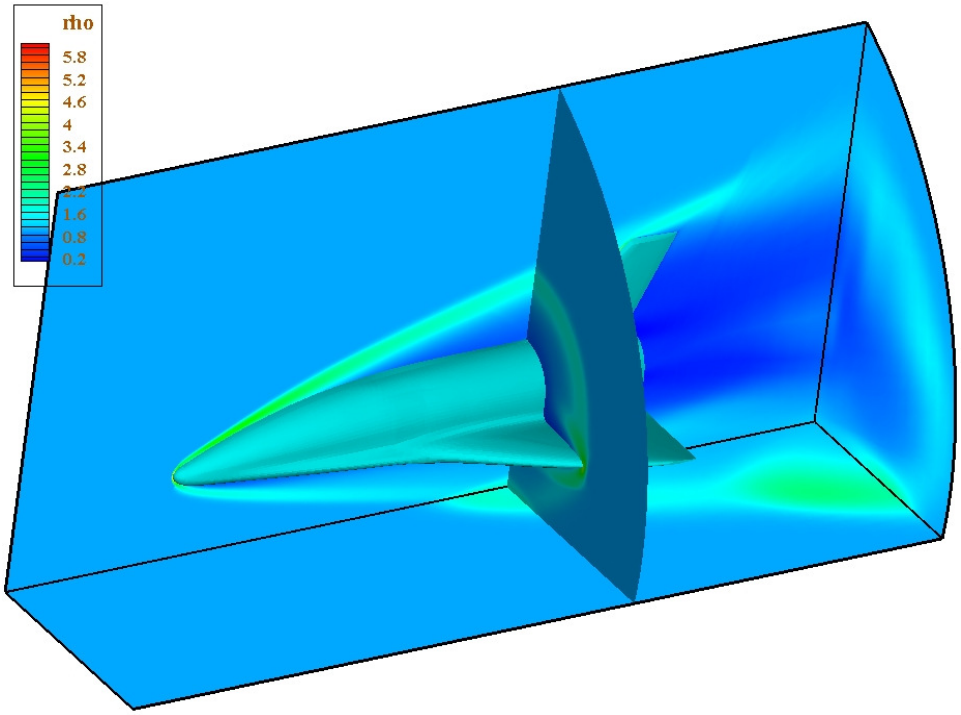

Figure 8.5: Contour of relative density ρ / ρ_∞ at $M_\infty = 6.8$, **h/L** = 0.1812, and $\Delta\alpha = 0°$ in inviscid flow.

The most important part of the bow shock affecting the separation process goes downwards and hits the flat plate. The strongest impact on the flat plate occurs on the point, where the impingement of the bow shock superimposes the impingement of the shock from the wing on the flat plate. The

impingement points are usually located on the rear part of the flat plate. The shocks are reflected by the flat plate further to the rear part of the EOS. Accompanying the compressions, expansions also happen in some domains near the boundary of the EOS body, especially in the wake zone. In Figure 8.5 there is no boundary layer due to the characteristics of inviscid flow.

Because of the importance of the boundary layer, laminar freestream is used in Figure 8.6 to compare the above results. Except the boundary layers, the main shock structures are nearly the same as in Figure 8.5. Due to the streamline shape of the EOS, the boundary layer around the EOS is compressed very close to the surface of the EOS. It is very thin layer in contrast to the length of the EOS. The boundary layer structure could not be distinguished very clearly in Figure 8.6. As a result of the interaction between the bow shock and the boundary layer, the impingement and reflection points on the flat plate are a little separated. Its maximal magnitude of the relative density ρ/ρ_∞ on the flat plate is weaker than that in inviscid flow. The boundary layer above the flat plate and a weak shock wave are formed from the beginning of the flat plate. In this case the beginning position of the flat plate has some effects to the formation of the shock structures. A weak shock wave generated in the beginning of the flat plate could be hardly noticeable with this legend.

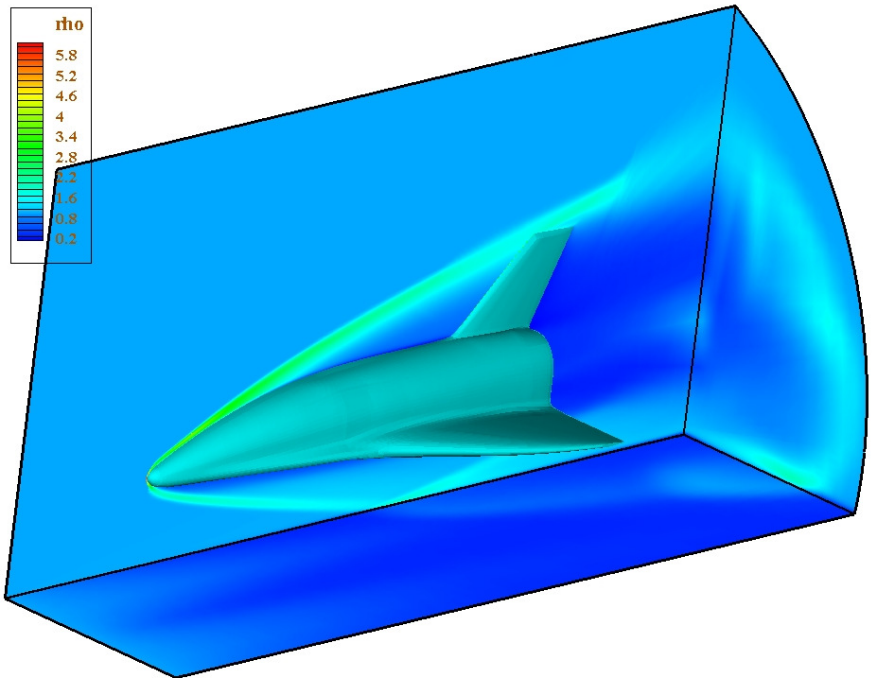

Figure 8.6: Contour of relative density ρ/ρ_∞ at $M_\infty = 6.8$, $\mathrm{Re_m} = 1.12\times10^6$, **h/L** = 0.1812, and $\Delta\alpha = 0°$ in laminar flow.

As a different contour presentation of the same numerical solution in laminar flow, a contour of Mach number is shown in Figure 8.7. Comparing with Figure 8.6, the most obvious difference between the shock structures in two pictures is on the solid surface, especially above the flat plate. There are intensive changes of Mach number in the zone near the solid surface. The boundary layers in Figure 8.7 could be observed more clearly on the symmetry plane. Because Mach number is always zero on the surface of the flat plate, there is no possible to distinguish the impingement points.

However, the interaction between boundary layer and the bow shock above the flat plate could be identified on the bottom of the symmetry plane.

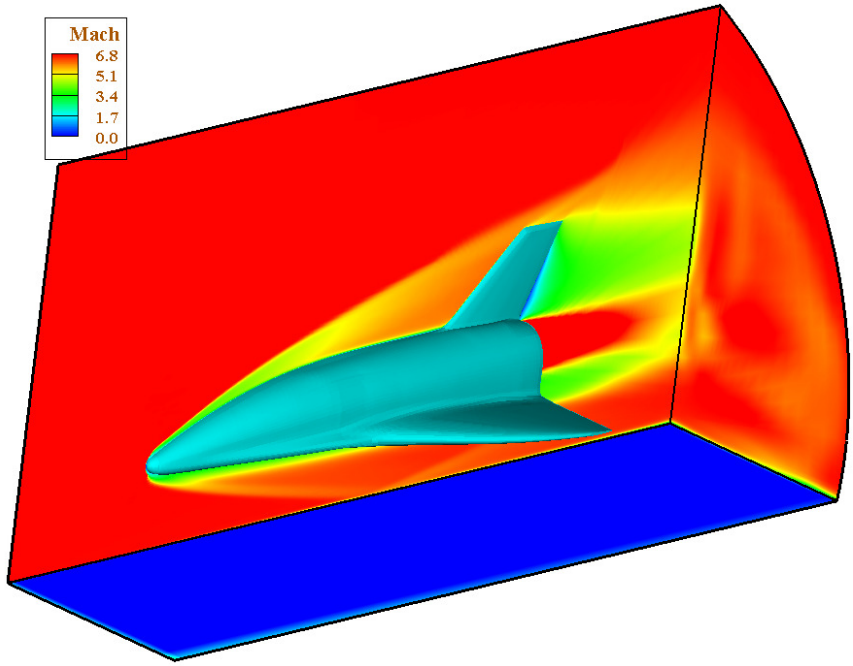

Figure 8.7: Contour of Mach number at $M_\infty = 6.8$, $\mathrm{Re}_m = 1.12\times10^6$, **h/L** = 0.1812, and $\Delta\alpha = 0°$ in laminar flow.

As another presentation of shock structure, the contour plot of relative pressure p/p_∞ is used in Figure 8.8. Both shock structures and the impingement points are clearly depicted also in laminar flow. On the flat plate, the strongest pressure impact appears behind of the EOS. It results from a combination of the bow shock and the shock from the wing.

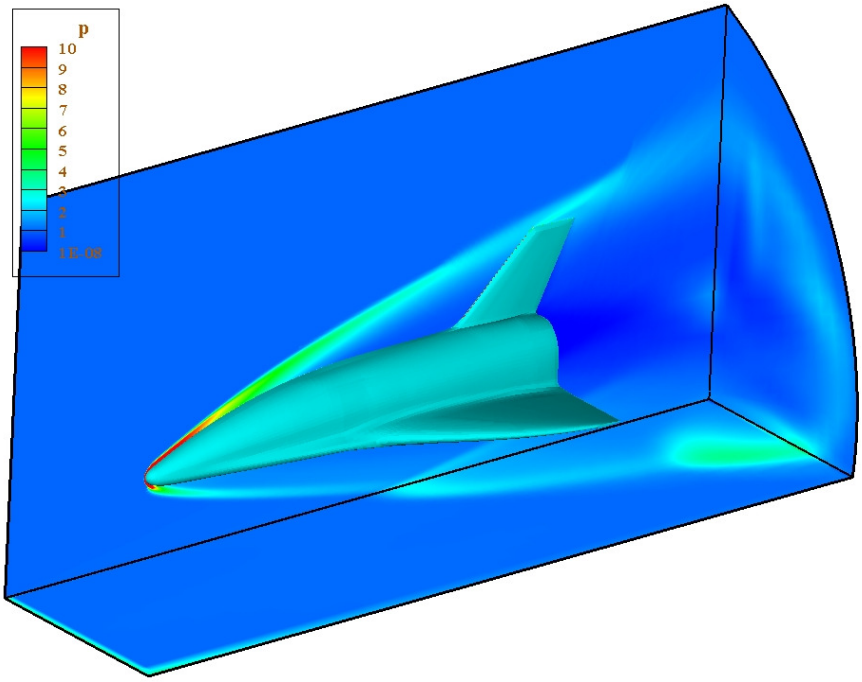

Figure 8.8: The contour of the relative pressure p/p_∞ at **h/L** = 0.1812, $M_\infty = 6.8$, $\mathrm{Re}_m = 1.12\times10^6$, $\Delta\alpha = 0°$ in laminar flow.

Including the cases with **h/L** = 0.1812 discussed just above, a series of steady separation processes are numerically investigated at Mach 6.8, corresponding to different separation distances from **h/L** = 0.0662 to infinity. To analyze the relation between shock and distance more clearly, the angles of attack are set to zero. Describing the contours of relative density ρ/ρ_∞, the shock structures are studied using inviscid flow in Figures 8.9.a and laminar flow in Figures 8.9.b, respectively.

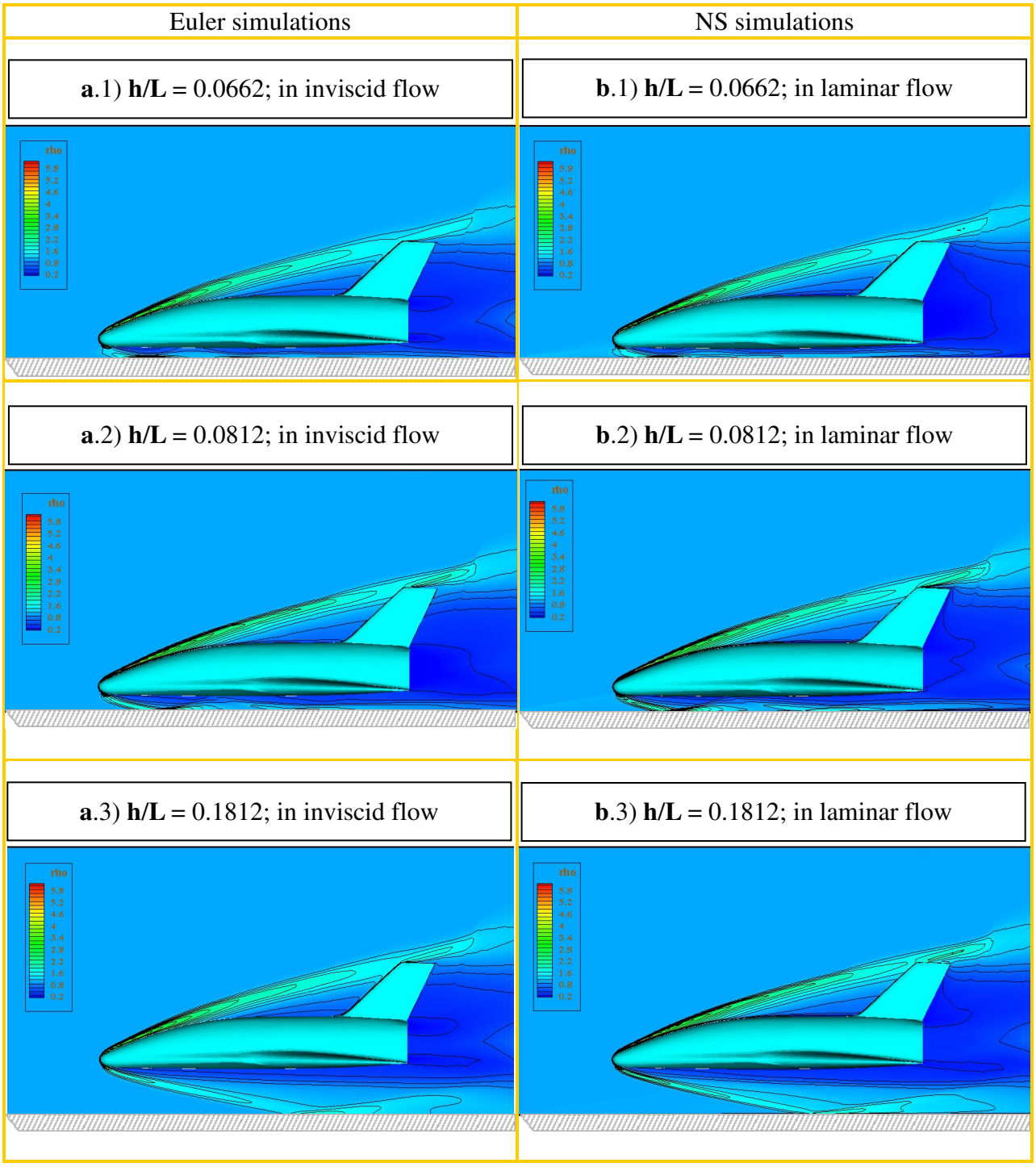

Figure 8.9 (1-3): The contour of the relative density ρ/ρ_∞ with different separation distances at $M_\infty = 6.8$, $\Delta\alpha = 0°$ in laminar and inviscid flows.

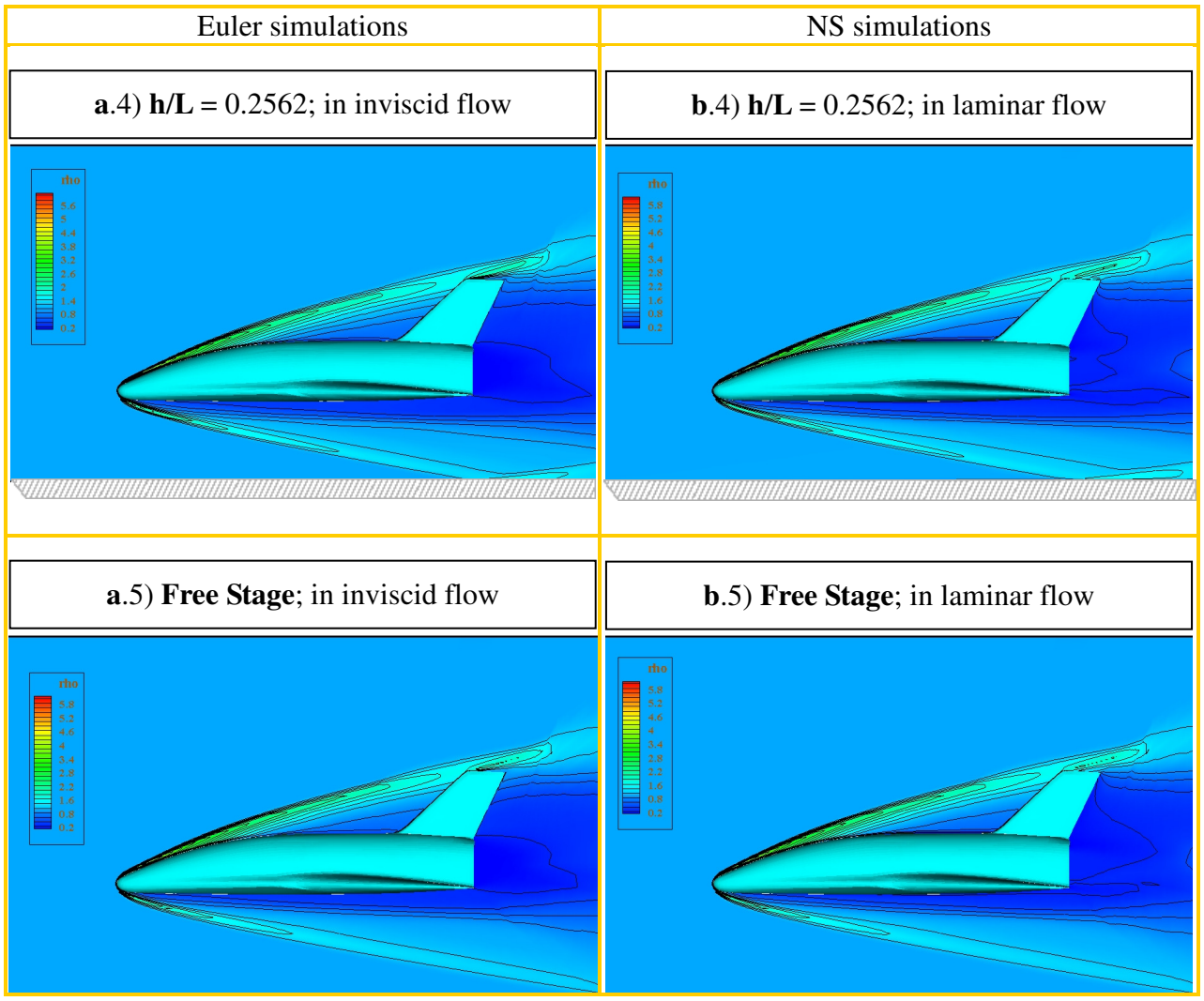

Figure 8.9 (4-5): The contour of the relative density ρ / ρ_{∞} with different separation distances at $M_{\infty} = 6.8$, $\Delta\alpha = 0°$ in laminar and inviscid flows.

The cases with **h/L**=0.0662 and **h/L**=0.0812 are labeled as **a**.1, **b**.1, **a**.2, and **b**.2 in Figure 8.9. The shocks reflected from the flat plate hit the lower surface of EOS more than two times. Part of the bow shock develops downwards and hits the flat plate. Thereafter, it is reflected upwards to the lower side of the EOS. After it hits the EOS lower surface, it is reflected again to the flat plate. The shock waves rebound in this way further. When the 2nd reflected shock from the flat plate strikes the lower surface of the EOS, it is already located on the rear part between the EOS and the flat plate. It becomes very weak and its further developing direction has not much difference comparing to the freestream. However, it still affects the expansion region behind the tail of the EOS.

When the separation distance **h/L** increases, the positions of the impingement points of the bow shock move rearwards. The number of reflected shock waves decreases. When the distance **h/L** is greater than 0.1812, such as for **a**.3, **b**.3, **a**.4, and **b**.4 in Figures 8.9, the impingement points of the reflected shockwave have already moved to the wake zone. The reflected shock could not reach the EOS body any more. The upwards reflected shock only progresses in the flow field behind the EOS tail. This tendency continues, until the two stages are separated with an enough distance. Subsequently, there is no reflected shock wave to affect the flow fields. The two flow fields around

the two stages do not interfere with each other anymore. They develop as shown in **a**.5 and **b**.5.

For the laminar cases, the boundary layers above the flat plate could well be distinguished in Figure 8.9.**b**. They interact with the bow shock in this thin layer and make the impingement points somewhat blurred. It also affects the expansion zones. Especially it results in difference of the wake zone. There are also very weak traces of the shock waves generated from the beginning of the flat plate in the pictures **b**.1 and **b**.2. They hit the region of EOS nose. The shock waves generated from the beginning of the flat plate become much weaker. There are nearly no traces in the pictures from **b**.3 to **b**.5. This means, the weak shock is not only dependent on the Mach number, but also depends on the distance between two stages.

Because the distances between EOS and flat plate confine the transfer of the shock wave, different distances **h/L** result in different shock structures. They affect the distributions of aerodynamic forces and pitching moment. In the next sections, the exact magnitudes of pressures affected by the shock waves are discussed corresponding to different distances **h/L**.

8.1.3 Shock Structures Dependent on Mach Numbers

The numerical simulations with Mach 4.05 in Chapter 6 and with Mach 7.9 in Chapter 7 have shown satisfied consistencies with the available experimental results. Due to the lack of experimental data, the simulation at Mach 6.8 is analyzed by comparing the numerical results with these of the two other Mach numbers in the above mentioned chapters.

Figure 8.10 illustrates a comparison of shock structures among the three Mach numbers, which are of Mach 4.05, 6.8, and 7.9 respectively. The contour lines of the relative density ρ / ρ_∞ are shown on the same symmetry plane with **h/L** = 0.1812 in laminar flow, but with different Reynolds numbers due to the different freestream velocities and with different viscosities.

Compare the bow shocks of EOS. The contour lines of relative density ρ / ρ_∞ with $M_\infty = 6.8$ are denser than those with $M_\infty = 4.05$, but sparser than those with $M_\infty = 7.9$. This means that the maximal value of the relative density in flow field with Mach number 6.8 is just between its counterparts with Mach 7.9 and with Mach 4.05. The impingement point of the bow shock on the flat plate with Mach 6.8 (refer the line **b**) is also between the impingement points with Mach 4.05 (refer the line **a**) and with Mach 7.9 (refer the line **c**). The bow shock with Mach 4.05 reflects to the rear parts of the EOS, but with Mach 6.8 and Mach 7.9 the reflected bow shocks have already been moved to the expansion parts behind the EOS tail. The pressure in the wake region becomes greater with increasing Mach numbers. At Mach 6.8, there is no reflected shock hitting the lower surface of the EOS. Consequently, there is no obvious pressure increment to affect the lift and pitching moment on that lower surface for **h/L** = 0.1812.

At Mach 7.9, the length selections of the flat plate already apparently affect the development of the bow shock. Its bow shock is clearly intersected by a weak shock generated from the beginning of the flat plate. There are nearly no trace for the corresponding shock wave in the other two cases with **h/L** = 0.1812. The boundary layer on the flat plate with Mach 6.8 is a little thicker than that with

Mach 4.05, but much thinner than that with Mach 7.9. The interaction between the boundary layer on flat plate and the shock waves could affect the aerodynamic properties of the EOS.

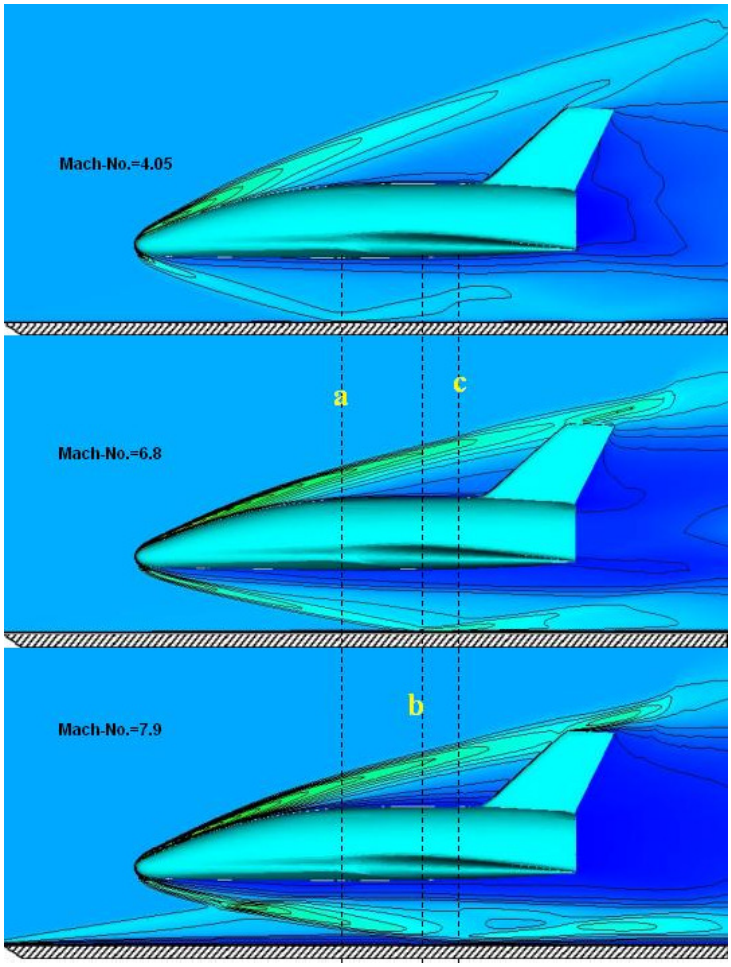

Figure 8.10: Comparison of shock waves in laminar flows at **h/L** = 0.1812 with different Mach numbers.

From these comparisons one can conclude that the shapes of bow shocks, the impingement points of the bow shock on the flat plate, and the formation of the boundary layers are all closely related with the Mach numbers. These dependencies are in nonlinear manner.

8.1.4 Shock Structures Dependent on Angles of Attack

As shown for the cases with Mach 4.05 and with Mach 7.9, the angles of attack of the EOS also affect the shock structure significantly. The shock structures of Mach 6.8 with angle of attack 0° and 3° degrees are discussed mostly in inviscid flow. It is assumed that the rotation center is on the point (0.65, 0, 0).

The separation distance is firstly set to **h/L** = 0.1812. Concentration on the flow field of the symmetry plane with angles of attack of 0° and 3°, a comparison of shock structure is shown in Figure 8.11. With angle of attack 3°, the nose of the EOS rises up and its tail approaches to the flat plate.

Referring to the line **b,** its bow shock under EOS hits the flat plate much more downstream than in the case with angle of attack 0° (referring the line **a**). With angle of attack 3°, the bow shock on the upper side leaves away from the stabilizer and the wake zone moves closer to the flat plate. The reflected shock of the flat plate influences the wake zone a little more than for the case with angle of attack of 0°.

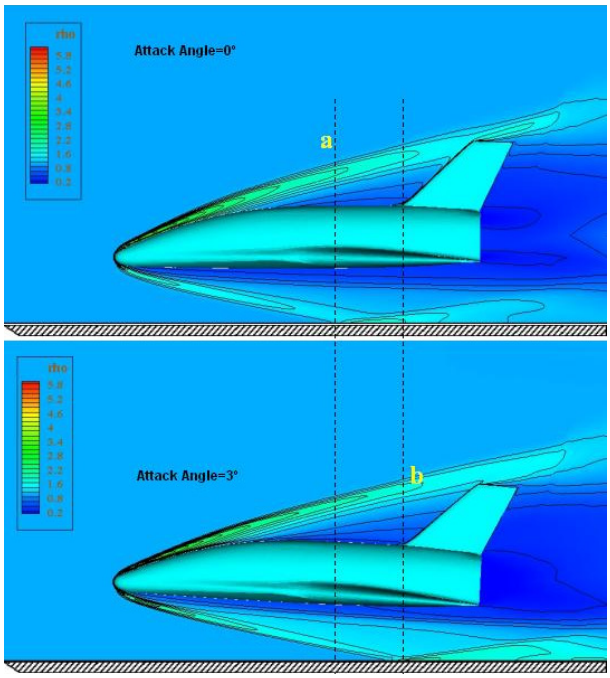

Figure 8.11: Comparison of shock waves in inviscid flow between different angles of attack with **h/L** = 0.1812, $M_\infty = 6.8$, and rotation center (0.65, 0, 0).

.

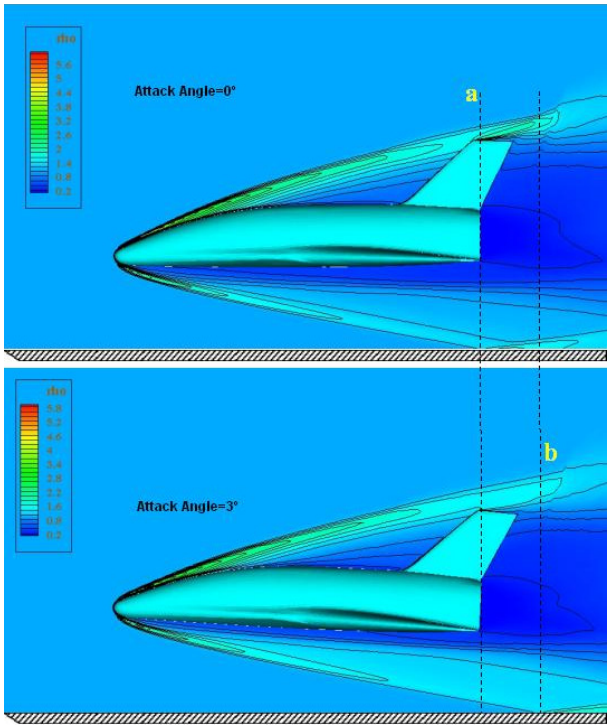

Figure 8.12: Comparison of shock waves in inviscid flow between different angles of attack with **h/L** = 0. 2562, $M_\infty = 6.8$, and rotation center (0.65, 0, 0).

Another example is shown in Figure 8.12. The impingement points of bow and wing shocks move much more rearward with a greater angle of attack, when the separation distance is **h/L** = 0.2562. The reflection of the shock from the flat plate nearly does not affect the movement of the EOS anymore, because these reflections are too far away from the tail of the EOS.

Figure 8.13 shows a further comparison between inviscid and laminar flows. With distance **h/L** = 0.2562 and angle of attack of 3°, the shocks and their reflections transfer nearly in the same way. The difference between Euler and NS simulation is only in the boundary layer and the wake region. The boundary layer is already thin in the upper picture of Figure 8.13. The line **a** labels the impingement points for both cases. The reflection point of the bow shocks in laminar flow is a little bit separate with the impingement point once more.

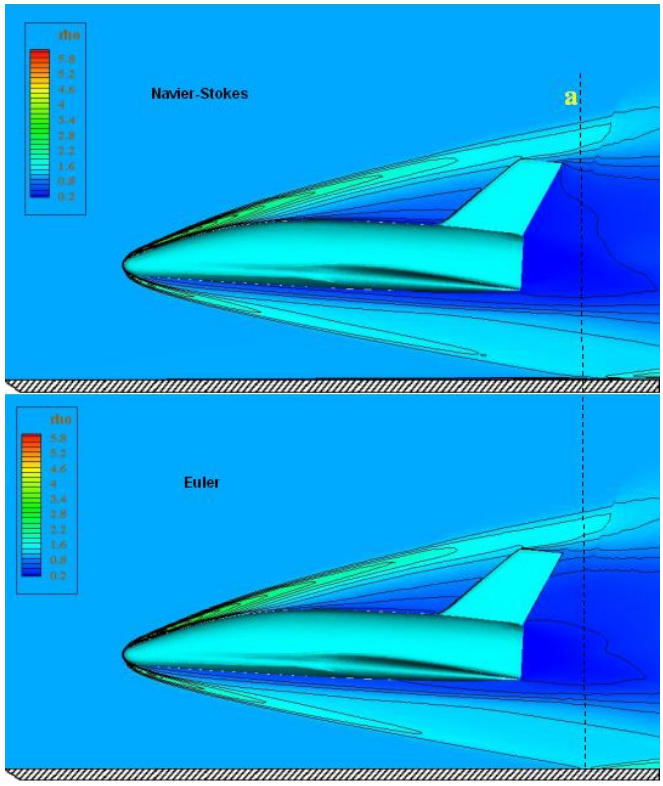

Figure 8.13: Comparison of shock waves between laminar and inviscid flow with $\Delta\alpha = 3°$, **h/L** = 0.2562, $M_\infty = 6.8$, and rotation center (0.65, 0, 0).

8.1.5 Shock Structures on 3D EOS Surface

Until now most of the shock structures are shown on the symmetry plane in the computing domain. Few are also shown on the sectional planes parallel or perpendicular to the freestream. In this section, the distribution of the relative density ρ / ρ_∞ is directly described on the whole surface of the EOS. The separation distance **h/L** is chosen as 0.0662 or 0.2562. The shock influence on the EOS surface is presented by contour plots. Avoiding that the shock structure is blurred by the thin boundary layer on the EOS surface, inviscid flow cases are first selected. It is assumed that the angle of attack $\Delta\alpha = 0^\circ$.

As depicted before, shock waves emanate from the EOS nose like a cone. The transfers of the shock waves are affected by the postures of the EOS and the flat plate. With a small separation distance between the two stages, shock waves could be reflected many times between two surfaces of the two stages.

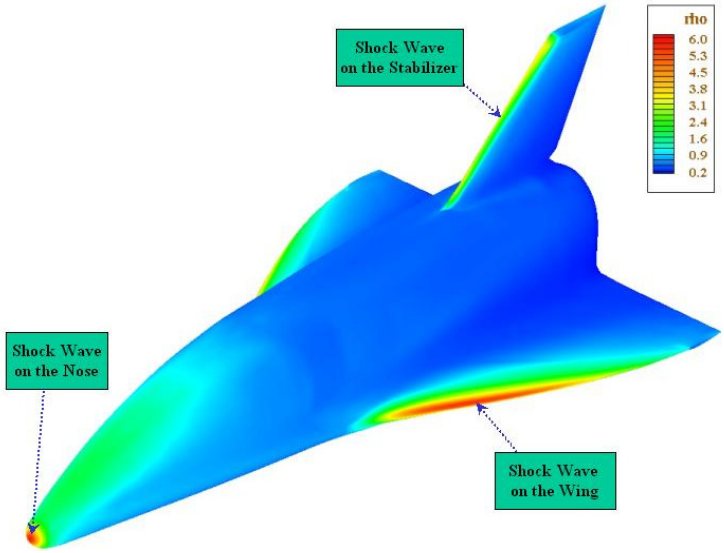

Figure 8.14: Shock structure illustrated by the relative density ρ / ρ_{∞}
on the upper part of the EOS with **h/L** = 0.0662, $\Delta\alpha = 0°$ in inviscid flow.

On the upper part of the EOS in Figure 8.14, we could find the air compressions on the nose of the EOS, on the leading edge of the wing, and on the vertical stabilizer. These great air compressions spread their influence to their neighborhood on the EOS surface. Due to the character of the EOS geometry, the other regions mainly belong to the expansion zones. Obviously, there is no other impact on the upper part of the EOS.

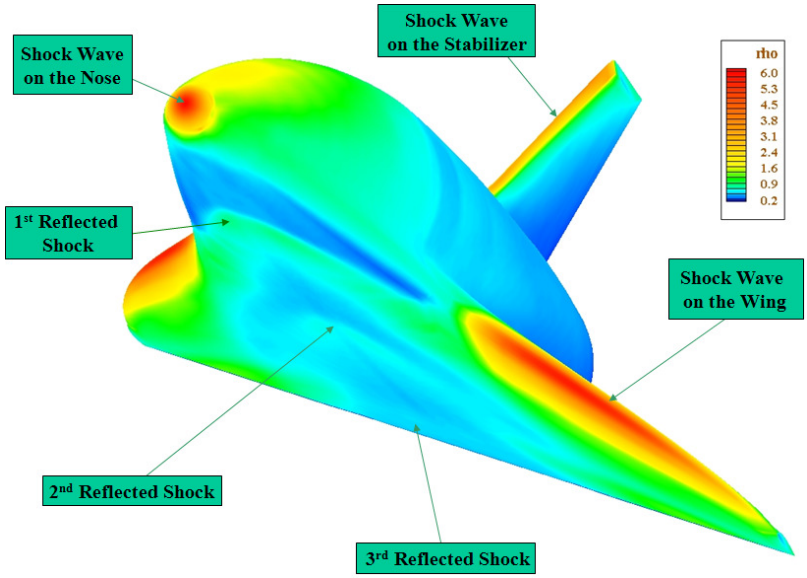

Figure 8.15: Shock structure illustrated by the relative density ρ / ρ_{∞}
on the lower part of the EOS with **h/L** = 0.0662, $\Delta\alpha = 0°$ in inviscid flow.

On the lower part of the EOS surface, the air is mainly compressed also in the region of the EOS nose and on the leading edge of the wing. Some reflected shocks by the flat plate also hit on the lower surface of the EOS. These reflected shock waves are described as the first and the second reflected shocks in Figure 8.15, in which we adjust the contour level more sensitive to the small relative density. These two induced compressions could be seen as two regions of increased density. They spread from the symmetry line of the EOS lower surface to the lower surface of the two wings. The first reflected bow shock nearly superimposes with the shock of the wing. For the second reflected shock wave, the middle part is weaker than the part directly under the wing. This middle part is purely generated by the wave, which is originated from the reflections of the bow shock. It becomes already very weak. The part under the wing is a combination of the reflected bow shock and the shock from the wing. The impingement points of the second reflected shock stretched to the most rear part under the wing. There is still a nearly imperceptible third hitting on the middle part of the lower surface of the EOS. Its trace is already very blurred in this picture.

With the increase of the distance between the EOS and the flat plate, the impingement points of the first reflected shock wave move rearwards, until the first reflected shock could not hit the lower side of the EOS any more. This is the case with the separation distance **h/L**=0.2562. In Figure 8.16, we only see some spreads of air compression from higher density area to lower density area in the neighbourhood of bow nose and the leading edge of the wing.

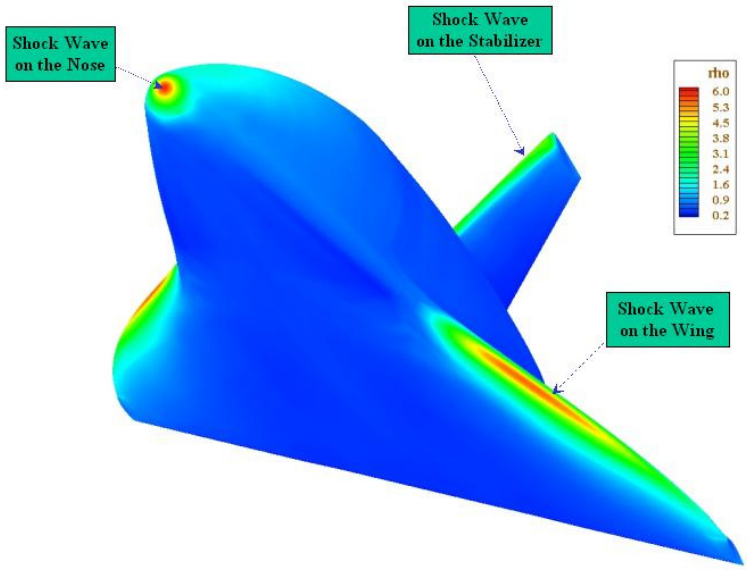

Figure 8.16: Shock structure illustrated by the relative density ρ / ρ_∞
on the lower part of the EOS with **h/L** = 0.2562, $\Delta\alpha = 0°$ in inviscid flow.

Corresponding to the traces of the reflected waves for inviscid flow as shown in Figure 8.15 and 8.16, there are similar numerical results in laminar flows. Their traces are much blurred because they are interfered by the boundary layer. To illustrate the 3rd shock structure at the distance **h/L**=0.0662, the contour legend is also adjusted in Figure 8.17. There are also three visible areas of reflected shocks. However, the weak trace of the relative density ρ / ρ_∞ in laminar flow does not mean that the pressure caused by the reflected shock is smaller than that in inviscid flow. Contrarily, the impact

pressure in laminar flow is usually slightly greater than or equal to the corresponding pressure in inviscid flow on these impingement points.

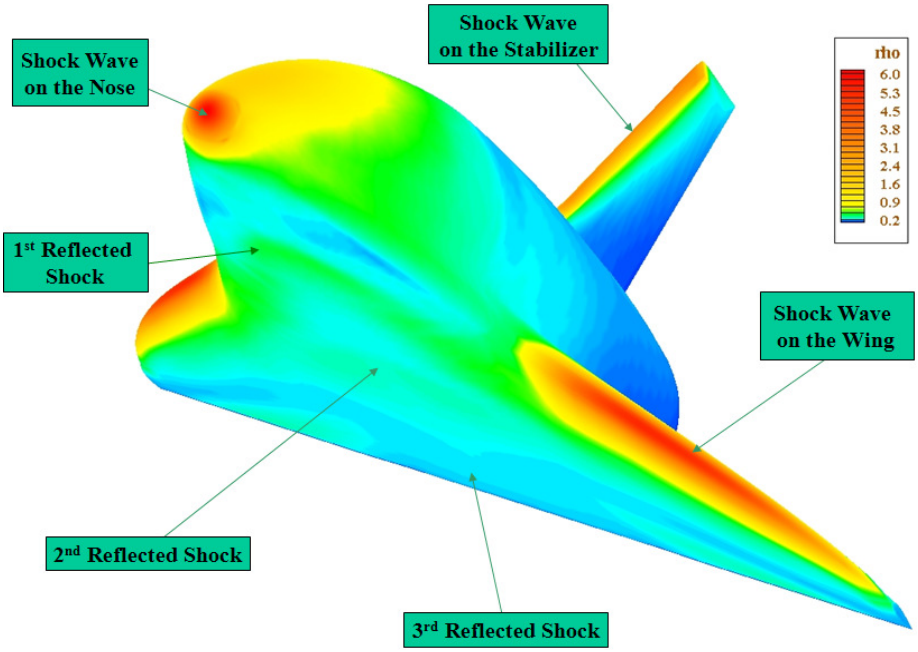

Figure 8.17: Shock structure illustrated by the relative density ρ / ρ_∞ on the lower part of the EOS with **h/L** = 0.0662, $\Delta\alpha = 0°$ in laminar flow.

8.2 Pressure Coefficients Related to Shock Structures

In the above sections, the shock structures have been intuitionally depicted in the computing domain related to different physical characters, different maneuvers, and different numerical models. Because the aerodynamic interaction affects the pressure distribution mainly on the lower surface of the EOS, the pressure distribution is quantitatively analyzed on this lower surface. Correspondingly, the impact of the shock wave is interpreted by a peak magnitude of the pressure coefficients. As the manner in Chapter 7, the pressure coefficients are also plotted along the lines defined in Figure 5.17 for different separation distances **h/L**, though there is no experiment to verify those numerical results. The environment is assumed the same as that in section 8.1, that is, $M_\infty = 6.8$, $\mathrm{Re}_m = 1.12\times10^6$, and $\Delta\alpha = 0°$.

At first, the same case as in Figure 8.9.**a**.1 and 8.9.**b**.1 with the smallest distance **h/L** = 0.0662 is quantitatively discussed. Herein, the pressure distribution on the lower surface of the EOS is depicted in Figure 8.18. Simulated with both inviscid and laminar freestreams, the pressure coefficients are plotted along the line described in Figure 5.17 with y = 0. Euler and NS simulations show good similarity relating to the impacts of the reflected shocks. They present almost the same peak magnitudes caused by the 1st and 2nd reflected shocks. Their peaks about pressure coefficients reach 0.07 and 0.033. Except these two peaks, the pressure coefficients of Euler simulation are always smaller than those of NS simulation. All of their pressure coefficients are greater than zero. Though the impingement point in laminar flow is blurred in the contour picture of the relative density in the

last section, the peak of the pressure in laminar flow is not smaller than that in inviscid flow. Around the point x=0.875, there is a weak trace of the third pressure peak, which originates from the bow shock reflected by the flat plate for the third time.

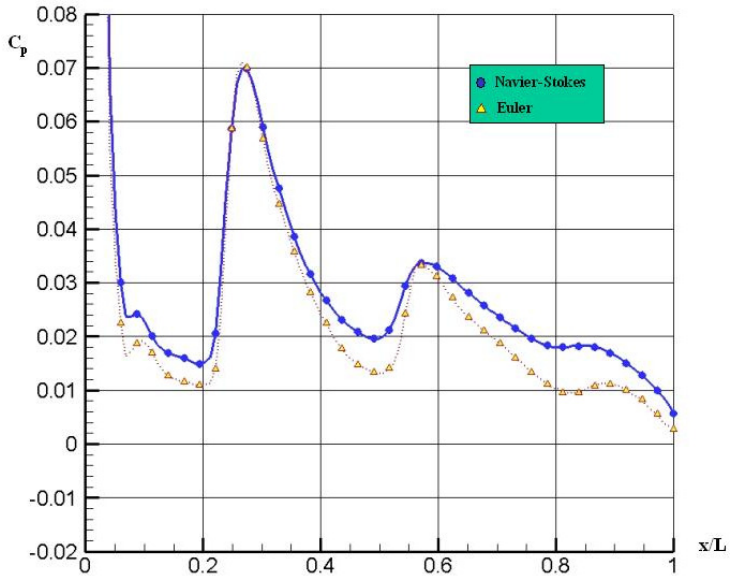

Figure 8.18: Pressure coefficients using laminar and inviscid flows on the lower surface of the EOS with y = 0, $M_\infty = 6.8$, $\Delta\alpha = 0°$, and **h/L** = 0.0662.

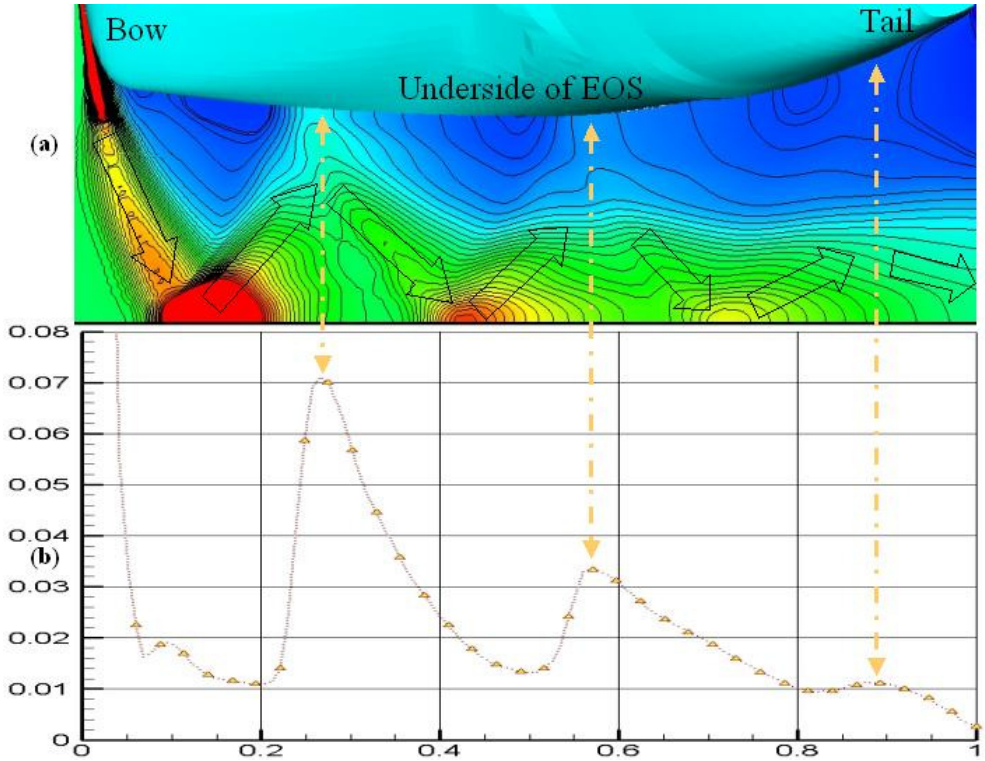

Figure 8.19: Shock development illustrated at **h/L** = 0.0662 in inviscid flow with
(**a**) the contour of relative density ρ / ρ_∞ on the symmetry plane;
(**b**) pressure distribution on the line shown in Figure 5.17 with y = 0.

To analyze the shock structure and the surface pressure distribution more closely, a direct comparison along the lower side of the EOS is presented in Figure 8.19 for inviscid flow. On the

symmetry plane, Figure 8.19 (**a**) shows the flow field above the flat plate and below the EOS lower surface. Its size in vertical direction is much magnified to illustrate the shock structure in this thin zone more clearly. Figure 8.19 (**b**) is the same picture as Figure 8.18, but excluding the NS simulation. This picture is compressed a little in vertical direction. Both pictures keep the same coordinate in **x/L** direction. By comparing Figure 8.19 (**a**) and Figure 8.19 (**b**), it is shown how the pressure coefficients on the lower side of the EOS depend closely on the shock structure. When the shock wave leaves EOS, the pressure coefficient will decrease. Contrarily, the pressure coefficient will increase, when the shock wave is reflected by the flat plate and heads to the lower surface of the EOS. In both Figure 8.19 (**a**) and Figure 8.19 (**b**), three reflected shocks exactly correspond to the three peaks of the surface pressure. The strength of the shock is directly expressed by the magnitude of the pressure coefficient. The first reflected shock is the strongest, then the second. The third reflected shock is very weak. Its associated third pressure peak is very flat. When a shock is reflected back, its magnitude of the pressure peak approximately remains less than half of its earlier peak magnitude. In Figure 8.19 (**b**)**,** the peak magnitudes related with three impingements are approximately 0.071, 0.033, and 0.011, respectively.

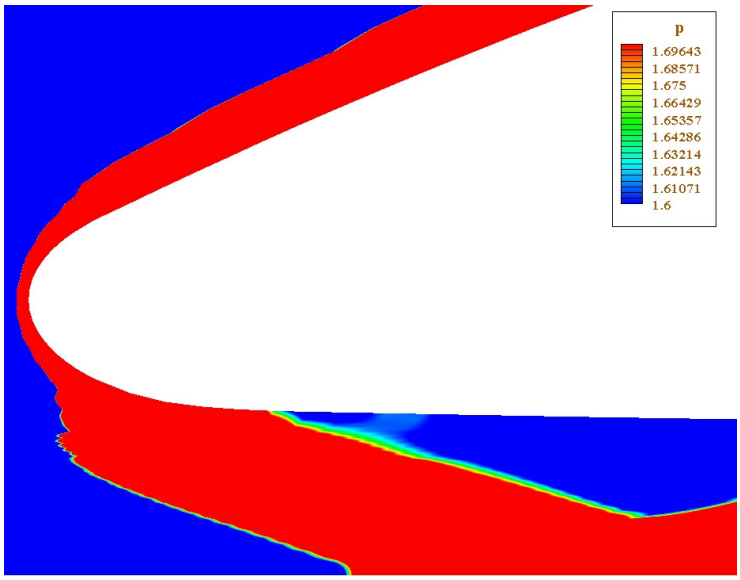

Figure 8.20: The relative pressure p/p_∞ on the symmetry plane in inviscid flow, where $M_\infty = 6.8$, $\Delta\alpha = 0°$, and **h/L** = 0.0662.

Except the shock influences, there is still another small disturbance. That is the first small increase of pressure coefficients in Figure 8.19 (**b**), for the **x/L** in the interval (0.06, 0.08). At a small distance **h/L** = 0.0662, the region between the lower side of the EOS and the flat plate forms a very narrow inlet for freestream. The small disturbance comes from an air compression in this narrow channel. To observe the pressure change in the head part of Figure 8.9.**a**.1, the region around the nose is magnified in Figure 8.20. The legend about the relative pressure is adjusted to the level [1.6, 1.7]. The contour of p/p_∞ between the bow shock and the lower surface of the EOS shows a weak compression trace.

In Chapters 6 and 7, we usually use the relative density ρ/ρ_∞ to express the shock structures,

because it could clearly illustrate the density gradient as the Schlieren picture does. Using the relative pressure p/p_∞ to describe the flow fields, some examples in this chapter have clearly shown the shock structures. Their traces do not be smeared by the influence of the boundary layer on the solid surface as the cases using the relative density. It is a valuable expression in the force analysis for the separation process.

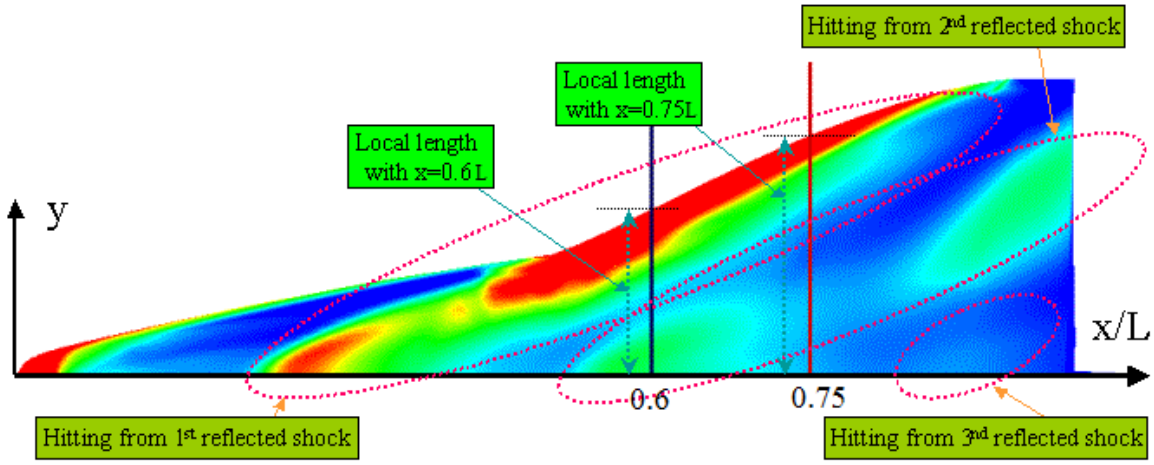

Figure 8.21: The relative pressure p/p_∞ on the lower surface of the EOS in inviscid flow with $M_\infty = 6.8$, $\Delta\alpha = 0°$, and **h/L** = 0.0662.

Still for the case with separation distance **h/L** = 0.0662 in inviscid flow, the pressure distribution is illustrated on the half part of the lower surface of the symmetric EOS geometry in Figure 8.21. To show the same shock structure illustrated by the relative density ρ/ρ_∞ in Figure 8.15, the legend about the relative pressure p/p_∞ is adjusted to the range [0, 0.08]. Then the impact of the three reflected shock waves on the lower side of the EOS surface could be noticeable with this very sensitive contour legend. Nevertheless, the hitting trace from the third reflected bow shock is still very blurred. As a drawback of the sensitive legend, the relative pressures are always be painted with a same colour, when relative pressures are great than 0.08.

In Figure 8.21, it illustrates that the biggest pressures appear also in the regions on the bow nose of the EOS, on the leading edge of wing, and on the neighbor regions of these direct compressions. In other regions, the magnitude values of the pressure coefficients are much smaller. Their impacts caused by the three reflected shock structures are also much weak comparing to the effects induced by these direct compressions.

As in Chapter 7, the pressures are quantitatively analyzed again on the other two lines as shown in Figure 5.17 with x = 0.6**L** and x = 0.75**L**. These two lines are vertical to the direction of freestream and located on the lower side of EOS. In Figure 8.21 it is shown that pressure coefficients on these two lines are very much affected by the second reflected shock wave and the compression zone of the wing. Accompanying the increase of y**/Local**, Cp decreases when y**/Local** leaves the region influenced by the second reflected shock wave. Thereafter, Cp increases when y**/Local** approaches to the compression zone of the wing. This tendency is exactly described with the pressure magnitude on the line with x=0.6**L** in Figure 8.22. When y**/Local** is in the value of 0 to 0.2, this area is influenced by the second reflected shock. From 0.2 to 0.625, it corresponds to a region between the two shock

impacts. From 0.625 to 1 the region is affected by the first reflected shock wave as well as by the shock from the wing. For laminar flow, similar results are presented also in Figure 8.22.

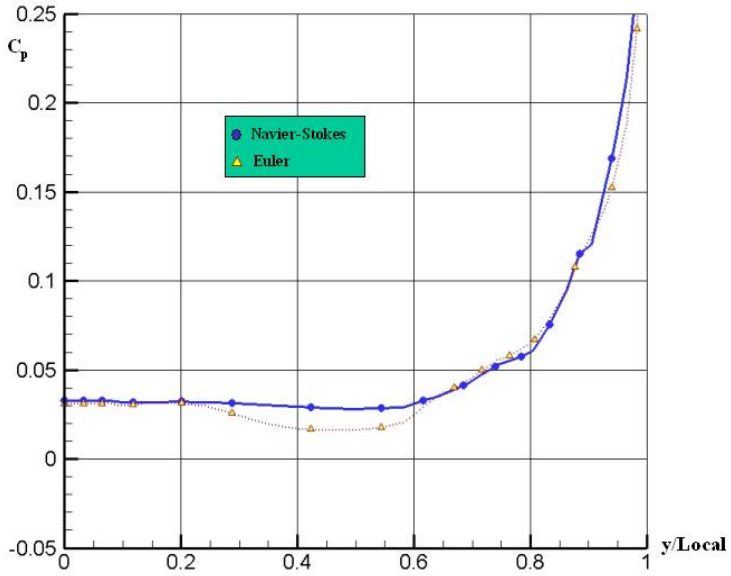

Figure 8.22: Pressure coefficient comparison between Euler and NS simulations on the lower surface of the EOS with x = 0.60**L** for the case of **h/L** = 0.0662.

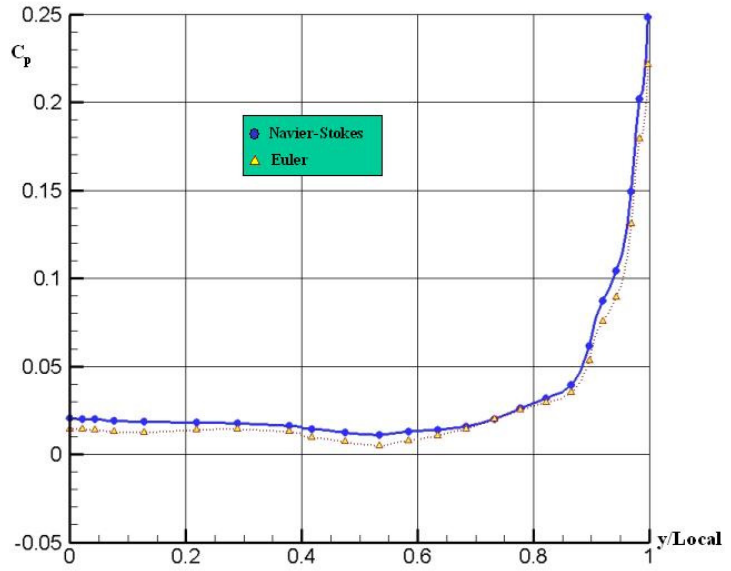

Figure 8.23: Pressure coefficient comparison between Euler and NS simulations on the lower surface of the EOS with x = 0.75**L** for the case of **h/L** = 0.0662.

On the line with x=0.75**L** the dependence of the pressure on the shock structure is more complex as shown in Figure 8.21 and in Figure 8.23. The section begins at the region affected by the second reflected shock. The magnitude of the pressure is about 2/3 times as great as the one in the corresponding point at x=0.6**L**. Then the cross section intersects the middle part of the wing, where the shock from the wing and the second reflected shock interfere with each other in a wide region. Since the second reflected shock and its interference with the wing shock are already weak, no strong

fluctuations occur. The superposition of the interference decreases the pressure magnitude. It forms a very shallow region between the impingement points of first and second reflected shocks. In Figure 8.23, the line with x=0.75**L** crosses this shallow region, when y**/Local** is in the range from 0.2 to 0.62. After leaving this region, the influence on the surface pressure is again dominated by the shock from the wing and its coefficient reaches 0.25.

When the two stages are separated further away, the shock waves as well as its reflected waves travel a longer distance before they reach a solid surface and are reflected. Their impingement points move downwards. Subsequently, the numbers of the pressure peaks decrease on the lower surface of the EOS.

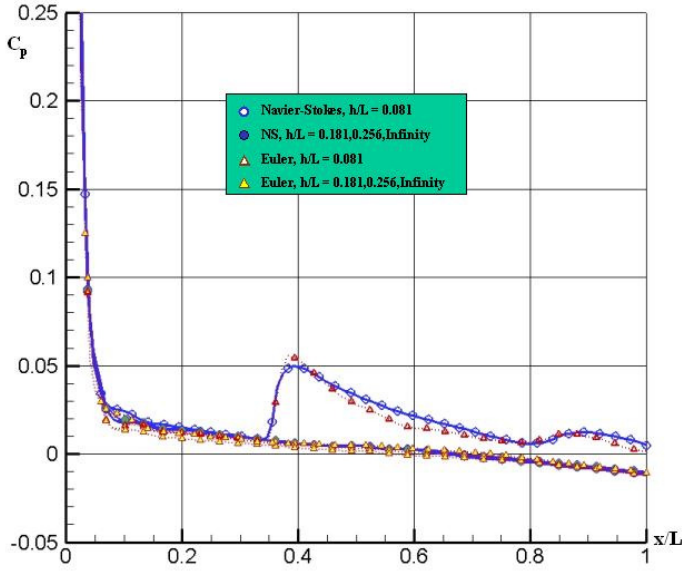

Figure 8.24: Comparison of pressure coefficients between Euler and NS simulations
on the lower surface of the EOS with y= 0
for the cases of **h/L** = 0.0812, 0.1812, 0.2562, and infinity.

Consider the pressure distribution on the line with y= 0 at different separation distances **h/L** = 0.0812, 0.1812, 0.2562. Because of bow shock, the biggest pressure achieves in the region of the EOS nose. When **x/L** leaves the EOS nose, the pressure coefficients decrease significantly as shown in Figure 8.24. In other respects, accompanying the increase of the separation distance **h/L**, the impingement points on the lower surface of EOS shift downstream. As a result, these impingement points could shift out of the lower surface of the EOS. The number of pressure peaks could become less. The shock dissipates more energy when it passes through a longer separation distance. Hence, the shock impact on the lower surface of the EOS with greater separation distances **h/L** is weaker than that with smaller separation distance. With great distances **h/L** =0.1812, 0.2562, and infinity, the influence of the reflected shocks becomes very weak. Their pressures on the line with y= 0 shows smooth decease when **x/L** > 0.05.

For **h/L** ≥ 0.1812, the contour of the pressure coefficients on the line with y=0 are nearly overlapped with different distances. To show the pressure change more clearly in Figure 8.24, only one Euler simulation and one NS simulation are presented.

For the case **h/L** = 0.0812, there are still two pressure peaks generated by the reflected shocks. The magnitude of the pressure peak is about 0.05, which remains 70% of the pressure strength comparing to the case with **h/L** = 0.0662. The magnitude of second peak is only 0.014. It attenuates much more and remains only 42% of the pressure peak value comparing to the case of **h/L** = 0.0662. For both inviscid and laminar flows, these pressure changes are synthesized quantitatively in Figure 8.25. Simultaneously, the first and second impingement positions with **h/L** = 0.0812 shift in the **x/L** direction about 0.13 and 0.32 downwards also comparing to the case of **h/L** = 0.0662.

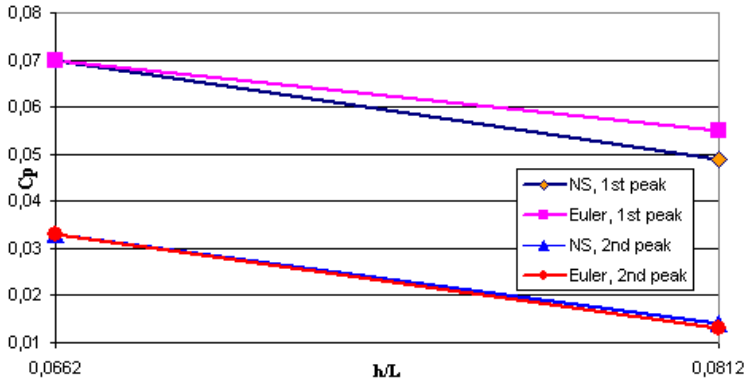

Figure 8.25: The diminishment of pressure peaks generated by two reflected shocks on the lower surface of the EOS with y= 0 for the cases of **h/L** = 0.0662 and 0.0812.

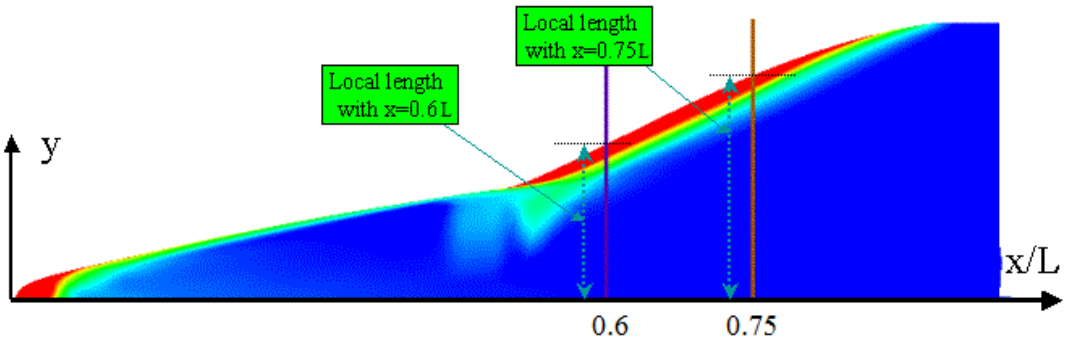

Figure 8.26: The distribution of the pressure on the lines with x = 0.6 and x = 0.75 for the case of **h/L** = 0.1812 in inviscid flow.

Also shown in Figure 8.24, pressure peaks induced from reflected shocks do not exist anymore, when the separation distance **h/L** ≥ 0.1812. In these cases, the separation distances are already too far away and the reflected shocks do not hit the EOS lower surface any more. They have been already depicted in Figure 8.9 as a series of two dimensional pictures. In Figure 8.26 with **h/L** = 0.1812, the great pressures are induced only by the air compressions directly from the EOS geometry, such as the EOS nose and the wing edge. Around these regions, compression spreads somewhat to their neighboured regions. There is no trace of the reflected bow shock on the lower surface of EOS.

On the line with **x/L**=0.6 in Figure 8.27, the distributions of the pressure coefficients are plotted at different distances respectively. For the case with **h/L** = 0.0812, there is a pressure increase between the point with **y/Local** = 0.3 and the point with **y/Local** = 0.8. The highest local peak is in the

range from 0.05 to 0.07 corresponding to viscous and inviscid flows.

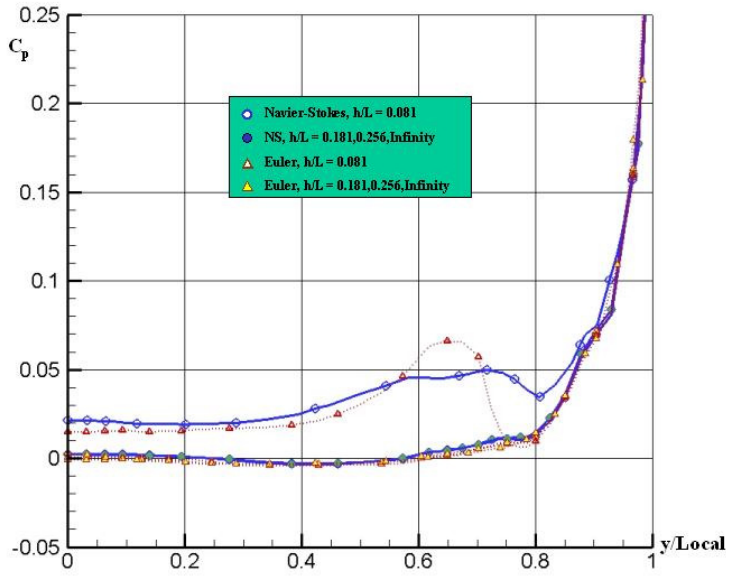

Figure 8.27: Comparison of pressure coefficients among Euler and NS simulations on the lower surface of the EOS at x = 0.60**L** for the cases of **h/L** = 0.0812, 0.1812, 0.2562, infinity.

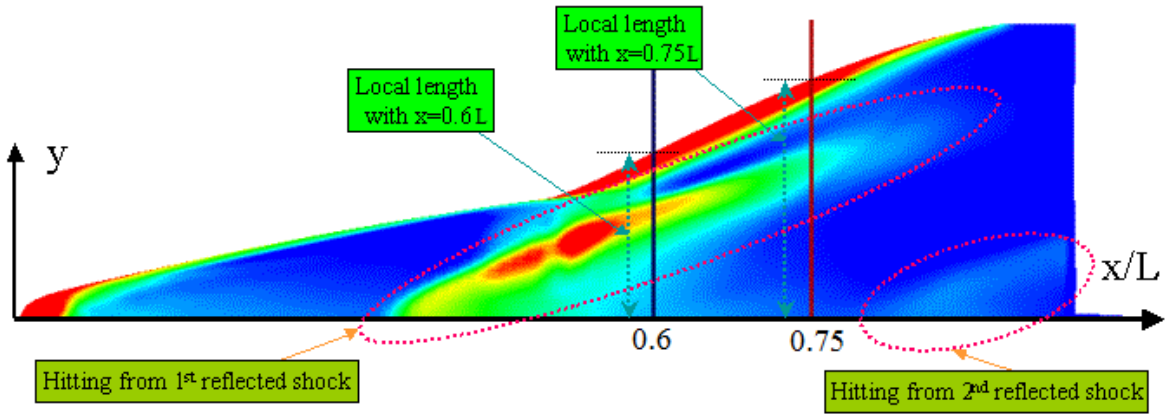

Figure 8.28: The distribution of the pressure on the lines with x = 0.6 and x = 0.75 for the case of **h/L** = 0.0812 in inviscid flow.

We could better understand the Figure 8.27 by referring to Figure 8.28. With **h/L** = 0.0812, the impingement point from the first reflected shock moves downstream and does not overlap with the shock from the wing. The line with **x/L**=0.6 intersects the region with pressure peak generated by the first reflected shock. Therefore, there are two local areas of reduced pressure and an extra local region with increased pressure. The first local area of reduced pressure is very flat.

Back to the Figure 8.27, when **h/L** ≥ 0.1812, there is no trace of reflected shock on the lower surface of the EOS, and all solutions are nearly identical. On the whole line with **x/L**=0.6, their pressure magnitudes are smaller comparing to that with smaller separation distances. Once more, one Euler simulation and one NS simulation are shown to present all overlapped solutions.

Similarly, along the line with **x/L**=0.75 in Figure 8.29, there is a pressure increase again with the smaller distance **h/L** = 0.0812 in inviscid flow. In contrast to Figure 8.28, this line crosses the region influenced by the first reflected shock. The magnitude of this peak is about one third of corresponding value in the line **x/L**=0.6. In laminar flow, the first reflected shock is already very weak and its impingement point is already connected with the shock of the wing. In Figure 8.29, the NS simulation shows a smooth increase of the pressure, and there is nearly no clear trace of the first reflected shock.

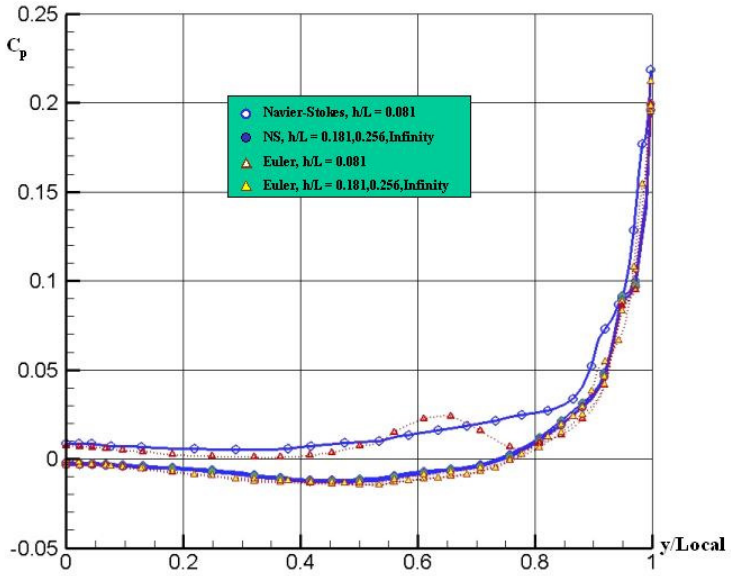

Figure 8.29: Comparison of pressure coefficients among Euler and NS simulations on the lower surface of the EOS at x = 0.75**L** for the cases of **h/L** = 0.0812, 0.1812, 0.2562, infinity.

When **h/L** ≥ 0.1812. All solutions are nearly identical. In addition, most of the pressure coefficients are negative, because these points on the line with **x/L**=0.75 already belong to the expansion zone. Pressure coefficients increase significantly in the vicinity of **y/Local=**1. This point is located on the leading edge of the wing. These pressure increments come purely from the air compression by wing geometry. There is no contribution from the impact of reflected shocks.

Figures 8.24, 8.27 and 8.29 illustrate the pressure distribution for both in inviscid flow and in laminar flow with distance **h/L** = 0.0812, 0.1812, 0.2562, and infinity. Some numerical differences between Euler simulation and NS simulation are exhibited with distance **h/L** ≤ 0.0812. When **h/L** ≥ 0.1812, NS simulations and Euler simulations are nearly identical. With these great separation distances, the flat plate and its reflection do not influence the pressure on the lower surface of the EOS practically. The NS simulations usually are smoother than Euler simulations. The Euler simulations show traces of the shock waves clearly.

Though there is no impingement from reflected shock for **h/L** ≥ 0.1812, the bow shock could directly hit the flat plate. This direct impact actually plays a more important role for the carrier stage. On the other hand, if considering a three-dimensional carrier stage, the bow shock or the shock from the wing from carrier stage may directly strike the orbital stage. Therefore, distances with **h/L** ≥ 0.1812 are still very important for the separation process with a complete carrier model. It changes the

pressure distribution of the orbital stage as well as its aerodynamic characteristics.

8.3 Aerodynamic Coefficients

The shock structures have been intensively and also quantitatively analyzed in the above sections. Related with these shocks, the aerodynamic properties, such as pressure, density and velocity, have been illustrated in the computing domain, especially for the lower side of the EOS. Except the bow shock and the shock from the wing, the reflected shock waves bring the strongest pressure impacts on the TSTO vehicles.

	C_D	C_L	C_M
Navier-Stokes, **Free EOS**	0.02270	-0.01616	-0.00905
Navier-Stokes, **h/L** = 0.2562	0.02263	-0.01626	-0.00908
Navier-Stokes, **h/L** = 0.1812	0.02262	-0.01571	-0.00928
Navier-Stokes, **h/L** = 0.0812	0.02315	-0.00064	-0.00998
Navier-Stokes, **h/L** = 0.0662	0.02399	0.00985	-0.01059
Euler, **Free EOS**	0.02259	-0.01615	-0.00915
Euler, **h/L** = 0.2562	0.02261	-0.01638	-0.00917
Euler, **h/L** = 0.1812	0.02246	-0.01624	-0.00906
Euler, **h/L** = 0.0812	0.02245	-0.00285	-0.01018
Euler, **h/L** = 0.0662	0.02286	0.00754	-0.01068

Table 8.1: Numerical lift-, drag- and pitching moment- coefficients for the EOS with $M_\infty = 6.8$, $\Delta\alpha = 0°$, and rotation center (0.65, 0, 0).

To predict the movement of the two stages in the separation process with Mach 6.8, the forces and moments, which summarize the pressures and the stresses around the whole surface of the orbital stage, are of most importance. Corresponding to different separation distances **h/L** between the EOS and the flat plate, the numerical drag-, lift-, and pitching moment- coefficients are tabulated for laminar and inviscid flows in Table 8.1.

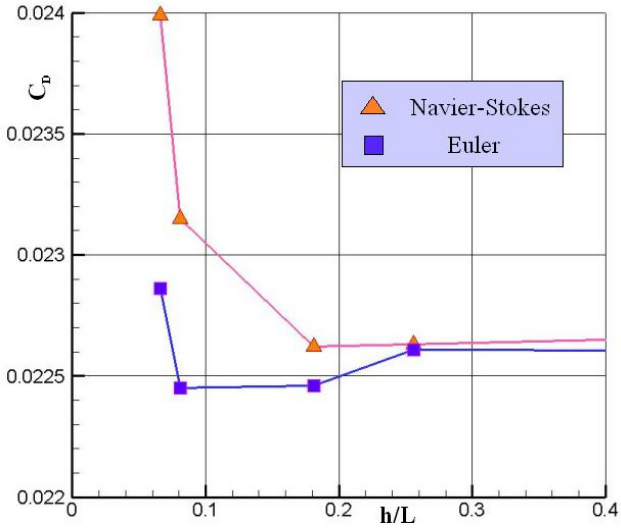

Figure 8.30: Drag coefficients dependent on the separation distances at $M_\infty = 6.8$ and $\Delta\alpha = 0°$.

To see the relationship associated with different distances **h/L** more clearly, the drag coefficients C_D are extracted firstly from Table 8.1 and shown visually in the Figure 8.30. These coefficients decrease in laminar flow when **h/L** increases to 0.1812. For inviscid flow the drags decrease only when **h/L** extends from 0.0662 to 0.0812. Thereafter, they increase from 0.0812 to 0.1812. After **h/L**$\geq$0.2562, they become nearly constant for both laminar and inviscid flows. The drag coefficients in inviscid flow are smaller than the corresponding values in laminar flow.

In the same way, the lift coefficients C_L are depicted in Figure 8.31. The lift coefficients in laminar flow are greater than those in inviscid flow. When the separation distances **h/L** increase, both lift coefficients decrease dramatically until **h/L=**0.1812. When **h/L** is between 0.1812 and 0.2562, lifts change only slightly. For **h/L**$\geq$0.2562, the lift coefficients become nearly constant, too.

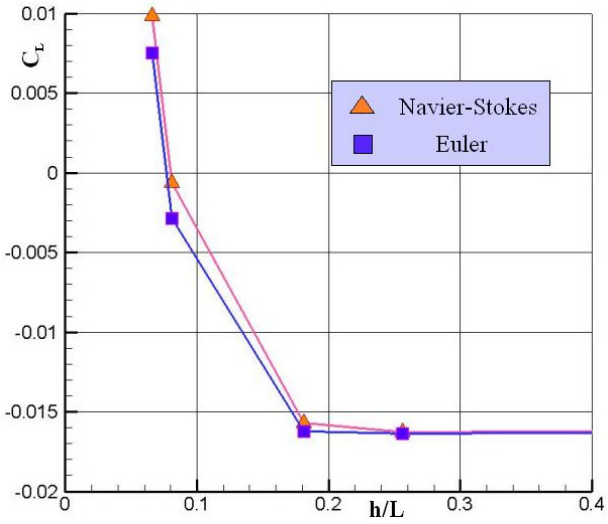

Figure 8.31: Lift coefficients dependent on the separation distances at $M_\infty = 6.8$ and $\Delta\alpha = 0°$.

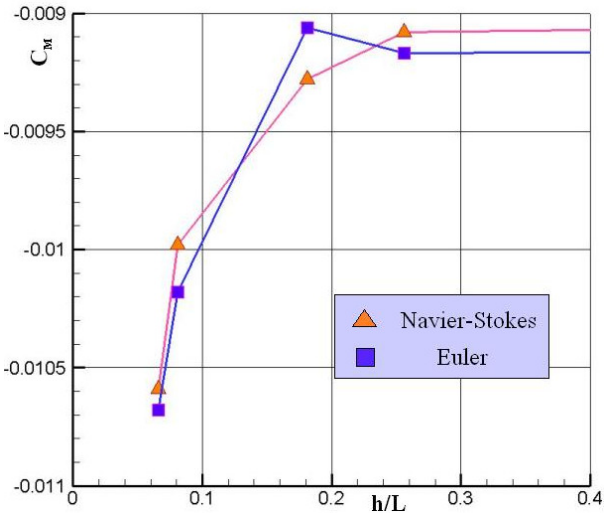

Figure 8.32: Pitching moment coefficients dependent on the separation distances at $M_\infty = 6.8$, $\Delta\alpha = 0°$, and rotation center (0.65, 0, 0).

For different separation distances **h/L**, Figure 8.32 presents the tendency of the pitching moment coefficients for the EOS. For laminar flow, the pitching moment increases when the distance **h/L**

increases, until **h/L** is greater than 0.2562. Then the pitching moment also becomes constant. The pitching moments from Euler simulations behave in a similar tendency, but with a little vibration. All of the pitching moments are negative. It means that the EOS is turned around the rotation center (0.65,0,0) in anticlockwise manner.

As it was shown in section 8.1 and 8.2, the shock structure affects pressure distribution on the lower surface of the EOS only when h/L is in the range of 0.0662 – 0.0812. When h/L ≥0.1812, the reflected shock waves do not obviously affect the pressure on the lower surface of the EOS. This leads to a nearly constant lift as shown in Figure 8.31. However, the drag and pitching moment have still some changes as presented in Figures 8.30 and 8.32. These phenomena could be attributed to the changes of the aerodynamic properties in the wake zone of the EOS.

Compare the aerodynamic coefficients in the cases with Mach 4.05, Mach 6.8 and Mach 7.9. Assuming the angle of attack $\Delta\alpha = 0°$ and separation distance **h/L** = 0.1812, Table 8.2 collects these coefficients for both laminar and inviscid flows. In laminar flow, the drag at Mach 6.8 is the smallest. Its lift is also the smallest. For the angle of attack $\Delta\alpha = 0°$, all the lift coefficients and the pitching moment coefficients with the three Mach numbers are negative. This means, if the separation process is set with the initial condition $\Delta\alpha = 0°$ and distance **h/L** = 0.1812, the EOS is pushed downwards and the nose of the EOS is turned anticlockwise at all these Mach numbers. The similar results could be obtained also for inviscid flow. Therefore, the initial condition with $\Delta\alpha = 0°$ should not be adopted for the EOS. It should be pointed out, that the rotation centers are defined differently in the above three cases. Their operating temperatures are also inconsistent.

	C_D	C_L	C_M
Navier-Stokes, $M_\infty = 4.05$	0.02872	-0.01076	-0.01082
Navier-Stokes, $M_\infty = 6.8$	0.02262	-0.01571	-0.00928
Navier-Stokes, $M_\infty = 7.9$	0.02347	-0.00925	-0.00748
Euler, $M_\infty = 4.05$	0.02788	-0.01358	-0.01093
Euler, $M_\infty = 6.8$	0.02246	-0.01624	-0.00906
Euler, $M_\infty = 7.9$	0.02183	-0.01619	-0.00519

Table 8.2: Numerical lift-, drag-, and pitching moment coefficients for the EOS with $\Delta\alpha = 0°$ and **h/L** = 0.1812.

	C_D	C_L	C_M
h/L = 0.1812	0.02177	0.01081	-0.00697
h/L = 0.2562	0.02189	0.01015	-0.00674

Table 8.3: Numerical lift-, drag-, and pitching moment- coefficients for the EOS with $\Delta\alpha = 3°$, $M_\infty = 6.8$, and the rotation center (0.65, 0, 0) in laminar flow.

Only changing the angle of attack to $\Delta\alpha = 3°$, the lift converts to a positive coefficient in Table 8.3. The drag becomes smaller and the pitching moment tends to less negative.

When the separation distance increases further from **h/L** = 0.1812 to **h/L** = 0.2562, the lift becomes a bit smaller shown also in Table 8.3, but it still remains positive. Oppositely, the drag

becomes greater. Only the pitching moment is improved to be less negative. These results support the assertion that the orbital stage should be released around $\Delta\alpha = 3°$.

8.4 Comparison with Mach 4.05 in Designed Environment

To discuss the influence of separation velocity in the same environment, another steady case is investigated at the altitude of 35 km. The TSTO vehicles fly at a Mach number of 4.05, instead of the Mach number of 6.8. The other environment parameters are the same as those listed in the beginning of this chapter. It could be derived that $\mathrm{Re}_m = 0.67\times10^6$ 1/m. In the following numerical simulation, the separation process is considered in both laminar and inviscid flows with $\Delta\alpha = 0°$, and **h/L** = 0.0662.

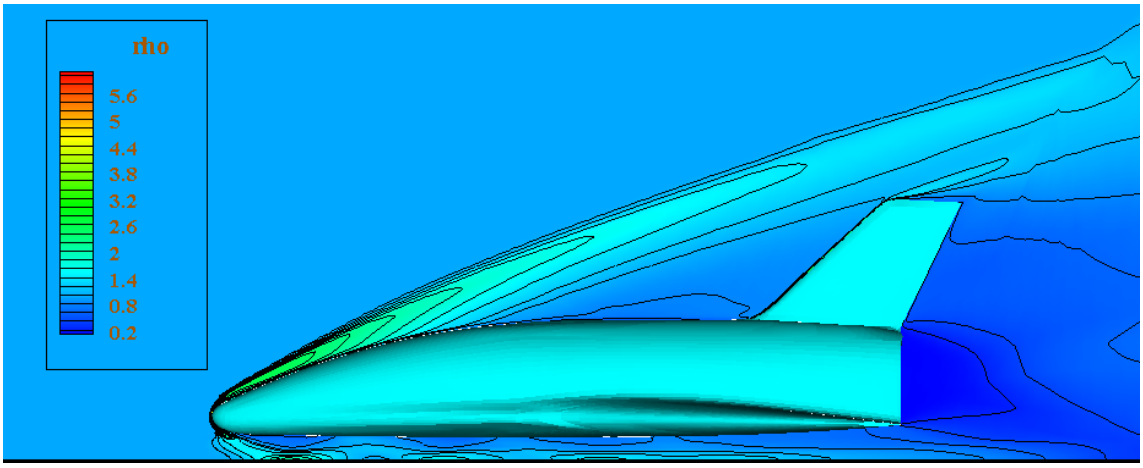

Figure 8.33: Contour of relative density ρ/ρ_∞
with $\Delta\alpha = 0°$, $M_\infty = 4.05$, and **h/L** = 0.0662 in inviscid flow.

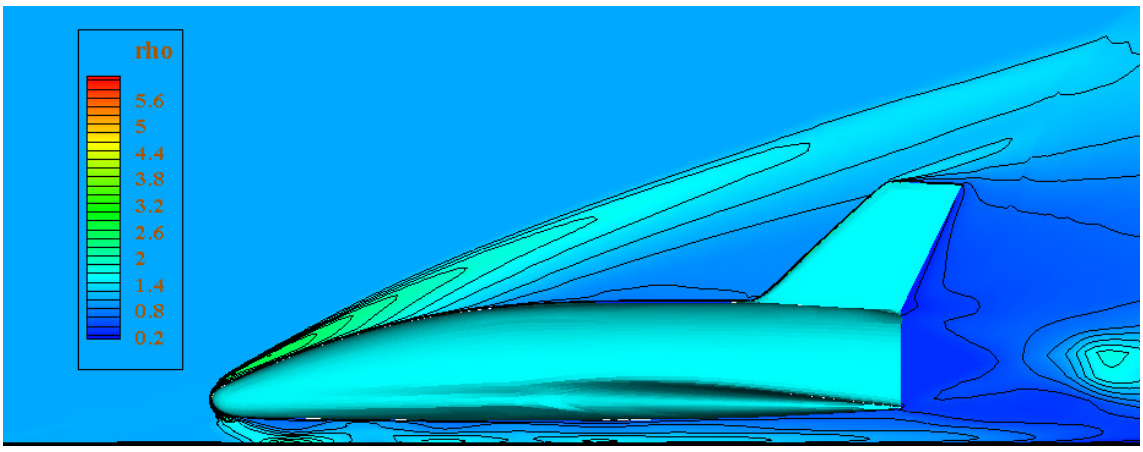

Figure 8.34: Contour of relative density ρ/ρ_∞
with $\Delta\alpha = 0°$, $M_\infty = 4.05$, and **h/L** = 0.0662 in laminar flow.

The contour plots of relative density ρ/ρ_∞ are used to illustrate the shock structures on the symmetry plane. In Figure 8.33 three impingements of the reflected bow shock on the lower surface of the EOS could be clearly seen in the inviscid flow. The shock angle between bow shock and the freestream is greater than that for the case with Mach 6.8. The flow field structures for the laminar

case are similarly presented in Figure 8.34. The most important aerodynamic properties are gathered in Table 8.4. The drag coefficients with Mach number of 4.05 are bigger than those with Mach number of 6.8. This is attributed to the different shock influences on the pressure field in the tail region. As expected, the drag coefficients in laminar flow are bigger than that in the inviscid flow.

	C_D	C_L	C_M
Navier-Stokes, $M_\infty = 4.05$	0.02933	0.03657	-0.01472
Euler, $M_\infty = 4.05$	0.02821	0.03531	-0.01485
Navier-Stokes, $M_\infty = 6.8$	0.02399	0.00985	-0.01059
Euler, $M_\infty = 6.8$	0.02286	0.00754	-0.01068

Table 8.4: Numerical lift-, drag-, and pitching moment- coefficients for the EOS with $\Delta\alpha = 0°$, and **h/L** = 0.0662.

Compare Figure 8.35 with Figure 8.18. With a greater shock angle, the bow shock passes through a short path to hit the flat plate. The shock dissipates its energy relatively little with a shorter path. In the same way, the impact on the lower surface of the EOS by the reflected shocks at Mach 4.05 dissipates less energy than the case at Mach 6.8. Then the peaks of the pressure coefficients at Mach 4.05 are much bigger than their counterparts at Mach 6.8. Its impingement points move upwind along the EOS lower side. The three pressure peaks at $M_\infty = 4.05$ are located on x/L =0.22, 0.43, and 0.66, respectively. Their correspond magnitudes of pressure coefficient peaks are 0.098, 0.061, and 0.052. In the case with $M_\infty = 6.8$, x/L = 0.26, 0.56, 0.89 and the magnitudes of pressure peaks are 0.070, 0.033, and 0.018 correspondingly. Its force components in the direction perpendicular to the freestream at Mach 4.05 are greater comparing to the case at Mach 6.8.

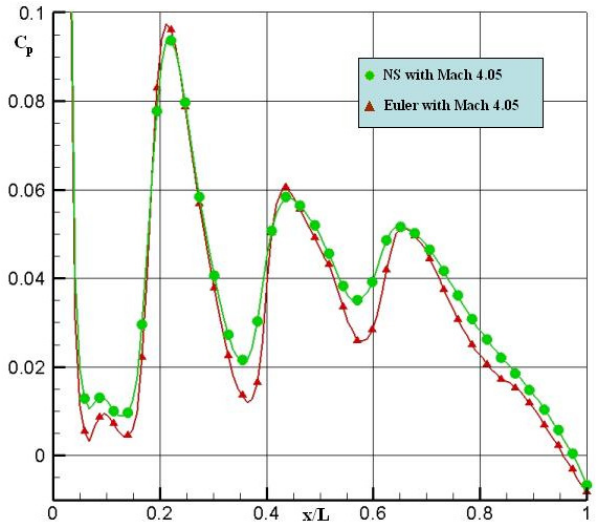

Figure 8.35: Pressure coefficients using laminar and inviscid flows on the lower surface of the EOS with y = 0, $M_\infty = 4.05$, $\Delta\alpha = 0°$, and **h/L** = 0.0662.

The lift coefficients at $M_\infty = 4.05$ are three times larger than those at $M_\infty = 6.8$. The pitching moment coefficients with a small Mach number are more negative than those at a big Mach number.

Further, the pitching moment coefficients in laminar flow are greater than their counterparts in inviscid flow.

8.5 Turbulence Simulation

In the separation process at Mach 6.8, the Reynolds number for the orbital stage $\mathrm{Re} = 3.24\times10^{7}$. It is already big enough to induce turbulent flows. Using the B-L turbulence model, a steady case for **h/L** = 0.1812 is simulated with the much refined grid (1.15 million nodes) at $\Delta\alpha = 0°$.

In Figure 8.36, the development of shock waves is described by the relative density on the symmetry plane. Because of the boundary layer and the big viscous effect, the shock waves on the upper side of the EOS become not very straight. They show some vorticity characteristics.

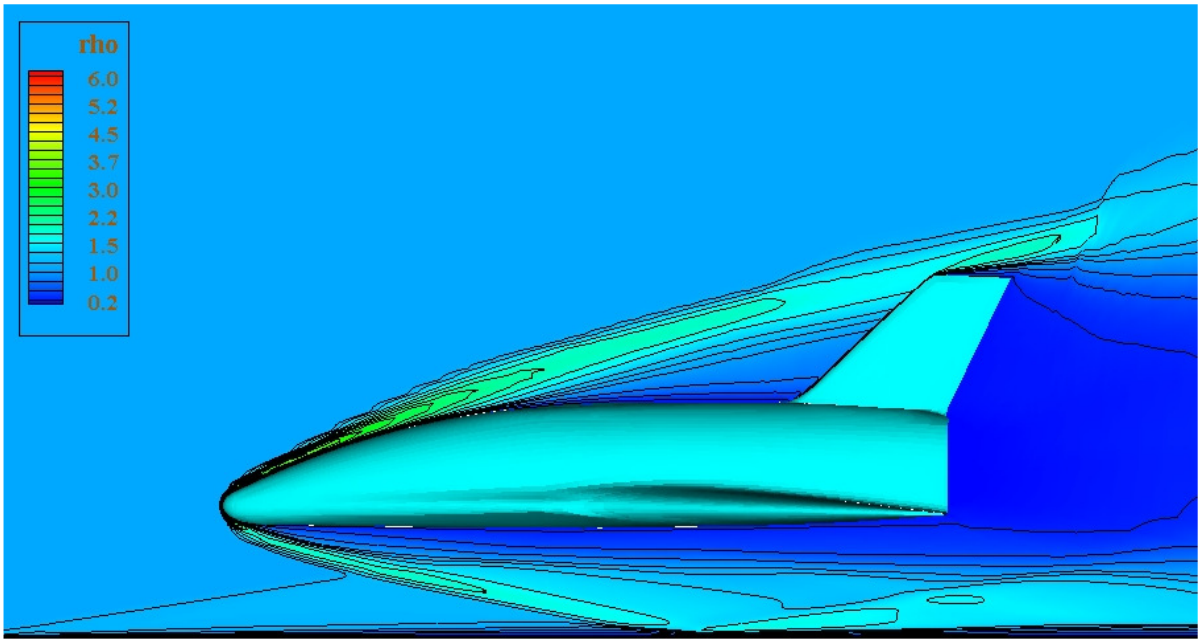

Figure 8.36: Contour of relative density ρ/ρ_{∞} using B-L model
with the much refined grid, $\Delta\alpha = 0°$, $M_{\infty} = 6.8$, and **h/L** = 0.1812.

On the lower side of the EOS, the flow field between the EOS and the flat plate becomes more complex. A weak shock wave is clearly generated from the beginning of the flat plate. It is a very weak oblique shock wave above the boundary layer and further intersects with the bow shock waves. Its compression ratio of the density ρ/ρ_{∞} is about 1.09 in a relative wide region. In Chapter 6.4, this value is 1.03 at Mach 4.05 also in a turbulence model. However, it is still weaker than ρ/ρ_{∞} of 1.29 in the case for laminar flow at Mach 7.9. Though this shock wave is still weak, the beginning position of the flat plate decides its intersection point to the bow shock and affects the aerodynamic results of the EOS.

The influence of the boundary layer on the flat plate becomes much bigger than the cases with laminar flow. The main reflected shock does not impinge lower surface of the EOS, but hits the wake zone. This increases the pressure and density in tail region.

In Table 8.5, the drag coefficient C_D simulated by the B-L model increases about 18% comparing

to that of the laminar model. That means that the friction in turbulent flow is much stronger than in laminar flow. Correspondingly, the lift coefficient C_L in turbulent flow increases about 20% and the pitching moment coefficient C_M changes less than 1%.

	C_D	C_L	C_M
Navier-Stokes, standard grid	0.02262	-0.01571	-0.00928
Euler, standard grid	0.02246	-0.01624	-0.00906
B-L model, much refined grid	0.02633	-0.01191	-0.00929

Table 8.5: Numerical lift-, drag-, and pitching moment- coefficients for the EOS with $\Delta\alpha = 0°$, $M_\infty = 6.8$, and **h/L** = 0.1812.

8.6 Unsteady Separation Process

For inviscid flow at Mach number of 6.8, an unsteady separation maneuver is simulated in the designed environment at the altitude of 35 km as described in the beginning of this chapter. More parameters about unsteady separation process are listed in Table 8.6.

Initial distance	**h/L** =0.0662
End distance	**h/L** =0.2562
Initial angle of attack	$\alpha_0 = 0^\circ$
Maximal angle of attack	$\alpha_{\max} = 5^\circ$
Reduced frequency	k_{red} =0.01
EOS length [m]	$L_{ref} = 28.8$

Table 8.6: The parameters describing the unsteady process.

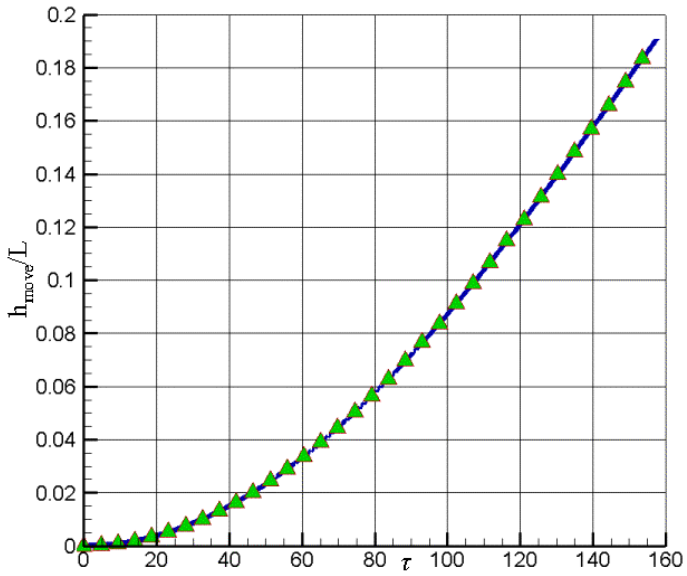

Figure 8.37: The separation distance $\mathbf{h_{move}/L}$ corresponding to τ in the unsteady separation process with k_{red} =0.01.

As discussed in section 6.2.3, the orbital stage is raised by a mechanical support mechanism from the carrier stage. At a proper position it will be released. This process could be described by the

simplified model as: the EOS is moved upwards turning its nose clockwise. The rotation center of the EOS is located at (0.65, 0, 0) at the beginning. Thereafter, the rotation center is fixed on the same position of the EOS, which is moving upwards. These changes of separation distance $\mathbf{h_{move}/L}$ and of the angle of attack α corresponding to the dimensionless time τ are depicted in Figures 8.37 and 8.38, respectively. Their dependences are the same formulas as in Eqs. (6.8) and (6.9).

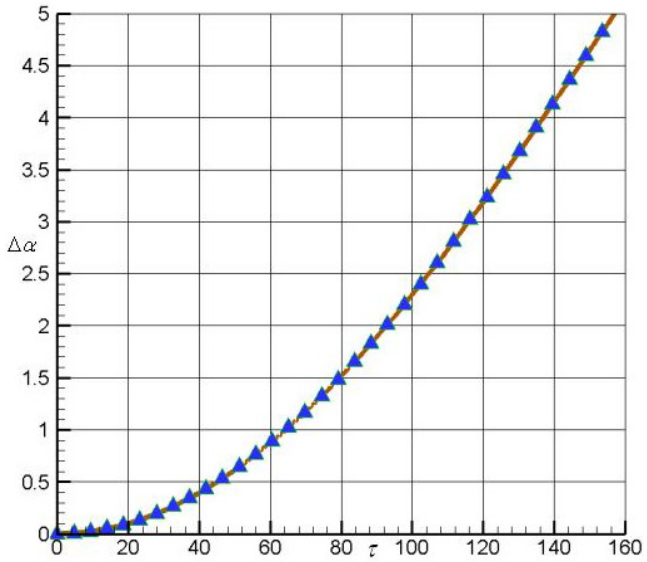

Figure 8.38: The angle of attack $\Delta\alpha$ [°] corresponding to the dimensionless time τ in the unsteady separation process with k_{red}=0.01.

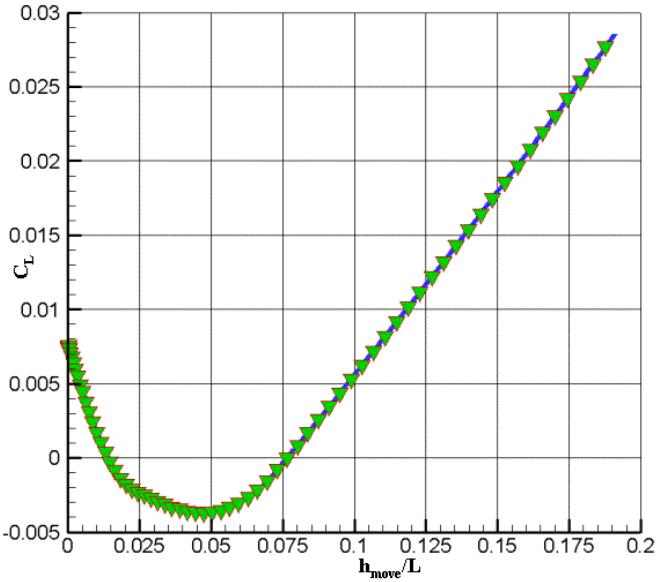

Figure 8.39: Lift coefficients in the separation process as function of $\mathbf{h_{move}/L}$ for the unsteady separation process in inviscid flow.

When the separation distance $\mathbf{h_{move}/L}$ increases, the space between the two stages becomes large and the flow field expands compared to the initial stage. The compression on the lower side of the EOS turns out to be weaker than before. As a result, the lift decreases from a positive value of 0.0075

to a negative value as described in Figure 8.39. This decrease tendency is converted until $\mathbf{h_{move}/L}$ is greater than 0.048. With the further increase of the angle of attack, the lift starts to increase. After the angle is greater than 2 degrees, the lift is positive again. This corresponds to the separation distance $\mathbf{h_{move}/L}$ =0.077. Since this point, the lift keeps positive.

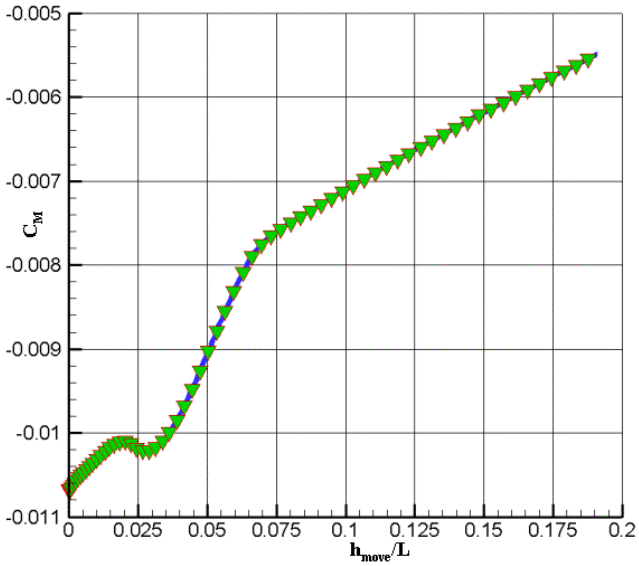

Figure 8.40: Pitching moment coefficients as function of $\mathbf{h_{move}/L}$ for the unsteady separation process in inviscid flow.

In Figure 8.40, the pitching moment always has negative values. It is harmful to the separation process, because it turns the nose of the orbital stage to the carrier stage and decreases the angle of attack. Consequently, it results in a decrease of lift. However, it shows that the absolute values of the pitching moment coefficients are very small. Accompanying the increase of distance $\mathbf{h_{move}/L}$, it becomes less negative.

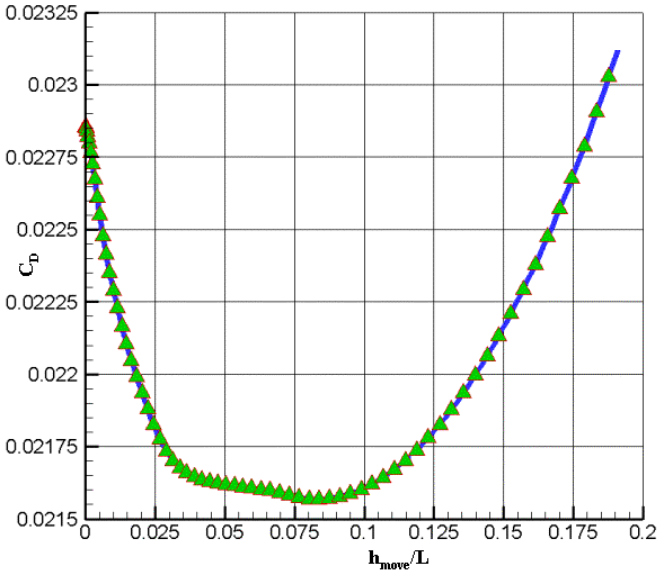

Figure 8.41: Drag coefficients $\mathbf{C_D}$ as function of $\mathbf{h_{move}/L}$ for the unsteady separation process in inviscid flow.

The drag coefficient fluctuates less than 7% for the whole separation process. Figure 8.41 presents a drag minimum corresponding to the angle of attack of 2.2 degrees or corresponding to the position $\mathbf{h_{move}/L}$ =0.083. The drag is dominated by the increase of the cross area relative to the freestream and by the transition of the pressure field on the tail region.

At M_∞=6.8, the relation between the separation distance $\mathbf{h_{move}/L}$ and the physical time t_{real} is presented in Eq. (6.10). Their dependences are visually shown in Figure 8.42. The distance $\mathbf{h_{move}/L}$ starts from zero to 0.19 corresponding to the total separation distance **h/L** from 0.0662 to 0.2562. It runs 1.426 seconds in the real environment. Similarly, the relation between the angle of attack and the physical time is described in Eq. (6.11).

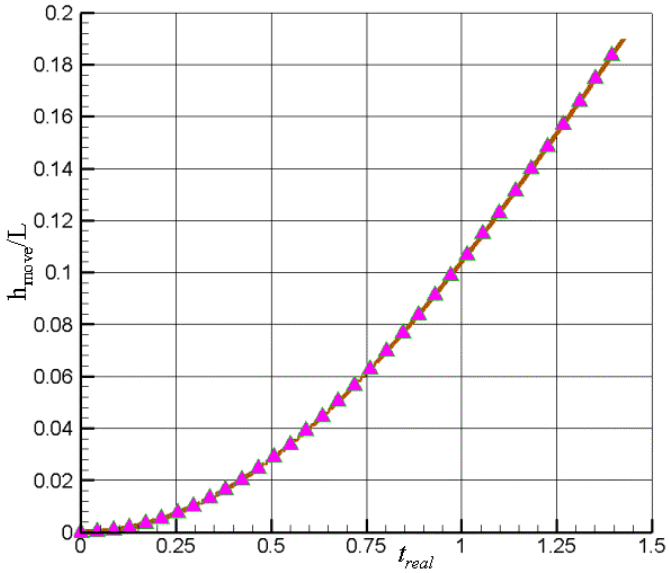

Figure 8.42: Separation distance $\mathbf{h_{move}/L}$ corresponding to time $\boldsymbol{t}_{\mathbf{real}}$ [s] in the unsteady separation process with k_{red}=0.01 and $M_\infty = 6.8$.

In Figure 8.43, a series of pictures are selected from the continuous separation process. They illustrate the development of the shock structure in this unsteady process. Every two pictures lapses with an interval of 0.23 seconds.

When the time refers to 0 second, it is the same picture as the steady case described in section 8.1.5 with **h/L** = 0.066. On the symmetrical plane there are three impingement points on the lower surface of the EOS, which are related to the reflected shocks. This three-impingement-structure sustains only to the next picture in Figure 8.43.

In the third picture of Figure 8.43, it is obvious only two reflected shock structures. Merely one reflected shock hits on the lower surface of the EOS in the fourth picture. From the fifth, the impingement point moves further downstream to the wake region. The reflected shock affects the pressure distribution weakly on the lower surface of the EOS. Nevertheless, they still affect the pressure distribution in the tail region. These influences could change the magnitude of the drag and the pitching moment.

From the above analysis about the lift for the EOS/flat plate model, we could conclude that the

orbital stage should be released with the angle of attack greater than 2 degrees, and its corresponding distance between the EOS and the flat plate is h/L=0.1432. Before this point, a strut system should hold two stages together. It adjusts the orbital stage to a desired posture, and finally releases the orbital stage.

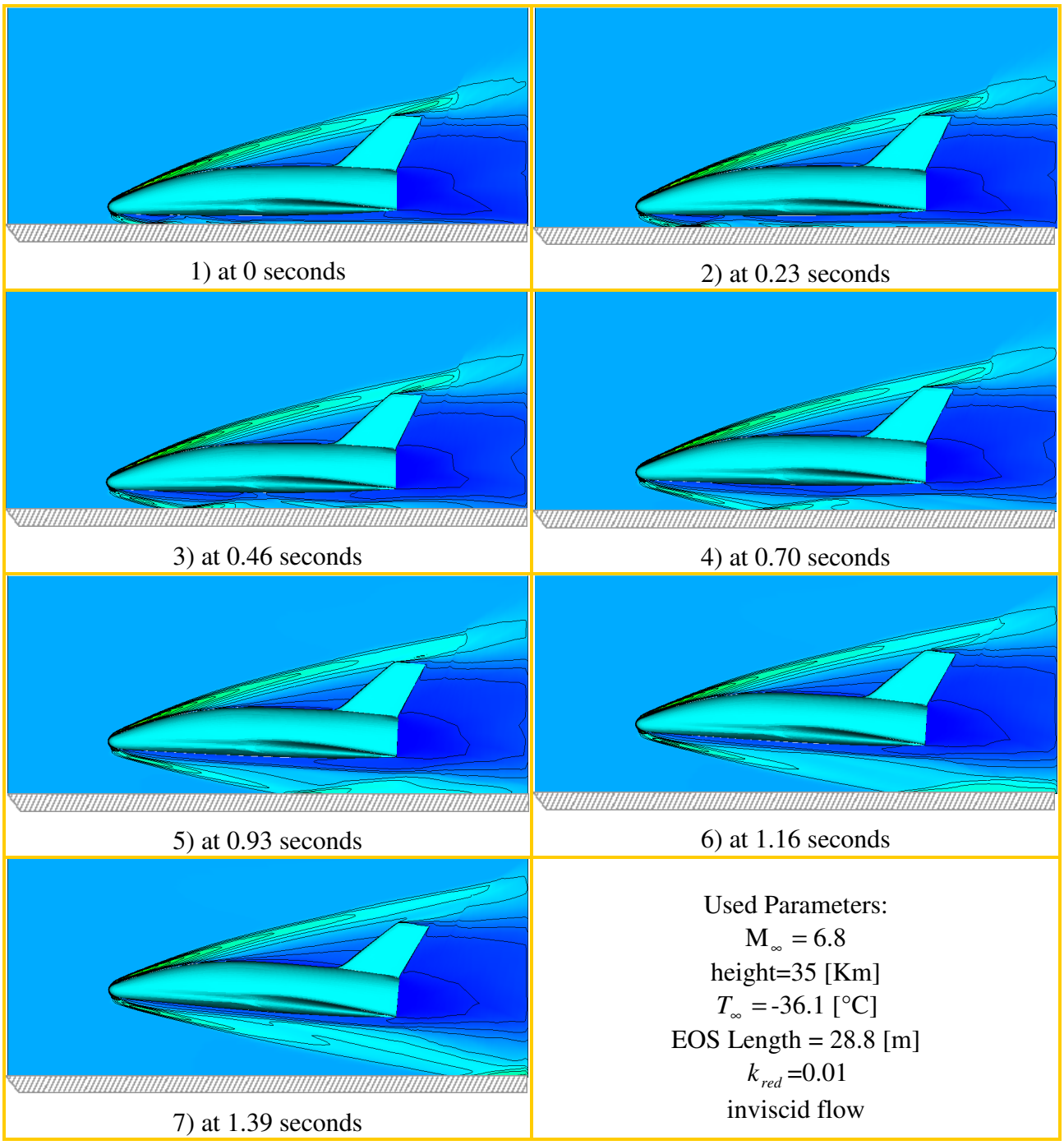

Figure 8.43: Shock structure in the designed separation environment at 35-kilometer altitudes in inviscid flow.

Though the release position could be selected to possess a positive lift, there is still a danger that the lift goes into a negative zone when the angle of attack becomes smaller. This danger originates from that the bow nose is turned anticlockwise by the negative pitching moment. To overcome the

negative pitching moment, the angle of attack could be chosen large enough. Consequently, the lift will not fall into negative zone in the whole separation process, even if the negative pitching moment could alter the angle of attack to be smaller. Another possibility is installing some extra equipment, such as elevator, flaps, and etc. The auxiliary equipment will revise the negative pitching moment.

9 Conclusion

To study the aerodynamic properties of the TSTO vehicle in separation processes, the software FLMNAV is developed especially for hypersonic flow. Corresponding to the experiments performed in the supersonic wind tunnel T-313 at ITAM SB RAS and in the hypersonic shock tunnel TH2-D at RWTH Aachen, a series of separation processes have been numerically simulated. The experimental results are used not only to analyze the separation process, but also to validate the software FLMNAV. Though there is no experimental data for the designed environment, it is still numerically researched that the TSTO vehicle separates at Mach 6.8 and at a height of 35 kilometers above the sea level.

The Navier-Stokes equation system is used to describe the separation process. Its numerical discretization associated with FLMNAV is based on the finite-volume approximation. The modified AUSM and MUSCL schemes are applied for the convection terms. The modified AUSM is a combined method of Advection Upstream Splitting Method and Upwind Flux-Vector Splitting Method. According to the characteristics of shock and slip line, the software could be inclined to UFVSM or AUSM automatically. The modified AUSM is good at catching the strong shock and describing boundary layers. The first order of spatial accuracy is achieved in the regions with strong shocks and in boundary layers with dramatic changes of the aerodynamic properties. The second order of spatial accuracy could be reached in the other regions. The diffusive flux vectors are discretized by the Chakravarthy method, which is of the 2^{nd} order accuracy in space. The time discretization possesses the 1^{st} order accuracy.

To benefit from the body-fitted mesh, the Cartesian coordinate system must be transformed into curvilinear system. All of the equations and the boundary conditions must be also transformed. Characteristic boundary conditions are applied for the Navier-Stokes equation system. Time-develop technique is also utilized to obtain the solution of steady cases. The steady solutions not only assign the initial values for the unsteady cases, but also provide most of the information for the aerodynamic design. Numerical iteration techniques are applied to solve these steady and unsteady separation cases.

The initial geometry and body-fitted meshes are generated by the software package ICEMCFD, and their orthogonality and smoothness are further improved by the in-house software GRIDFLM. According to the characteristics of supersonic and hypersonic flows, a very compact computational domain around the orbital stage is confined to save computational effort. Four grids with different resolution are utilized in the numerical simulations.

The aerodynamic properties are studied with a variety of Mach numbers, angles of attack, and separation distances between carrier and orbiter. In different simulations the carrier stages are idealized as flat plates and the orbital stages are considered as the EOS geometries, which are delta wing space vehicles. The inviscid, laminar, and turbulent models are investigated to show the influence of different flows.

Comparing to the available experiments performed in wind tunnel T-313 and in tunnel TH2-D, the computational results agree well with the experimental results in most of the cases, especially for

the cases at Mach 4.05. The numerical methods mentioned above are suitable to simulate the flow physics associated with the two-stage separation process. It also indicates that the code FLMNAV can provide aerodynamic properties in describing the separation process with an acceptable accuracy.

In majority, the NS simulations approach the experimental data closer than Euler simulations. The contour of the relative density in inviscid flow presents very clear shock structures between the two stages. The pressures generated by the shock waves in laminar flow are usually greater than that in inviscid flow. The turbulent flow results in a much thicker boundary layer as well as an increased drag of the orbital stage at Mach 6.8.

In the case with high Mach number 7.9 as well as turbulent flow, radical changes of the physical properties between the two stages lead to a very slow numerical convergence. The convergence depends significantly on the mesh quality. If the solution system is sorted with the expenditure of computing time, then Baldwin-Lomax turbulent model spends the most CPU time. The Navier-Stokes system and the Euler system rank the second and the third. The software FLMNAV still needs to be improved, when it is applied for cases with higher Mach number, with turbulent flow, with complex geometry, as well as with unsteady process.

All of the numerical and experimental results illustrate that a bow shock is formed around the blunt nose of the orbital stage. The greatest relative density in this bow shock can be compressed to a magnitude of about 6.5 times as great as that of the freestream at the Mach 7.9. The shock wave stretched somewhat like a curved cone to the downstream. Its lower part hits the upper surface of the carrier stage, and then is reflected back to the lower surface of the orbital stage. With a small separation distance, the shock waves may rebound many times between the two stages. Assuming that the separation distance **h/L** is smaller than 0.0662, the lower surface of the EOS is hit three times by the shock waves reflected from the lower stage for the case of Mach 6.8. These impacts yield pressure peaks on the impingement points. Therefore, the shock waves dominate the lift and pitching moment of the orbital stage remarkable. In the wake zone of the orbital stage, the fluid expands very much. The shock waves reflected by the carrier stage could hit the wake region. It could change the pressure distribution in this wake region significantly. The boundary layer becomes thicker, when the Mach number of the freestream increases. The great friction on the flat plate in the viscous flow forms a slope of boundary layer. It could result to a weak oblique shock wave at a great Mach number. This shock wave stretches downwards and further intersects the bow shock wave. The shock structures could be altered by a different beginning position of the flat plate. This is also true even if considering the separation at a small Mach number, but for turbulent flow.

For a very small separation distance between the two stages, the lift coefficients are positive for the orbital stage. The lift decreases with the increase of the separation distance. It could even become negative with a greater distance. The angle of attack also influences the aerodynamic properties dramatically. When the angle of attack of the orbital stage is bigger than 2 degrees, the lift coefficients could be positive. Unfortunately, the pitching moment coefficients are always negative in all investigated cases. When the EOS moves closer to the flat plate, the lift coefficient will increase. Consequently, the aerodynamic force tends to separate the two stages automatically. But the pitching

moment coefficient becomes more negative in this process. This means that the nose of the orbital stage may turn down to the carrier stage and decrease the angle of attack. Therefore, it is very important to set the orbital stage at a certain angle of attack to achieve a positive lift when carrier releases the orbiter. In the separation process, the negative pitching moment should not turn the nose down to an angle, with which the lift becomes negative.

It is suggested that a strut system fixes the orbital stage to carrier stage. It raises the orbital stage to the starting separation position with an angle of attack greater than 2 degrees with a moderate separate velocity. This incidence should assure that the lift would not become negative in the whole separation process, although the negative pitching moment may reduce that angle. Some carefully designed elevators, flaps or other equipment could be used to adjust the pitching moment. By setting these apparatuses properly, the whole orbital stage may obtain a suitable pitching moment characteristics. Together with a positive lift, two stages could be separated safely by the aerodynamic properties in the designed environment.

References

[1] **Abbott, M. B.; Basco, D. R.:**
Computational Fluid Dynamics, an Introduction for Engineers, Longman Scientific & Technical, 1989.

[2] **Aftosmis, M. J.; Berger M. J.; Alonso J. J.:**
Applications of a Cartesian Mesh Boundary-Layer Approach for Complex Configurations, 44th AIAA Aerospace Sciences Meeting, Reno NV, January 9-12, 2006, AIAA 2006-0652.

[3] **Allen, J. E.:**
Aerodynamics, the Science of Air in Motion, Granada, 1982.

[4] **Anderson, Jr. J. D.:**
Computational Fluid Dynamics, the Basics with Application, McGraw-Hill, Inc., 1995.

[5] **Anderson, Jr. J. D.:**
Fundamentals of Aerodynamics, McGraw-Hill, Inc., 2001.

[6] **Anderson, Jr. J. D.:**
Hypersonic and High Temperature Gas Dynamics, McGraw-Hill, Inc., 1989.

[7] **Baldwin, B. S.; Lomax, H.:**
Thin Layer Approximation and Algebraic Model for Separated Turbulent Flows, AIAA paper 78-0257, Huntsville, AL, 1978.

[8] **Bernot, P. T.:**
Abort Separation Study of a Shuttle Orbiter and External Tank at Hypersonic Speed, NASA TM X-3212, May 1975.

[9] **Bonnefond, T.; Adamov, N. P.; Brodetsky, M. D.; Vasenyov, L. G.; Derunov, E. K.; Kharitonov, A. M.:**
An Experimental Investigation of Aerodynamic Interference of STO Winged during Separation, J. Thermophysics and Aeromechanics, Vol. 3, No. 3 and No. 4, 1996.

[10] **Bonnefond, T.; Kharitonov, A. M.; Brodetsky, M. D.; Vasenyov, L. G.; Adamov, N. P.; Derunov, E. K.:**
Separation of Winged Vehicles in Supersonic, AIAA-95-6092, 6th International Aerospace Planes and Hypersonic Technologies Conference, 3-7 April 1995.

[11] **Breitsamter, C.:**
Aerodynamic High-Speed Measurements on EOS/Flat Plate Configuration, ITAM Reference Measurements on EOS/Flat Plate Interference, Internal Document of SFB 255, Jan. 2003.

[12] **Breitsamter, C.; Jiang, L.; Moelyadi, M. A.:**
DFG-Abschlussbuch zu den Hyperschall Sonderforschungsbereichen SFB 253, SFB 255 und SFB 259, Wiley-Vch, 2003.

[13] **Breitsamter, C.; Laschka, B.; Jiang, L.; Moelyadi, M. A.; et al.:**
Aerodynamics and Thermodynamics, Basic Research and Technologies for Two-Stage-to-Orbit Vehicles, Wiley-Vch Verlag GmbH & Co. KGaA, Mai 2005, ISBN 3-527-27735-8.

[14] **Brenner, P.:**
Numerical Simulation of Three Dimensional and Unsteady Aerodynamics about Bodies in Relative Motion Applied to a TSTO Separation, AIAA Paper 93-5142, 1993.

[15] **Burgess, E. G. III; Lewis, C. H.:**
Empirical Equations for the Thermodynamic Properties of Air and Nitrogen to $15000^0\,K$, AEDC-TDR-63-138, July 1963.

[16] **Burkhardt, J.; Gräßlin, M.; Schöttle, U. M.:**
Impact of Mission Constraints on Optimal Flight Trajectories for the Lifting Body X-38, AIAA Paper 99-4167, AIAA atmospheric Flight Mechanics Conference, Portland, Oregon, Aug. 1999.

[17] **Cebeci T.; Shao J. P.; Kafyeke F.; Laurendeau E.:**
Computational Fluid Dynamics for Engineers, Horizons Publishing Inc., 2005.

[18] **Cercignani, C.:**
Rarefied Gas Dynamics: From Basic Principles to Actual Calculations, Cambridge Univ. Press, Cambridge, 2000.

[19] **Chakravarthy, S.-R.:**
High-Resolution Upwind Formulations for the Navier-Stokes Equations, Computational Fluid Dynamics, Lecture Series 1988-05, 1988.

[20] **Cvrlje, T.:**
Abschlußbericht des SFB 255, Projekt A1: Instationäre Aerodynamik des Separationsvorgangs zwischen Träger und Orbiter, TUM-FLM-2001/7, Lehrstuhl für Fluidmechanik, Technische Universität München, Juli 2001.

[21] **Cvrlje, T.:**
Instationäre Aerodynamik des Separationsvorgangs zwischen Träger und Orbiter, Dissertation, Technische Universität München, Dez. 2001.

[22] **Cvrlje, T.; Breitsamter, C.; Heller M.; Sachs G.:**
Lateral Unsteady Aerodynamics and Dynamic Stability Effects in Hypersonic Flight, International Conference on Methods of Aerophysical Research – ICMAR 98 Novosibirsk (Russia), June 1998.

[23] **Cvrlje, T.; Breitsamter, C.; Laschka, B.:**
Unsteady and Coupling Aerodynamic Effects on the Lateral Motion in Hypersonic Flight, AIAA Paper 99-4832, 9th International Space Planes and Hypersonic Systems and Technologies Conference, Norfolk (VA), USA, Nov. 1-5, 1999.

[24] **Cvrlje, T.; Breitsamter, C.; Weishäupl, C.; Laschka, B.:**
Euler and Navier-Stokes Simulations of Two-Stage Hypersonic Vehicle Longitudinal Motions, Journal of Spacecraft and Rockets, Vol. 37, No. 2, 2000, pp. 242-251.

[25] **Decker, J. P.; Gera, J.:**
An Exploratory Study of Parallel-Stage Separation of Reusable Launch Vehicles, NASA TN D-4765, 1968.

[26] **Decker, K.:**
Aerodynamik eines zweistufigen Raumtransportsystems beim Wiedereintritt und während der Separation. Dissertation, Technische Universität München, Dez. 2003.

[27] **Decker, K.:**
Glätten von strukturierten Multiblockgittern über Blockgrenzen, Bericht, Lehrstuhl für Fluidmechanik, Technische Universität München, 2003.

[28] **Decker, K.; Laschka, B.:**
Unsteady Aerodynamics of a Hypersonic Vehicle during a Separation Phase, AIAA Paper 2001-1852, 10th International Space Planes and Hypersonic Systems and Technologies Conference, Kyoto, Japan, April 124-27, 2001.

[29] **Degani, D.; Schiff, L. B.:**
Computation of Turbulent Supersonic Flows About Pointed Bodies Having Crossflow Separation, Journal of Computational Physics, vol. 66, pp. 183–196, Sept. 1986.

[30] **Eberle, A.; Rizzi, A.; Hirschel, E. H.:**
Numerical Solutions of the Euler Equations for Steady Flow Problems, Notes on Numerical Fluid Mechanics and Multidisciplinary Design, Vol. 34, Vieweg, 1992.

[31] **Esch, H.:**
Kraftmessungen zur Stufentrennung am MBB-Sängerkonzept bei M_∞=6 im Hyperschallkanal H2K, Forschungsbericht DLR-IB-39113-90C18, 1990.

[32] **Ferziger, J. H.; Peric, M.:**
Computational Method for Fluid Dynamics, 3rd Edition, Springer, 2002.

[33] **Fielding, J. P.:**
Introduction to Aircraft Design, Cambridge University Press, 1999.

[34] **Fletcher, C. A. J.:**
Computational Techniques for Fluid Dynamics, Springer, 1997.

[35] **Freeman, D.; Reubush, D.; McClinton, C.; Rausch, V.; Crawford, L.:**
The NASA Hyper-X Program, IAF-97-V.4.07, 48th International Astronautical Congress, Turin, Italy, Oct. 1997.

[36] **Gao T.; Tseng Y.; Lu X.:**
An Improved Hybrid Cartesian/Immersed Boundary Method for Fluid–Solid Flows, Int. J. Numer. Meth. Fluids 2007, 55:1189–1211.

[37] **Glößner, C.:**
Druck- und Wärmestromverteilung und aerodynamische Beiwerte auftriebsgestützter Wiedereintrittskörper, Arbeits- und Ergebnisbericht, Sonderforschungsbereich 253, Juni 2001.

[38] **Habermann, M.; Olivier, H.:**
Upgrade of the Aachen Shock Tunnel with a Detonation Driver Shock Wave Laboratory, ICMAR 2000, in Novosibirsk, Russia, July 9-15, 2000.

[39] **Hauser, Th.:**
Hyperschallströmungen um stumpfe Kegel bei externen wellenartigen Störungen, Dissertation, Technische Universität München, 1997.

[40] **Heller, G.:**
Aerodynamik von Deltaflügelkonfigurationen bei Schieben und Gieren, Dissertation, Technische Universität München, 1997.

[41] **Hilsenrath, I.; Klein, M.:**
Tables of Thermodynamic Properties of Air in Chemical Equilibrium Including Second Virial Corrections from $1500^0\,K$ *to* $15000^0\,K$, AEDC-tr-65-58, 1965.

[42] **Hirsch, Ch.:**
Numerical Computation of Internal and External Flows, Vol. 1: Fundamentals of Numerical Discretization, John Wiley & Sons, 1988.

[43] **Hirsch, Ch.:**
Numerical Computation of Internal and External Flows, Vol. 2: Computational Methods for Inviscid and Viscous Flows, John Wiley & Sons, 1988.

[44] **Hirschel, E. H.:**
The Technology Development and Verification Concept of the German Hypersonic Technology Programme, Aerothermodynamics and Propulsion Integration for Hypersonic Vehicles, AGARD-R-813, pp. 12-1-12-15, Oct. 1996.

[45] **Hoffmann, K. A.; Chiang, S. T.:**
Computational Fluid Dynamics, Vol. I-III, Engineering Education System, Fourth Edition, 2000.

[46] **Humphrey, R. L.; Neel, C. A.:**
Tables of Thermodynamic Properties of Air from $90^0\,K$ *to* $1500^0\,K$, AEDZ-TN-61-103, 1961.

[47] **Iatrou, M.; Weishäupl, C.; Laschka, B.:**
Entwicklung eines instationären Navier-Stokes-Verfahrens bei kleinen Störungen für aeroelastische Problemstellungen, FLM-TUM-2002/09, Lehrstuhl für Fluidmechanik, Technische Universität München, 2002.

[48] **Jiang, L.; Breitsamter, C.; Laschka, B.:**
Numerical Simulation of the Stage Separation Flow Physics of an Idealized Two Stage Space Transport Vehicle, Jahrbuch der Deutschen Gesellschaft für Luft- und Raumfahrt – Lilienthal-Oberth e.V., DGLR-JT2003-131, Deutscher Luft- und Raumfahrtkongress / DGLR-Jahrestagung, München, Nov. 17-20, 2003.

[49] **Jiang, L.; Breitsamter, C.; Laschka, B.:**
Numerical Simulation of the Unsteady Separation Process for a Two-Stage Space Transport System, Computational Mechanics, WCCM VI in conjunction with APCOM'04, Sept. 5-10, 2004, Beijing, China.

[50] **Jiang, L.; Moelyadi, M. A.; Breitsamter, C.:**
Aerodynamic Investigations on the Unsteady Stage Separation of a TSTO Space Transport System, FLM-TUM-2003/34, Lehrstuhl für Fluidmechanik, Technische Universität München, 2003.

[51] **Jiang, L.; Zähringer, C.; Breitsamter, C.; Sachs, G.:**
Experimentelle und numerische Simulationen zur Konfiguration „EOS/ebene Platte", Seminar des Sonderforschungsbereichs 255, 12. Dez. 2002, München, Tagungsband ISBN 3-89791-334-8, Technische Universität München, pp. 21-36, 2004.

[52] **John, J. E. A.; Haberman, W. L.:**
Introduction to Fluid Mechanics, Third Edition, Prentice-Hall, 1988.

[53] **Kermode, A. C.:**
Mechanics of Flight, Ninth (Metric) Edition, Longman Scientific & Technical, 1987.

[54] **Kharitonov, A.; Brodetsky, M.; Vasenyov, L.; Adamov, L.; Breitsamter, C.; Heller, M.:**
Investigation of Aerodynamic Characteristic of the Models of a Two-Stage Aerospace System during Separation, Final Report, Institute of Theoretical and Applied Mechanics, Russian Academy of Sciences, Siberian Division, Novosibirsk, Russia, and Lehrstuhl für Fluidmechnik and Lehrstuhl für Flugmechnik und Flugreglung, Technische Universität München, Nov. 2000.

[55] **Kreiselmaier, E.:**
Berechnung instationärer Tragflügelumströmungen auf der Basis der zeitlinearisierten Eulergleichungen, Dissertation, Technische Universität München, 1998.

[56] **Kuczera, H.; Hauck, H.; Krammer, P.; Sacher, P. W.:**
The German Hypersonics Technology Programme-Status 1993 and Perspectives, AIAA Paper 93-5159, Nov. 1993.

[57] **Kuczera, H.; Johnson, C.:**
The Major Results of the FESTIP System Study, AIAA 9th International Space Planes and Hypersonic Systems and Technologies Conference, Norfolk, Virginia, Nov. 1999.

[58] **Kuethe, A. M.; Chow, C.-Y.:**
Fundamentals of Aerodynamics, Bases of Aerodynamic Design, Wiley & Sons, November 1997.

[59] **Laschka, B.:**
Instationäre Aerodynamik I/II, Vorlesungsskript, Lehrstuhl für Fluidmechanik, Technische Universität München, 1996.

[60] **Laschka, B.:**
Grundlagen Instationärer Strömungen, Vorlesungsskript, Lehrstuhl für Fluidmechanik, Technische Universität München, 1991.

[61] **Laschka, B.:**
Strömungsmechanik I/II, Vorlesungsskript, Lehrstuhl für Fluidmechanik, Technische Universität München, 1995.

[62] **Laschka, B.; Breitsamter, C.:**
Transatmosphärische Flugsysteme – Grundlagen der Aerothermodynamik, Antriebe und Flugmechanik, Sonderforschungsbereich 255, Juni 2001.

[63] **Laurent, S.:**
Towards a Low Risk Airbreathing SSTO Program: A Continuous Robust PREPHA-Based TSTO, AIAA Paper 99-4946, AIAA 9th International Space Planes and Hypersonic Systems and Technologies Conference, Norfolk, Virginia, Nov. 1999.

[64] **Lewis, C. H.; Neel, C. A.:**
Specific Heat and Speed of Sound Data for Imperfect Air, AEDC-TDR-64-36, 1964.

[65] **Li, X. M.:**
Hydrodynamics (in Chinese), Ocean University of Qingdao, 1996.

[66] **Liou, M.-S.; Steffen, Ch.:**
A New Flux Splitting Scheme, Journal of Computational Physics, Vol. 107, pp. 23-39, 1992.

[67] **Marconi, F.; Salas, M. D.; Yaeger, L. S.:**
Development of a Calculating the Steady Super/Hypersonic Inviscid Flow around Real Configurations, NASA CR-2675, 1976.

[68] **McCormick, B. W.:**
Aerodynamics, Aeronautics, and Flight Mechanics, second Edition, John Wiley & Sons, Inc., 1995.

[69] **Moelyadi, M. A.; Jiang, L.; Breitsamter, C.:**
Investigation of Steady and Unsteady Flow Characteristics of Space Transport System During Separation, AIAA-2005-3248, AIAA/CIRA 13th International Space Planes and Hypersonic Systems and Technologies Conference, Capua, Italy, May 16-20, 2005.

[70] **Moretti, G.; Abbett, M.:**
A Time–Dependent Computational Method for Blunt Body Flows, AIAA J., vol. 4, no. 12, pp. 2136-2141, December 1966.

[71] **Mukovozov, M. V.:**
Method for Determining Interference Components of Aerodynamic Characteristics of Aircrafts Integrated with a Body of Revolution at Mach 3 and 6, Applied Problem of Aeromechanics and Geo-Cosmic Physics, Moscow, 1990, p.73.

[72] **Oertel, H. Jr.:**
Aerothemodynamik, Springer, 1994.

[73] **Oertel, H. Jr.; Laurien, E.:**
Numerische Strömungsmechanik, Springer-Verlag, New York, Berlin, Heidelberg, 1995.

[74] **Olivier, H.; Grönig, H.:**
The Aachen Shock Tunnel TH2, Report of Shock Wave Laboratory, Aachen, 1995.

[75] **Peskin C. S.:**
The Immersed Boundary Method, Acta Numerica (2002), pp. 479-517.

[76] **Qu, Zh. H.; Liu, W.; Zong, M.; Liu, J.:**
Hypersonic Aerodynamics (in Chinese), National University of Defense Technology, 2001.

[77] **Radespiel, R.; Kroll, N.:**
Accurate Flux Vector Splitting for Shock and Shear Layers, Journal of Computational Physics, Vol. 121, pp. 66-78, 1995.

[78] **Radespiel, R.; Kroll, N.:**
An Improved Flux Vector Split Discretization Scheme for Viscous Flows, Forschungsbericht DLR-FB 93-53, 1993.

[79] **Rochholz, H.:**
Eulerlösungen für den Separationsvorgang von Träger/Orbitersystemen im Hyperschall, Dissertation, Technische Universität München, 1994.

[80] **Rochholz, H.; Huber, T.; Matyas, F.:**
Unsteady Airloads during Separation of an Idealized Two-Stage Hypersonic Vehicle, Zeitschrift für Flugwissenschaften und Weltraumforschung, Band 19, Heft 1, pp.2-9, 1995.

[81] **Russo, G.:**
Next Generation Space Transportation System, Aerotecnica Missili e Spazio, Vol. 81, Feb. 2002.

[82] **Schröder, W.; Behr, R.; Menne, S.:**
Analysis of Hypersonic Flows around Space Transportation System via CFD Methods, AIAA Paper 93-5067, 1993.

[83] **Sonar, Th.:**
Grid Generation Using Elliptic Partial Differential Equations, Forschungsbericht, DFVLR-FB 89-15.

[84] **Su, M. D.; Huang, S. Y.:**
The Foundation of Computational Fluid Mechanics (in Chinese), Qinghua University, 1997.

[85] **Tannehill, J. C.; Mugge, P. H.:**
Improved Curve Fits for the Thermodynamic Properties of Equilibrium Air Suitable for Numerical Computation Using Time-Dependent or Shock-Capturing Methods, NASA CR-2470, 1974.

[86] **Thompson, J. F.; Soni, B. K.; Weatherill, N. P.:**
Handbook of Grid Generation, CRC Press LLC, 1999.

[87] **United States Committee on Extension to the Standard Atmosphere:**
U.S. Standard Atmosphere, 1976, National Oceanic and Atmospheric Administration, National Aeronautics and Space Administration, United States Air Force, Washington D.C., 1976.

[88] **Van Leer, B.:**
Flux-Vector Splitting for the Euler Equations, Lecture Notes in Physics, Vol. 170, Springer-Verlag, pp. 507, 1982.

[89] **Van Leer, B.; Thomas, J. L.; Roe, P. L.; Newsome, R. W.:**
A Comparison of Numerical Flux Formulas for the Euler and Navier-Stokes Equations, AIAA Paper 87-1104, 1987.

[90] **Vinci, L.:**
Space Planes – An Advanced Means of Space Transportation, Tenth Blue Book, Delft, 1995.

[91] **Wang, Ch. Sh.; Zhang, H. W.:**
Flow Field Measurement of the Reduced Space Shuttle Model, Experiments and Measurements in Fluid Mechanics, Vol. 13, No 1, Mar., 1999.

[92] **Weiland, C.:**
Stage Separation Aerodynamics, Aerothermodynamics and Propulsion Integration for Hypersonic Vehicles, R-813, AGARD, pp 11-1-11-28, 1996.

[93] **Weiland, C.; Pfitzner M.:**
3-D Euler Solution For Hypersonic Mach Numbers, AGARD-CP 428, Paper No. 22, Bristol - U.K. 1987.

[94] **Wendt, J. F.:**
Computational Fluid Dynamics, an Introduction, Springer-Verlag, 1992.

[95] **Whitfield, D. L.; Janus, J. M.:**
Three-Dimensional Unsteady Euler Equation Solution Using Flux Vector Splitting, AIAA Paper 84-1552, 1984.

[96] **Yang, H.:**
The Foundation of Fluid Mechanics (in Chinese), Department of Dynamics, the University of Aeronautics and Astronautics of Peking, 1993.

[97] **Yee, H. C.:**
Upwind and Symmetric Shock-Capturing Schemes, NASA TM-89464, May 1987.

[98] **Yuang, S. X.:**
Engineering Fluid Mechanics (in Chinese), Petroleum Industry Publishing Company, 2005.

[99] **Zähringer, C.; Breitsamter, C.; Sachs, G.; Laschka, B.:**
Windkanalversuche zum Trennvorgang eines zweistufigen Hyperschall-Flugsystems, Jahrbuch der Deutschen Gesellschaft für Luft- und Raumfahrt – Lilienthal-Oberth e.V., DGLR- JT2001-165, Deutscher Luft- und Raumfahrtkongress / DGLR- Jahrestagung, Hamburg, September 17-20, 2001.

[100] **Zeeuw D. D.; Powell K. G.:**
An Adaptively Refined Cartesian Mesh Solver for the Euler Equations, J. of Computational Physics, 104, 56-68 (1993).

[101] **Zhang, X. M.; Ren, Z. P.; Mei, F. M.:**
Heat Transfer (in Chinese), Third Edition, China Architecture & Building Press, 1993.

APPENDICES

A Vector Operation

The Navier-Stokes equation system, the Euler equation system, the turbulence model, and their boundary conditions involve high level of generality and high degree of abstraction. To express them clearly and shortly, vectors and tensors are intensively used in this thesis. Their definitions and operations are collected in this section as some useful mathematical tools.

In Cartesian orthogonal coordinate system, the unit vectors of x, y, z axes are defined as $\vec{e}_x, \vec{e}_y, \vec{e}_z$, respectively. Any two vectors $\vec{a}$ and $\vec{b}$ in this coordinate system could be expressed as

$$\vec{a} = a_x \cdot \vec{e}_x + a_y \cdot \vec{e}_y + a_z \cdot \vec{e}_z = (a_x, a_y, a_z)^T, \tag{A.1}$$

and

$$\vec{b} = b_x \cdot \vec{e}_x + b_y \cdot \vec{e}_y + b_z \cdot \vec{e}_z = (b_x, b_y, b_z)^T. \tag{A.2}$$

Given the angle θ between $\vec{a}$ and $\vec{b}$, the scalar product between two vectors is defined as

$$\vec{a} \bullet \vec{b} = a_x \cdot b_x + a_y \cdot b_y + a_z \cdot b_z = |\vec{a}| \cdot |\vec{b}| \cdot \cos\theta, \tag{A.3}$$

where $|\vec{i}| = \sqrt{i_x \cdot i_x + i_y \cdot i_y + i_z \cdot i_z}$, for $i = a, b$.

Related with the area of the parallelogram based with the above two vectors, the vector product is presented as

$$\vec{a} \times \vec{b} = \begin{bmatrix} \vec{e}_x & \vec{e}_y & \vec{e}_z \\ a_x & a_y & a_z \\ b_x & b_y & b_z \end{bmatrix} = \begin{bmatrix} a_y b_z - a_z b_y \\ a_z b_x - a_x b_z \\ a_x b_y - a_y b_x \end{bmatrix} = |\vec{a}| \cdot |\vec{b}| \cdot \sin\theta \cdot \vec{n}. \tag{A.4}$$

$\vec{n}$ is a unit vector perpendicular to the plane containing $\vec{a}$ and $\vec{b}$. Its direction could be determined by the right-hand rule. The tensor product of $\vec{a}$ and $\vec{b}$ is given as

$$\vec{a} \otimes \vec{b} = \begin{bmatrix} a_x \cdot b_x & a_x \cdot b_y & a_x \cdot b_z \\ a_y \cdot b_x & a_y \cdot b_y & a_y \cdot b_z \\ a_z \cdot b_x & a_z \cdot b_y & a_z \cdot b_z \end{bmatrix}. \tag{A.5}$$

It is also convenient that the Del operator is used as a vector in the derivation

$$\nabla = \left(\frac{\partial}{\partial x}, \frac{\partial}{\partial y}, \frac{\partial}{\partial z}\right)^T. \tag{A.6}$$

The similar operations as Eqs. (A.3) and (A.4) with gradient operator are listed as shown below:

$$\nabla \bullet \vec{a} = \frac{\partial a_x}{\partial x} + \frac{\partial a_y}{\partial y} + \frac{\partial a_z}{\partial z}, \tag{A.7}$$

$$\nabla \times \vec{b} = \begin{bmatrix} \vec{e}_x & \vec{e}_y & \vec{e}_z \\ \dfrac{\partial}{\partial x} & \dfrac{\partial}{\partial y} & \dfrac{\partial}{\partial z} \\ b_x & b_y & b_z \end{bmatrix} = \begin{bmatrix} \dfrac{\partial}{\partial y} b_z - \dfrac{\partial}{\partial z} b_y \\ \dfrac{\partial}{\partial z} b_x - \dfrac{\partial}{\partial x} b_z \\ \dfrac{\partial}{\partial x} b_y - \dfrac{\partial}{\partial y} b_x \end{bmatrix}. \tag{A.8}$$

Physically Eqs. (A.7) and (A.8) describe divergence and vorticity in flow field, respectively. Given a three-dimensional tensor as

$$\overline{\overline{\sigma}} = \begin{bmatrix} \sigma_{x,x} & \sigma_{x,y} & \sigma_{x,z} \\ \sigma_{y,x} & \sigma_{y,y} & \sigma_{y,z} \\ \sigma_{z,x} & \sigma_{z,y} & \sigma_{z,z} \end{bmatrix}. \tag{A.9}$$

The inner product between a tensor and a vector is

$$\overline{\overline{\sigma}} \bullet \vec{b} = \begin{bmatrix} \sigma_{x,x} \cdot b_x + \sigma_{x,y} \cdot b_y + \sigma_{x,z} \cdot b_z \\ \sigma_{y,x} \cdot b_x + \sigma_{y,y} \cdot b_y + \sigma_{y,z} \cdot b_z \\ \sigma_{z,x} \cdot b_x + \sigma_{z,y} \cdot b_y + \sigma_{z,z} \cdot b_z \end{bmatrix}. \tag{A.10}$$

As an extension of Eq. (A.7), the inner product between a gradient operator and a tensor is

$$(\nabla \bullet \overline{\overline{\sigma}})^T = \begin{bmatrix} \dfrac{\partial \sigma_{x,x}}{\partial x} + \dfrac{\partial \sigma_{y,x}}{\partial y} + \dfrac{\partial \sigma_{z,x}}{\partial z} \\ \dfrac{\partial \sigma_{x,y}}{\partial x} + \dfrac{\partial \sigma_{y,y}}{\partial y} + \dfrac{\partial \sigma_{z,y}}{\partial z} \\ \dfrac{\partial \sigma_{x,z}}{\partial x} + \dfrac{\partial \sigma_{y,z}}{\partial y} + \dfrac{\partial \sigma_{z,z}}{\partial z} \end{bmatrix}. \tag{A.11}$$

That is the diffusive term in Navier-Stokes equation. Subsequently, a useful identical formula below could be easily derived:

$$[\nabla \bullet (\vec{a} \otimes \vec{b})]^T = (\nabla \bullet \vec{a}) \cdot \vec{b} + (\vec{a} \bullet \nabla) \cdot \vec{b}. \tag{A.12}$$

In a closed surface **S** and volume **V**, Gauss theorem can be written as below for any smooth vector function $\vec{g}$,

$$\int_{\mathbf{V}} \nabla \bullet \vec{g} \, d\mathbf{V} = \oint_{\mathbf{S}} \vec{g} \bullet \vec{n} \cdot d\mathbf{S}. \tag{A.13}$$

More generally a vector form is

$$\int_{\mathbf{V}} (\nabla \bullet \overline{\overline{\sigma}})^T \cdot d\mathbf{V} = \oint_{\mathbf{S}} \overline{\overline{\sigma}} \bullet \vec{n} \cdot d\mathbf{S}, \tag{A.14}$$

where $\vec{n}$ is an outward unit normal vector on the surface **S**. The above Gaussian theorems are used to discretize convection and diffusion terms in the finite volume method.

B Conservation Equations

In fluid dynamics, the conservation laws [65, 84] describe the equilibrium effects of internal sources and fluxes crossing boundary surfaces. They completely determine a fluid system by adding few extra specifications about the nature of the fluid.

B.1 Mass Conservation Equations

With the Eulerian view, a control volume **V** for our observation is fixed. In a small time period Δt, the net mass decrement, which flows out of the volume **V** through its closed surface **S**, could be calculated as

$$\oint_{\mathbf{S}} \rho \vec{V} \bullet \vec{n} \cdot d\mathbf{S} \cdot \Delta t, \tag{B.1}$$

where $\vec{n}$ is the outward unit normal vector on the infinitesimal surface $d\mathbf{S}$. $\vec{V}$ is the fluid velocity and ρ is the density. The net increment of the mass in the volume **V** in a small time period Δt is

$$\int_{\mathbf{V}} \frac{\Delta \rho}{\Delta t} d\mathrm{V} \cdot \Delta t \approx \int_{\mathbf{V}} \frac{\partial \rho}{\partial t} d\mathrm{V} \cdot \Delta t. \tag{B.2}$$

In most aerodynamic cases, it is usually assumed that there is no source term. The pure mass flowing out through the closed surface is equal to the decrement of the mass in the whole volume. The conservation of the mass could be obtained from Eqs. (B.1) and (B.2) as

$$\oint_{\mathbf{S}} \rho \vec{V} \bullet \vec{n} d\mathbf{S} \cdot \Delta t = -\int_{\mathbf{V}} \frac{\partial \rho}{\partial t} d\mathbf{V} \cdot \Delta t. \tag{B.3}$$

Using Gauss's theorem by substituting $\vec{g} = \rho \vec{V}$ into Eq. (A.13) yields

$$\oint_{\mathbf{S}} \rho \vec{V} \bullet \vec{n} d\mathbf{S} = \int_{\mathbf{V}} \nabla \bullet \left(\rho \vec{V} \right) d\mathbf{V}. \tag{B.4}$$

The conservation law of mass is rewritten as

$$\int_{\mathbf{V}} \left[\frac{\partial \rho}{\partial t} + \nabla \bullet \left(\rho \vec{V} \right) \right] d\mathbf{V} = 0. \tag{B.5}$$

Because **V** is an arbitrary volume, its differential equation in conservation form is presented as

$$\frac{\partial \rho}{\partial t} + \nabla \bullet \left(\rho \vec{V} \right) = 0. \tag{B.6}$$

The total differential operator is defined as

$$\frac{\partial}{\partial t} + \left(\vec{V} \bullet \nabla \right) \equiv \frac{D}{Dt}. \tag{B.7}$$

The non-conservation form of Eq. (B.6) is expressed as

$$\frac{D\rho}{Dt} + \rho \nabla \bullet \vec{V} = 0. \tag{B.8}$$

B.2 Momentum Conservation Equations

The conservation equation of the momentum can be derived from Newton's 2nd law $\vec{F} = \partial(m\vec{V})/\partial t$. With the Lagrangian view, let's follow with a movement of a given infinitesimal fluid element $d\mathbf{V}$. In a very small time interval Δt, the force acting on the fluid element could be considered as a constant and presented as

$$\rho\ \vec{f} \cdot d\mathbf{V}, \tag{B.9}$$

where $\vec{f}$ denotes the body force per unit mass acting on the fluid element. The force acting on an arbitrary volume **V** is integrated as

$$\int_{\mathbf{V}} \rho\ \vec{f} \cdot d\mathbf{V}. \tag{B.10}$$

Similarly, the net surface force in time *t* is expressed as

$$\oint_{\mathbf{S}} \vec{\sigma}_n \cdot d\mathbf{S}, \tag{B.11}$$

where $\vec{\sigma}_n := \overline{\overline{\sigma}} \bullet \vec{n}$. $\overline{\overline{\sigma}}$ is a stress tensor. $\vec{\sigma}_n$ is a stress vector acting on the closed surface **S**, $\vec{n}$ is still the outward unit normal vector. Since we follow a moving element, the mass has not been changed in the small time interval Δt. The acceleration of the flow element is

$$\frac{D(m\vec{V})}{Dt} = m\frac{D(\vec{V})}{Dt} = \rho \cdot d\mathbf{V} \cdot \frac{D(\vec{V})}{Dt}. \tag{B.12}$$

Hence, the whole acceleration on the given arbitrary volume **V** is

$$\int_{\mathbf{V}} \rho \frac{D(\vec{V})}{Dt} \cdot d\mathbf{V}. \tag{B.13}$$

From the Newton's 2nd law we have

$$\int_{\mathbf{V}} \rho \frac{D(\vec{V})}{Dt} \cdot d\mathbf{V} = \oint_{\mathbf{S}} \vec{\sigma}_n \cdot d\mathbf{S} + \int_{\mathbf{V}} \rho\, \vec{f} \cdot d\mathbf{V}. \tag{B.14}$$

Applying Gauss theorem Eq. (A.14) to the first term in the right hand side of the above equation,

$$\oint_{\mathbf{S}} \vec{\sigma}_n \cdot d\mathbf{S} = \oint_{\mathbf{S}} \overline{\overline{\sigma}} \bullet \vec{n} \cdot d\mathbf{S} = \int_{\mathbf{V}} (\nabla \bullet \overline{\overline{\sigma}})^T \cdot d\mathbf{V}. \tag{B.15}$$

Substituting Eq. (B15) into Eq. (B.14), the conservation law of the momentum in integral form is derived for any volume **V** as

$$\int_{\mathbf{V}} \rho \frac{D\vec{V}}{Dt} \cdot d\mathbf{V} = \int_{\mathbf{V}} [(\nabla \bullet \overline{\overline{\sigma}})^T + \rho\, \vec{f}] \cdot d\mathbf{V}. \tag{B.16}$$

Finally the conservation law of the momentum in differential equation form is as

$$\rho \frac{D\vec{V}}{Dt} = (\nabla \bullet \overline{\overline{\sigma}})^T + \rho \vec{f} \,. \tag{B.17}$$

Due to

$$\frac{\partial}{\partial t} + \left(\vec{V} \bullet \nabla\right) \equiv \frac{D}{Dt}, \tag{B.18}$$

the non-conservation form of Eq. (B.17) is derived as

$$\rho\left[\frac{\partial \vec{V}}{\partial t} + \left(\vec{V} \bullet \nabla\right)\vec{V}\right] = (\nabla \bullet \overline{\overline{\sigma}})^T + \rho \vec{f} \,. \tag{B.19}$$

For the aerodynamic separation process, it is assumed that the body force acting on the orbital stage $\vec{f} = 0$. Using the continuity equation (B.8) and the identity (A.12), the momentum vector equation is written in the conservation form as

$$\frac{\partial(\rho\vec{V})}{\partial t} + [\nabla \bullet (\rho\vec{V} \otimes \vec{V})]^T = (\nabla \bullet \overline{\overline{\sigma}})^T \,. \tag{B.20}$$

B.3 Energy Conservation Equations

Again we use the Langrangian view. The body force does a work on a fluid element moving at a velocity $\vec{V}$ in a small time period Δt

$$\int_{\mathbf{V}} \rho \vec{f} \bullet \vec{V}\, d\mathbf{V} \cdot \Delta t \,. \tag{B.21}$$

The work resulting from the surface force is expressed as

$$\oint_{\mathbf{S}} \overline{\overline{\sigma}}_n \bullet \vec{V} d\mathbf{S} \cdot \Delta t \,. \tag{B.22}$$

Using Fourier's heat transfer theorem [101], we get the work done by the thermal conduction

$$\oint_{\mathbf{S}} k \frac{\partial T}{\partial n} d\mathbf{S} \cdot \Delta t \,, \tag{B.23}$$

where T is the temperature and k is the coefficient of the heat conductivity. Volumetric heating is related with a rate of volumetric heat source $\dot{q}$ as

$$\int_{\mathbf{V}} \rho \dot{q} d\mathbf{V} \cdot \Delta t \,. \tag{B.24}$$

The net increment of energy can be obtained as

$$\int_{\mathbf{V}} \rho \frac{D}{Dt}\left[\frac{|\vec{V}|^2}{2} + e\right] d\mathbf{V} \,, \tag{B.25}$$

where e=c$_v$ T . e is specific internal energy, c$_v$ as specific heat at constant volume.

Assuming that the energy exchanges only between mechanic energy and heat energy, we use the first law of thermodynamics, that is, the energy is conserved, to combine Eqs. (B.21) - (B.25).

$$\int_{\mathbf{V}} \rho \frac{D}{Dt}\left[\frac{|\vec{V}|^2}{2}+e\right]d\mathbf{V} = \int_{\mathbf{V}} \rho\, \vec{f} \bullet \vec{V} d\mathbf{V} + \oint_{\mathbf{S}} \overline{\overline{\sigma}}_n \bullet \vec{V} d\mathbf{S} + \oint_{\mathbf{S}} k \frac{\partial T}{\partial n} d\mathbf{S} + \int_{\mathbf{V}} \rho \dot{q}\, d\mathbf{V} . \tag{B.26}$$

The integrations on the surface are changed to the integrations on the volumes using the Gauss theorem:

$$\oint_{\mathbf{S}} \overline{\overline{\sigma}}_n \bullet \vec{V} d\mathbf{S} = \oint_{\mathbf{S}} (\vec{n} \bullet \overline{\overline{\sigma}}) \bullet \vec{V} d\mathbf{S} = \oint_{\mathbf{S}} \vec{n} \bullet (\overline{\overline{\sigma}} \bullet \vec{V}) d\mathbf{S} = \int_{\mathbf{V}} \nabla \bullet (\overline{\overline{\sigma}} \bullet \vec{V})\, d\mathbf{V} , \tag{B.27}$$

and

$$\oint_{\mathbf{S}} k \frac{\partial T}{\partial n} d\mathbf{S} = \int_{\mathbf{V}} \nabla \bullet (k \nabla T)\, d\mathbf{V} . \tag{B.28}$$

After substituting Eqs. (B.27) and (B.28) into Eq. (B.26),

$$\int_{\mathbf{V}} \rho \frac{D}{Dt}\left[\frac{|\vec{V}|^2}{2}+e\right]d\mathbf{V} = \int_{\mathbf{V}} [\rho\, \vec{f} \bullet \vec{V} + \nabla \bullet (\overline{\overline{\sigma}} \bullet \vec{V}) + \nabla \bullet (k \nabla T) + \rho \dot{q}] d\mathbf{V} . \tag{B.29}$$

The differential equation form of the energy conservation could be expressed as

$$\rho \frac{\partial}{\partial t}\left[\frac{|\vec{V}|^2}{2}+e\right] + \rho \vec{V} \bullet \nabla \left[\frac{|\vec{V}|^2}{2}+e\right] = \rho\, \vec{f} \bullet \vec{V} + \nabla \bullet (\overline{\overline{\sigma}} \bullet \vec{V}) + \nabla \bullet (k \nabla T) + \rho \dot{q} . \tag{B.30}$$

Using Eq. (B.6), the conservation form of the energy conservation is

$$\frac{\partial}{\partial t}\left[\rho(\frac{|\vec{V}|^2}{2}+e)\right] + \nabla \bullet \left[\rho \vec{V}(\frac{|\vec{V}|^2}{2}+e)\right] = \rho\, \vec{f} \bullet \vec{V} + \nabla \bullet (\overline{\overline{\sigma}} \bullet \vec{V}) + \nabla \bullet (k \nabla T) + \rho \dot{q} . \tag{B.31}$$

According to the total energy density $E_S := \rho(\frac{|\vec{V}|^2}{2}+e)$, the body force $\vec{f} = 0$, and heat source $\dot{q} = 0$, the conservation form for the separation process is simplified as

$$\frac{\partial}{\partial t}(E_S) + \nabla \bullet (E_S \vec{V}) = \nabla \bullet (\overline{\overline{\sigma}} \bullet \vec{V}) + \nabla \bullet (k \cdot \nabla T) . \tag{B.32}$$

C Navier-Stokes Equations

Though the awareness of the conservation laws is already one of the greatest achievements in science, it is still not enough to completely describe the dynamic properties of a fluid. The stress tensor $\overline{\overline{\sigma}}$ in the conservation laws is still unknown. In Navier-Stokes equations [20, 45], the stresses $\overline{\overline{\sigma}}$ are related to the deformation rates of the fluid elements linearly. Added the equation of state as well as proper initial and boundary conditions, the Navier-Stokes system becomes completely closed for the state variables.

C.1 Stress Tensor

In Figure C.1, a small tetrahedron with a volume **V** has three coordinate planes with areas S_x, S_y, S_z, and an inclined surface with an area S. The latter has the orientation $\vec{n} = (n_x, n_y, n_z)^T$ with $n_i = S_i / S$ (i=x, y, z). On these three coordinate planes and inclined surface we define stresses on different planes as $\vec{\tau}_i$ (i=x, y, z) and $\vec{\tau}$ correspondingly.

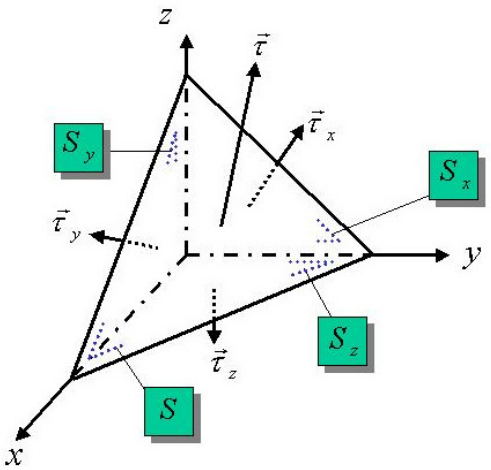

Figure C.1: The stresses acting on a tetrahedron in an orthogonal coordinate system.

The body force acting on this element is

$$\rho \vec{f} \cdot \mathbf{V} . \tag{C.1}$$

The surface traction is expressed as

$$\vec{\tau} \cdot S - \vec{\tau}_x \cdot S_x - \vec{\tau}_y \cdot S_y - \vec{\tau}_z \cdot S_z . \tag{C.2}$$

Using again the Newton's second law to the small tetrahedron yields

$$\rho \frac{d\vec{V}}{dt} \cdot \mathbf{V} = \rho \vec{f} \cdot \mathbf{V} + \vec{\tau} \cdot S - \vec{\tau}_x \cdot S_x - \vec{\tau}_y \cdot S_y - \vec{\tau}_z \cdot S_z . \tag{C.3}$$

The above equation can be rewritten as

$$\rho(\frac{d\vec{V}}{dt} - \rho\,\vec{f}) \cdot \mathbf{V}/S = \vec{\tau} - (\vec{\tau}_x \cdot S_x + \vec{\tau}_y \cdot S_y + \vec{\tau}_z \cdot S_z)/S\,. \tag{C.4}$$

When the tetrahedron shrinks to one point, $\mathbf{V}/S$ is an infinitesimal. Accordingly any stress could be expressed by

$$\vec{\tau} = (\vec{\tau}_x \cdot S_x + \vec{\tau}_y \cdot S_y + \vec{\tau}_z \cdot S_z)/S = \vec{\tau}_x \cdot n_x + \vec{\tau}_y \cdot n_y + \vec{\tau}_z \cdot n_z\,. \tag{C.5}$$

The stress vector $\vec{\tau}_i$ (i=x, y, z) can be expressed by three orthogonal unit vectors $\vec{e}_x$, $\vec{e}_y$, $\vec{e}_z$,

$$\vec{\tau}_i = \sum_{j=x,\,y,\,z} T_{j,i} \cdot \vec{e}_j\,, \quad (i=x,\,y,\,z), \tag{C.6}$$

where $T_{j,i}$ is a stress component that acts on the plane perpendicular with vector $\vec{e}_j$ and its direction along the vector $\vec{e}_i$. Substitute Eq. (C.6) into Eq. (C.5), we have

$$\vec{\tau} = \sum_{i=x,\,y,\,z} n_i \cdot \vec{\tau}_i = \sum_{i,\,j=x,\,y,\,z} n_i \cdot T_{j,i} \cdot \vec{e}_j = \sum_{j=x,\,y,\,z} \tau^{(j)} \cdot \vec{e}_j\,, \tag{C.7}$$

where $\vec{\tau}^{(i)}$ (i=x, y, z) are the components of $\vec{\tau}$ on x, y, z axes. In vector form the above equation is

$$\vec{\tau} = \begin{bmatrix} \tau^{(x)} \\ \tau^{(y)} \\ \tau^{(z)} \end{bmatrix} = \begin{bmatrix} T_{x,x} & T_{x,y} & T_{x,z} \\ T_{y,x} & T_{y,y} & T_{y,z} \\ T_{z,x} & T_{z,y} & T_{z,z} \end{bmatrix} \begin{bmatrix} n_x \\ n_y \\ n_z \end{bmatrix}. \tag{C.8}$$

The stress tensor is obtained as

$$\overline{\overline{\sigma}} := \begin{bmatrix} T_{x,x} & T_{x,y} & T_{x,z} \\ T_{y,x} & T_{y,y} & T_{y,z} \\ T_{z,x} & T_{z,y} & T_{z,z} \end{bmatrix}, \tag{C.9}$$

and the stress vector in Eq. (C.8) can be abbreviated as

$$\vec{\tau} = \overline{\overline{\sigma}} \bullet \vec{n}\,. \tag{C.10}$$

C.2 Symmetrical Stress Matrix

Consider a two-dimensional case for simplicity. The stresses are distributed as shown in Figure C.2. They generate a torque around axis z

$$M_z = [(2 \cdot T_{x,y} + \Delta T_{x,y}) \cdot \Delta y \cdot \Delta z] \cdot \Delta x - [(2 \cdot T_{y,x} + \Delta T_{y,x}) \cdot \Delta x \cdot \Delta z] \cdot \Delta y\,. \tag{C.11}$$

Using the principle of angular momentum, we have

$$M_z = \frac{1}{12}\rho \Delta x \cdot \Delta y \cdot \Delta z \cdot (\Delta x^2 + \Delta y^2)\frac{d\omega_z}{dt}\,. \tag{C.12}$$

Combining Eqs. (C.11) and (C.12), and dividing the equation by $\Delta x \cdot \Delta y \cdot \Delta z$, we obtain

$$2 \cdot T_{x,y} + \Delta T_{x,y} - 2 \cdot T_{y,x} - \Delta T_{y,x} = \frac{1}{12} \rho (\Delta x^2 + \Delta y^2) \frac{d\omega_z}{dt}. \tag{C.13}$$

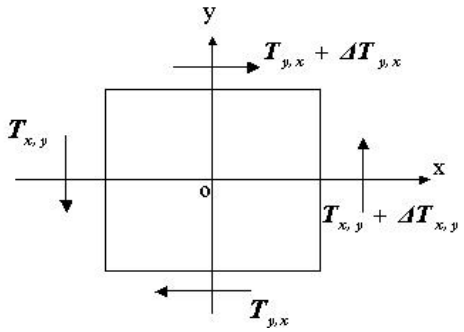

Figure C.2: Stresses and their directions in x-y plane.

Let Δx and Δy converge to zero and use the continuity of stress,

$$T_{x,y} = T_{y,x}. \tag{C.14}$$

In the similar way, it could be derived that

$$T_{x,z} = T_{z,x}, \quad T_{z,y} = T_{y,z}. \tag{C.15}$$

Then the stress matrix is symmetric:

$$\left(\overline{\overline{\sigma}}\right)^T = \overline{\overline{\sigma}}. \tag{C.16}$$

C.3 Navier-Stokes and Euler Equations

Related with shear stress tensor and pressure, the stress tensor $\overline{\overline{\sigma}}$ in Eq. (B.19) could be expressed as

$$\overline{\overline{\sigma}} = -p\overline{\overline{I}} + \overline{\overline{\tau}}. \tag{C.17}$$

Here p is the pressure, $\overline{\overline{I}}$ a unit tensor, and $\overline{\overline{\tau}}$ a symmetric tensor of viscous shear stress.

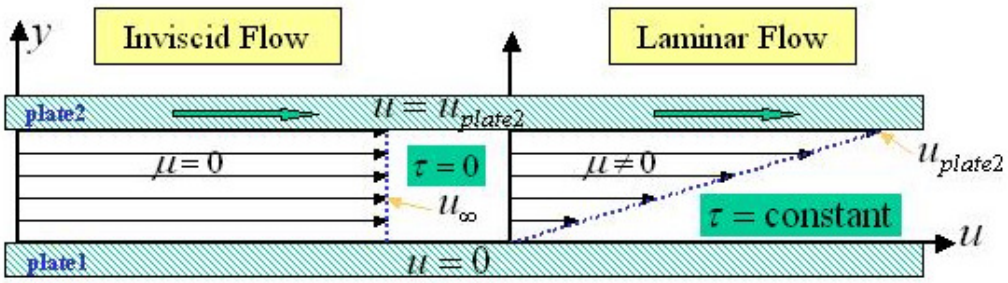

Figure C.3: Relationship among viscosity μ, stress τ, and velocity u in viscous and inviscid flows confined by two plates.

The Navier-Stokes equations could be used to describe the flow field of the Newtonian fluid, in which the stress components are linearly proportional to the strain rates [61, 98]. In nature, most of common fluids belong to this type of fluid, such as water, air, gasoline, oil, etc. Relations among coefficient of (dynamic) viscosity μ, stress τ and the flow velocities *u* between two flat plates are shown by two special examples in Figure C.3. In the left picture, the plates do not affect the movement of inviscid fluid and $\tau = 0$. On the right side, viscous effect leads to a linear distribution of velocity. Stress τ is a constant there.

The components of the stress could be generally expressed as

$$\tau_{xx} = 2\mu\frac{\partial u}{\partial x} + (\mu_{\mathbf{v}} - \frac{2}{3}\mu)\nabla \bullet \vec{V}, \qquad \tau_{xy} = \tau_{yx} = \mu\left(\frac{\partial v}{\partial x} + \frac{\partial u}{\partial y}\right), \tag{C.18}$$

$$\tau_{yy} = 2\mu\frac{\partial v}{\partial y} + (\mu_{\mathbf{v}} - \frac{2}{3}\mu)\nabla \bullet \vec{V}, \qquad \tau_{zy} = \tau_{yz} = \mu\left(\frac{\partial w}{\partial y} + \frac{\partial v}{\partial z}\right), \tag{C.19}$$

$$\tau_{zz} = 2\mu\frac{\partial w}{\partial z} + (\mu_{\mathbf{v}} - \frac{2}{3}\mu)\nabla \bullet \vec{V}, \qquad \tau_{zx} = \tau_{xz} = \mu\left(\frac{\partial u}{\partial z} + \frac{\partial w}{\partial x}\right), \tag{C.20}$$

where $\mu_{\mathbf{v}}$ is the volume-expanding coefficient. *u*, *v*, *w* are the components of the velocity vector $\vec{V}$ projected on *x*, *y*, *z* axes. The coefficient of dynamic viscosity of the ideal gas μ could be accurately determined by Sutherland's law:

$$\frac{\mu}{\mu_0} = \left(\frac{T}{T_0}\right)^{\frac{3}{2}} \frac{1 + T_s / T_0}{T / T_0 + T_s / T_0}, \tag{C.21}$$

where the Sutherland's constant $T_s = 110.4$ K. At any point in the air, when its temperature *T* is known, we could derive its coefficient of viscosity by using the reference viscosity μ_0 and temperature T_0. As a reference point at the sea level, $\mu_0 = 1.7894 \cdot 10^{-5}$ Pa · s, and $T_0 = 288.15$ K. The deviation of the Sutherland's law is less than 10% with $0 < T < 555$ K and pressure < 3.45 MPa.

It is assumed that the average of three normal stresses in $\overline{\overline{\sigma}}$ on any point is just equal to its pressure *p*. This leads to the Stokes hypothesis in the Navier-Stokes equations:

$$\mu_{\mathbf{v}} = 0. \tag{C.22}$$

Substituting equations (C.17) - (C.22) into the conservation forms of the momentum Eq. (B.20) and energy conservation laws Eq. (B.32), separating inviscid and viscous terms, neglecting the gravity force as well as the volumetric heating, the conservation form of the Navier-Stokes equation for the separation process is abbreviated as

$$\frac{\partial \mathbf{q}}{\partial t} + \frac{\partial(\mathbf{f}^I - \mathbf{f}^V)}{\partial x} + \frac{\partial(\mathbf{g}^I - \mathbf{g}^V)}{\partial y} + \frac{\partial(\mathbf{h}^I - \mathbf{h}^V)}{\partial z} = \mathbf{0}, \tag{C.23}$$

with the vector of the state variables $\mathbf{q} = (\rho, \rho u, \rho v, \rho w, E_S)^T$, the density ρ, the velocity vector

$\vec{V}=(u,\ v,\ w)^T$, the total energy density $E_S := \rho(\frac{|\vec{V}|^2}{2}+e)$, and the specific internal energy e. The inviscid flux terms are:

$$\mathbf{f}^I=\begin{bmatrix}\rho u\\ \rho u^2+p\\ \rho uv\\ \rho uw\\ (E_S+p)u\end{bmatrix}, \mathbf{g}^I=\begin{bmatrix}\rho v\\ \rho vu\\ \rho v^2+p\\ \rho vw\\ (E_S+p)v\end{bmatrix}, \mathbf{h}^I=\begin{bmatrix}\rho w\\ \rho wu\\ \rho wv\\ \rho w^2+p\\ (E_S+p)w\end{bmatrix}, \tag{C.24}$$

and viscous flux terms:

$$\mathbf{f}^V=\begin{bmatrix}0\\ \tau_{xx}\\ \tau_{yx}\\ \tau_{zx}\\ \Pi_x\end{bmatrix}, \mathbf{g}^V=\begin{bmatrix}0\\ \tau_{xy}\\ \tau_{yy}\\ \tau_{zy}\\ \Pi_y\end{bmatrix}, \mathbf{h}^V=\begin{bmatrix}0\\ \tau_{xz}\\ \tau_{yz}\\ \tau_{zz}\\ \Pi_z\end{bmatrix}. \tag{C.25}$$

Further there are

$$\Pi_x=u\cdot\tau_{xx}+v\cdot\tau_{xy}+w\cdot\tau_{xz}-q_x, \tag{C.26}$$

$$\Pi_y=u\cdot\tau_{yx}+v\cdot\tau_{yy}+w\cdot\tau_{yz}-q_y, \tag{C.27}$$

$$\Pi_z=u\cdot\tau_{zx}+v\cdot\tau_{zy}+w\cdot\tau_{zz}-q_z, \tag{C.28}$$

where the fluxes of heat transfer q_i $(i=x,y,z)$ are given as

$$q_x=-k\frac{\partial T}{\partial x},\quad q_y=-k\frac{\partial T}{\partial y},\quad q_z=-k\frac{\partial T}{\partial z}, \tag{C.29}$$

and

$$\tau_{xx}=2\mu\frac{\partial u}{\partial x}-\frac{2}{3}\mu\cdot\nabla\bullet\vec{V},\qquad \tau_{xy}=\tau_{yx}=\mu\left(\frac{\partial v}{\partial x}+\frac{\partial u}{\partial y}\right), \tag{C.30}$$

$$\tau_{yy}=2\mu\frac{\partial v}{\partial y}-\frac{2}{3}\mu\cdot\nabla\bullet\vec{V},\qquad \tau_{zy}=\tau_{yz}=\mu\left(\frac{\partial w}{\partial y}+\frac{\partial v}{\partial z}\right), \tag{C.31}$$

$$\tau_{zz}=2\mu\frac{\partial w}{\partial z}-\frac{2}{3}\mu\cdot\nabla\bullet\vec{V},\qquad \tau_{zx}=\tau_{xz}=\mu\left(\frac{\partial u}{\partial z}+\frac{\partial w}{\partial x}\right). \tag{C.32}$$

In Navier-Stokes equations, we have five equations but with six unknowns ρ, u, v, w, T, and p. Let us consider calorically perfect gas and add the equation of state, finally the Navier-Stokes equation system becomes closed. The equation of state is in the form of

$$p=\rho RT, \tag{C.33}$$

where a specific gas constant for the dry air $R=287$ (N·m)/(kg·K). For a calorically perfect gas, the

specific heat at constant volume c_v and the specific heat at constant pressure c_p are further postulated as constants. It is also satisfied that

$$e = c_v T\,, \tag{C.34}$$

and

$$c_p - c_v = R\,. \tag{C.35}$$

Defining $\gamma = c_p / c_v$ as the ratio of specific heats, the equation of state Eq. (C.33) is rewritten as

$$p = (\gamma - 1)\cdot[E_S - \frac{\rho}{2}(u^2 + v^2 + w^2)]\,, \tag{C.36}$$

where γ is usually equal to constant 1.4 for the air.

The conservation equations of the momentum with Navier-Stokes stresses are composed of second order partial differential equations. For the unknowns $\vec{V}$ and E_S, they are parabolic equations, but they are changed into elliptic equations for steady cases. The conservation equation of mass is a first order partial differential equation. For the unknown ρ, it is hyperbolic equation. The coupled system of the Navier-Stokes equation is a hybrid differential system. For steady case it is an elliptic-hyperbolic system, and for unsteady case it is a parabolic-hyperbolic system.

Euler equations can be directly derived from Navier-Stokes equations by assuming that the viscosity of fluid is equal to zero. That is, the shear stress tensor in Navier-Stokes equations is neglected. Because Prandtl number depends on the physical character of the fluid, it is approximately a constant. For the air in our code FLMNAV, the Prandtl Number is given as

$$\mathrm{Pr} = \frac{\mu \cdot c_p}{k} = 0.72\,, \tag{C.37}$$

and

$$k = 1.39 \cdot \mu \cdot c_p\,, \text{ with } c_p = 1000\ \mathrm{J/(Kg\cdot K)}. \tag{C.38}$$

The thermal conductivity could be also neglected, when viscosity tends to zero.

Mathematically, the Euler equation system is an elliptic system in the area of steady subsonic flow, but a hyperbolic system in the area of steady supersonic flow. For the unsteady case, it is a parabolic-hyperbolic system. It is used to describe the flow at high Reynolds numbers and small thermal conductivity, which is usually away from the solid surfaces. Comparing with the Navier-Stokes system, the Euler system could be realized with much less computing work.

D Nondimensionlization

A dimensionless Navier-Stokes equation system could be applied much widely [47, 65]. Some similarity parameters, such as Reynolds number and Mach number, could be originated from the dimensionless forms. We define the variables with superscript * as the dimensionless variables, and with subscript *ref* as the reference values for the non-dimensional from. The transformations are:

$$x = x^* \cdot L_{ref}, \quad y = y^* \cdot L_{ref}, \quad z = z^* \cdot L_{ref}, \quad t = t^* \cdot t_{ref}, \tag{D.1}$$

$$\rho = \rho^* \cdot \rho_{ref}, \quad u = u^* \cdot V_{ref}, \quad v = v^* \cdot V_{ref}, \quad w = w^* \cdot V_{ref}, \tag{D.2}$$

$$\mu = \mu^* \cdot \mu_{ref}, \quad T = T^* \cdot T_{ref}, \quad p = p^* \cdot p_{ref}, \quad E_S = E_S^* \cdot E_{ref}, \tag{D.3}$$

where L_{ref} is the length of the EOS. In the code FLMNAV, most of referential parameters are related to the corresponding values in freestream, which are labeled with a subscript ∞.

$$\rho_{ref} = \rho_\infty, \; p_{ref} = p_\infty, \tag{D.4}$$

$$V_{ref} = \sqrt{p_\infty / \rho_\infty} = \frac{V_\infty}{\sqrt{\gamma} \cdot M_\infty}, \; T_{ref} = \frac{T_\infty}{\gamma \cdot M_\infty{}^2}, \tag{D.5}$$

$$\mu_{ref} = \frac{\rho_\infty \cdot V_\infty \cdot L_{ref}}{\sqrt{\gamma} \cdot M_\infty}, \; t_{ref} = L_{ref} / V_{ref}, \tag{D.6}$$

$$E_{ref} = p_{ref} / (\gamma - 1) + 0.5 \cdot M_\infty \cdot V_{ref}{}^2. \tag{D.7}$$

Some important dimensionless numbers are defined as following: the Reynolds number

$$Re_\infty = \frac{\rho_\infty \cdot V_\infty \cdot L_{ref}}{\mu_\infty}, \tag{D.8}$$

the speed of sound in the air

$$a = \sqrt{\gamma \cdot R \cdot T_\infty} = \sqrt{(\gamma - 1) \cdot c_p \cdot T_\infty}, \tag{D.9}$$

and the Mach number

$$M_\infty = \frac{V_\infty}{a}. \tag{D.10}$$

Using equations from (D.1) to (D.7), the continuity equation is transformed into

$$\frac{\rho_{ref} \cdot V_{ref}}{L_{ref}} \left(\frac{\partial \rho^*}{\partial t^*} + \frac{\partial}{\partial x^*}(\rho^* u^*) + \frac{\partial}{\partial y^*}(\rho^* v^*) + \frac{\partial}{\partial z^*}(\rho^* w^*) \right) = 0. \tag{D.11}$$

Furthermore, the *x*-, *y*-, *z*- components of the momentum equations are as follows:

$$\frac{\rho_{ref}\cdot V_{ref}{}^2}{L_{ref}}\left[\frac{\partial(\rho^* u^*)}{\partial t^*}+\frac{\partial(\rho^* u^{*2}+p^*)}{\partial x^*}+\frac{\partial(\rho^* u^* v^*)}{\partial y^*}+\frac{\partial(\rho^* u^* w^*)}{\partial z^*}-(\frac{\partial \tau_{xx}{}^*}{\partial x^*}+\frac{\partial \tau_{yx}{}^*}{\partial y^*}+\frac{\partial \tau_{zx}{}^*}{\partial z^*})\right]=0, \tag{D.12}$$

$$\frac{\rho_{ref}\cdot V_{ref}{}^2}{L_{ref}}\left[\frac{\partial(\rho^* v^*)}{\partial t^*}+\frac{\partial(\rho^* u^* v^*)}{\partial x^*}+\frac{\partial(\rho^* v^{*2}+p^*)}{\partial y^*}+\frac{\partial(\rho^* v^* w^*)}{\partial z^*}-(\frac{\partial \tau_{xy}{}^*}{\partial x^*}+\frac{\partial \tau_{yy}{}^*}{\partial y^*}+\frac{\partial \tau_{zy}{}^*}{\partial z^*})\right]=0, \tag{D.13}$$

$$\frac{\rho_{ref}\cdot V_{ref}{}^2}{L_{ref}}\left[\frac{\partial(\rho^* w^*)}{\partial t^*}+\frac{\partial(\rho^* w^* u^*)}{\partial x^*}+\frac{\partial(\rho^* w^* v^*)}{\partial y^*}+\frac{\partial(\rho^* w^{*2}+p^*)}{\partial z^*}-(\frac{\partial \tau_{xz}{}^*}{\partial x^*}+\frac{\partial \tau_{yz}{}^*}{\partial y^*}+\frac{\partial \tau_{zz}{}^*}{\partial z^*})\right]=0. \tag{D.14}$$

In the above Eqs. (D.12) - (D.14), the dimensionless stresses are expressed as

$$\tau_{xx}{}^*=\frac{\mu^*}{Re_\infty}\left(2\frac{\partial u^*}{\partial x^*}-\frac{2}{3}\nabla^*\bullet\vec{V}^*\right), \qquad \tau_{xy}{}^*=\tau_{yx}{}^*=\frac{\mu^*}{Re_\infty}\left(\frac{\partial v^*}{\partial x^*}+\frac{\partial u^*}{\partial y^*}\right), \tag{D.15}$$

$$\tau_{yy}{}^*=\frac{\mu^*}{Re_\infty}\left(2\frac{\partial v^*}{\partial y^*}-\frac{2}{3}\nabla^*\bullet\vec{V}^*\right), \qquad \tau_{zy}{}^*=\tau_{yz}{}^*=\frac{\mu^*}{Re_\infty}\left(\frac{\partial w^*}{\partial y^*}+\frac{\partial v^*}{\partial z^*}\right), \tag{D.16}$$

$$\tau_{zz}{}^*=\frac{\mu^*}{Re_\infty}\left(2\frac{\partial w^*}{\partial z^*}-\frac{2}{3}\nabla^*\bullet\vec{V}^*\right), \qquad \tau_{zx}{}^*=\tau_{xz}{}^*=\frac{\mu^*}{Re_\infty}\left(\frac{\partial u^*}{\partial z^*}+\frac{\partial w^*}{\partial x^*}\right). \tag{D.17}$$

The energy equation has the following dimensionless form:

$$\frac{\partial E_S{}^*}{\partial t^*}+\frac{\partial}{\partial x^*}\left\{(E_S{}^*+p^*)u^*-\Pi_x{}^*\right\}+\frac{\partial}{\partial y^*}\left\{(E_S{}^*+p^*)v^*-\Pi_y{}^*\right\}+\frac{\partial}{\partial z^*}\left\{(E_S{}^*+p^*)w^*-\Pi_z{}^*\right\}=0, \tag{D.18}$$

where the viscous terms are listed in the following

$$\prod_x{}^*=u^*\cdot\tau_{xx}{}^*+v^*\cdot\tau_{yx}{}^*+w^*\cdot\tau_{zx}{}^*-q_x^*, \tag{D.19}$$

$$\prod_y{}^*=u^*\cdot\tau_{xy}{}^*+v^*\cdot\tau_{yy}{}^*+w^*\cdot\tau_{zy}{}^*-q_y^*, \tag{D.20}$$

$$\prod_z{}^*=u^*\cdot\tau_{xz}{}^*+v^*\cdot\tau_{yz}{}^*+w^*\cdot\tau_{zz}{}^*-q_z^*, \tag{D.21}$$

and the dimensionless heat conductions are given as

$$q_x^*=-\frac{\mu^*}{Re_\infty\cdot\Pr\cdot M_\infty^2\cdot(\gamma-1)}\frac{\partial T^*}{\partial x^*}, \tag{D.22}$$

$$q_y^*=-\frac{\mu^*}{Re_\infty\cdot\Pr\cdot M_\infty^2\cdot(\gamma-1)}\frac{\partial T^*}{\partial y^*}, \tag{D.23}$$

$$q_z^*=-\frac{\mu^*}{Re_\infty\cdot\Pr\cdot M_\infty^2\cdot(\gamma-1)}\frac{\partial T^*}{\partial z^*}. \tag{D.24}$$

It is more clearly that an infinitesimal viscosity μ^* or an infinite Re_∞ in Eqs. (D.15) - (D.17) and

(D.22) - (D.24) leads the dimensionless stresses and heat conductions away in inviscid flow.

With the state variable vector $\mathbf{q}^* = \left(\rho^*, \rho^* u^*, \rho^* v^*, \rho^* w^*, E_S^*\right)^T$, the above equations are composed of a new vector equation:

$$\frac{\partial \mathbf{q}^*}{\partial t^*} + \frac{\partial (\mathbf{f}^{I^*} - \mathbf{f}^{V^*})}{\partial x^*} + \frac{\partial (\mathbf{g}^{I^*} - \mathbf{g}^{V^*})}{\partial y^*} + \frac{\partial (\mathbf{h}^{I^*} - \mathbf{h}^{V^*})}{\partial z^*} = \mathbf{0}, \tag{D.25}$$

where

$$\mathbf{f}^{I^*} = \begin{bmatrix} \rho^* u^* \\ \rho^* u^{*2} + p^* \\ \rho^* u^* v^* \\ \rho^* u^* w^* \\ \left(E_S^* + p^*\right) u^* \end{bmatrix}, \mathbf{g}^{I^*} = \begin{bmatrix} \rho^* v^* \\ \rho^* v^* u^* \\ \rho^* v^{*2} + p^* \\ \rho^* v^* w^* \\ \left(E_S^* + p^*\right) v^* \end{bmatrix}, \mathbf{h}^{I^*} = \begin{bmatrix} \rho^* w^* \\ \rho^* w^* u^* \\ \rho^* w^* v^* \\ \rho^* w^{*2} + p^* \\ \left(E_S^* + p^*\right) w^* \end{bmatrix}, \tag{D.26}$$

$$\mathbf{f}^{V^*} = \begin{bmatrix} 0 \\ \tau_{xx}^* \\ \tau_{yx}^* \\ \tau_{zx}^* \\ \Pi_x^* \end{bmatrix}, \ \mathbf{g}^{V^*} = \begin{bmatrix} 0 \\ \tau_{xy}^* \\ \tau_{yy}^* \\ \tau_{zy}^* \\ \Pi_y^* \end{bmatrix}, \mathbf{h}^{V^*} = \begin{bmatrix} 0 \\ \tau_{xz}^* \\ \tau_{yz}^* \\ \tau_{zz}^* \\ \Pi_z^* \end{bmatrix}. \tag{D.27}$$

The superscript "*" denoting the dimensionless quantities will be omitted in the following appendixes and also in the chapters after Chapter 2.2. We always consider the non-dimensional form in this thesis unless it is specially specified.

E Curvilinear Transformation

To simplify the implementation of boundary conditions and to enhance the efficiency and accuracy of numerical schemes, the physical space in Cartesian coordinates (*x, y, z, t*) is transformed into the computational space in curvilinear coordinates (ξ, η, ζ, τ). Correspondingly, the Navier-Stokes equation is also transformed in the following sections [45, 84].

E.1 Coordinate Transformation

Let's define the transformation from (ξ, η, ζ, τ) coordinates into coordinates (*x*, *y*, *z*, *t*) as:

$$t = \tau, \tag{E.1}$$

$$x = x(\xi, \eta, \zeta, \tau), \tag{E.2}$$

$$y = y(\xi, \eta, \zeta, \tau), \tag{E.3}$$

$$z = z(\xi, \eta, \zeta, \tau). \tag{E.4}$$

The inverse transformation can be written as:

$$\tau = t, \tag{E.5}$$

$$\xi = \xi(x, y, z, t), \tag{E.6}$$

$$\eta = \eta(x, y, z, t), \tag{E.7}$$

$$\zeta = \zeta(x, y, z, t). \tag{E.8}$$

From the definition of the total differential, we have

$$\begin{pmatrix} dt \\ dx \\ dy \\ dz \end{pmatrix} = \begin{pmatrix} 1 & 0 & 0 & 0 \\ x_\tau & x_\xi & x_\eta & x_\zeta \\ y_\tau & y_\xi & y_\eta & y_\zeta \\ z_\tau & z_\xi & z_\eta & z_\zeta \end{pmatrix} \begin{pmatrix} d\tau \\ d\xi \\ d\eta \\ d\zeta \end{pmatrix}, \tag{E.9}$$

$$\begin{pmatrix} d\tau \\ d\xi \\ d\eta \\ d\zeta \end{pmatrix} = \begin{pmatrix} 1 & 0 & 0 & 0 \\ \xi_t & \xi_x & \xi_y & \xi_z \\ \eta_t & \eta_x & \eta_y & \eta_z \\ \zeta_t & \zeta_x & \zeta_y & \zeta_z \end{pmatrix} \begin{pmatrix} dt \\ dx \\ dy \\ dz \end{pmatrix}. \tag{E.10}$$

Substituting Eq. (E.9) into Eq. (E.10), one concludes

$$\mathbf{J} \equiv \begin{pmatrix} 1 & 0 & 0 & 0 \\ x_\tau & x_\xi & x_\eta & x_\zeta \\ y_\tau & y_\xi & y_\eta & y_\zeta \\ z_\tau & z_\xi & z_\eta & z_\zeta \end{pmatrix} = \begin{pmatrix} 1 & 0 & 0 & 0 \\ \xi_t & \xi_x & \xi_y & \xi_z \\ \eta_t & \eta_x & \eta_y & \eta_z \\ \zeta_t & \zeta_x & \zeta_y & \zeta_z \end{pmatrix}^{-1}. \tag{E.11}$$

Equation (E.11) transfers the metrics to be calculated in (ξ, η, ζ, τ) coordinates as

$$\xi_x = J^{-1}\left(y_\eta z_\zeta - z_\eta y_\zeta\right), \quad \xi_y = J^{-1}\left(z_\eta x_\zeta - x_\eta z_\zeta\right), \quad \xi_z = J^{-1}\left(x_\eta y_\zeta - y_\eta x_\zeta\right), \tag{E.12}$$

$$\xi_t = J^{-1}\left[x_\tau\left(y_\zeta z_\eta - y_\eta z_\zeta\right) + y_\tau\left(x_\eta z_\zeta - x_\zeta z_\eta\right) + z_\tau\left(x_\zeta y_\eta - x_\eta y_\zeta\right)\right], \tag{E.13}$$

$$\eta_x = J^{-1}\left(z_\xi y_\zeta - y_\xi z_\zeta\right), \quad \eta_y = J^{-1}\left(x_\xi z_\zeta - z_\xi x_\zeta\right), \quad \eta_z = J^{-1}\left(x_\zeta y_\xi - y_\zeta x_\xi\right), \tag{E.14}$$

$$\eta_t = J^{-1}\left[x_\tau\left(y_\xi z_\zeta - y_\zeta z_\varsigma\right) + y_\tau\left(x_\zeta z_\xi - x_\xi z_\zeta\right) + z_\tau\left(x_\xi y_\zeta - x_\zeta y_\xi\right)\right], \tag{E.15}$$

$$\zeta_x = J^{-1}\left(y_\xi z_\eta - z_\xi y_\eta\right), \quad \zeta_y = J^{-1}\left(x_\eta z_\xi - z_\mu x_\xi\right), \quad \zeta_z = J^{-1}\left(x_\xi y_\eta - y_\xi x_\eta\right), \tag{E.16}$$

$$\zeta_t = J^{-1}\left[x_\tau\left(y_\eta z_\xi - y_\xi z_\eta\right) + y_\tau\left(x_\xi z_\eta - x_\eta z_\xi\right) + z_\tau\left(x_\eta y_\xi - x_\xi y_\eta\right)\right], \tag{E.17}$$

where the Jacobian determinant of transformation J is defined by

$$J = |\mathbf{J}| = \frac{\partial(t, x, y, z)}{\partial(\tau, \xi, \eta, \zeta)} = x_\xi\left(y_\eta z_\zeta - z_\eta y_\zeta\right) - y_\xi\left(x_\eta z_\zeta - z_\eta x_\zeta\right) + z_\xi\left(x_\eta y_\zeta - y_\eta x_\zeta\right). \tag{E.18}$$

In unsteady process, ξ_t, η_t, and ς_t are the velocities of moving meshes. The practical calculations of the metrics β_i ($\beta = \xi, \eta, \zeta, \tau$ and i = *x, y, z, t*), which is used in software FLMNAV, have been discussed in Chapter 3.1.

The chain rule of partial differentiation transfers the derivatives in the Cartesian coordinates to the derivatives in the curvilinear coordinates

$$\frac{\partial}{\partial x} = \xi_x \frac{\partial}{\partial \xi} + \eta_x \frac{\partial}{\partial \eta} + \zeta_x \frac{\partial}{\partial \zeta}, \tag{E.19}$$

$$\frac{\partial}{\partial y} = \xi_y \frac{\partial}{\partial \xi} + \eta_y \frac{\partial}{\partial \eta} + \zeta_y \frac{\partial}{\partial \zeta}, \tag{E.20}$$

$$\frac{\partial}{\partial z} = \xi_z \frac{\partial}{\partial \xi} + \eta_z \frac{\partial}{\partial \eta} + \zeta_z \frac{\partial}{\partial \zeta}, \tag{E.21}$$

$$\frac{\partial}{\partial t} = \frac{\partial}{\partial \tau} + \xi_t \frac{\partial}{\partial \xi} + \eta_t \frac{\partial}{\partial \eta} + \zeta_t \frac{\partial}{\partial \zeta}. \tag{E.22}$$

E.2 Dimensionless and Curvilinear NS Equations

Using formulas (E.19) - (E.22), the Navier-Stokes vector equation (D.25) could be written in curvilinear system as

$$\begin{aligned}
&\frac{\partial \mathbf{q}}{\partial \tau} + \xi_t \frac{\partial \mathbf{q}}{\partial \xi} + \eta_t \frac{\partial \mathbf{q}}{\partial \eta} + \zeta_t \frac{\partial \mathbf{q}}{\partial \zeta} \\
&+ \xi_x \frac{\partial(\mathbf{f}^I - \mathbf{f}^V)}{\partial \xi} + \eta_x \frac{\partial(\mathbf{f}^I - \mathbf{f}^V)}{\partial \eta} + \zeta_x \frac{\partial(\mathbf{f}^I - \mathbf{f}^V)}{\partial \zeta} \\
&+ \xi_y \frac{\partial(\mathbf{g}^I - \mathbf{g}^V)}{\partial \xi} + \eta_y \frac{\partial(\mathbf{g}^I - \mathbf{g}^V)}{\partial \eta} + \zeta_y \frac{\partial(\mathbf{g}^I - \mathbf{g}^V)}{\partial \zeta} \\
&+ \xi_z \frac{\partial(\mathbf{h}^I - \mathbf{h}^V)}{\partial \xi} + \eta_z \frac{\partial(\mathbf{h}^I - \mathbf{h}^V)}{\partial \eta} + \zeta_z \frac{\partial(\mathbf{h}^I - \mathbf{h}^V)}{\partial \zeta} = 0.
\end{aligned} \tag{E.23}$$

Eqs. (E.13), (E.15), and (E.17) lead to a helpful identity

$$\frac{\partial J}{\partial \tau}+\frac{\partial (J\xi_t)}{\partial \xi}+\frac{\partial (J\eta_t)}{\partial \eta}+\frac{\partial (J\zeta_t)}{\partial \zeta}=0. \tag{E.24}$$

Multiplying the Jacobian determinant of transformation J to two sides of the equation Eq. (E.23), and using Eqs. (E.12) - (E.17) and (E.24), the non-conservation form of Navier-Stokes equation Eq. (E.23) could be reorganized into a conservation form:

$$\begin{aligned}&\frac{\partial}{\partial \tau}(J\mathbf{q})+\frac{\partial}{\partial \xi}\left[J\left(\xi_t\mathbf{q}+\xi_x(\mathbf{f}^I-\mathbf{f}^V)+\xi_y(\mathbf{g}^I-\mathbf{g}^V)+\xi_z(\mathbf{h}^I-\mathbf{h}^V)\right)\right]\\&+\frac{\partial}{\partial \eta}\left[J\left(\eta_t\mathbf{q}+\eta_x(\mathbf{f}^I-\mathbf{f}^V)+\eta_y(\mathbf{g}^I-\mathbf{g}^V)+\eta_z(\mathbf{h}^I-\mathbf{h}^V)\right)\right]\\&+\frac{\partial}{\partial \zeta}\left[J\left(\zeta_t\mathbf{q}+\zeta_x(\mathbf{f}^I-\mathbf{f}^V)+\zeta_y(\mathbf{g}^I-\mathbf{g}^V)+\zeta_z(\mathbf{h}^I-\mathbf{h}^V)\right)\right]=0.\end{aligned} \tag{E.25}$$

The solution variables $\mathbf{Q}=J\mathbf{q}=J(\rho,\rho u,\rho v,\rho w,E_S)^T$ and the inviscid terms as

$$\mathbf{F}^I=J\left(\xi_t\mathbf{q}+\xi_x\mathbf{f}^I+\xi_y\mathbf{g}^I+\xi_z\mathbf{h}^I\right), \tag{E.26}$$

$$\mathbf{G}^I=J\left(\eta_t\mathbf{q}+\eta_x\mathbf{f}^I+\eta_y\mathbf{g}^I+\eta_z\mathbf{h}^I\right), \tag{E.27}$$

$$\mathbf{H}^I=J\left(\zeta_t\mathbf{q}+\zeta_x\mathbf{f}^I+\zeta_y\mathbf{g}^I+\zeta_z\mathbf{h}^I\right). \tag{E.28}$$

The contravariant velocities are given as

$$U=\xi_x u+\xi_y v+\xi_z w+\xi_t, \tag{E.29}$$

$$V=\eta_x u+\eta_y v+\eta_z w+\eta_t, \tag{E.30}$$

$$W=\zeta_x u+\zeta_y v+\zeta_z w+\zeta_t. \tag{E.31}$$

Associate Eqs. (E.26) - (E.31) with (D.26) - (D.27). The dimensionless superscripts "*" in the latter equations are neglected. Then we have

$$\mathbf{F}^I=J\begin{pmatrix}\rho U\\ \rho uU+\xi_x p\\ \rho vU+\xi_y p\\ \rho wU+\xi_z p\\ U(E_S+p)-\xi_t p\end{pmatrix},\ \mathbf{G}^I=J\begin{pmatrix}\rho V\\ \rho uV+\eta_x p\\ \rho vV+\eta_y p\\ \rho wV+\eta_z p\\ V(E_S+p)-\eta_t p\end{pmatrix},\ \mathbf{H}^I=J\begin{pmatrix}\rho W\\ \rho uW+\zeta_x p\\ \rho vW+\zeta_y p\\ \rho vW+\zeta_z p\\ W(E_S+p)-\zeta_t p\end{pmatrix}. \tag{E.32}$$

In the same way, viscous terms are expressed as

$$\mathbf{F}^V=J\left(\xi_x\mathbf{f}^V+\xi_y\mathbf{g}^V+\xi_z\mathbf{h}^V\right), \tag{E.33}$$

$$\mathbf{G}^V=J\left(\eta_x\mathbf{f}^V+\eta_y\mathbf{g}^V+\eta_z\mathbf{h}^V\right), \tag{E.34}$$

$$\mathbf{H}^V = J\left(\zeta_x \mathbf{f}^V + \zeta_y \mathbf{g}^V + \zeta_z \mathbf{h}^V\right). \tag{E.35}$$

After reorganizing

$$\mathbf{F}^V = J\begin{pmatrix} 0 \\ \Pi_1 \\ \Pi_2 \\ \Pi_3 \\ u\Pi_1 + v\Pi_2 + w\Pi_3 - \Pi_{10} \end{pmatrix}, \tag{E.36}$$

$$\mathbf{G}^V = J\begin{pmatrix} 0 \\ \Pi_4 \\ \Pi_5 \\ \Pi_6 \\ u\Pi_4 + v\Pi_5 + w\Pi_6 - \Pi_{11} \end{pmatrix}, \tag{E.37}$$

$$\mathbf{H}^V = J\begin{pmatrix} 0 \\ \Pi_7 \\ \Pi_8 \\ \Pi_9 \\ u\Pi_7 + v\Pi_8 + w\Pi_9 - \Pi_{12} \end{pmatrix}, \tag{E.38}$$

where

$$\Pi_1 = \xi_x\tau_{x,x} + \xi_y\tau_{y,x} + \xi_z\tau_{z,x}, \Pi_2 = \xi_x\tau_{x,y} + \xi_y\tau_{y,y} + \xi_z\tau_{z,y}, \Pi_3 = \xi_x\tau_{x,z} + \xi_y\tau_{y,z} + \xi_z\tau_{z,z}, \tag{E.39}$$

$$\Pi_4 = \eta_x\tau_{x,x} + \eta_y\tau_{y,x} + \eta_z\tau_{z,x}, \Pi_5 = \eta_x\tau_{x,y} + \eta_y\tau_{y,y} + \eta_z\tau_{z,y}, \Pi_6 = \eta_x\tau_{x,z} + \eta_y\tau_{y,z} + \eta_z\tau_{z,z}, \tag{E.40}$$

$$\Pi_7 = \zeta_x\tau_{x,x} + \zeta_y\tau_{y,x} + \zeta_z\tau_{z,x}, \Pi_8 = \zeta_x\tau_{x,y} + \zeta_y\tau_{y,y} + \zeta_z\tau_{z,y}, \Pi_9 = \zeta_x\tau_{x,z} + \zeta_y\tau_{y,z} + \zeta_z\tau_{z,z}, \tag{E.41}$$

$$\Pi_{10} = \xi_x q_x + \xi_y q_y + \xi_z q_z, \quad \Pi_{11} = \eta_x q_x + \eta_y q_y + \eta_z q_z, \quad \Pi_{12} = \zeta_x q_x + \zeta_y q_y + \zeta_z q_z. \tag{E.42}$$

In the curvilinear system, the stresses are presented as

$$\tau_{xx} = \frac{\mu}{Re_\infty}\left[\frac{4}{3}\left(\xi_x u_\xi + \eta_x u_\eta + \zeta_x u_\zeta\right) - \frac{2}{3}\left(\xi_y v_\xi + \eta_y v_\eta + \zeta_y v_\zeta\right) - \frac{2}{3}\left(\xi_z w_\xi + \eta_z w_\eta + \zeta_z w_\zeta\right)\right], \tag{E.43}$$

$$\tau_{yy}=\frac{\mu}{Re_\infty}\left[\frac{4}{3}\left(\xi_y v_\xi+\eta_y v_\eta+\zeta_y v_\zeta\right)-\frac{2}{3}\left(\xi_x u_\xi+\eta_x u_\eta+\zeta_x u_\zeta\right)-\frac{2}{3}\left(\xi_z w_\xi+\eta_z w_\eta+\zeta_z w_\zeta\right)\right], \tag{E.44}$$

$$\tau_{zz}=\frac{\mu}{Re_\infty}\left[\frac{4}{3}\left(\xi_z w_\xi+\eta_z w_\eta+\zeta_z w_\zeta\right)-\frac{2}{3}\left(\xi_x u_\xi+\eta_x u_\eta+\zeta_x u_\zeta\right)-\frac{2}{3}\left(\xi_y v_\xi+\eta_y v_\eta+\zeta_y v_\zeta\right)\right], \tag{E.45}$$

$$\tau_{xy}=\tau_{yx}=\frac{\mu}{Re_\infty}\left(\xi_y u_\xi+\eta_y u_\eta+\zeta_y u_\zeta+\xi_x v_\xi+\eta_x v_\eta+\zeta_x v_\zeta\right), \tag{E.46}$$

$$\tau_{xz}=\tau_{zx}=\frac{\mu}{Re_\infty}\left(\xi_z u_\xi+\eta_z u_\eta+\zeta_z u_\zeta+\xi_x w_\xi+\eta_x w_\eta+\zeta_x w_\zeta\right), \tag{E.47}$$

$$\tau_{yz}=\tau_{zy}=\frac{\mu}{Re_\infty}\left(\xi_z v_\xi+\eta_z v_\eta+\zeta_z v_\zeta+\xi_y w_\xi+\eta_y w_\eta+\zeta_y w_\zeta\right). \tag{E.48}$$

The heat conduct terms are rewritten as

$$q_x=-\frac{\mu}{\mathrm{Pr}\cdot Re_\infty(\gamma-1)M_\infty^2}(\xi_x T_\xi+\eta_x T_\eta+\zeta_x T_\zeta), \tag{E.49}$$

$$q_y=-\frac{\mu}{\mathrm{Pr}\cdot Re_\infty(\gamma-1)M_\infty^2}(\xi_y T_\xi+\eta_y T_\eta+\zeta_y T_\zeta), \tag{E.50}$$

$$q_z=-\frac{\mu}{\mathrm{Pr}\cdot Re_\infty(\gamma-1)M_\infty^2}(\xi_z T_\xi+\eta_z T_\eta+\zeta_z T_\zeta). \tag{E.51}$$

Finally we rewrite the conservation form of the dimensionless Navier-Stokes vector equation in curvilinear coordinate as:

$$\frac{\partial\mathbf{Q}}{\partial\tau}+\frac{\partial\left(\mathbf{F}^I-\mathbf{F}^V\right)}{\partial\xi}+\frac{\partial\left(\mathbf{G}^I-\mathbf{G}^V\right)}{\partial\eta}+\frac{\partial\left(\mathbf{H}^I-\mathbf{H}^V\right)}{\partial\zeta}=0. \tag{E.52}$$

F Quasi-Linear Euler Equations

From Eq. (E.52), the non-conservation form of Euler equation system [79] can be derived as:

$$\frac{\partial \mathbf{Q}}{\partial \tau}+\frac{\partial \mathbf{F}^I}{\partial \mathbf{Q}}\frac{\partial \mathbf{Q}}{\partial \xi}+\frac{\partial \mathbf{G}^I}{\partial \mathbf{Q}}\frac{\partial \mathbf{Q}}{\partial \eta}+\frac{\partial \mathbf{H}^I}{\partial \mathbf{Q}}\frac{\partial \mathbf{Q}}{\partial \zeta}=0, \tag{F.1}$$

where $\mathbf{Q}=J(\rho,\rho u,\rho v,\rho w,E_S)^T$. We abbreviate $\mathbf{Q}:=J(\rho,l,m,n,E_S)^T$. Then

$$\frac{\partial \mathbf{F}^I}{\partial \mathbf{Q}}=\frac{1}{J}\left(\frac{\partial \mathbf{F}^I}{\partial \rho},\frac{\partial \mathbf{F}^I}{\partial l},\frac{\partial \mathbf{F}^I}{\partial m},\frac{\partial \mathbf{F}^I}{\partial n},\frac{\partial \mathbf{F}^I}{\partial E_S}\right). \tag{F.2}$$

We define

$$\boldsymbol{K}(k)=\boldsymbol{I}\cdot k_t+$$

$$\begin{bmatrix} 0 & k_x & k_y & k_z & 0 \\ k_x\phi-u\theta_k^* & \theta_k^*+(2-\gamma)k_x u & k_y u-(\gamma-1)k_x v & k_z u-(\gamma-1)k_x w & (\gamma-1)k_x \\ k_y\phi-v\theta_k^* & k_x v-(\gamma-1)k_y u & \theta_k^*+(2-\gamma)k_y v & k_z v-(\gamma-1)k_y w & (\gamma-1)k_y \\ k_z\phi-w\theta_k^* & k_x w-(\gamma-1)k_z u & k_y w-(\gamma-1)k_z v & \theta_k^*+(2-\gamma)k_z w & (\gamma-1)k_z \\ (2\phi-\frac{\gamma e}{\rho})\theta_k^* & (\frac{\gamma e}{\rho}-\phi)k_x-(\gamma-1)\theta_k^* u & (\frac{\gamma e}{\rho}-\phi)k_y-(\gamma-1)\theta_k^* v & (\frac{\gamma e}{\rho}-\phi)k_z-(\gamma-1)\theta_k^* w & \gamma\theta_k^* \end{bmatrix},$$

$$\text{with } k=\xi,\eta,\varsigma, \tag{F.3}$$

where $\boldsymbol{I}$ is the unit matrix, $\theta_k^*=k_x u+k_y v+k_z w$, $\phi=\frac{k-1}{2}(u^2+v^2+w^2)$, and the ratio of specific heats $\gamma=c_p/c_v$ [79]. We could derive

$$\frac{\partial \mathbf{F}^I}{\partial \mathbf{Q}}=\boldsymbol{K}(\xi),\ \frac{\partial \mathbf{G}^I}{\partial \mathbf{Q}}=\boldsymbol{K}(\eta),\ \frac{\partial \mathbf{H}^I}{\partial \mathbf{Q}}=\boldsymbol{K}(\varsigma). \tag{F.4}$$

Let $\boldsymbol{M}:=\frac{\partial \mathbf{Q}}{\partial \boldsymbol{q}}$ with $\boldsymbol{q}=J(\rho,u,v,w,p)^T$. It results

$$\boldsymbol{M}=\begin{bmatrix} 1 & 0 & 0 & 0 & 0 \\ u & \rho & 0 & 0 & 0 \\ v & 0 & \rho & 0 & 0 \\ w & 0 & 0 & \rho & 0 \\ \frac{\phi}{\gamma-1} & \rho u & \rho v & \rho w & \frac{1}{\gamma-1} \end{bmatrix}, \tag{F.5}$$

and

$$\boldsymbol{M}^{-1}=\begin{bmatrix} 1 & 0 & 0 & 0 & 0 \\ -\dfrac{u}{\rho} & \dfrac{1}{\rho} & 0 & 0 & 0 \\ -\dfrac{v}{\rho} & 0 & \dfrac{1}{\rho} & 0 & 0 \\ -\dfrac{w}{\rho} & 0 & 0 & \dfrac{1}{\rho} & 0 \\ \phi & -u(\gamma-1) & -v(\gamma-1) & -w(\gamma-1) & (\gamma-1) \end{bmatrix}. \tag{F.6}$$

Multiplying $\boldsymbol{M}^{-1}$ on the left side of equation Eq. (F.1), we obtain

$$\frac{\partial \boldsymbol{q}}{\partial \tau}+\boldsymbol{M}^{-1}\cdot\boldsymbol{K}(\xi)\cdot\boldsymbol{M}\frac{\partial \boldsymbol{q}}{\partial \xi}+\boldsymbol{M}^{-1}\cdot\boldsymbol{K}(\eta)\cdot\boldsymbol{M}\frac{\partial \boldsymbol{q}}{\partial \eta}+\boldsymbol{M}^{-1}\cdot\boldsymbol{K}(\varsigma)\cdot\boldsymbol{M}\frac{\partial \boldsymbol{q}}{\partial \zeta}=0. \tag{F.7}$$

Given

$$\boldsymbol{k}(k):=\begin{bmatrix} \theta_k & k_x\rho & k_y\rho & k_z\rho & 0 \\ 0 & \theta_k & 0 & 0 & \dfrac{k_x}{\rho} \\ 0 & 0 & \theta_k & 0 & \dfrac{k_y}{\rho} \\ 0 & 0 & 0 & \theta_k & \dfrac{k_z}{\rho} \\ 0 & \gamma k_x p & \gamma k_y p & \gamma k_z p & \theta_k \end{bmatrix}, \quad \text{for } k=\xi,\eta,\varsigma, \tag{F.8}$$

it could be proved that

$$\boldsymbol{M}^{-1}\cdot\boldsymbol{K}(\xi)\cdot\boldsymbol{M}=\boldsymbol{k}(\xi),\ \ \boldsymbol{M}^{-1}\cdot\boldsymbol{K}(\eta)\cdot\boldsymbol{M}=\boldsymbol{k}(\eta),\ \ \boldsymbol{M}^{-1}\cdot\boldsymbol{K}(\varsigma)\cdot\boldsymbol{M}=\boldsymbol{k}(\zeta). \tag{F.9}$$

Finally, the non-conservation form of the Euler vector equation is obtained as

$$\frac{\partial \boldsymbol{q}}{\partial \tau}+\boldsymbol{k}(\xi)\frac{\partial \boldsymbol{q}}{\partial \xi}+\boldsymbol{k}(\eta)\frac{\partial \boldsymbol{q}}{\partial \eta}+\boldsymbol{k}(\varsigma)\frac{\partial \boldsymbol{q}}{\partial \zeta}=0. \tag{F.10}$$

The above vector equation Eq. (F.10) is widely used to determine the characteristic boundary conditions.

G Initial and Boundary Conditions

Initial and boundary conditions are needed to solve Navier-Stokes equation systems. There exists still no general initial and boundary conditions suitable for any Navier-Stokes system. There are six state variables. They are three dimensional velocity components, density, temperature, and pressure. From the state equation, anyone of them could be derived by the others.

In this thesis, a steady flow is simulated by an unsteady process. Its initial values are assigned as the same as in freestream in all computing domain. Usually this assumption should not affect the solution, but may affect the convergent speed.

Using quasi-linear Euler equations, characteristic boundary conditions [21, 40, 95] are derived in this chapter. They are applied for both Euler equations and Navier-Stokes equations.

G.1 Characteristic Variables

Characteristic boundary conditions are derived from the non-conservation form of the Euler vector equation (F.10). It is assumed that the flow is one-dimension locally. To simplifying the derivation, the speed of sound is noted as $a = \sqrt{\frac{\gamma p}{\rho}}$. It is further abbreviated that $\sigma := \frac{\rho}{\sqrt{2}a}$, $\upsilon := \frac{1}{\sqrt{2}\rho \cdot a}$. For any $k = \xi, \eta, \varsigma$, $\nabla k := k_x \vec{e}_x + k_y \vec{e}_y + k_z \vec{e}_z$ and $|\nabla k| := \sqrt{k_x^2 + k_y^2 + k_z^2}$, where $\vec{e}_x$, $\vec{e}_y$, $\vec{e}_z$ are the unit vectors in *x*, *y*, *z* axes. The unit vector

$$\vec{e}(k) = \frac{\nabla k}{|\nabla k|} = \frac{k_x \vec{e}_x + k_y \vec{e}_y + k_z \vec{e}_z}{(k_x^2 + k_y^2 + k_z^2)^{1/2}}, \text{ for } k = \xi, \eta, \varsigma. \tag{G.1}$$

We also define

$$\boldsymbol{P}(k) := \begin{bmatrix} \tilde{k}_x & \tilde{k}_y & \tilde{k}_z & \sigma & \sigma \\ 0 & -\tilde{k}_z & \tilde{k}_y & \frac{\tilde{k}_x}{\sqrt{2}} & -\frac{\tilde{k}_x}{\sqrt{2}} \\ \tilde{k}_x & 0 & -\tilde{k}_x & \frac{\tilde{k}_y}{\sqrt{2}} & -\frac{\tilde{k}_y}{\sqrt{2}} \\ -\tilde{k}_y & \tilde{k}_x & 0 & \frac{\tilde{k}_z}{\sqrt{2}} & -\frac{\tilde{k}_z}{\sqrt{2}} \\ 0 & 0 & 0 & \sigma a^2 & \sigma a^2 \end{bmatrix}, \tag{G.2}$$

where $\tilde{k}_i := \frac{k_i}{|\nabla k|}$, for $k = \xi, \eta, \varsigma$, and $i = x, y, z$. We get its inverse matrix

$$\boldsymbol{P}^{-1}(k)=\begin{bmatrix} \tilde{k}_x & 0 & \tilde{k}_z & -\tilde{k}_y & -\dfrac{\tilde{k}_x}{a^2} \\ \tilde{k}_y & -\tilde{k}_z & 0 & \tilde{k}_x & -\dfrac{\tilde{k}_y}{a^2} \\ \tilde{k}_z & \tilde{k}_y & -\tilde{k}_x & 0 & -\dfrac{\tilde{k}_z}{a^2} \\ 0 & \dfrac{\tilde{k}_x}{\sqrt{2}} & \dfrac{\tilde{k}_y}{\sqrt{2}} & \dfrac{\tilde{k}_z}{\sqrt{2}} & \upsilon \\ 0 & -\dfrac{\tilde{k}_x}{\sqrt{2}} & -\dfrac{\tilde{k}_y}{\sqrt{2}} & -\dfrac{\tilde{k}_z}{\sqrt{2}} & \upsilon \end{bmatrix}. \tag{G.3}$$

Given the diagonal eigenvalue matrix as:

$$\boldsymbol{\Lambda}(k)=\begin{bmatrix} \lambda_1(k) & 0 & 0 & 0 & 0 \\ 0 & \lambda_2(k) & 0 & 0 & 0 \\ 0 & 0 & \lambda_3(k) & 0 & 0 \\ 0 & 0 & 0 & \lambda_4(k) & 0 \\ 0 & 0 & 0 & 0 & \lambda_5(k) \end{bmatrix}, \text{ for } k=\xi,\eta,\varsigma, \tag{G.4}$$

the matrix $\boldsymbol{k}(\xi)$, $\boldsymbol{k}(\eta)$, $\boldsymbol{k}(\varsigma)$ in non-conservation form Eq. (F.10) can be transformed as:

$$\boldsymbol{k}(\xi)=\boldsymbol{P}(\xi)\cdot\boldsymbol{\Lambda}(\xi)\cdot\boldsymbol{P}^{-1}(\xi),\ \boldsymbol{k}(\eta)=\boldsymbol{P}(\eta)\cdot\boldsymbol{\Lambda}(\eta)\cdot\boldsymbol{P}^{-1}(\eta),\ \boldsymbol{k}(\varsigma)=\boldsymbol{P}(\varsigma)\cdot\boldsymbol{\Lambda}(\varsigma)\cdot\boldsymbol{P}^{-1}(\varsigma). \tag{G.5}$$

Assuming one-dimensional flow along the characteristic line, substituting Eq. (G.5) into Eq. (F.10), and multiplying $\boldsymbol{P}^{-1}(k)$ on the left, we obtain

$$\boldsymbol{P}^{-1}(k)\cdot\frac{\partial\boldsymbol{q}}{\partial\tau}+\boldsymbol{\Lambda}(k)\cdot\boldsymbol{P}^{-1}(k)\cdot\frac{\partial\boldsymbol{q}}{\partial k}=0,\ \text{for } k=\xi,\eta,\varsigma. \tag{G.6}$$

The variables ρ and a in $\boldsymbol{P}^{-1}(k)$ are locally constants on the boundary as ρ_0 and a_0, respectively. Hence, $\boldsymbol{P}^{-1}(k)$ is also a constant matrix. Defining the characteristic vector as

$$\boldsymbol{W}(k):=\boldsymbol{P}^{-1}(k)\cdot\boldsymbol{q}, \tag{G.7}$$

we obtain the characteristic vector equation as

$$\frac{\partial\boldsymbol{W}(k)}{\partial\tau}+\boldsymbol{\Lambda}(k)\frac{\partial\boldsymbol{W}(k)}{\partial k}=0, \text{ for } k=\xi,\eta,\varsigma. \tag{G.8}$$

In one-dimensional form, that is

$$\frac{\partial W_l(k)}{\partial\tau}+\lambda_l(k)\frac{\partial W_l(k)}{\partial k}=0, \text{ for } k=\xi,\eta,\varsigma \text{ and } l=1,\cdots,5. \tag{G.9}$$

Their eigenvalues are

$$\lambda_1(k)=\lambda_2(k)=\lambda_3(k)=k_x u+k_y v+k_z w+k_t\equiv\theta(k), \tag{G.10}$$

$$\lambda_4(k) = \theta(k) + a \cdot |\nabla k|, \tag{G.11}$$

$$\lambda_5(k) = \theta(k) - a \cdot |\nabla k|. \tag{G.12}$$

The contravariant velocity $\theta(k)$ presents the velocity of fluid minus the velocity of moving meshes. With these eigenvalues for l=1,⋯,5, the characteristic curves are the lines $k + \lambda_l(k)\tau$ =constant, along which the eigenvectors $W_l(k)$ are conserved, where the characteristic variables $W_l(k)$ are also called Riemann invariants. With $k = \xi, \eta, \varsigma$, they are given by

$$W_1(k) = J\left[\tilde{k}_x\left(\rho - \frac{p}{a_0^2}\right) + \tilde{k}_z v - \tilde{k}_y w\right], \tag{G.13}$$

$$W_2(k) = J\left[\tilde{k}_y\left(\rho - \frac{p}{a_0^2}\right) - \tilde{k}_z u + \tilde{k}_x w\right], \tag{G.14}$$

$$W_3(k) = J\left[\tilde{k}_z\left(\rho - \frac{p}{a_0^2}\right) + \tilde{k}_y u - \tilde{k}_x v\right], \tag{G.15}$$

$$W_4(k) = \frac{J}{\sqrt{2}}\left[\frac{p}{\rho_0 a_0} + \left(\tilde{k}_x u + \tilde{k}_y v + \tilde{k}_z w\right)\right], \tag{G.16}$$

$$W_5(k) = \frac{J}{\sqrt{2}}\left[\frac{p}{\rho_0 a_0} - \left(\tilde{k}_x u + \tilde{k}_y v + \tilde{k}_z w\right)\right]. \tag{G.17}$$

The variables on the boundary with subscript 0 take their corresponding values in the last time step. The signs of the eigenvalues decide the propagation direction of their eigenvectors.

G.2 Boundary Conditions for Inflow and Outflow

In numerical simulations, the grids are fixed on the boundaries of the computing domain. The mesh velocity is usually neglected on these boundaries. Therefore, $k_t|_b = 0$ for $k = \xi, \eta, \varsigma$. In Cartesian system (x, y, z), assuming normal direction of the boundary surface with increase k is $\vec{e}(k)$, and $\vec{V} = (u, v, w)^T$, then

$$\lambda_1(k) = \lambda_2(k) = \lambda_3(k) = \theta(k) = \vec{V} \bullet \vec{e}(k) \cdot |\nabla k|, \tag{G.18}$$

$$\lambda_4(k) = (\vec{V} \bullet \vec{e}(k) + a)|\nabla k|, \tag{G.19}$$

$$\lambda_5(k) = (\vec{V} \bullet \vec{e}(k) - a)|\nabla k|. \tag{G.20}$$

Using the above formulas, the sign of the eigenvalues could be determined by the direction and magnitude of the inflow $\vec{V}$ as well as the direction of $\vec{e}(k)$. Any boundary apart away from solid surfaces could use one of the listed boundary conditions: subsonic inflow, subsonic outflow,

supersonic inflow, and supersonic outflow.

For the subsonic inflow case, the inflow and $\vec{e}(k)$ have the same directions in Figure G.1. The eigenvalues $\lambda_1(k)=\lambda_2(k)=\lambda_3(k)>0,\ \lambda_4(k)>0,$ and $\lambda_5(k)<0.$ Then the first to fourth characteristic invariant variables are transferred along the direction of the inflow and the fifth is transferred oppositely as:

$$[W_1(k)]_b=[W_1(k)]_{\text{inflow}}, \tag{G.21}$$

$$[W_2(k)]_b=[W_2(k)]_{\text{inflow}}, \tag{G.22}$$

$$[W_3(k)]_b=[W_3(k)]_{\text{inflow}}, \tag{G.23}$$

$$[W_4(k)]_b=[W_4(k)]_{\text{inflow}}, \tag{G.24}$$

$$[W_5(k)]_b=[W_5(k)]_i. \tag{G.25}$$

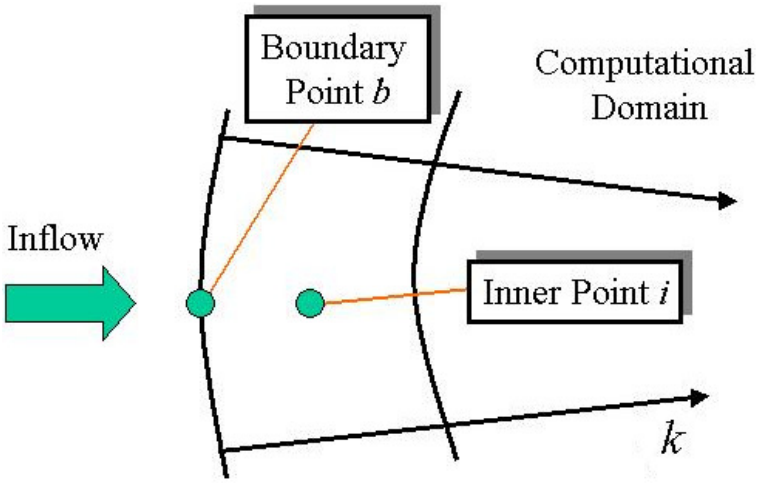

Figure G.1: The directions of k and inflow for the inlet boundary condition.

When the directions of inflow and $\vec{e}(k)$ are not the same, three eigenvalues are equal and satisfy $\lambda_1(k)=\lambda_2(k)=\lambda_3(k)<0$. The other eigenvalues keep their sign as $\lambda_4(k)>0$, and $\lambda_5(k)<0$. The first three characteristic invariant variables are transferred still along the direction of the inflow and the fourth and fifth changed their directions as:

$$[W_4(k)]_b=[W_4(k)]_i, \tag{G.26}$$

$$[W_5(k)]_b=[W_5(k)]_{\text{inflow}}. \tag{G.27}$$

On the inflow boundary, Jacobian matrixes and the components of area vectors $J\cdot k_x$, $J\cdot k_y$, $J\cdot k_z$ could be assumed as constants. Substituting Eqs. (G.13) - (G.17) into Eqs. (G.21) - (G.27), we get the inflow boundary condition for the state variables on the boundary point *b*,

$$p_b=\frac{1}{2}\left\{p_{\text{inflow}}+p_i\pm\rho_0 a_0\left[\tilde{k}_x(u_{\text{inflow}}-u_i)+\tilde{k}_y(v_{\text{inflow}}-v_i)+\tilde{k}_z(w_{\text{inflow}}-w_i)\right]\right\}, \tag{G.28}$$

$$u_b = u_{\text{inflow}} \pm \tilde{k}_x \frac{p_{\text{inflow}} - p_b}{\rho_0 a_0}, \tag{G.29}$$

$$v_b = v_{\text{inflow}} \pm \tilde{k}_y \frac{p_{\text{inflow}} - p_b}{\rho_0 a_0}, \tag{G.30}$$

$$w_b = w_{\text{inflow}} \pm \tilde{k}_z \frac{p_{\text{inflow}} - p_b}{\rho_0 a_0}, \tag{G.31}$$

$$\rho_b = \rho_{\text{inflow}} \pm \frac{p_{\text{inflow}} - p_b}{a_0^2}. \tag{G.32}$$

The options with positive sign in equations (G.28) - (G.32) refer that both the inflow direction and coordinate increasing direction are the same (cf. Figure G.1), and the options with minus sign refer oppositely.

For the subsonic out flow, we consider two cases that the outwards flow direction is the same as the direction of $\vec{e}(k)$ and the outwards flow direction is opposite to the direction of $\vec{e}(k)$. The first three invariants transferred always towards the outflow direction. We have

$$[W_1(k)]_b = [W_1(k)]_{\text{i}}, \tag{G.33}$$

$$[W_2(k)]_b = [W_2(k)]_{\text{i}}, \tag{G.34}$$

$$[W_3(k)]_b = [W_3(k)]_{\text{i}}. \tag{G.35}$$

When the out flow direction is the same as the direction of $\vec{e}(k)$,

$$[W_4(k)]_b = [W_4(k)]_{\text{i}}, \tag{G.36}$$

$$[W_5(k)]_b = [W_5(k)]_{\text{outflow}}. \tag{G.37}$$

When directions are opposite,

$$[W_4(k)]_b = [W_4(k)]_{\text{outflow}}, \tag{G.38}$$

$$[W_5(k)]_b = [W_5(k)]_{i}. \tag{G.39}$$

Nearly the same form as the inflow conditions, this yields the outflow boundary conditions

$$p_b = \frac{1}{2}\left\{p_{\text{outflow}} + p_i \pm \rho_0 a_0 \left[\tilde{k}_x (u_{\text{outflow}} - u_i) + \tilde{k}_y (v_{\text{outflow}} - v_i) + \tilde{k}_z (w_{\text{outflow}} - w_i)\right]\right\}, \tag{G.40}$$

$$u_b = u_i \pm \tilde{k}_x \frac{p_i - p_b}{\rho_0 a_0}, \tag{G.41}$$

$$v_b = v_i \pm \tilde{k}_y \frac{p_i - p_b}{\rho_0 a_0}, \tag{G.42}$$

$$w_b = w_i \pm \tilde{k}_z \frac{p_i - p_b}{\rho_0 a_0}, \tag{G.43}$$

$$\rho_b = \rho_i \pm \frac{p_i - p_b}{a_0^2}. \tag{G.44}$$

The difference about the boundary condition between inflow and outflow is: five characteristic conditions must be given for the inflow, but only one characteristic condition is needed to be given for the outflow, and the other four conditions could be given by extrapolation from the computing domain. Four state variables in outflow boundary (G.40) are needed.

The pressure could be determined in a different form. Considering no reflected outflow through far field, the pressure could be given as

$$p_b^{n+1} = p_b^n + \frac{p_i^{n+1} - p_i^n}{2} \pm \frac{\rho^n \cdot a^n}{2}\left[\tilde{k}_x\left(u_i^{n+1} - u_i^n\right) + \tilde{k}_y\left(v_i^{n+1} - v_i^n\right) + \tilde{k}_z\left(w_i^{n+1} - w_i^n\right)\right]. \tag{G.45}$$

Using Eq. (G.45) to replace Eq. (G.40) for the outflow boundary condition, no state variable is needed any more in the far field.

For the supersonic cases, the velocity of the inflow (or outflow) $\vec{V}$ is greater than the sound velocity. All of the eigenvalues $\lambda_j(k)$ (j=1,⋯,5) have the same sign derived from Eqs. (G.18) - (G.20). In these cases, the characteristic variables are always transferred in the flow direction. Not like the subsonic cases, its pressure on the boundary does not be affected by the downstream. All of the state variables p_b, u_b, v_b, w_b, ρ_b on the boundary simply take the upstream values. That means that the five extra boundary conditions are needed for the inflow, but no extra boundary conditions are needed for the outflow. The boundary condition for the outflow can be gotten from the extrapolation of the computing domain.

G.3 Euler Impermeable Boundary Conditions

In the curvilinear coordinate system, the body surfaces are usually perpendicular to the k, where $k = \xi$, or η, or ς. The contravariant velocity on the solid surface should be zero on the normal direction $\vec{e}(k)$ referring to Eq. (G.10). That is

$$\lambda_1(k) = \lambda_2(k) = \lambda_3(k) = \theta(k) = k_x u + k_y v + k_z w + k_t \equiv 0, \tag{G.46}$$

and

$$\lambda_4(k) = a\left|\nabla k\right| > 0, \tag{G.47}$$

$$\lambda_5(k) = -a\left|\nabla k\right| < 0. \tag{G.48}$$

Depending on the signs of these eigenvalues, the transfer of the characteristic variables on the boundary can be determined as following:

$$\left[W_1(k)\right]_b = \left[W_1(k)\right]_i, \tag{G.49}$$

$$\left[W_2(k)\right]_b = \left[W_2(k)\right]_i, \tag{G.50}$$

$$\left[W_3(k)\right]_b = \left[W_3(k)\right]_i, \tag{G.51}$$

When $\vec{e}(k)$ direction is pointing away from the solid surface as shown in Figure G.2.a, i.e. $\lambda_j(k)\cdot\vec{e}(k)>0$, the fourth characteristic variable is used,

$$[W_4(k)]_b = [W_4(k)]_i . \tag{G.52}$$

Otherwise, the fifth characteristic variable is used when $\vec{e}(k)$ direction goes into the solid surface as shown in Figure G.2.b.

$$[W_{k,5}]_b = [W_{k,5}]_i . \tag{G.53}$$

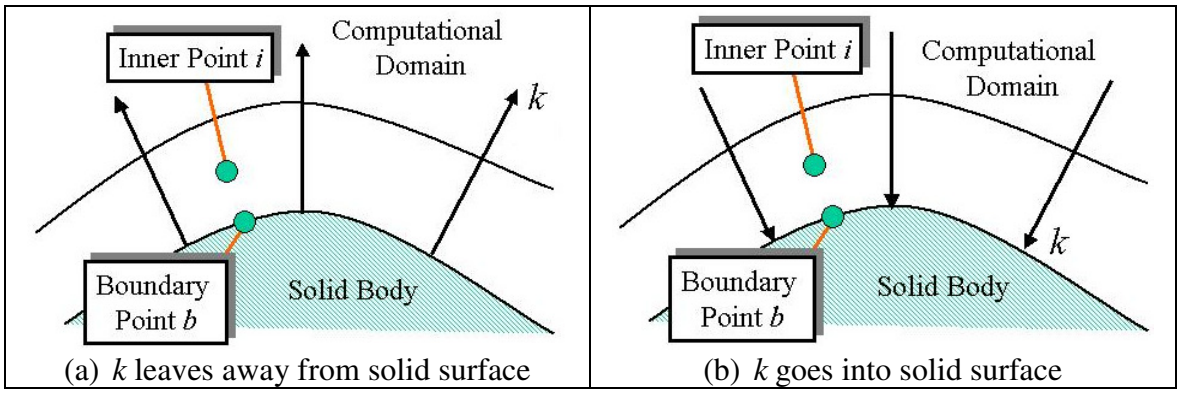

(a) k leaves away from solid surface (b) k goes into solid surface

Figure G.2: The direction of k for the boundary condition of solid surface.

There are five boundary conditions to determine five state variables. Three of them are taken from Eqs. (G.49) - (G.51), one from Eq. (G.52) or (G.53), and the fifth from $\theta(k)\equiv 0$. Finally, we get the boundary condition on the solid surface for the state variables:

$$p_b = p_i \mp p_0 a_0 \left(\tilde{k}_x u_i + \tilde{k}_y v_i + \tilde{k}_z w_i + \tilde{k}_{tb}\right), \tag{G.54}$$

$$\rho_b = \rho_i + \frac{p_b - p_i}{a_0^2}, \tag{G.55}$$

$$u_b = u_i - \tilde{k}_x \left(\tilde{k}_x u_i + \tilde{k}_y v_i + \tilde{k}_z w_i + \tilde{k}_{tb}\right), \tag{G.56}$$

$$v_b = v_i - \tilde{k}_y \left(\tilde{k}_x u_i + \tilde{k}_y v_i + \tilde{k}_z w_i + \tilde{k}_{tb}\right), \tag{G.57}$$

$$w_b = w_i - \tilde{k}_z \left(\tilde{k}_x u_i + \tilde{k}_y v_i + \tilde{k}_z w_i + \tilde{k}_{tb}\right). \tag{G.58}$$

G.4 Navier-Stokes Impermeable Boundary Conditions

In the Navier-Stokes equations, the contravariant velocity $\theta(k)$ should be zero in all three directions $\vec{e}(k)$ on the solid surface

$$\theta(k)|_b = (k_x u + k_y v + k_z w + k_t)|_b \equiv 0, \text{ for } k = \xi, \eta, \varsigma . \tag{G.59}$$

Neumann boundary condition is used for pressure

$$\frac{dp}{dn}|_b = 0 . \qquad \text{(G.60)}$$

Isothermal or adiabatic condition is specified as the boundary condition for temperature,

$$T|_b = T|_{isotherm} \text{, or } \frac{dT}{dn}|_b = 0 . \qquad \text{(G.61)}$$

There are five boundary conditions from Eqs. (G.59) - (G.60) to determine five state variables.

G.5 Symmetric Boundary Conditions

Numerically the state variables are defined on the center of every cell. Mirror points for the numerical calculation are introduced to achieve symmetry boundary conditions. They are located on the other side of the boundary as shown in Figure G.3. The state variables on the mirror point is often given as

$$\psi|_m = 2\,\psi|_b - \psi|_i , \qquad \text{(G.62)}$$

where ψ may take one of the contravariant velocities $\theta(k)$ ($k = \xi$, or η, or ς), or pressure p, or temperature T, or density ρ.

Symmetry boundary conditions are used to save computing work. The state variables are nearly the same between the inner point and the mirror point, except the component of the velocity, which is perpendicular to the symmetry surface. This velocity component on the mirror point has a different sign compared to the inner point.

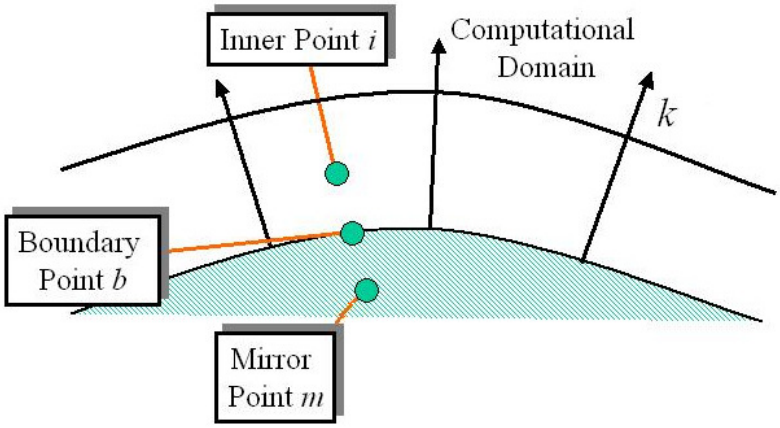

Figure G.3: The positions of mirror points for the symmetric boundary condition.

H Baldwin-Lomax Turbulence Model

Already in 1895 Osborne Reynolds began his research about the irregularity or chaotic nature in turbulent flow. He derived a time-averaged Navier-Stokes equation system. Later his followers added higher order correlations about fluctuating quantities of flow variables. They also used semi-empirical mathematical models to form a close solvable equation system [1, 17].

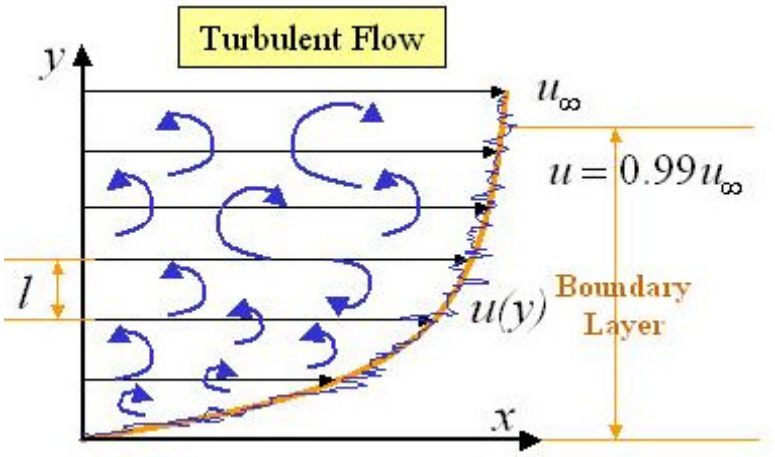

Figure H.1: The mean free path length *l* in the turbulent flow.

In 1925 Prandtl introduced the concept of the mixing-length model to explain the turbulent flow. As shown in Figure H.1, fluid particle agglomerations collide and transfer their momentum, when they move in *y*-direction across a mean free path length *l*. Based on Prandtl's work, the algebraic or zero-equation models were further developed: the viscous damping correction by Van Driest in 1956, eddy viscosity and mixing-length concept by Cebeci and Smith in 1974.

In 1978, Baldwin and Lomax improved those models with a practical computing of mixing length and got satisfied numerical results in comparisons with experiments of Mach number from 0.756 to 2.85 [7]. They replace the viscosity μ in the Navier-Stokes equations with the sum of viscosity $\mu + \mu_t$, where μ_t is an extra viscosity related to turbulence, namely eddy viscosity. Correspondingly, the coefficient of the heat conductivity is replaced by:

$$k = c_p \cdot \left(\frac{\mu}{\mathrm{Pr}} + \frac{\mu_t}{\mathrm{Pr}_t} \right), \tag{H.1}$$

where the turbulent Prandtl number Pr_t is 0.9 for the air in B-L model. For other fluids, it usually ranges from 0.6 to 1.0. Actually, it is a ratio of eddy viscosity and eddy thermal diffusivity.

The main task of the Baldwin-Lomax (B-L) Model is to determine the eddy viscosity μ_t related with Reynolds stress. It is actually a two-layer algebraic 0-equation model. In the layer near the wall, the Prandtl model is used. In the outer layer, μ_t is determined by empirical functions and constants. Baldwin and Lomax give

$$\mu_t = \begin{cases} (\mu_t)_{inner} & if \quad y \le y_{crossover} \\ (\mu_t)_{outer} & if \quad y > y_{crossover} \end{cases}, \tag{H.2}$$

where $y_{crossover}$ is the smallest distance from the surface where $(\mu_t)_{inner}$ is equal to $(\mu_t)_{outer}$. In the inner layer, μ_t is determined by mean vorticity as

$$(\mu_t)_{inner} = \rho l^2 |\omega|, \tag{H.3}$$

where the magnitude of the vorticity vector for three dimensional flows ω is given by

$$|\omega| = \sqrt{\left(\frac{\partial u}{\partial y} - \frac{\partial v}{\partial x}\right) + \left(\frac{\partial u}{\partial z} - \frac{\partial w}{\partial y}\right) + \left(\frac{\partial w}{\partial x} - \frac{\partial u}{\partial z}\right)}. \tag{H.4}$$

The mean free path length is gotten from mean flow characteristics

$$l = k \cdot y \cdot \left[1 - \exp\left(- y^+ / A^+\right)\right], \tag{H.5}$$

where $A^+ = 26$, $k = 0.4$. y is the normal distance from the wall. From the notation in the law of the wall, the dimensionless wall coordinate

$$y^+ = \frac{\sqrt{\rho_w \tau_w}}{\mu_w} y, \tag{H.6}$$

where the lower indices *w* means the point on the wall. Proportional to the gradient of flow velocity parallel to the wall $V_{parallel}$, the wall shear stress

$$\tau_w = \left(\mu \frac{\partial V_{parallel}}{\partial y}\right)_w. \tag{H.7}$$

When a point locates in the outer layer, the eddy viscosity is determined as

$$(\mu_t)_{outer} = K \cdot C_{CP} \cdot \rho \cdot F_{WAKE} \cdot F_{KLEB}(y), \tag{H.8}$$

where the Clauser constant $K = 0.0168$, and $C_{CP} = 1.6$. The wake function is

$$F_{WAKE} = \min(Y_{MAX} \cdot F_{MAX}, C_{WK} \cdot Y_{MAX} \cdot u_{DIF}^2 / F_{MAX}). \tag{H.9}$$

A Van-Driest damping function is given as

$$F(y) = y \cdot |\omega| \cdot \left[1 - \exp(-y^+ / A^+)\right]. \tag{H.10}$$

Eq. (H.10) is used to determine Y_{MAX} and F_{MAX}. Y_{MAX} is a normal distance at which maximum force F_{MAX} achieves.

The Klebanoff intermittency function is given as

$$F_{KLEB}(y) = \left[1 + 5.5\left(\frac{C_{KLEB} \cdot y}{Y_{MAX}}\right)^6\right]^{-1}. \tag{H.11}$$

The difference between maximum and minimum of total velocity in the profile is define as

$$U_{DIF} = \left(\sqrt{u^2 + v^2 + w^2}\right)_{MAX} - \left(\sqrt{u^2 + v^2 + w^2}\right)_{MIN}. \tag{H.12}$$

In the wake region, the Van-Driest damping function is defined specifically as

$$F(y) = y \cdot |\omega| \,, \tag{H.13}$$

and

$$U_{DIF} = \left(\sqrt{u^2 + v^2 + w^2}\right)_{MAX} . \tag{H.14}$$

The other used constants in the above B-L model are given as

$$C_{KLEB} = 0.3, C_{WK} = 0.25 . \tag{H.15}$$

When eddy viscosity μ_t is very small, it will be totally neglected. That is

$$\mu_t = 0, \quad if \ (\mu_t)_{\max} < 14\mu_\infty \tag{H.16}$$

Furthermore, Degani and Schiff found there may be more than one maximum solution for Y_{max}. The first Y_{max} usually shows less diffusive in Eq. (H.8). The second Y_{max} should be used, if it exists.

I Dimensionless Aerodynamic Coefficients

In aerodynamics, dimensionless force and moment coefficients are used to evaluate the dynamic properties of a flying body. The most important coefficients for the separation process are the lift coefficient C_L, the pitching moment coefficient C_M, and the drag coefficient C_D [5, 53].

$$C_L = \frac{L}{q_\infty \cdot F}, \tag{I.1}$$

$$C_M = \frac{M}{q_\infty \cdot F \cdot l_\mu}, \tag{I.2}$$

$$C_D = \frac{D}{q_\infty \cdot F}, \tag{I.3}$$

where L, M, D are the lift, pitching moment, and drag respectively. F is a reference area, and l_μ is the mean chord length.

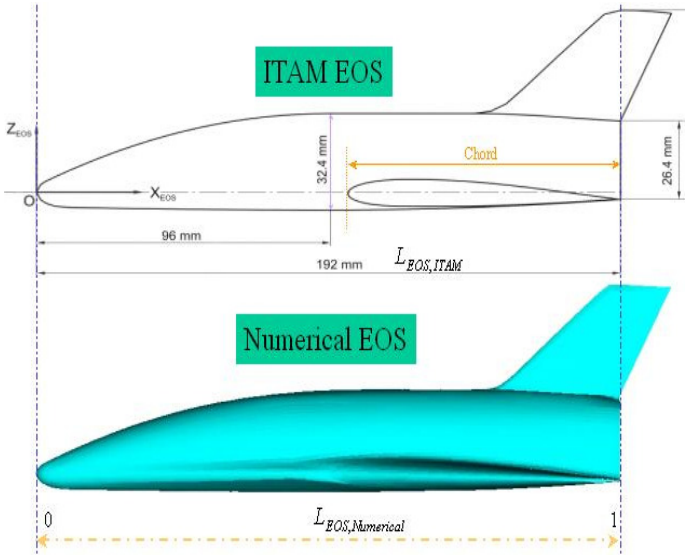

Figure I.1: The sizes of the EOS geometries.

In Figure I.1, two geometries of EOS are compared. The ITAM EOS is the definition of experimental geometry of ITAM. Its whole surface area $F_{ITAM} = 0.010644$ m^2; the mean chord length $l_{\mu,ITAM}$ =0.1270 m; the EOS length $L_{EOS,ITAM}$ =0.192 m; the span $S_{ITAM} = 0.1080$ m.

For convenience, the lower index "*Numer*" denotes a corresponding variable for the numerical model. The numerical EOS geometry is presented with the colored picture in the lower side of Figure I.1. Its EOS length is $L_{EOS,Numer} = 1$. The scale factor from experimental definition to numerical computation is

$$f_{ITAM,Numer} = \frac{L_{EOS,Numer}}{L_{EOS,ITAM}} = 5.208. \tag{I.4}$$

We could derive that the surface area $F_{Numer} = 0.288737$. The mean chord length is $l_{\mu,Numer} = 0.661458$, and the span $S_{Numer} = 0.5625$. Actually we only simulate half EOS, which is divided by the symmetric plane. For the half EOS, $F_{Numer} = 0.1443685$ and $S_{Numer} = 0.28125$.

By the density ρ_∞ and velocity V_∞, the dynamic pressure is determined in freestream as

$$q_\infty = \frac{1}{2}\rho_\infty V_\infty^2 . \tag{I.5}$$

The pressure coefficient is expressed as

$$C_p = \frac{p - p_\infty}{q_\infty} . \tag{I.6}$$

The lift and drag are calculated by the integration of the pressure and stresses along the body surface. The pitching moment is yielded by the integration of the moment on the whole body surface at a given rotation center around the *y*-axis [52, 58, 59].

From the Buckingham PI theorem in dimensional analysis, the aerodynamic coefficients for our separation process could be mainly determined by three dynamic similarity parameters: Reynolds number Re_∞, Mach number M_∞, and the angle of attack α related with a similar geometry. They are

$$C_L = f_1(Re_\infty, M_\infty, \alpha), \tag{I.7}$$

$$C_M = f_2(Re_\infty, M_\infty, \alpha), \tag{I.8}$$

$$C_D = f_3(Re_\infty, M_\infty, \alpha). \tag{I.9}$$

As seen in experiments, very small EOS configurations are used in wind tunnels to simulate the real orbital stage. When they possess the same similarity parameters, such as Re_∞, M_∞, and α, their C_L, C_M, and C_D are correspondingly the same. The forces between model and prototype are proportional with a constant scale factor. Using C_L, C_M, and C_D gotten from an arranged experiment, we could derive lift L, pitching moment M, and drag D for the orbital stage in the environment at the altitude of 35 kilometers above the sea level.

In the aerodynamic research, it is appropriate using the dimensionless force coefficients and moment coefficients other than using the forces and moments directly.

J Characteristics of the Hypersonic Flow

Conventionally the hypersonic flow is usually related with the astronautic phenomena and used to describe that vehicles fly at a high Mach number (greater than 5). The hypersonic flow is characterized as following [6]:

1) Sparse air and thin shock layers. The density decreases with the increase of the flight altitude above the sea level. The continuum assumption is challenged at high altitude. The shock layer is defined as the volume between the body and shock wave. The higher the Mach number is, the thinner the shock layer becomes. The ratio of the density before shock to the density after shock in our separation process is usually around the order of 1/7 to 1/5.

2) Strong entropy gradient layer. The stronger the shock is, the greater the entropy increases. From Crocco's theorem we have the relationship between vorticity and entropy layer:

$$\vec{V} \times (\nabla \times \vec{V}) = -T \cdot \nabla S, \tag{J.1}$$

with the flow velocity $\vec{V}$, the vorticity $\nabla \times \vec{V}$, the temperature T, and entropy S. In stronger entropy gradient layer, ∇S is greater. Consequently, the vorticity is stronger.

3) Strong viscous interaction. The boundary layer thickness δ above a flat plate could be described as

$$\delta \propto \frac{M_{\infty}^{2}}{\sqrt{\mathrm{Re}_{x}}}, \tag{J.2}$$

where M_{∞} is the Mach number in freestream and Re_{x} is a local Reynolds number. With a higher Mach number, the boundary layer is thicker.

4) High temperature. When the space vehicle comes back into atmosphere, the air is compressed and fractionized. A large amount of kinetic energy is transformed into the internal energy of the air. Then high temperature appears in the parts of blunt-nose, the leading edge of the wing, and the contour of engine.

K Standard Atmosphere Properties

The earth retains the air from sea level up to 10000 kilometers by the gravity force. According to physical properties, the atmosphere is divided into several layers by the altitude. Troposphere: from sea level to 11 km accompanying a temperature decrease; stratosphere: from 11 km to 50 km and warming up with height; mesosphere: from 50 km to 85 km and cooling down with height; thermosphere: from 85 km to 640-800 km, and exosphere: from the top of thermosphere to 22000 km. In the last two layers the particles separate very far away and their temperatures increase when altitude is higher up. The usual commercial flight is located in the troposphere. Special jet airplane could reach a height of about 24 km; weather balloons can rise to about 30 km; the designed separation altitude of TSTO vehicle is 35 km. Those three examples are located in the stratosphere. The space vehicle reentry to the atmosphere usually means that the vehicle comes back into the atmosphere at the altitude of 120 km. Higher than 120 km, the gas is hardly noticeable. The nominal circular orbit is at the altitude of about 300 km.

K.1 US Standard Atmosphere 1976

Based on the data collected by rocket and satellite as well as perfect gas theory, the model of the U.S. Standard Atmosphere was first established in 1953 by the U.S. Committee on Extension to the Standard Atmosphere (COESA). It is further revised in 1958, 1962, 1966, and 1976 [87]. It is an average, piece-wise continuous, mid-latitude profile of the earth's atmosphere. The characteristics of air used in this thesis are cited from the latest version.

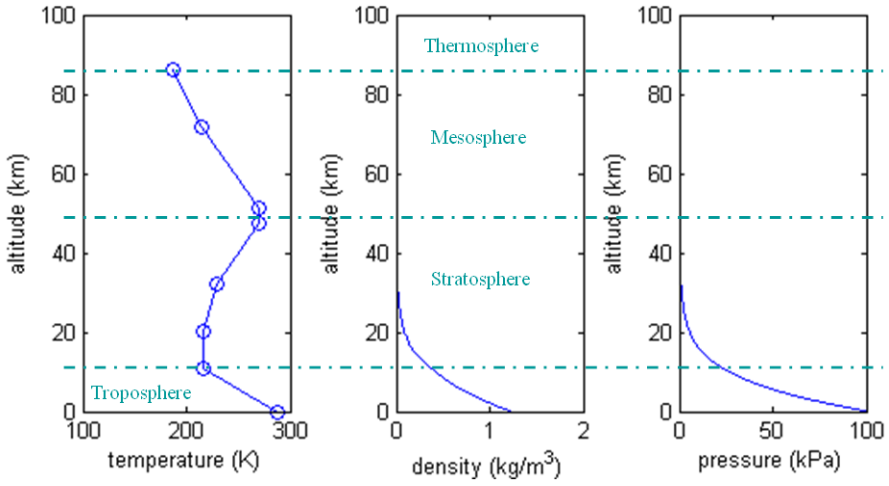

Figure K.1: The changes of air properties in the lower part of the earth's atmosphere[4].

As a function of altitude from sea level to 1000 km, these atmospheric properties include temperature, pressure, density, acceleration caused by gravity, pressure scale height, number density,

[4] Picture refers to http://en.wikipedia.org/wiki/File:Us_standard_atmosphere_model.png.

mean particle speed, mean collision frequency, mean free path length, mean molecular weight, sound speed, dynamic viscosity, kinematical viscosity, and thermal conductivity. The altitude resolution varies from 0.05 km at low altitudes to 5 km at high altitudes.

Some important properties in the lower layer of the earth's atmosphere are shown in Figure K.1. Accompanying the increase of the altitude, the pressure and density always decrease. The temperature fluctuates somewhat in different atmosphere layers. There is a tropopause in the connection part of the troposphere and stratosphere. It describes a relative stable atmosphere from 11 km to 20 km and its air temperature keeps nearly a constant around 217 K. Similarly, there is a stable stratopause in the connection part between the stratosphere and mesosphere. Its temperature is around 270 K.

It is assumed that the temperature is 288.15 K and the air pressure is 101325 Pa at the mean sea level (height = 0 km). It is further assumed that the relative humidity is zero throughout the atmosphere. The U.S. Standard Atmosphere is divided into two different parts: the lower atmosphere below altitude of 86 km and the upper atmosphere from 86 to 1000 km. In Table K.1 the pressure, temperature, and density in the lower atmosphere till 35 km are computed by a FORTRAN code listed in section K.2.

LOWER LAYER of STANDARD ATMOSPHERE

--- FROM U.S. STANDARD ATMOSPHERE, 1976

Height [METERS]	Pressure [hPa]	Temperature [DEG C]	DENSITY [KG/M3]
0.00	1013.2500	15.00	1.224999
1000.00	898.7457	8.50	1.111642
2000.00	794.9521	2.00	1.006490
3000.00	701.0854	-4.50	0.909121
4000.00	616.4023	-11.00	0.819129
5000.00	540.1991	-17.50	0.736115
6000.00	471.8103	-24.00	0.659697
7000.00	410.6074	-30.50	0.589501
8000.00	355.9981	-37.00	0.525167
9000.00	307.4246	-43.50	0.466348
10000.00	264.3627	-50.00	0.412706
11000.00	226.3206	-56.50	0.363918
12000.00	193.3041	-56.50	0.310828
13000.00	165.1041	-56.50	0.265483
14000.00	141.0180	-56.50	0.226753
15000.00	120.4457	-56.50	0.193674

16000.00	102.8746	−56.50	0.165420
17000.00	87.8668	−56.50	0.141288
18000.00	75.0484	−56.50	0.120676
19000.00	64.1001	−56.50	0.103071
20000.00	54.7489	−56.50	0.088035
21000.00	46.7789	−55.50	0.074874
22000.00	39.9979	−54.50	0.063727
23000.00	34.2243	−53.50	0.054280
24000.00	29.3049	−52.50	0.046267
25000.00	25.1102	−51.50	0.039466
26000.00	21.5309	−50.50	0.033688
27000.00	18.4746	−49.50	0.028777
28000.00	15.8629	−48.50	0.024599
29000.00	13.6296	−47.50	0.021042
30000.00	11.7187	−46.50	0.018012
31000.00	10.0823	−45.50	0.015429
32000.00	8.6802	−44.50	0.013225
33000.00	7.4823	−41.70	0.011262
34000.00	6.4612	−38.90	0.009609
35000.00	5.5892	−36.10	0.008214

Table K.1: Some important air properties in the standard atmosphere at the height from sea level till 35 km.

K.2 FORTRAN Program for Standard Atmosphere

A short and practical code[5] is listed below. It calculates the air properties not only till 35 km as shown in Table K.1, but it could also simulate the whole lower layer.

```
!
!------------------- Main Program ----------------------
!
    PROGRAM STANDARD_ATMOSPHERE
    ! Calculate the pressure, temperature,
    ! and density as a function of altitude
    ! till to 84852.0 [m]

    IMPLICIT NONE

    ! The pressure will be calculated from sea level to Km_Number
    INTEGER :: Km_Number=35    ! It should be smaller than 85
```

[5] Code refers to http://dss.ucar.edu/libraries/meteorology/stdatm76.f.

```
    REAL ::    Pressure,Altitude,Temperature_Deg_C,Density

    ! loop variable
    INTEGER :: I

1002 FORMAT("LOWER LAYER of STANDARD ATMOSPHERE ", /1x, &
           6X,'   --- FROM U.S. STANDARD ATMOSPHERE, 1976 ',/)
1007 FORMAT(1X,F12.2,3x,F12.4,3x,F10.2,3x,F14.6)
1008 FORMAT(1X,'     Height        Pressure     Temperature       DENSITY')
1009 FORMAT(1X,'    [METERS]         [hPa]        [DEG C]         [KG/M3]')

    ! Open output file
    OPEN(188, FILE="US_STANDARD_ATMOSPHERE_1976.txt")

    ! Write the title
    WRITE(188,1002)
    ! Write variable name
    WRITE(188,1008)
    ! Write unit
    WRITE(188,1009)

    ! Loop from 0 to Km_Number [km]
    DO I= 0,Km_Number

        Altitude=I*1000 ! Altitude [m]
        ! Call subroutine which calculate the pressure, temperature,
        ! and density as a function of altitude
        CALL STDZ2P(Pressure,Altitude, 0, Temperature_Deg_C, Density)

        ! Output
        WRITE (188,1007) Altitude,Pressure,Temperature_Deg_C,Density

    ENDDO

    CLOSE(188)

    END PROGRAM STANDARD_ATMOSPHERE
!
!----------------- Subroutine ------------------------
!
      SUBROUTINE STDZ2P(P,H1,L,TCENT,RHO)
!
! COMPUTES PRESSURE, TEMPERATURE, AND DENSITY VALUES FROM INPUT HEIGHTS
!  BASED ON US STANDARD ATMOSPHERE, 1976
!  VALUES NOT VALID ABOVE 84852 M.
!
! INPUT
!       H1    - HEIGHT IN FEET OR METERS
!       L     - UNITS FLAG - 0=METERS, 1=FEET
! OUTPUT
!       P     - PRESSURE IN MB
!       TCENT - TEMPERATURE IN DEG C
!       RHO   - DENSITY IN KG/M3
!
      DIMENSION HBASE(10),HTOP(10),TB(10),GRAD(10),ABS(10)
      DIMENSION PB(11),RB(10)
      DATA HBASE/ 0.,1.1E4,2.E4,3.2E4,4.7E4,5.1E4,7.1E4,3*84852.0/
      DATA HTOP /1.1E4,2.E4,3.2E4,4.7E4,5.1E4,7.1E4,4*84852.0/
      DATA TB / 15.,2*-56.5,-44.5,2*-2.5,-58.5,3*-86.2/
      DATA GRAD/-.0065,0.,.001,.0028,0.,-.0028,-.002,3*0./
      DATA CHECK/0./
!     H1 IS ALTITUDE, IF IN METERS SET L .LE. 0.  IF IN FEET SET L .GE. 1
!     P IS PRESSURE IN MB.  TCENT IS TEMP CELSIUS.  RHO IS DENSITY IN KG/M**3
```

```
!

      IF(CHECK.NE.0.) GO TO 16
      ABSZ = 273.15
      PZERO=1013.250
      G=980.665
      R = 83143200./28.9644
      PB(1) = PZERO
      DO 3  I=1,8
      ABS(I) = TB(I) + ABSZ
    3 CONTINUE
       DO 15  I=1,8
      IF (GRAD(I) .EQ. 0)  GO TO 10
!  HERE FOR TEMP GRADIENT NOT ZERO
    5 PB(I+1) = PB(I)*((ABS(I+1)/ABS(I))**(100.*G/(-GRAD(I)*R)))
      GO TO 12
!  HERE FOR TEMP GRADIENT ZERO
   10 PB(I+1) = PB(I)*2.7182818**((-100.*G/(R*ABS(I)))*(HTOP(I)-HBASE(I) ))
   12 RB(I) = 1000.*PB(I)/(R*ABS(I)) * 1000.
   15 CONTINUE
      CHECK=10.
   16 CONTINUE
!
      IF(L<1) GO TO 30
!
      H = H1*.3048
      GO TO 4
30    H = H1
4     CONTINUE
!  FIND THE ATMOSPHERIC LAYER WE ARE IN
   35 DO 55  I = 1,8
      IF  (H .GT. HBASE(I+1)) GO TO 55
   37 IF (GRAD(I)) 39,43,39
!  TEMP GRADIENT NOT ZERO
   39 P= PB(I)*((H-HBASE(I))*GRAD(I)/ABS(I)+1)**(-100.*G/(GRAD(I)*R))
      GO TO 45
!  ISOTHERMAL LAYER
   43 P= PB(I)*EXP((H-HBASE(I))*(-G)/(.01*R*ABS(I)))
   45 T = ABS(I) + GRAD(I)*(H-HBASE(I))
      TCENT = T - ABSZ
      RHO = 1.E6* P/(R*T)

      RETURN

! WRITE INFORMATION WHEN H IS TOO HIGH
   55 CONTINUE
    OPEN(189, FILE="Height_Out_of_Range.txt", POSITION="APPEND")
      WRITE(189,98)H
98    FORMAT(' STDATM -  ALTITUDE OUT OF RANGE, H>84852[km] ',F12.2,//)
    CLOSE(189)

      END SUBROUTINE STDZ2P
```

L Real Gas Effect

Using the calorically perfect gas model, the temperature in hypersonic flows is overestimated. To predict the temperature more exactly, the real gas model should be used. It considers chemical reaction, dissociation, and ionization among N_2, O_2, NO, N, and O [6, 15].

When space vehicle flies at a very high Mach number, a great amount of kinetic energy is converted into internal energy of the gas across the strong shock wave. It results to a very high temperature. Intense frictional dissipation within the hypersonic boundary layer releases a lot of heat and can lead to chemical reaction. If the temperature of the shock layer is high enough, the air emits and absorbs radiation. For our TSTO, the maximal temperature on the blunt nose, the front of the wing, and the contour of the scramjet engine are estimated as 1300 °C, 1200 °C, and 1350 °C, respectively. Since the highest temperature in the separation process is less than 2000 K, the dissociation of O_2 and its chemical reaction could be neglected.

When a temperature of gas is less than 800 K, the vibration energy of the molecules is not significant. With a low pressure, the air could be still considered as a calorically perfect gas and the state equation is given in Eq. (C.36), where the ratio of specific heats $\gamma = \frac{c_p}{c_v}$ is constant.

If the temperature is raised over 800 K, but less than 2000 K, the vibration energy of the molecules becomes significant. The excitation of vibration degrees of freedom causes the specific heats dependent on temperature. In NASA-Ames, the calorically perfect gas model is replaced by real gas model with a similar mathematical form

$$p = (\tilde{\gamma} - 1)[E_S - \frac{\rho}{2}(u^2 + v^2 + w^2)]. \tag{L.1}$$

The variable $\tilde{\gamma}$ is calculated in a "curve fit routine" to replace the constant ratio of specific heats at high temperature.

$$\tilde{\gamma} = A_1 + A_2 Y + A_3 Z + A_4 YZ + A_5 Y^2 + A_6 Z^2 + A_7 YZ^2 + A_8 Z^3 + \frac{A_9 + A_{10} Y + A_{11} Z + A_{12} YZ}{1 + \exp[(A_{13} + A_{14} Y) + (Z + A_{15} Y + A_{16})]}, \tag{L.2}$$

$$Y = \log_{10}(\rho / 1.292), \tag{L.3}$$

$$Z = \log_{10}(e / 78408.4), \tag{L.4}$$

where e is the specific internal energy. In this real gas model, the speed of sound in air a is further superseded by

$$a^2 = \varepsilon\left\{B_1(\tilde{\gamma} - 1)\left[\tilde{\gamma} + B_{2\varepsilon}(\frac{\partial \tilde{\gamma}}{\partial e})_\rho\right] + B_{3\rho}(\frac{\partial \tilde{\gamma}}{\partial \rho})_\varepsilon\right\}. \tag{L.5}$$

The constants A_i (i=1,⋯,16) and $B_1, B_{2\varepsilon}, B_{3\rho}$ are given in Mollier-fit routines [41, 85].